BULGARIAN CHEMICAL COMMUNICATIONS

Dear readers,

This special issue of Bulgarian Chemical Communications is dedicated to the *Fifth scientific seminar in physical chemistry for young scientists and PhD students* that has been organized by the Institute of physical chemistry "Acad. Rostislaw Kaischew", Bulgarian Academy of Sciences, and held in Sofia, Bulgaria, 19-21 April 2016. Initiated five years ago by a team of young researchers, the seminar became an annual event covering a wide range of research fields related to physical chemistry. More than 60 young scientists attended the fifth edition of the conference. Five sponsors were attracted to fund the organization of the meeting and to promote their activities in natural science. The papers of this issue represent full text articles written on topics that were vastly discussed at the *Fifth scientific seminar in physical chemistry for young scientists and PhD students*.

Anna Gyurova & Ivaylo Dimitrov
Guest Editors

Effect of cerium ions on the protective ability of Al$_2$O$_3$ films formed anodically during their sealing in aqueous solutions

R. A. Andreeva[1], E. A. Stoyanova[1], A. S. Tsanev[2], D. S. Stoychev[1]*

[1]*Institute of Physical Chemistry „Acad. Rostislaw Kaishew", Bulgarian Academy of Sciences, „Acad. G. Bonchev" Str., Block 11, Sofia 1113, Bulgaria*
[2]*Institute of General and Inorganic Chemistry, Bulgarian Academy of Sciences, „Acad. G. Bonchev" Str., Block 11, Sofia 1113, Bulgaria*

The influence of the process of sealing has been studied in aqueous solutions of Ce(III) ions in regard to the protective ability of Al$_2$O$_3$ film prepared anodically on aluminum. The oxide film was being formed on aluminum Al-1050 in electrolyte, containing H$_3$PO$_4$ – 40g/l, under voltostatic conditions of anodizing. The sealing of the films has been carried out in 0.5M CeCl$_3$ solution at 25° and 60°C. The composition, the morphology, the structure and the chemical state of the elements of the investigated systems have been characterized by means of scanning electron microscope (SEM), energy dispersive analysis (EDS) and X-ray photoelectron spectroscopy (XPS). Potentiodynamic and chronoamperometric studies have also been carried out aiming at establishing the influence of the Ce^{3+} ions, Ce$_2$O$_3$ phase respectively, involved and appearing in the anodically formed porous Al$_2$O$_3$ film upon its corrosion protective ability. It has been ascertained that as a result of the so accomplished sealing of the Al$_2$O$_3$ film both inside the pores, as well as on its surface Ce(OH)$_3$ and/or Ce$_2$O$_3$ are formed and occluded, which determines the decrease in the corrosion currents of the system Al$_2$O$_3$/Al in the model corrosive medium (0.1M NaCl) and this fact leads to promoting its stability with respect to pitting corrosion.

Keywords: anodization, aluminum and cerium oxides, sealing, corrosion

INTRODUCTION

Aluminum has been used in many fields, such as aerospace systems, aviation systems, auxiliary parts of locomotives and so on. However, aluminum alloys manifest many disadvantages, such as poor corrosion resistance and lower mechanical strength. It is of essential importance to improve the corrosion stability of aluminum alloys through anodization technology or passivation directly [1].

The anodization is among the most widely applied methods for surface treatment of aluminum and its alloys aiming at enhancement of the corrosion stability. It is known that the protective anodic oxide films consist of two layers: an internal one – barrier layer and an external one – porous layer. The porous layers could be the defects reducing corrosion resistance of anodized aluminum. Pitting corrosion could be easily developing in porous layers due to electrochemical processes occurring between intermetallics and grain boundaries [2]. Hence, it is necessary to develop such kind of methods leading to sealing of the pores within porous layers, which would help to improve mechanical and chemical properties [3-5].

Sealing concepts involve various combinations of temperature and sealing bath chemical composition – all of them promoting the corrosion resistance to a certain degree [6]. Sealing traditionally is being done through immersion in boiling water – the so called "hot water sealing" method [7-9]. The need of applying high temperature to achieve slow kinetics, however, means considerable energy consumption [10]. As a result the hot water process has been gradually replaced since 1980s by cold sealing [8]. Dichromate and nickel acetate sealing are well established now to be the most effective sealing methods for corrosion prevention [6]. However, it has been proved that Cr^{6+} ions have toxic effect [9, 11-13]. A number of sealants have been put forward for sealing applications and some new sealing processes are also developed [14]. In spite of these efforts to improve the performance, more convenient and effective processes are still needed [15].

The aim of the present work was to study the influence of the cerium ions, included as component of the solution for sealing of anodically formed oxide films, respectively the role of cerium oxides/hydroxides being deposited from this solution inside the pore sand on the surface, in

regard to the corrosion behavior of the system Al/Al_2O_3 in aggressive medium containing chloride ions.

EXPERIMENTAL

In the present work we have applied a conventional procedure of anodization of Al in aqueous solution of H_3PO_4. High degree of purity aluminum Al-1050 was used for anodization. The aluminum substrates (10x2x0.2 cm) were degreased in aqueous solution of NaOH (6wt. %) at 60ºC followed by etching and surface activation in aqueous solution of HNO_3 (50 wt. %) for 30s at room temperature. Anodization was conducted under constant cell potential in 4wt.% H_3PO_4 aqueous solution. The temperature in each case was maintained constant at 25ºC. The DC voltage in each case was 40 V. The current density was varied from 2 to 0.2 mA.cm^{-2}. The aluminum sample was anodized for 120 min. After anodizing the samples were rinsed with distilled water and then sealed. The thickness of the formed Al_2O_3 layers varied between 5 and 7 µm.

Two different sealing techniques were applied to the anodic films after anodizing:
1. Boiling distilled water sealing (pH 6–7.5) for 60 min.
2. $CeCl_3$ sealing: The specimens were dipped in 0.5M $CeCl_3$ solution (at 25ºC for 48 h and at 60ºC for 2 h).

All the samples were rinsed by cold (25º C) water after sealing and air dried. The thickness of formed conversion layers was about 2 µm.

The morphology, structure and elemental composition of the aluminum oxide films, as well as the distribution of the elements on the aluminum surface, prior to and after the deposition and sealing of the protective layers, were observed by the electron microscope JEOL JSM 6390 (under the conditions of secondary electron image - SEI, back-scattered electrons - BEC and characteristic energy dispersive X-rays EDS, the applied voltage was 20 kV, $I \sim 100$ µA) and XPS studies. The XPS measurements were carried out on AXIS Supra electron- spectrometer (Kratos Analitycal Ltd.) using monochromatic AlK$_\alpha$ radiation with a photon energy of 1486.6 eV. The energy calibration was performing by normalizing the C1s line of adsorbed adventitious hydrocarbons to 285.0 eV. The binding energies (BE) characterize the surrounding in the depth of the films and they were determined monitoring the areas and binding energies of C1s, O1s, Al2p, Na1s and N1s photoelectron peaks. Using the commercial data-processing software of Kratos Analytical Ltd. the concentrations of the

different chemical elements (in atomic %) were calculated by normalizing the areas of the photoelectron peaks to their relative sensitivity factors.

The corrosion behavior of the samples was tested in 0.1M NaCl ("p.a." Merck) model medium at 25°C. Platinum electrode was used as the counter electrode having dimensions 10x10x0.6 mm, while the reference electrode was saturated calomel electrode (SCE), (E_{SCE}=+0.240V vs. SHE). All the potentials in this study are compared to SCE. The anodic and cathodic polarization curves were obtained by means of a potentiostat/galvanostat Gamry Interface 1000, whereupon the obtained results were processed with the help of specialized software. The curves were recorded at a sweeping rate of the potential 1.0 mV.s^{-1} in the range of potentials from –2500 up to + 2500 mV.

RESULTS AND DISCUSSION

Figure 1 illustrates SEM images of as deposited anodically formed protective Al_2O_3 films on aluminum Al-1050 (Fig. 1a); the same films after their sealing in boiling distilled water (Fig. 1b) and those sealed in 0.5M $CeCl_3$ solution (Fig. 1c -1f), respectively at 25º and 60ºC. Figure 1a illustrates the porous structure of Al_2O_3 prior to subjecting the anodically prepared film to the so called "sealing procedure", with the purpose to enhance its protective ability. As a result of the process of sealing in boiling distilled water (the widely applied standard sealing procedure) one can observe a definite decrease in the size of the pores of the oxide film (Figure 1b). Obviously, the reason for this effect is owing to the fact that the sealing in boiling distilled water results in partial filling up of the pores by the hydrated aluminum oxide - boehmite (Al_2O_3+ H_2O → 2AlO(OH)) [1].

Figure 1c – e illustrates the morphology on the surface of the treated samples after sealing of the anodic layer in aqueous solution of 0.5M $CeCl_3$ at temperature 25ºC in the course of 48 hours. It can be seen in the figure that in the case of such treatment on the surface of the anodic film a thick coating has been formed, which was screening the pores of the anodic film. It is built up of segments having macro-cracks (Fig.1c), whereupon the boundaries between them (the darker zones Fig.1d) are also formed by a layer of similar structure, but having smaller thickness. The EDS analyses of these layers in the bright spots and in the dark spots of the formed layer shows that a coating of cerium oxide has been deposited [16]. Evidently, as a result of the processes of sealing a cerium oxide layer is being deposited, which initially is filling up the

pores on the surface of aluminum oxide and there after a conversion film is being formed, which is covering up the treated surface entirely. Figure 1f shows SEM image of the anodized aluminum surface after the sealing process in the course of 2 hours in aqueous solution of 0.5M CeCl$_3$ at
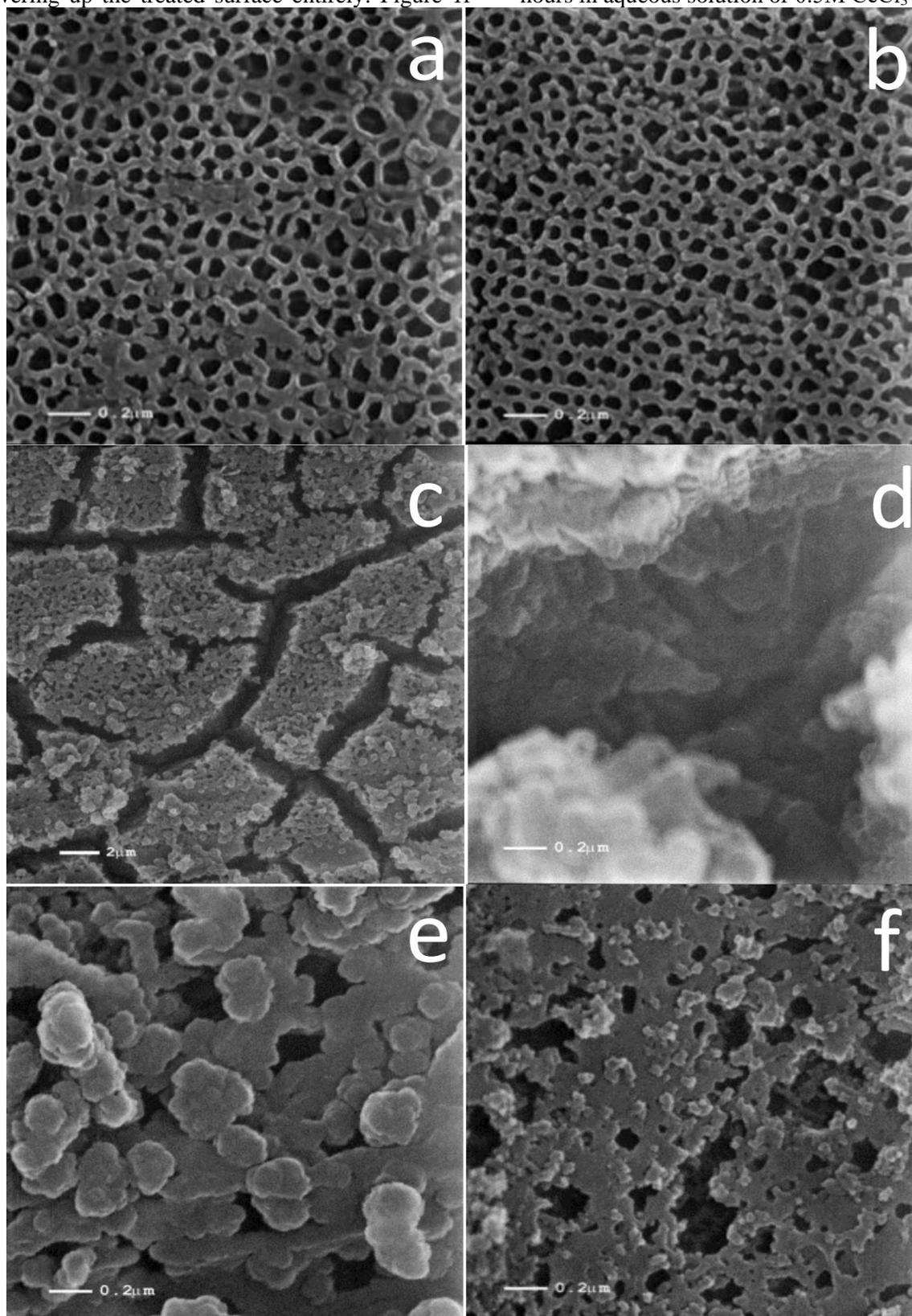

Fig.1. Surface morphology of anodically formed films: (a) unsealed Al$_2$O$_3$ film formed at 40V for 2 hours, X 50 000; (b) sealed in boiling water (1h), X 50 000; (c) sealed in cold CeCl$_3$ (48h), X 5000; (d and e) sealed as in (c) at magnification X 50000; (f) sealed in hot CeCl$_3$ (2h), X 50000.

temperature of 60°C. The so obtained conversion film on the anodized surface in this case is continuous and uninterrupted and it consists of some smaller aggregates. The EDS proved that depending on the conditions of sealing the thickness of the conversion film grows up,

respectively the concentration of cerium on the anodized aluminum substrate is growing up from 5.29% after time interval of sealing 120 minutes in hot solution (60°C) of 0.5M $CeCl_3$, up to 10.42 wt.% in the case of sealing at room temperature for 48 hours of immersion time interval [16].
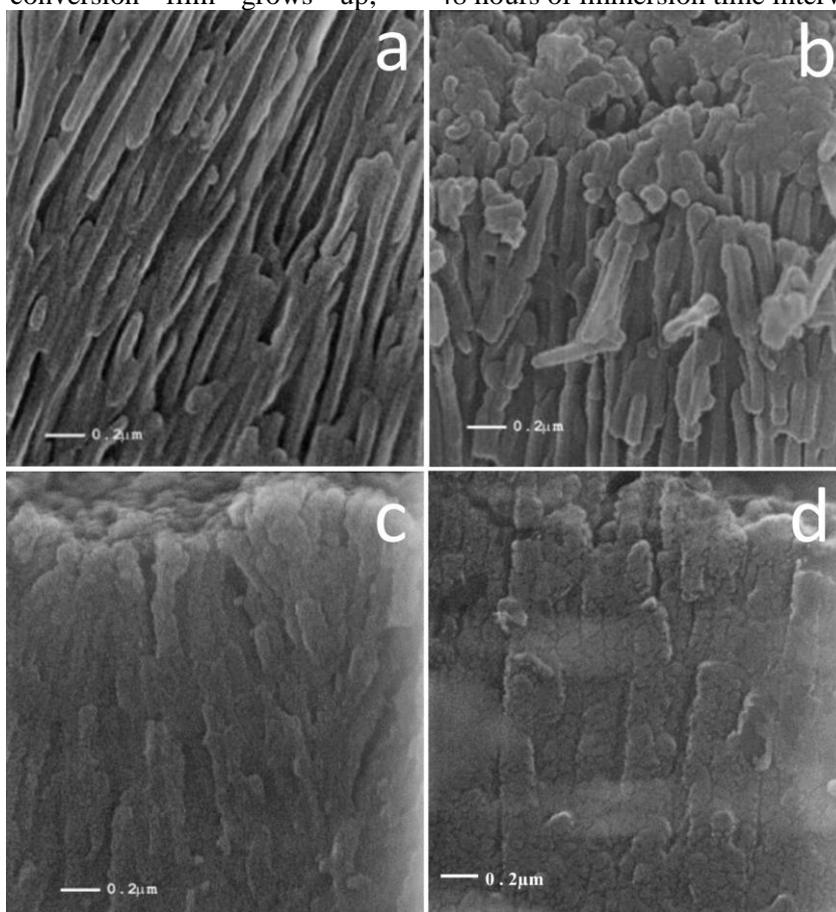

Fig. 2. The cross section structures of: (a) unsealed as deposited Al_2O_3 film formed at 40V for 2 hours on Al-1050; (b) the same layer sealed for 1h in boiling water; (c) sealed in cold $CeCl_3$ for 48h; (d) sealed in hot $CeCl_3$ for 2h.
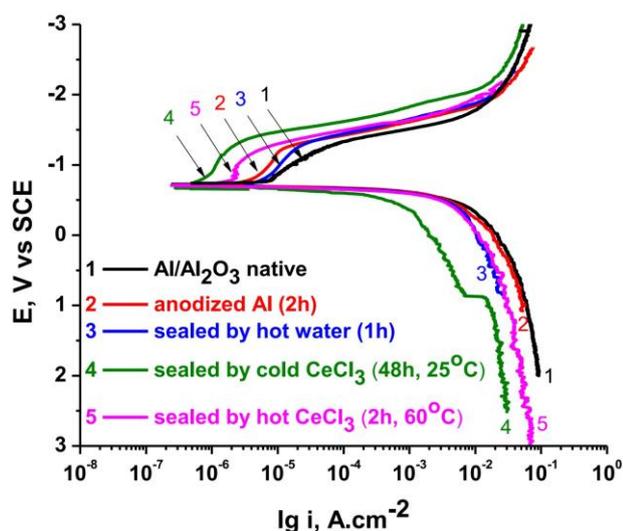

Fig. 3. Polarization curves of systems tested in 0.1M NaCl at 25°C.

Figure 2 presents the morphology of the cross section of the anodic film, obtained in phosphoric acid before and after its treatment in boiling

distilled water or in aqueous solution of 0.5M $CeCl_3$. It is seen that as a result of the sealing carried out in boiling distilled water the anode layer becomes more compact (Figure 2b). In the case of the samples, sealed in 0.5M $CeCl_3$ (Figure 2c and 2d), in addition to the even stronger sealing of the porous part of the anodic film one can observed also difference in the thickness of the formed surface film. This effect is the result of occurring of the processes of sealing–filling up of the pores of Al_2O_3 by cerium oxides and hydroxides and deposition of a superficial conversion cerium oxide film upon the anodically formed Al_2O_3 layer.

Figure 3 presents the anodic and cathodic potentiodynamic curves for: non-anodized aluminum (Al-1050) sample; anodized aluminum sample, as well as for the anodized aluminum sample, sealed respectively in boiling distilled water and in aqueous solution of 0.5M $CeCl_3$ (at temperatures 25° and 60°C) in corrosive medium of 0.1M NaCl.

Judging from the changes in the course of the polarization curves one can conclude that the sealing of the anodic oxide films in 0.5M aqueous solution of $CeCl_3$ at temperature ~~60~~25°C (Fig. 3) leads to more substantial decrease in the corrosion current of the system Al/Al_2O_3 under the conditions of a steady state, observed at the chosen rate of sweeping the potential (Table 1).

Table 1. Electrochemical parameters (E_{corr} and i_{corr}) obtained from the potentiodynamic curves.

Investigated samples	Corrosion potential, E_{corr}, V	Corrosion current, $i_{corr,}$ Acm^{-2}
Al/Al_2O_3 native system	-0.660	8×10^{-6}
Unsealed anodically formed Al/Al_2O_3 system	-0.710	1.75×10^{-6}
Anodically formed Al/Al_2O_3 system sealed in boiling water	-0.701	1.65×10^{-6}
Anodically formed Al/Al_2O_3 system sealed in cold $CeCl_3$ (48h)	-0.674	2.27×10^{-7}
Anodically formed Al/Al_2O_3 system sealed in hot $CeCl_3$ (2h)	-0.702	3.16×10^{-7}

The juxtaposition of the cathodic polarization curves, characterizing the depolarization reaction of reduction of oxygen, shows that the filling up of the pores of the anodic oxide film with $Ce(OH)_3$ and Ce_2O_3 (see Fig.5b) inhibits the reaction of reduction of oxygen, which is most strongly expressed for treatment time intervals respectively 48 hours, at room temperature – Fig. 3 and 2 hours–at temperature 60°C. A similar effect, although weakly expressed, is observed also with the respective anodic potentiodynamic curves. For comparison Fig. 3 gives the anodic and the cathodic potentiodynamic curves for anodized samples, sealed in boiling distilled water for 60 minutes. Obviously, the standard sealing in boiling distilled water, leading to filling up of the pores of the anodic film by hydrated aluminum oxide (boehmite) [1], whose influence has a barrier effect, is resulting in insignificant changes in the kinetics of the corrosion process (Fig.3) and it is characterized by significantly weaker protective effect comparing with sealing in solutions of 0.5M $CeCl_3$.

In order to check the validity of this conclusion, we carried out a parallel cycle of chronoamperometric measurements with analogous samples, where upon the samples were exposed to corrosive medium for 60 minutes at a potential, close to the potential of pitting formation [17] of aluminum Al-1050. This cycle was accomplished by recording the chronoamperometric curves for each one of the studied samples. After conducting this set of experiments, the samples were washed thoroughly with distilled water and subjected to XPS analyses, with the aim to establish the occurring changes in the chemical composition and in the chemical state of the elements in the surface layer of the systems Al/Al_2O_3 and $Al/Al_2O_3/Ce_2O_3$.
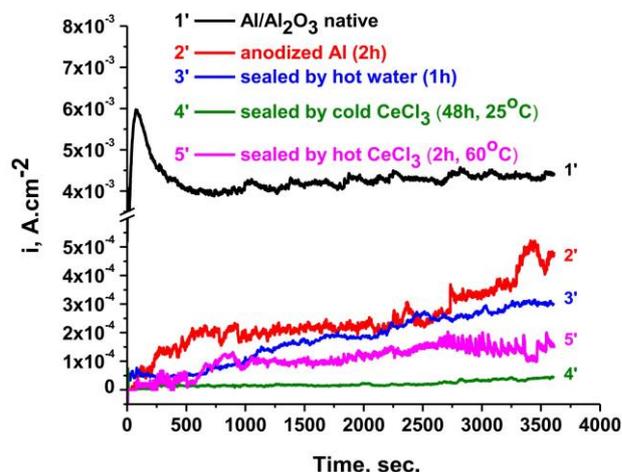

Fig. 4. Chronoamperometric curves of the systems tested in 0.1M NaCl at 25°C

Figure 4 represents the results of chronoamperometric measurements, carried out at potential -0.5V (SCE), close to the potential of pitting formation of the studied aluminum in 0.1M NaCl. Based on the course of the separate curves we can derive the character of the corrosion attack judging from the type of the appearing pitting defects. It is seen that in the case of non-treated aluminum (Al-1050) sample, after its immersion at the potential in the corrosive medium, the density of the corrosion current is increasing sharply (curve 1'), which is an indication of the appearance and development of pitting corrosion, after 75 seconds of interaction with the chloride ions. No substantial fluctuations of the current density are observed with the sample, upon which anodic film is formed, but it is not subjected to consecutive sealing procedure, until about 3400 seconds time interval (curve 2'). Thereupon the current density relatively low values

– of the order of 5.2×10^{-4} A.cm^{-2}, which is an indication for the appearance of pittings, which, however undergo quickly repassivation and they do not reach the stage of further development. It can be seen in the chronoamperogram that the relatively thick porous layer Al₂O₃, which had been formed during the anodic treatment, is prolonging the incubation period for the appearance of pitting corrosion on aluminum from ~75 to ~3400 seconds. The samples, sealed in boiling distilled water (curve 3'), both in cold solution (curve 4') and in hot solution (curve 5') of CeCl₃, are characterized by stable protective film. The proofs for this conclusion are the low values of the corrosion currents and the lack of fluctuations of their values in the respective chronoamperograms (Fig.4).

It follows from the results, obtained with the additionally subjected to sealing procedure samples, that in accordance with the established stability of the studied systems with respect to the appearance and development of general and pitting corrosion, they can be arranged in the following order: Al<Al/Al₂O₃<Al/Al₂O₃ (sealed in boiling distilled water) <Al/Al₂O₃/Ce₂O₃ (sealed in 0.5M CeCl₃ at 60°C for 120 minutes) <Al/Al₂O₃/Ce₂O₃ (sealed in 0.5M CeCl₃ at 25° C for 48 hours).

On the basis of the XPS analyses, carried out with the studied samples, including the corrosion products being formed on their surface under the conditions of anodic polarization at potential close to that of the pitting formation on aluminum in 0.1M NaCl, an attempt was made to explain the character of the corrosion process of the studied systems, when during the sealing process of the anodically formed Al₂O₃ layer cerium ions are also participating. It was based on juxtaposition of the data for the composition and the chemical state of the elements on the surface of the samples. This includes comparison of the data on as deposited samples, the samples after applying the sealing procedure and those after the occurring changes, which appear on their surface during anodic polarization (the chronoamperometric measurements), simulating corrosion process under conditions close those for pitting formation.
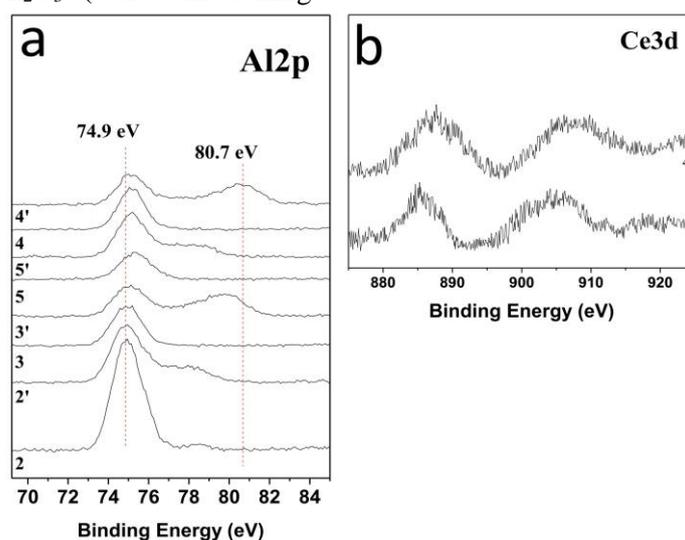

Fig. 5. a)Al2p spectra of the investigated samples: 2 – Al/Al₂O₃ unsealed; 2' – the same system after chronoamperometry; 3 – Al/Al₂O₃ sealed in boiling water; 3'– the same system after chronoamperometry; 4 –Al/Al₂O₃ sealed in cold CeCl₃ for 48h; 4' – the same system after chronoamperometry; 5 – Al/Al₂O₃ sealed in hot CeCl₃ for 2h; 5'– the same system after chronoamperometry; **b)** Ce3d spectra of the films: 4 – corresponds to the curve 4 on Fig.3 – Al/Al₂O₃ sealed in cold CeCl₃ for 48h; 4' – corresponds to the curve 4' on Fig.4 – the same system after chronoamperometry measurements.

Figure 5a represents the spectra ofAl2p for the studied samples. It can be seen in the figure, that the spectra of the samples, non-treated by anodic polarization at potential close to that of pitting formation (i.e. after the chronoamperometric measurements) are comparatively widely extended. The spectra of the samples, subjected to chronoamperometric investigtion, are considerably different. Most of them (spectrum 2', 3', 4', 5') display additional peaks at higher binding energies. Aiming at more precise identification of the nature

and the quantity of the separate chemical compounds on the surface of the films, a deconvolution of the basic peaks of Al2p (Fig.6 a-h) and O1s was made (not given here).

It is seen in the deconvoluted spectrum of Al2p for the anodized Al sample (Fig.6a) that it can be divided into three peaks – two of them have binding energies of 74.7 eV, 76.0 eV and there is a small peak at 78.5 eV. In this way the presence mainly of Al₂O₃ on the surface of the sample not undergoing chronoamperometric investigation is proven

(characteristic peak at 74.7 eV) [18] and also some small quantities of $Al(OH)_3$ (the characteristic peak 76.0 eV) [19]. The third peak at BE 78.5 eV is owing to the presence of agglomerates of $Al(OH)_3$ having various sizes, which determines the different extent of their charging [20]. For all the samples we have compared the areas of the deconvoluted peaks of Al2p, normalized with respect to corresponding value of Relative Sensitivity Factors (RSF), with the areas of the peaks normalized in regard to the respective value of RSF for the deconvoluted peaks of O1s. The obtained ratio between them is in correspondence with the stoichiometry of the respective compounds: Al_2O_3 and $Al(OH)_3$. The spectrum of Al2p (Fig.6b) on the surface of the same sample, subjected to anodic polarization up to a potential close to the potential of pitting formation (i.e. after the chronoamperometric characterization) shows that the surface consists again of Al_2O_3 and $Al(OH)_3$ mainly, however here, as a result of the occurred corrosion processes of anodic dissolution, the quantity of $Al(OH)_3$ is smaller (see Table 2, sample of anodized aluminum prior to and after the chronoamperometry). One samples decreases from 4.55 to 1.19.

Table.2. Comparison of the areas of the integrated peaks, calculated after deconvolution of the spectra of Al2p

Different treatment methods	Area of the integrated peak(s) associated with Al_2O_3, [a. u.]*	Area of the integrated peak(s) associated with AlOOH (and $Al(OH)_3$), [a. u.]*	Ratio of the areas of Al_2O_3 to AlOOH (or/and $Al(OH)_3$), [a. u.]*
Al/Al_2O_3 unsealed	4653	1023	4.55
Al/Al_2O_3 unsealed – after chronoamperometry	2294	1923	1.19
Al/Al_2O_3 sealed in boiling water	1280	730	1.75
Al/Al_2O_3 sealed in boiling water– after chronoamperometry	1784	1618	1.10
Al/Al_2O_3 sealed in hot $CeCl_3$ for 2h	0	1443	-
Al/Al_2O_3 sealed in hot $CeCl_3$ for 2h– after chronoamperometry	0	3191	-
Al/Al_2O_3 sealed in cold $CeCl_3$ for 48h	0	1852	-
Al/Al_2O_3 sealed in cold $CeCl_3$ for 48h– after chronoamperometry	0	3174	-

*arbitrary units

A similar picture is also observed with the anodized sample, subjected to sealing in boiling distilled water (in the course of 1 hour at 100°C – Fig. 6c). In the Al2p-spectrum of the studied sample again peaks are observable, characteristic of Al_2O_3 and $Al(OH)_3$, but here the ratio $Al_2O_3/Al(OH)_3$ is substantially different from that of the sample, not subjected to this treatment. In the case of the anodized sample, sealed in boiling distilled water, the amount of $Al(OH)_3$ is significantly higher than that of the anodized but not sealed sample, whereupon the ratio $Al_2O_3/Al(OH)_3$ for the latter sample is 4.55, while in the case of former sample it is 1.75. No peaks are displayed by this sample, which could be associated with the presence of particles having different extent of charging, i.e. the surface is more homogeneous. After carrying out chrono-amperometric measurements with this sample, one can observed again on the surface the presence of Al_2O_3 and $Al(OH)_3$, and in this case also the quantity of $Al(OH)_3$ is decreasing again (from 1.75 down to 1.10 – see Fig. 6c, d). In contrast to the sample, not subjected to chronoamperometric investigation, here the presence of phases is observable having different extent of charging, due to particles of various sizes (hence different charging) both of Al_2O_3 (the peak at 76.2 eV), as well as that of $Al(OH)_3$ (the peak at 79.9 eV). This splitting of the peaks is visible also in the spectrum of O1s (not given here).

In the case of the sample, sealed in solution of $CeCl_3$ in the course of 2 hours at 60°C – Fig. 6e and 6f, the presence of one basic peak is observable at 75.0 eV, characteristic of AlO(OH). Considering this peak, after carrying out the chronometric investigation, again an additional splitting of the basic peak at 75 eV is observed – splitting into two additional peaks. Their presence is again due to the

appearance (after the chronoamperometric investigation) of agglomerates of AlO(OH) on the surface having different charge.

The spectrum of Al2p for sample anodized and sealed in 0.5 M $CeCl_3$ for 48h at temperature 25°C, indicates the presence of a single peak at 75.1 eV, characteristic of AlO(OH) (Fig. 6g). A specific feature of this samples is the fact that after subjecting it to chronoamperometric investigation,

a multitude of agglomerates of AlO(OH) appears on the surface having various sizes and therefore different charging (Fig. 6h). This phenomenon is observed also in the spectrum of O1s of these samples. The spectra of Ce3d for these samples – before and after the chronoamperometric investigation (Figure 5b) – prove the formation of Ce_2O_3 layer.
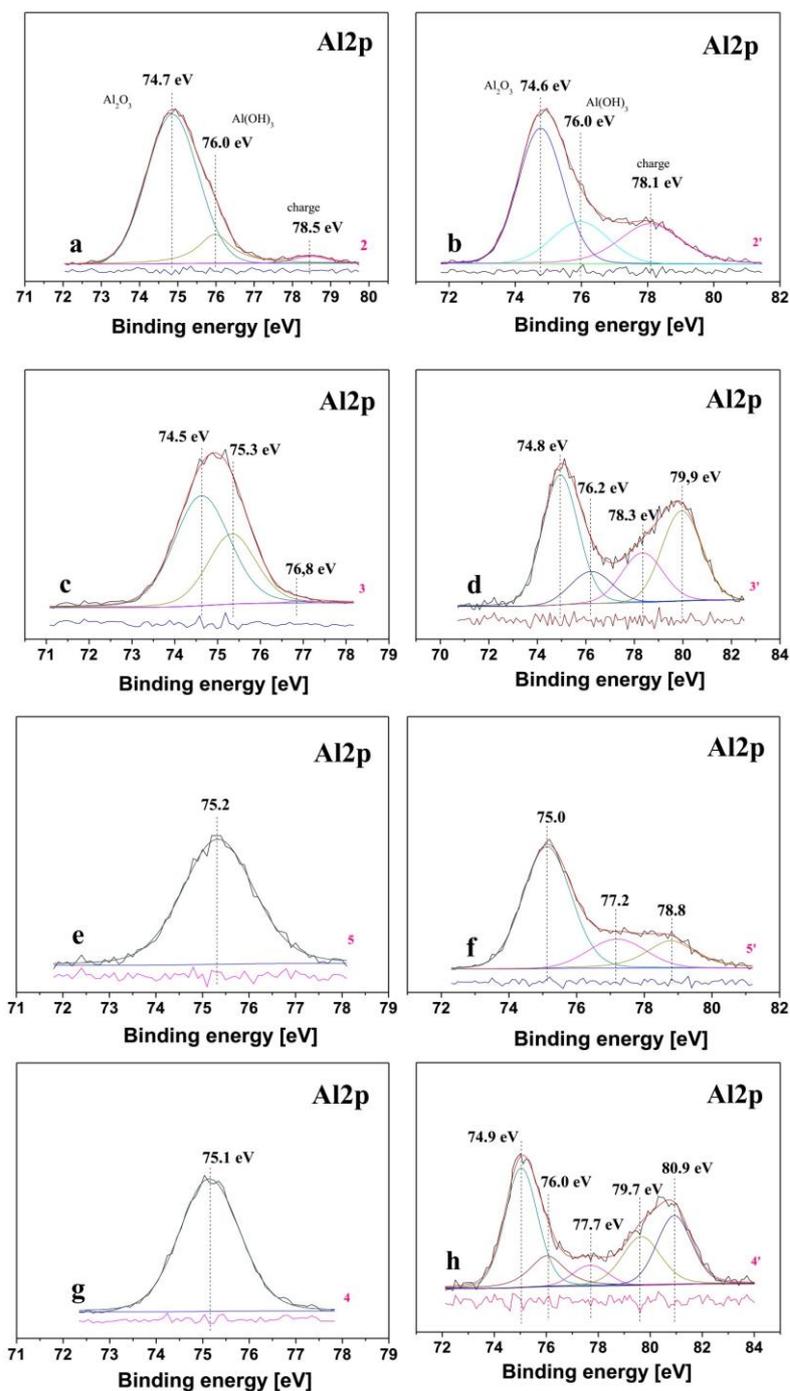
Fig 6. Deconvoluted Al2p spectra of the films: (a) Al/Al₂O₃ unsealed; (b) – the same system after chronoamperometry; (c) – Al/Al₂O₃ sealed in boiling water; (d) – the same system after chronoamperometry; (e) Al/Al₂O₃ sealed in hot CeCl₃ for 2h; (f) the same system after chronoamperometry; (g) Al/Al₂O₃ sealed in cold CeCl₃ for 48h; (h) – the same system after chronoamperometry.

Table. 3. Concentrations of the chemical elements in the investigated films. The concentrations are calculated from XPS spectra of the elements, presented in atomic percents.

Different treatment methods	Amount of Al in the layer [at.%]	Amount of Ce in the layer [at.%]	Amount of O in the layer [at.%]
Al/Al_2O_3 sealed in hot $CeCl_3$ for 2h	9.5	0.9	89.6
Al/Al_2O_3 sealed in hot $CeCl_3$ for 2h– after chronoamperometry	18.7	0.9	80.4
Al/Al_2O_3 sealed in cold $CeCl_3$ for 48h	14.0	0.8	85.2
Al/Al_2O_3 sealed in cold $CeCl_3$ for 48h – after chronoamperometry	18.5	0.8	80.7

The spectrum of the cerium oxide layer, formed on the surface of the oxidized Al substrate, sealed in $CeCl_3$ solution in the course of 2 hours at temperature 60°C, is characterized by complex structure, owing to hybridization of cerium ions with the ligand orbitals of oxygen and partial occupation of the 4f valence orbital [21]. As a result of this there occurs spin-orbital splitting of the doublet peaks, whereupon each doublet as an additional structure, owing to the effect of the final state. The peaks, denoted by u''' and v''' at 916.9 eV and 898.4 eV are characteristic of CeO_2 and result from a $3d^{10}4f^1$ final state. The spectrum shows that as a result of the process of immersion treatment, a layer of Ce_2O_3 has been formed.

It is seen in Table 3 that the relative concentrations of cerium oxide of both samples, prior to and after the chronoamperometric investigation, remain constant. In the case of the sample, sealed in solution of $CeCl_3$ in the course of 2 hours at 60°C, the concentration of Ce_2O_3 prior to the chronoamperometric investigation is 0.9 at.% (see Table 3). No change in the concentration of Ce_2O_3 after chronoamperometric investigation. In the case of the sample anodized and sealed in 0.5M $CeCl_3$ for 48h at temperature 25°C, the concentration of Ce_2O_3, before the chronoamperometric investigation, is 0.8 at.% (see Table 3). After the investigation it is again 0.8 at.%. This fact gives evidence that as a result of the chronoamperometric measurements, the chemical composition with respect to the concentration of ceria on the surface of the samples is preserved unchanged. Therefore we can conclude that the corrosion attack in this case does not lead to any disruption of the integrity of the oxide films and no localization of the corrosion process has been registered.

CONCLUSIONS

The obtained results show that the sealing of the anodic oxide films in boiling water or in aqueous solution of $CeCl_3$, determines different corrosion-protection behavior of the systems Al/Al_2O_3 and $Al/Al_2O_3/Ce_2O_3$. It follows from these results that the anodic formation of porous protective layers of Al_2O_3 on Al-1050 improves to a considerable extent its corrosion behavior. The accomplishment of an additional post-treatment "sealing procedure" in boiling water improves even better the protective effect of the anodic film in regard to the processes of pitting corrosion and general corrosion. The XPS analyses, registering changes in the composition on the surface of the studied samples as a function of the different treatment procedures carried out, showed that under conditions close to the appearance of pitting corrosion, depending on the type of these treatment processes, during the corrosion process changes in the chemical composition are occurring (in favor of increasing the concentration of $Al(OH)_3$), which improve the corrosion behavior of the system Al/Al_2O_3.

In the course of sealing procedure accomplished in the presence of cerium ions, in addition to the partial blocking of the pores of the anodic Al_2O_3 layer, there appears also a barrier action of the conversion formed cerium oxide layer upon the anodic coating. There upon the conversion cerium oxide layer is not influenced practically by the corrosion attack of the aggressive medium. The changes occurring in the zone of potentials close to the potential of pitting formation on aluminum, consist mainly in increasing the concentration of the corrosion products being formed (AlOOH and $Al(OH)_3$). As a result of these two effects the corrosion stability of the system $Al/Al_2O_3/Ce_2O_3$ promoted, inclusively in respect to the appearance and development of pitting corrosion.

REFERENCES

1. S. Wernick, R. Pinner, P. Sheasby, The surface treatments ofaluminium and its alloys, 5th Edition, ASM International and Finishing Publications Ltd. Metals Park, Ohio, 1987.
2. Y. Guo, G.S. Frankel, *Surf. Coat. Technol.,* **206**, 3895 (2012).
3. K.Z. Chong, T.S. Shih, *Mater. Chem. Phys..* **80**, 191 (2003).
4. C. Quan, Y.D. He, *Surf. Coat. Technol.,* **269**, 319 (2015).
5. X.K. Yang, Q. Li, S.Y. Zhang, F. Liu, S.Y. Wang, H.X. Zhang, *J. Alloys Compd.,* **495**, 189 (2010).
6. Y. Zuo, P. Zhao, J. Zhao,*Surf. Coat. Technol*., **166,** 237 (2003).
7. M.C. Garcia-Alonso, M. Escudero, J. Gonzalez-Carrasco, *Materials and Corrosion-Werkstoffe Und Korrosion*, **52,** 524 (2001).
8. J.A. Gonzalez, V. Lopez, E. Otero, A. Bautista, R. Lizarbe, C. Barba, J. Baldonedo, *Corros. Sci.*, **39,**1109 (1997).
9. H. Herrera-Hernandez, J. R. Vargas-Garcia, J.M. Hallen-Lopez, F. Mansfeld, *Materials and Corrosion-Werkstoffe Und Korrosion*, **58,** 825 (2007).
10. V. Lopez, J. Gonzalez, A. Bautista, E. Otero, R. Lizarbe, *Corros. Sci*., **40**,693(1998).
11. M. Whelan, K. Barton, J. Cassidy, J. Colreavy, B. Duffy, *Surf. Coat. Technol*., **227**, 75(2013).
12. M. Whelan, J. Cassidy, B. Duffy, *Surf. Coat. Technol*., **235**, 86 (2013).
13. J.M. Zhao, S.L. Chen, P. Huo, *Corros. Eng. Sci. Techn*., **47**, 203 (2012).
14. L. Hao, B.R. Cheng, *Metal Finishing*, **98**, 8 (2000).
15. J. Lee,Y. Kim, H. Jang, U. Jung, W. Chung, *Procedia Engineering*, **10**, 2803 (2011).
16. R. Andreeva, E. Stoyanova, A. Tsanev, D. Stoychev, *Corr. Eng. Sci. Techn*., in press
17. P. Szklarska-Smialowska, *Corros. Sci.* **41,** 1743 (1999).
18. A. Lippitz, E. Kemnitz, O. Bose, W.E.S. Unger, *Fresenius J. Anal. Chem*., **358**, 175 (1997).
19. A. Nylund, I. Olefjord, *Surface and Interface Analysis*, **21**, 283 (1994).
20. D. Stoychev, I. Valov, P. Stefanov, G. Atanasova, M. Stoycheva, Ts. Marinova, *Materials Science and Engineering C,* **23,** 123 (2003).
21. X. Yu, G. Li, *Journal of Alloys and Compounds,* **364**, 193 (2004).

ЕФЕКТ НА ЦЕРИЕВИТЕ ЙОНИ ВЪРХУ ЗАЩИТНАТА СПОСОБНОСТ НА АНОДНО ФОРМИРАНИ Al₂O₃ СЛОЕВЕ ПРИ УПЛЪТНЯВАНЕТО ИМ ВЪВ ВОДНИ РАЗТВОРИ

Р. А. Андреева[1], Е. А. Стоянова[1], А. С. Цанев[2], Д. С. Стойчев[1]*

[1]Институт по физикохимия „Академик Ростислав Каишев“, Българска академия на науките, ул. „Акад. Г. Бончев“ бл. 11, София 1113, България.
[2]Институт по обща и неорганична химия,Българска академия на науките, ул. „Акад. Г. Бончев“ бл. 11, София1113, България.

(Резюме)

Изучено е влиянието на процеса на уплътняване във водни разтвори на Ce(III) йони върху защитната способност на анодно получен Al₂O₃ филм върху алуминий. Оксидният филм е формиран върху алуминий Al-1050 в електролит, съдържащ 40g/l H₃PO₄, при волтастатични условия на анодиране. Уплътняването на филмите е осъществено в 0.5M разтвор на CeCl₃ при температури 25° и 60ºC. Съставът, морфологията, структурата и химичното състояние на елементите на изследваните системи са охарактеризирани с помощта на сканираща електронна микроскопия (SEM), енергийно дисперсионен анализ (EDS) и рентгенова фотоелектронна спектроскопия (XPS). Проведени са и потенциодинамични и хроноамперометрични изследвания, с цел установяване на влиянието на включващите се в анодно формирания Al₂O₃ филм цериеви йони, респ. формираща се Ce₂O₃ фаза, върху корозионно-защитната му способност. Установено е, че в резултат на проведеното уплътняване на Al₂O₃ филм както в порите, така и на повърхността му се формират и включват Ce(OH)₃ и/или Ce₂O₃, което обуславя понижаване на корозионните токове на системата Al₂O₃/Al в моделната корозионна среда (0.1M NaCl) и води до повишаване на устойчивостта й към питингова корозия.

Activated nano-porous carbons as electrode materials for supercapacitors in aqueous electrolyte

L. Soserov[1]*, A. Stoyanova[1], R. Stoyanova[2]

[1]Institute of Electrochemistry and Energy Systems, Bulgarian Academy of Sciences, 10, G. Bonchev Str., 1113 Sofia, Bulgaria

[2]Institute of General and Inorganic Chemistry, Bulgarian Academy of Sciences, 11, G. Bonchev Str., 1113 Sofia, Bulgaria

In the present work is studied the effect of two types binders (polyvinylidene fluoride (PVDF) and polytetrafluoroethylene (PTFE)) on the pore structure of chosen nanocarbons as electrode materials for symmetric supercapacitors. The PVDF influences both the micro and macro pores, while PTFE attacks preferentially the macropores. The commercial product TDA-Research with PTFE binder, which possess the highest micropore volume and micropore surface, shows the highest and stable discharge capacity in comparison to both other studied carbons. The addition of 6.2% β-Ni(OH)$_2$ to the positive electrode in the supercapacitor increases the discharge capacity significantly (around 35-40% at 30-60 mAg^{-1}). The obtained result is promising and it deserves further examination.

Keywords: activated nanocarbon, binder, supercapacitor, aqueous electrolyte, Ni(OH)$_2$

INTRODUCTION

In the recent years many research groups work on the development and the use of alternative energy sources in order to respond to the enhanced needs of light and compact high capacity sources [1].

Among the various realistic solutions, energy can in particular be stored electrochemically in accumulators (batteries) and supercapacitors. Supercapacitor is one of the most promising electric energy storage devices, which possesses high power density, ultrafast charge discharge capability as well as long cycling life. It has a great application potential in the fields of hybrid electric vehicles (HEVs), EVs, portable electronic devices, and renewable energy [2].

Recently, supercapacitors have been proposed and widely marketed for variousapplications. Coupled for example with a battery/internal combustion engine in hybrid vehicles, supercapacitors improve the battery lifetime/fuel economy and the energy recovery efficiency in braking. They can also stabilize current when intermittent renewable energies are introduced in the energetic mix [3].

Although supercapacitors are now commercially available, they still require improvements, especially for enhancing their energy density and cut the cost at the same time. It requires a fundamental understanding of their properties and exact operating principles, inaddition to improving electrode materials, electrolytes and integration in systems.

The physical and electrochemical characteristics of used materials are very important for the development of supercapacitors. A very important problem is associated with the physical gas phase properties of nanoporous material, like the nanopore diameter and pore size distribution, the conductivity and the accumulation of energy in the space-charge surface layer, i.e., the so-called capacitance of the thin layer obtaining the characteristic relaxation frequencies, specific energy and power densities and other characteristics of the supercapacitors [4].

A various carbon materials are investigated as electrode materials for electrical double-layer capacitors, owing to their high conductivity and surface area, a rich variety of dimensionality, excellence corrosion resistance, high thermal stability, controlled pore size distribution, processability andcompatibility in composites, relatively low cost, etc. It is usually anticipated that the capacitance of the porous carbon should be proportional to its available surface-area. In practice, the major factors that contribute to this relationship, often with a complex non-linear character, are: the assumptions in the measurement of electrode surface-area, variations in the specific capacitance with differing morphology and pore-size distribution, variation in surface chemistry, conductivity of the carbon particles, etc. There are contradictory reports in the literature on the effect of increasing surface area and porosity on the intrinsic electronic conductivity of compact carbon

* To whom all correspondence should be sent:
E-mail: l_stefanov@iees.bas.bg

powders, but the presence of micro pores is very desirable. A developed surface area and controlled distribution of pores for porous carbons, produced by well established chemical and physical activation methods, determine the electrode/electrolyte interface in supercapacitor applications [5-7].

Activated carbon is the most widely used active material due to its high surface area and relatively low cost. Its activation is used for the addition formation of porous network in the bulk of the carbon particles with high specific surface area [8]. Other advantage of those materials is the possibility to produce highly porous structures with high specific surface area and to develop various composite electrode structures by adding electrochemically active materials to the carbon matrix [4].

Further improvement of the performance of activated carbon can be achieved by a modification with transition metal oxides or hydroxides. Recently, β-Ni(OH)$_2$ has been proposed as a suitable agent for the modification of electrochemical properties of carbonaceous materials [9-12]. It has been shown that the capacity of hydroxide modified carbonaceous materials increases at the expense of the loss of cyclic stability. In fact, an ideal performance of supercapacitors included high capacitance, good stability and wide voltage window, its mass balance needs reevaluation [13]

By the construction of the supercapacitor electrode the metallic current collector is coated by slurry containing the electrochemically active material (activated carbon) together with a binder and the conductive agents (carbon black, etc.) playing as percolator between the AC grains [9]. The nature of the binder plays an important role for the capacitor performances too. The most used materials are polyvinylidene fluoride (PVDF) and polytetrafluoroethylene (PTFE).

The electrolyte also plays an important role in the supercapacitors performance. The electrolyte must possess certain properties, such as high ionic conductivity, wide voltage window, and high electrochemical and thermal stability, low viscosity, low toxicity, low cost, etc. The currently used electrolytes are aqueous electrolytes (H$_2$SO$_4$ and KOH), organic electrolytes (propylene carbonate and acetonitrile based ones), and recently ionic liquids [14]. Compared with non-aqueous electrolytes, the aqueous medium provides a much higher conductivity leading to higher power density. On the other hand, low cost and easy manipulation could be further advantages for

aqueous electrolytes. Unfortunately, the lower voltage of aqueous medium is restricted via the thermodynamic window of water at 1.23 V and it is much lower than in non-aqueous electrolytes [15].

The aim of the present work is to study effect of the binder on the pore structure of chosen carbons (commercial and synthesized products) as electrode materials for symmetric supercapacitors in alkaline solutions on their capacitance behavior. The modification of the positive electrode with 6.2% β-Ni(OH)$_2$ is also electrochemically tested.

EXPERIMENTAL
Electrode materials

In the present work three kinds of activated carbons are studied as electrode materials for supercapacitor cells – two commercial products (TDA-Research and Norit-CGP) and one synthesized carbon (AC-1400). AC-1400 is prepared by carbonization of mixtures of coal tar pitch and furfural, with a subsequent hydrothermal treatment [4]. As an additive commercial β-Ni(OH)$_2$ containing 4.2% Co (FC05(III), Umicore Cobalt & Specialty Materials) is used.

Morphological and structural characterization of the electrode materials

The materials used are structurally characterized by X-diffraction (XRD) method. The powder X-ray diffraction patterns are collected in the range from 5.3º to 80º 2θ with a constant step of 0.02º 2θ angle on Bruker D8 Advance diffractometer with Cu Kα radiation and Lynx Eye detector. Phase identification was performed with the Diffractplus EVA using ICDD-PDF2 Database.

The morphology of the electrode materials is examined by Transmission electron microscopy (TEM).

The pore structure of the carbons is evaluated by nitrogen gas adsorption. The adsorption isotherm of the sample at −196 °C is recorded and used to calculate the specific surface area, pore volumes and pore size distributions [4].

Electrochemical tests

The activated carbon materials are used to fabricate electrodes for electrochemical cells for capacity measurements. The supercapacitor cell contains two identical electrodes (surface area ~1.75 cm^2) from activated carbon (80%), graphite ABG 1005 EG-1 (10%), binder (10%) and alkaline electrolyte containing potassium hydroxide with the addition 35gL^{-1} lithium hydroxide (7M KOH/LiOH) [15]. The electrodes are fabricated by

applying two kinds of binders: PTFE difluoride). The supercapacitor cells are assembled with the addition of 6.2% β-Ni(OH)$_2$ to the positive electrode.

The formed sheet electrodes are dried at 140 °C for 12 hours and pressed under pressure of 20 MPa. The obtained electrodes are soaked in the same electrolyte under vacuum and then mounted in a coin-type cell with Glassmat separator and filled with electrolyte. The capacitor cells were subjected to galvanostatic charge-discharge cycling using an Arbin Instrument System BU-2000 [16, 17]. The test program is carried out at constant current mode at different current load (from 30 to 360 mAg^{-1}) at 25 cycles and room temperature. Some cells are subjected to continuous cycling charge/discharge at current rate 60 mAg^{-1} up to 700 cycles.

RESULTS AND DISCUSSIONS
Physicochemical characteristics

Figure 1 shows powder X-ray diffraction patterns of the carbonaceous materials. Both commercial TDA-Research and Norit-CGP samples display typical amorphous hums in the range of 20-25º and of 38-48º, respectively. These not-well resolved diffraction peaks are due to (00l) and (101) diffraction planes of the graphite–type structure. The XRD pattern of Norit-CGP sample shows lower value of graphitization in comparison to the TDA-Research sample [18]. The XRD pattern of AC-1400 shows several stronger amorphous "humps", located at 2θ values of about 24.5º and 43.5º, corresponding to the (002) and (100)+(101) peaks of 2H-hexagonal crystalline

(Polytetraflourethylene) and PVDF (polyvinylidene graphite and indicate the formation of graphite domains with higher crystallite sizes [19].

Table 1 summarized the data on specific surface area and pore volume for carbonaceous materials. For each of the materials, there are three types of pores - micro, mezo and macro, conventionally divided according to their size. Although the TDA-Research sample exhibit mainly micro pores (about 80% of the total pore volume), the other two samples AC-1400 and Norit-CGP are characterized with 70% and 30% of micropores, respectively. It is seen that the investigated carbons have very high specific surface area, as the micropore volume of TDA-Research is the highest compared to the two other carbon materials.
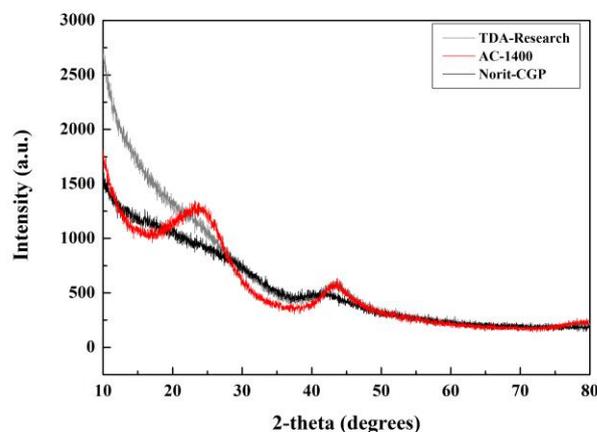

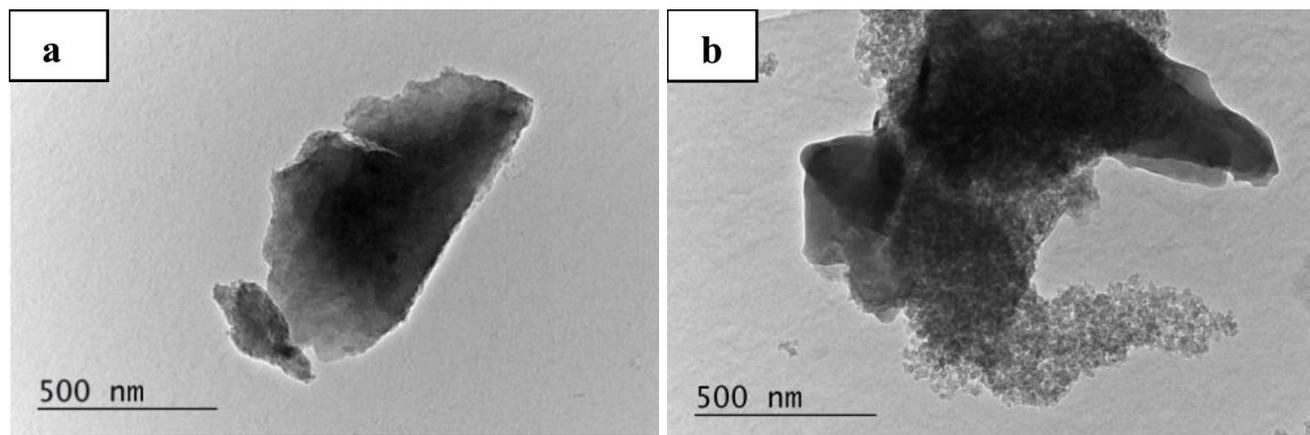**Fig. 1.** XRD patterns of the used carbon material.

Fig. 2. TEM image of activated carbon samples: TDA Research (a) and Norit-CGP (b).

The TEM images show that for TDA-Research sample the large plate-like aggregates dominate, while the Norit-CGP carbon consists of both plate-like aggregates and small thin particles (Fig. 2). In AC-1400, there are mainly small particles. All these

data suggest that Norit-CGP surface is highly developed, which corresponds to the data from Table 1.

17

Electrochemical characteristics

The assembled symmetric capacitance cells with different activated carbons and binders are electrochemical studied at constant current charge–discharge mode in the voltage window 0.1-1.0 V and at low current density of 60 mAg^{-1} during prolonged cycling (700 cycles). The specific discharge capacitance of the electrodes was calculated according to [20].

The value of the specific capacity C is obtained from the charge-discharge cycling measurements according to the following equation:

$$C = 4 \, I \, \Delta t / m \, \Delta V \qquad (1)$$

where *I, Δt, ΔV* and *m* are respectively, the constant current applied, charge/discharge time, voltage window and the total mass of the electrode material.

Figure 3 gives the dependences of the discharge capacity as a function of discharge current density for studied carbon electrodes fabricated by using PVDF and PTFE as binders. The comparison shows that the structure of the binder plays a significant role on the supercapacitor performances. By using of PVDF as a binder (Fig. 3a), it appears that the electrochemical performances of three types of carbonaceous materials are similar. Contrary, the discharge capacity curves of supercapacitators with different carbons and PTFE as a binder are essential different. The highest capacity values are observed for commercial AC-TDA Research in the whole range of current rates. In the system with AC Norit-**CGP the** capacity drastically reduced (Fig. 3b).
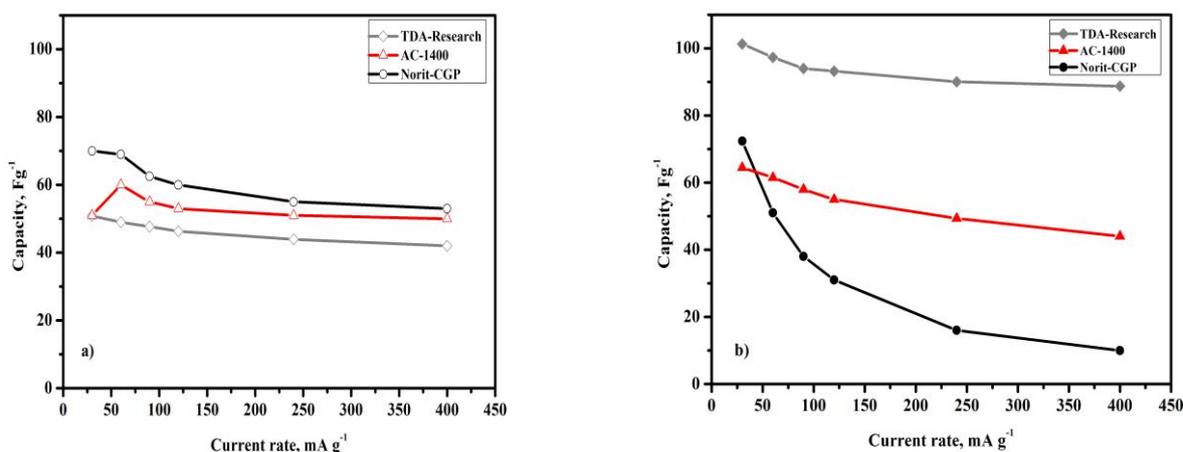
Fig. 3. Dependence of the discharge capacity of supercapacitors with different carbons on the current load: a) PVDF-binder and b) PTFE-binder.
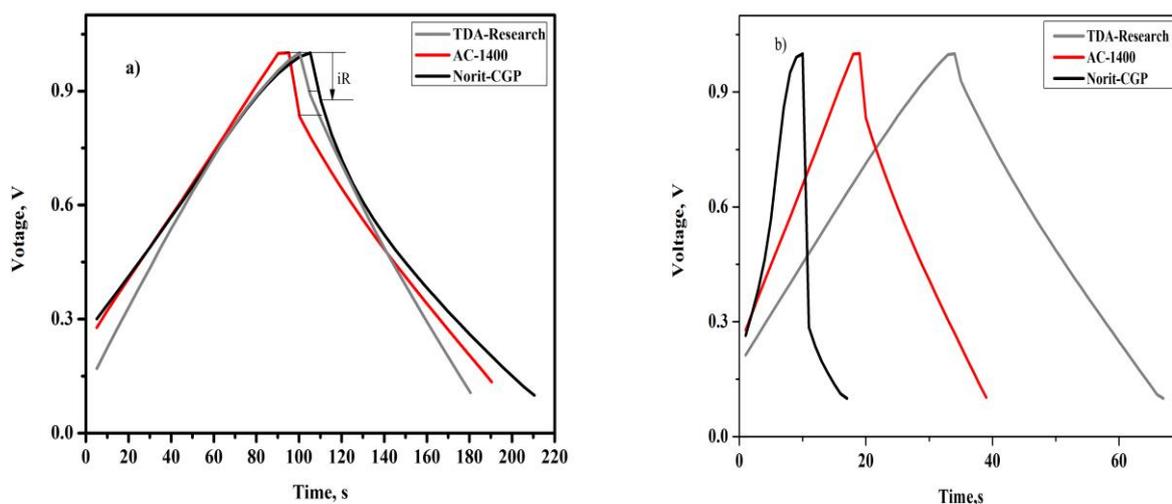

Fig. 4. Galvanostatic charge-discharge profiles of activated carbons with different binders: a) PVDF and b) PTFE at current rate 240 mAg^{-1}

To rationalize the effect of the binder on the electrochemical performance of carbonaceous materials, Figure 4 illustrates the charge-discharge profile curves of all studied samples

fabricated in electrodes with PVDF and PTFE-binders. The profiles of all curves shown are typical for supercapacitor systems, and here it is evident the influence of the binder on the capacitive properties of nanoporous carbons as electrode materials. From the discharge curves, the "ohmic potential drop" (iR-drop) can be calculated, the values being giving in Table 1. The iR drop has a great influence on electrochemical measurements, and their effects should be considered during the interpretation of electrochemical data.

Table 1. Pore parameters of the carbon materials: activated surface (S_{BET}), total pore volume (V_{tot}), micropore volume (V_{micro}) micropore surface (S_{micro}) of activated carbon samples and iR-drop.

Sample	S_{BET}, m^2g^{-1}	V_{tot}, cm^3g^{-1}	V_{micro}, cm^3g^{-1}	S_{micro}, m^2g^{-1}	iR^{PTFE}, V (at 240 mAg^{-1})	iR^{PVDF}, V (at 240 mAg^{-1})
AC-1400	1400	0.630	0.453	1008	0.17	0.17
TDA- Research	1524	0.680	0.550	1234	0.08	0.11
Norit-CGP	1825	1.400	0.380	495	0.71	0.12

As one can see, the calculated values of IR-drop are close for carbonaceous materials fabricated in electrodes with a PVDF binder, while for the PTFE-binder there is a clear tendency for increasing the IR-drop for AC-1400 having lowest micropore volume. These results suggest that the PVDF binder affects both micro and macro pores, as a result of which the capacitive values are close for all samples studied irrespective of their porous structure. In addition, Norit-CGP has a largest surface and the highest discharge capacity is observed in this case.

The presence of PTFE in the electrode, however, substantially alters the electrochemical characteristics of the supercapacitors, since it preferentially influences the macropores. The highest capacity values, excellent cycle ability and very stable capacity at prolong cycling are registered for commercial AC-TDA Research with PTFE-binder compared to other tested materials. This carbon possesses much high micropore surface area and the highest micropore volume (Tabl.1) and significantly lower resistance compared to Norit-CGP (around 9 times at 240 mAg^{-1}).

Figure 5 compares the charge-discharge profiles at low and high current loads (60 and 240 mA g^{-1}) of supercapacitors with TDA-Research based electrodes assembled with the both PVDF and PTFE binders. The curve profiles and the calculated iR-drops show that already at low current density, the electrode resistance with PVDF-binder is higher than that with PTFE. This is in agreement with the suggestion that the electrode binder acts differently on the macro- and micro pores of the nanocarbons and thus on their adsorption ability.
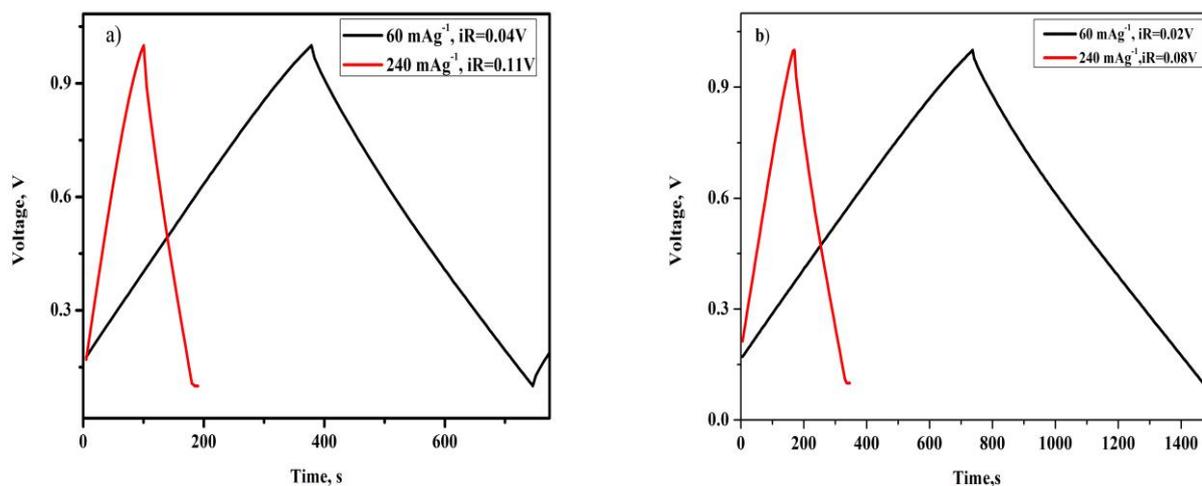

Fig. 5 Galvanostatic charge-discharge profiles of TDA Research with different binders: a) PVDF and b) PTFE at current rates 60 and 240 mAg^{-1}.
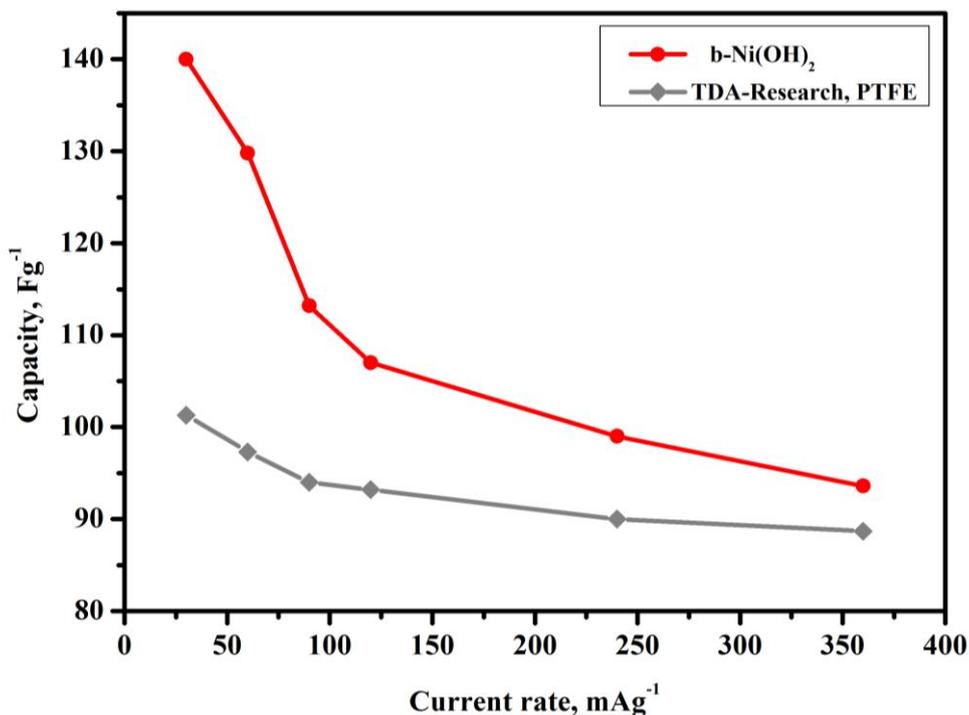
Fig. 6. Dependence of the discharge capacity of supercapacitors with TDA-Research /PTFE and modified with 6.2% $Ni(OH)_2$ on the current load.

Based on the best electrochemical performance of TDA-Research sample with PTFE binder, we further modified the properties of the sample by β-$Ni(OH)_2$ (Fig. 6). The electrochemical cell consists of TDA-Research/PTFE as a negative electrode and modified with 6.2% β-$Ni(OH)_2$ TDA-Research/PTFE as a positive electrode.

The comparison of the capacity-discharge current plots shows that the addition of small amount of β-$Ni(OH)_2$ to the positive electrode in the supercapacitor increases the discharge capacity significantly (around 35-40% at 30-60 mAg^{-1}) at low current density. This effect of β-$Ni(OH)_2$ becomes smaller when higher current density is used. This result implies that at low current density, the mechanism of the electrochemical reaction is changed. The obtained result is very interesting and it deserves further examination.

CONCLUSIONS

Three types of activated nanoporous carbons having different micropore structure are investigated as electrode materials for supercapacitors. It was found that the binder affect strongly their electrochemical characteristics, acting differently on the pore structure. The PVDF binder influences both the micro and macro pores, while PTFE attacks preferentially the macropores. The highest and stable discharge capacity demonstrates the commercial activated carbon TDA-Research (USA) with PTFE binder, which possesses the highest micropore volume and surface.

The modification of the positive electrode with 6.2% β-$Ni(OH)_2$ increase the discharge capacity by around 35-40 Fg^{-1} at low current density.

REFERENCES

1. R.Kotz, M.Carlen, *Electrochim. Acta,* **45**, 2483 (2000).
2. W. Sun, X. Rui, M.Ulaganathan, S. Madhavi, Q.Yan, *J. Power Sources,* **295**, 323 (2015).
3. G.Yu, X.Xie, L. Pan, Z. Bao, Yi Cui, *Nano Energy*, **2**, 213 (2013).
4. M. Mladenov, P. Zlatilova, R. Raicheff, S. Vassilev, N. Petrov,K. Belov, V. Trenev, D. Kovacheva, *Bulg. Chem.Commun*., **40**, 360 (2008).
5. S. Bose, T. Kuila, A. K. Mishra, R. Rajasekar, N. H. Kim, J. H. Lee, *J. Mater.Chem*., **22,** 767 (2012).

6. C. Liu, F. Li, L-P. Ma, H-M. Cheng, *Adv.Mater,* **22**, E28-E62 (2010).

7. K.Naoi, A. Nishino, T. Morinoto (Eds), Electro-chemical Capacitors Compact Dictionary, **NTS**, 89 (2004).

8. A.González, E. Goikolea, JonA. Barrena, R. Mysyk, *Ren.&Sust.Energy Reviews,* **58**, 1189 (2016).

9. Sh Shi, Ch. Xu, Ch. Yang, Jia Li, H. Du, B. Li, F. Kang, *Particuology,* **11**, 371, (2013).

10. J. Pu, Y. Tong, S.B. Wang, E.H. Sheng, Z.H. Wang, J. Power Sources, **250**, 250 (2014).

11. X.H. Xiong, D. Ding, D.C. Chen, G. Waller, Y.F. Bu, Z.X. Wang, M.L. Liu, Nano Energy, **11**, 154 (2015).

12. M. Li, K.Y. Ma, J.P. Cheng, D.H. Lv, X.B. Zhang, J. Power Sources, **286**, 438 (2015).

13. Y.Tian, J.Yan, L. Huang, R. Xue, L. Hao, B.Yi, *Mater. Chem. &Phys.,* **143**, 1164 (2014).

14. A.Burke, *Electrochim, Acta,* **52**, 1083 (2007).

15. Wang, L. Zhang, J. Zhang, *Chem. Soc. Rev.*, **41**, 797 (2012).

16. L. Stoyanov, A. Stoyanova, S. Veleva, Ch. Girginov, M. Mladenov, D. Kovacheva, R. Raicheff, *Bulg. Chem. Commun.,* **48** (2016) (in press)

17. M. Mladenov, K. Alexandrova, N. Petrov, B. Tsynsarski, D. Kovacheva, N. Saliyski, R. Raicheff, J. *Solid State Electrochem.* **17**, 2101 (2013).

18. Ch. Girginov, L. Stoyanov, S. Kozhukharov, A. Stoyanova, M. Mladenov, R. Raicheff , Сб. Научни трудове на Русенския университет „Ангел Кънчев", **54**, 89 (2015).

19. M. Mladenov, N. Petrov, T. Budinova, B. Tsyntsarski, T. Petrov, D. Kovacheva, R. Raicheff, *Bulg. Chem. Commun.* **43**, 125 (2011).

20. M. Stoller, R. Ruoff, *Energy&Env. Sci.*, **3**, 1294 (2010).

21. M. Mladenov, R. Raicheff, D. Kovacheva, R. Nickolov, V. Trenev, D. Bacvarov, K. Belov, in: Proc. of 4M/ICOMM Conference, 23-25 September 2009, Karlsruhe, Germany.

АКТИВИРАНИ НАНОВЪГЛЕРОДИ КАТО ЕЛЕКТРОДНИ МАТЕРИАЛИ ЗА СУПЕРКОНДЕНЗАТОРИ ВЪВ ВОДЕН ЕЛЕКТРОЛИТ

Л. С. Сосеров[1]*, А. Е. Стоянова[1], Р. К. Стоянова[2]

[1]*Институт по електрохимия и енергийни системи, БАН, 1113 София, България*
[2]*Институт по обща и неорганична химия, БАН, 1113 София, България*

(Резюме)

В настоящата работа е изследван ефектът на два вида свързващи вещества (polyvinylidene fluoride (PVDF) и polytetrafluoroethylene (PTFE)) върху структурата на порите на избрани наноразмерни въглероди като електродни материали за симетрични суперкондензатори. PVDF оказва влияние върху микро- и макропорите, докато PTFE атакува приемуществено макропорите. Търговският продукт TDA-Research със свързващо вещество PTFE, притежаващ най-висок обем и повърхност на микропорите, показва най-висок и стабилен разряден капацитет спрямо останалите два вида изследвани въглероди.

Добавката на 6.2% β-Ni(OH)$_2$ към положителния електрод на суперкондензатора увеличава съществено разрядния му капацитет (с около 35-40% при 30-60 mAg^{-1}). Полученият резултат е многообещаващ и изисква по-нататъшни изследвания.

Electrochemical recovery of copper in the presence of contaminant ferrous ions

G. A. Hodjaoglu

Institute of Physical Chemistry-Bulgarian Academy of Sciences (IPC-BAS), Acad. G. Bonchev Str., block 11, 1113 Sofia, Bulgaria

The aim of this study was to collect specific electrochemical conditions for separate copper deposition from mixed copper-iron model electrolytes. The investigation is devoted for further utilization of copper rich industrial wastes. Reasonable, the composition of studied model electrolytes was considered with real solid and leach secondary wastes. The electroextraction of copper has been studied in the presence of ferrous ions from acidic sulphate electrolytes by means of potentiodynamic and galvanostatic methods. The potentiodynamic behaviour of copper was tested by adding or inclusion the ferrous ions from the investigated system. The obtained experimental results show that the harmful effect of ferrous ions on copper deposition could be minimized or modulated favorable without removing the iron contamination only by increaseng the cupric content. Ferrous ions could be separated potentiodynamically from copper ions by restriction of the range of the scanning potential. In all cases the presence of ferrous ions at the potentiodynamic studies reduces the anodic peaks of copper dissolution. In galvanostatic regime the monitored current efficiency declines abruptly with increase of ferrous ions concentration. At sufficiency high cupric ion concentrations this important parameter was higher than 90% and practically was independent from the presence of ferrous ions. The copper coatings obtained from equally mixed Cu^{2+}/Fe^{2+} electrolytes were dark red in color, brittle and powdery. In comparison at higher Cu^{2+}/Fe^{2+} ratio 5:1 the coatings were light red in color, smooth and semi-bright in appearance. In both cupric ions concentrations the coatings were composed only by copper metal phase proven by powder diffraction and scanning electron microscopy methods.

Keywords: selective electroextraction; cupric ions; ferrous ions, cyclic voltamperometry; galvanostatic deposition, SEM, XRD

INTRODUCTION

After a number of pyro or hydrometallurgical ore treatments, large amounts of wastes with high metal content remain. The waste product known as "blue powder" that results from condensing furnace gases during the thermometallurgical processing of non-ferrous ores contains large amounts of zinc, iron and copper compounds [1, 2]. Lead-zinc cake, produced as a result of zinc concentrate leaching, contains extractable zinc, lead, copper and iron compound residues [3]. Similar composition could be attributed to other specific wastes as "Flue dusts" at a secondary copper smelter treated in the electrowinning zinc plant [4]. The industrial "Zinc residue", which is a mixture of zinc scrap and zinc dross resulting from the zinc cathode industry contains large amounts of valuable zinc in the presence of copper and iron contaminants [5]. The residue discarded as a "cake" from a Waelz kiln processing zinc-lead carbonate ores contains mainly lead, zinc and iron compounds [6]. There are numerous papers concerning the recovery of metals contained in low concentrations in the wastewater produced in the metal plating industry by means of liquid extraction or other chemical methods. These methods, however, are inapplicable to the extraction of metals from solid wastes like powders, cakes, dusts, drosses, scraps, etc., where the content of non-ferrous metals is much higher.

We found in the literature only three papers that discuss in a systematic way the influence of ferric and ferrous ions on the electroextraction of copper from electrolytes with low metal concentration. By means determination of polarisation curves Dew et al. studied the effect of ferrous and ferric ions on the cathodic and anodic reactions for dilute acid copper sulphate electrolytes with varying concentrations and mixtures of reacting species [7]. The results describe the limiting rate of mass transfer for the deposition of copper and reduction of ferric ions. The cathodic reduction of ferric to ferrous ions results in a mixed potential at the cathode during copper electrowinning, and consequently the current efficiency of deposition would decrease significantly at high ferric concentration. Re-oxidation of ferrous to ferric ions at the anode would increase the effect of the ferric ions concentration on the current efficiency [7]. In a following study the same authors also investigated the effect of ferrous and ferric ions on the efficiency

of copper recovery from solutions containing less than 2 g/L cupric ions, with an equivalent or greater concentration of iron as ferrous and ferric ions [8]. Experiments showed that the current efficiency decreased in proportion to the increase in the ferric ions concentration. The work has shown that by using of the Chemelec cell can achieve reasonable efficiencies for direct electrowinning from dilute leach liquors [8]. Das et al. studied the influence of ferric ions concentration (varied from 0.5 to 6.0 g/L) on the current efficiency, power consumption and cathode quality during copper electrowinning in an open channel cell [9]. A decrease in current efficiency started with increasing ferric ions concentration at each of the flow rates studied. When ferrous ions were added to Cu^{2+}-Fe^{3+} electrolyte, the harmful effect of ferric ions on the current efficiency was reduced. More than 90% current efficiency may be achieved if the Fe^{3+}/ Fe^{2+} ratio is maintained at less than or equal to 1. A marginal increase in the current efficiency was observed during increase in Cu^{2+} concentration. The authors referred this tendency to increased solution viscosity at higher cupric ion concentrations and thus retarding the distribution of ferric ions over the cathode surface [9]. A decrease in current efficiency was observed when the ferric ions concentration were increased from 1.0 to 2.0 g/L at each sulphuric acid concentration.

For more details on the investigated system were examined some noticeable works on iron electrodeposition from sulphate electrolytes. For example Mostad et al. were collected the long experience from an industrial plant and semi-plant pilot electrolytic cell and paid attention for using electrode diaphragm for separation of anode side reaction involving iron ions [10]. The authors reported for the important role of solution pH and its role on the current efficiency. At the same time Diaz et al. published polarization curves and impedance diagrams with detailed step increase of the cathode potential and solution pH. After a deep analysis the authors suggest an interesting mechanism of "at least three adsorbed species" of iron electrodeposition from acid sulphate solutions. For more details on the proposed kinetic model see reference [11].

Nevertheless the complicated electrochemical behavior of iron the paper is devoted to the practical importance of ferrous ions on the process of copper recovery. All experiments were carried out from sulphate electrolytes containing cupric ions and ferrous ions in ratios close to the proportion of these two metals in the solid

metallurgical wastes, especially secondary precipitates from zinc hydrometallurgy.

EXPERIMENTAL

Analytical grade iron (II) sulfate heptahydrate, copper (II) sulphate pentahydrate and sulphuric acid were used for electrolyte composition. Ferrous ions (1, 5 or 10 g/L) were added to electrolytes containing 10 or 50 g/L cupric ions in the presence (60 or 130 g/L) and absence of free sulphuric acid (pH=0.1). For metal compounds dissolution and acid dilution laboratory bi-distilled water was used. All chemicals and electrodes gravimetric measurements were carried out on a precise analytical vessel Sartorius BP 301 S.

The potentiodynamic experiments were carried out in a thermostated (37 ± 1^oC), three-electrode glass cell (300ml) without stirring of the electrolyte. The cathode (2.0 cm^2) and both anodes (4.0 cm^2 total area) were Pt plates. The reference electrode was a mercury/mercurous sulphate electrode in 0.5M H_2SO_4 (SSE), its potential *vs*. NHE being +0.720 V. The cyclic potentiodynamic studies were carried out by potential scanning at a rate of 30 mV sec^{-1} in the potential range starting from +1.200 to - 1.800 V *vs* SSE using a computerized PAR 263A potentiostat/galvanostat with Soft Corr II software. Galvanostatic depositions were carried out in sulphate electrolytes (500ml) on copper cathodes (5.0 cm^2) and Pb-Ag (1%) alloy anodes at a current density of 2 A dm^{-2} for 5 hours.

Current efficiency (CE) in the potentiodynamic regime was determined by graphical integration of obtained cyclic voltammograms (CVA) curves by the help of potentiodynamic software. For more details see next section. In galvanostatic deposition current efficiency was determined by precise gravimetric measurement of the metal quantity deposited on the cathode. Copper plates prepared for working cathode in form were tarred before and after the electrolysis. A special attention was paid when the final deposit was rough and powderly for any losses in the total mass of the working cathode.

To determine the yield at current efficiency is used the relationship between the real gravitate mass of deferred copper coating to the theoretical multiplied by a hundred:

$$CE \% = (\triangle m_{cath.} / \triangle m_{theor.}) . 100$$

In the case of cathodic deposition of copper sulphate electrolyte, where copper ions are second valence, k_e accepted values 0,329 mg /C or 1,186 g / A.h relative time one hour:

$\triangle m_{theor.}$ [g] = 1,186 [g/A.h] I [A] $\triangle t$ [h]

A Philips PW 1050 X-ray powder diffractometer with angular scanning range of 20-110 (2θ) was used. The surface morphology of the deposits was examined and EDX Analysis was performed by scanning electron microscopy (SEM) using a JEOL JSM 6390 microscope.

RESULTS AND DISCUSSION

1. Cyclic voltammetry

In order to assess the intimate role of ferrous ions in cupric electrolyte potentiodynamic scans were performed. In Figure 1 (a, b, c) by curve 1 was recorded the behavior of copper electrolyte in absence of ferrous ions. The potentials of very first scans were extended to -1.6 V to detect hydrogen evolution area. Potentiodynamic investigations were started with an electrolyte containing 10 g/L cupric ions and 130 g/L sulphuric acid. The electrolyte composition is referred in the auxiliary table in Fig. 1.
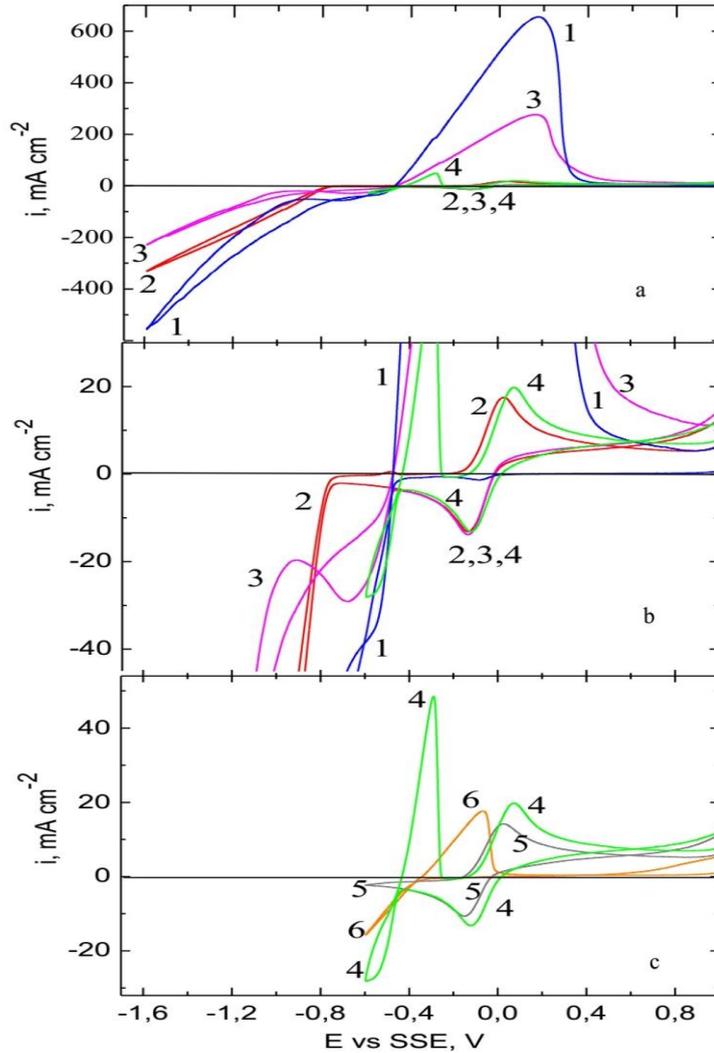
CVA	Evertex,V	composition of the electrolyte		
		Cu^{2+} (g/L)	Fe^{2+} (g/L)	H2SO4 (g/L)
1	-1.6	10	-	130
2	-1.6	-	10	130
3	-1.6	10	10	130
4	-0.6	10	10	130
5	-0.6	-	10	130
6	-0.6	10	10	-

Fig. 1. Cyclic voltamperograms of electrolytes containing cupric and ferrous ions: a) view to full negative scan; b) spread area near iron deposition/dissolution; c) restricted scan to E_{vertex} = -0.6 V.

Following the first recorded potential-current trace some important points can be observed. Importantly, at potential -0.400 V the cathodic current starts to increase resulting from the reduction of cupric ions. On further increase in the potential (in negative direction), the cathodic current decreases from -57.1 mA cm^{-2} at -0.745 V to -54.4 mA cm^{-2} at -0.860 V due to the concentration polarization of reaction 1 (Table 1).

Table 1. Specific reactions in potentiodynamic regime and standard potentials with reference to a standard hydrogen electrode or a saturated mercury sulphate electrode.

CVA scanning		Order of standard potentials			
Reaction	**№**	**Half-Reaction**	**№**	**E vs NHE, V**	**E vs SSE, V**
$Cu^{2+} + 2e^- = Cu$	1	$Fe^{2+} + 2e^- \rightleftharpoons Fe$	1S	-0.44	-1.16
$2H^+ + 2e^- = H_2$	2	$Fe^{3+} + 3e^- \rightleftharpoons Fe$	2S	-0.04	-0.76
$Cu - 2e^- = Cu^{2+}$	3	$2H^+ + 2e^- \rightleftharpoons H_2 (g)$	3S	0.00	-0.72
$2H_2O - 4e^- = 4H^+ + O_2$ (g)	4	$Cu^{2+} + e^- \rightleftharpoons Cu^+$	4S	0.16	-0.56
$Fe^{3+} + e^- = Fe^{2+}$	5	$Cu^{2+} + 2e^- \rightleftharpoons Cu$	5S	0.34	-0.38
$Fe^{2+} - e^- = Fe^{3+}$	6	$Cu^+ + e^- \rightleftharpoons Cu$	6S	0.52	-0.20
$Fe^{3+} + 3e^- = Fe$	7	$Fe^{3+} + e^- \rightleftharpoons Fe^{2+}$	7S	0.77	+0.05
$Fe - 3e^- = Fe^{3+}$	8	$O_2 (g) + 4H^+ + 4e^- \rightleftharpoons 2H_2O$	8S	1.23	+0.51
$Cu^{2+} + Fe^{2+} = Cu^+ + Fe^{3+}$	9				
$2Cu^+ = Cu^{2+} + Cu$	10				

Then the cathodic current begins to increase again as a result of the reactions 1 and 2. During the reverse potential scan (in positive direction), dissolution of the copper coatings starts at -0.470 V (reaction 3) yielding an anodic peak. At +0.900 V, evolution of oxygen commences and the current rises again. Curve 2 shows scan to -1.6 V in an electrolyte containing only 10 g/L ferrous ions and 130 g/L sulphuric acid. At potential -0.020 V, the cathodic current starts to increase resulting from the reduction of ferric ions (reaction 5). The ferric ions are a result of the reaction 6 proceeding on the working or counter electrodes when their potentials are sufficiently positive for the oxidation of ferrous ions to commence. On further increase in potential, the cathodic current decreases due to the concentration polarization of reaction 5. Then (at -0.720 V), the cathodic current begins to increase again as a result of the reactions 2 and 7. During the reverse potential scan dissolution of the iron coating starts at -0.525 V (reaction 8) yielding at -0.485 V very little (0.7 mA cm^{-2}) anodic peak. At -0.230V oxidation of ferrous to ferric ions starts and the current rises (reaction 6). At +0.900 V, evolution of oxygen commences and the current rises again as a result of reaction 4.

In the presence of ferrous ions, the reaction 9 proceeds in the bulk electrolyte. Cuprous ions disproportionate rapidly to cupric i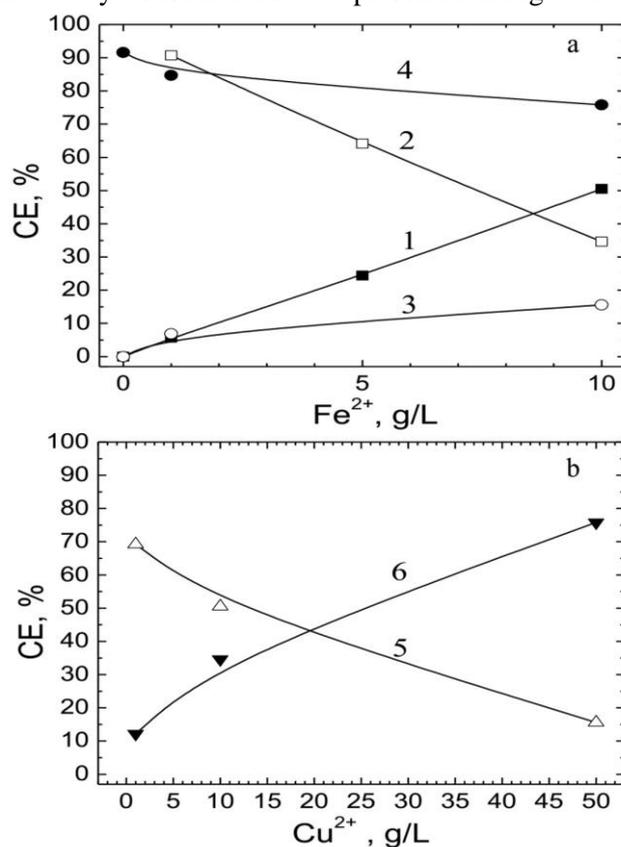ons and elemental copper (reaction 10). Since no copper precipitate is observed in the studied electrolytes, it can be concluded that the amount of cuprous ions produced by reaction 9 is very small.

Curves 3 and 4 show scans to -1.6 V or -0.6 V in an electrolyte containing 10 g/L cupric ions, 10 g/L ferrous ions and 130 g/L sulphuric acid. At potential of -0.020 V, the cathodic current starts to increase and at potential -0.130 V the curves feature peaks resulting from the reduction of ferric ions (reaction 5). In this case the ferric ions are as a result both of the oxidation of ferric ions by the reaction 9 taking place in the bulk electrolyte and the reaction 6 proceeding on the working or counter electrodes when their potentials are sufficiently positive for the oxidation of ferrous ions. On further increase in potential, the cathodic current decreases due to the concentration polarization of the reaction 5. At -0.475 V the cathodic current begins to increase again to -29.5 mA cm^{-2} (-0.680 V) as a result of the reactions 1. On further potential increase, the cathodic current decreases to -19.4 mA cm^{-2} (-0.910 V) due to the concentration polarization of the reaction 1. Then the current rises again as a result both of Cu deposition (reaction 1) and hydrogen evolution (reaction 2). During the reverse potential scan, dissolution of the copper coating starts at -0.480 V yielding an anodic peak as a result of reaction 3 with a standard potential of -0.380 V. On further scanning to more positive potentials, the current starts to increase and new,

25

considerably lower anodic peak (curve 4) occur due to the ferrous ions oxidation (reaction 6). At +0.900 V, evolution of oxygen commences (reaction 4) and the current rises.

The graphical integration of the cathodic and anodic peaks of the cyclic voltammograms recorded on scanning to -0.6 V vs. SSE in electrolytes with different composition, allows determination the quantity of electricity ($q_{cath.}$) consumed by the different reactions. Integration of the cathodic peak resulting from reaction 5 and of the anodic peak produced by reaction 3 gives the values of the quantity of electricity consumed for

the reduction of ferric ions to ferrous ions ($q_{Fe3+/Fe2+}$) and for the dissolution of copper to cupric ions ($q_{Cu/Cu2+}$), respectively. The remaining part of the cathodic electricity goes for the evolution of hydrogen. This approach is mostly based on the fact that no side chemical reactions proceed during the potential scanning and that no other reactions take place within the integration regions, except for reaction 3 or 5, respectively [12]. The obtained results of the above calculations, which may be called partial contribution (or current efficiency) of the respective reactions to the overall process are presented in Figure 2 a,b.

№	electrolyte composition			E vertex, V
	Cu (g/L)	Fe²⁺ (g/L)	H₂SO₄ (g/L)	
1	10	0-10		
2	10	0-10		
3	50	0-10	130	- 0.6
4	50	0-10		
5	0-50	10		
6	0-50	10		

Fig. 2. Partial contribution of the reactions taking place on the electrodes.

At the lower cupric ion concentration, the part of the reduction of ferric ions increases and even becomes predominating (50.5%) in the electrolyte containing 10 g/L ferrous ions (Fig. 2a, curve 1). The partial contribution of the reduction of cupric ions decreases rapidly with increase of the ferrous ions concentration and becomes 34.6% at 10 g/L ferrous ions (Fig.2a, curve 2). Similar relationships have been observed at 50 g/L cupric ions

concentration (Fig. 3a, curves 3 and 4), but in this case the influence of the higher ferrous ions concentration is considerably weaker.

The part of the reduction of ferric ions decreases with the increase of cupric ions concentration (Fig.3 b, curve 5). The partial contribution of the reduction of cupric ions increases rapidly with the increase of cupric ion concentration (Fig. 3 b, curve 6).

2. Galvanostatic deposition

Current efficiency of copper decreases sharply with increase in ferrous ions concentration during deposition in electrolytes containing 10 g/L cupric ions and 130 g/L sulphuric acid (Fig. 3 a) and is practically independent on ferrous ions concentration during deposition in electrolytes containing 50 g/L cupric ions and 130 g/L sulphuric acid (Fig. 3 b). When the deposition is conducted in electrolytes containing 50 g/L cupric ions and 130 g/L sulphuric acid, the current efficiency is higher than 90%. The very weak influence of ferrous ions on the recovery of copper from electrolytes containing 50 g/L cupric ions can be explained by the impeded access to the cathode of the ferric ions formed on the anodes. The reduction of ferric ions to ferrous ions on the cathode and increased hydrogen gas evolution may lead to a decrease in copper current efficiency. This is, probably, the reason for the significantly lower current efficiency when the concentrations of cupric ions and ferrous ions are equal (10 g/L).

The results of the microprobe analysis indicate that obtained metal coatings contains only copper phase (Fig. 4 a-d). However, in the presence of ferrous ions the coatings have a more fine-grain structure. The coatings are dark red, fragile and brittle (powdery).

In structural aspect it is seen that the preferred orientation of the Cu coating changes from a plane of lower density (220) (Fig. 5 a) to a plane of higher density (111) (Fig.5 b) despite the fact that EDX results show that no iron is co-deposited with the copper. However, the EDX technique is not sufficiently accurate to detect small quantities of metals due to its poor precision. A more detailed information can be obtained if the value of cell
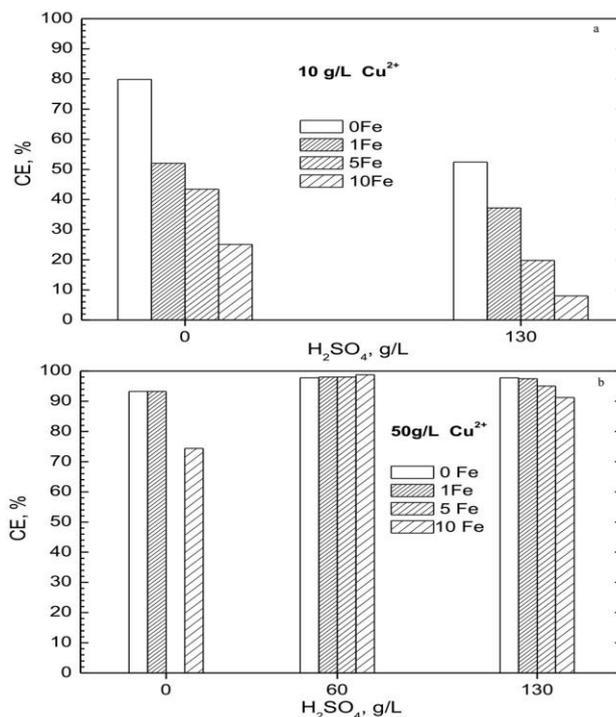
Fig. 3. Current efficiency of copper depositions depending on ferrous ion concentration and the presence of free sulfuric acid. Deposition at current density 2.0 A/dm^2 for 5 hours.

parameter is calculated from the X-ray diffraction data. If small quantities of ferrous ions are incorporated in the cell, it would provoke a distortion in the copper cell parameter. The formation of alloys, even in small portion, could also explain the change in the preferred orientation observed in the copper deposit. It is possible also iron ions to inhibit the growth of crystal face with (220) orientation.
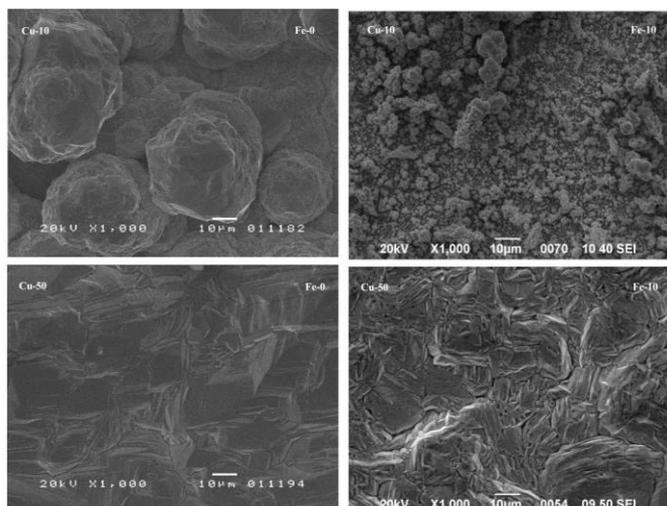
Fig. 4. Morphology of deposited copper coatings in the presence and absence of ferrous ions. SEM images x1000, current density 2.0 A/dm^2, deposition time 5.0 h, free sulphuric acid 130 g/L. Metal ion concentrations shown on pictures in g/L.
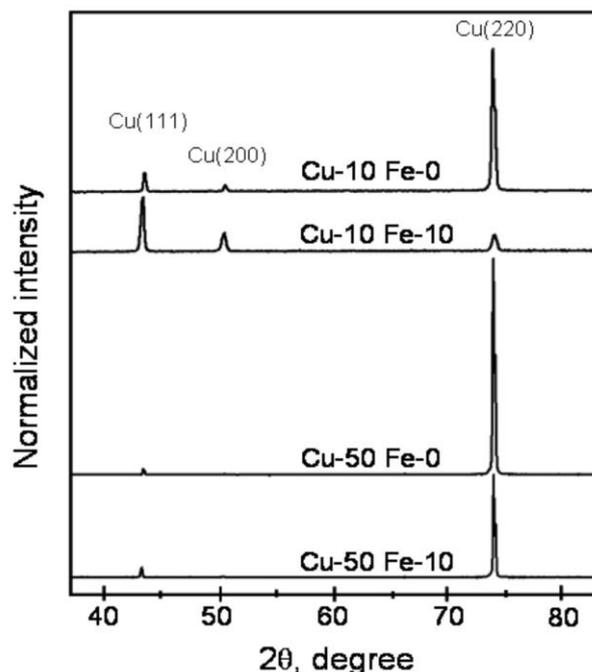
27

Fig. 5. Powder diffraction analyses of copper samples.

The surface morphology of coatings is not changed in the presence of ferrous ions when cupric ions dominate in the solution (Fig. 5 c, d). At similar ratio between cupric and ferrous ions the microstructure is changed substantially (Fig. 5 a, b). In both cases the obtained coatings are light red in color, smooth and semi-bright. The SEM microprobe analysis detects only copper content in all tested samples (Fig. 4 a-d).

The results of X-ray diffraction analysis of coatings deposited in acidic electrolytes in the absence of ferrous ions (Fig. 5 a, c) and in the presence of ferrous ions (Fig. 5 b, d) shows that at higher (50 g/L) cupric ions concentration the preferred (220) orientation of the coatings is not changed which can be explained by the impeded access to the cathode of the ferric ions formed on the anodes.

The ferrous ions have a similar potential to that of copper ions. This circumstance makes it almost impossible their electrochemical separation, although the influence of the sulphuric acid the two metals have separate, distinct peaks anodic dissolution. In cathodic reduction, however, cupric and ferrous ions practically tend to a codeposition process. Therefore, attention to ferrous ions is mainly directed to their role on the morphology and purity of the resulting coatings and the extraction stream.

CONCLUSIONS

Using classical electrochemical methods as cyclic voltamperometry and galvanostatic deposition was demonstrated the contribution of ferrous ions on the behavior of copper sulphate electrolytes. The obtained results were aimed for application to real systems by selective electroextraction of valuable non-ferrous metals from secondary wastes. By scanning of the electrode potential were selected the specific conditions for best observation of separate and mixed copper and iron metallic phases. The presence of free sulfuric acid affirmatively contributes to copper-iron separation and minimization of their co-deposition. At comparatively large amounts of ferrous ions the observed reduction of current efficiency was overcome by simply increasing the cupric part. In galvanostatic regime this allows practical recovery of copper metal despite the presence of iron contaminants with low electricity losses and sufficient purity. In this study ferrous ions have a significant influence in cases where the copper ions are at a concentration up to 10 g / L, the current efficiency by reducing of the copper ions of less than 40%. At high concentrations of copper ions in the electrolyte, in the range of 50 g/ L, the presence of ferrous ions decreases the current efficiency to a level not lower than 90%. This reduction occurs at concentrations comparable to those of copper ions (10 g/L). In this case, the impurity ferrous ions will mostly have a role on the morphology and purity of

the resulting copper coatings without compromising recovery as a whole. In all cases where the content of minded copper is low and in the same time ferrous ions in the waste electrolyte is around and above 1.0 g/L it is appropriate that they should be removed before conducting selective electrochemical recovery.

REFERENCES

1. L. Muresan, A. Nicoara, S. Varvara, G. Maurin, *J. Appl. Electrochem.*, 29, 719 (1999).
2. L. Muresan , S. Varvara, G. Maurin, S.Dorneanu, *Hydrometallurgy*, 54, 1 (2000).
3. V. Karoleva, Metallurgy of heavy non-ferrous metals, Part II, c/o Jusautor, Sofia (in Bulgarian) (1986).
4. R. Kammel, M. Goktepe, H. Oelmann, *Hydrometallurgy*, 19, 11 (1987).
5. L. Blanco, V. Zapata, D. Garcia, *Hydrometallurgy*, 54, 41 (1999).
6. M. Turan, H. Altundogan, F. Tumen, *Hydrometallurgy*, 75, 169 (2004).
7. D. Dew, C. Phillips, *Hydrometallurgy*, 14, 331 (1985).
8. D. Dew, C. Phillips, *Hydrometallurgy*, 14, 351 (1985).
9. S. Das, C. Krishna, *International J. Mineral Process.*, 46, 91 (1996).
10. E. Mostad, S. Rolseth, J. Thonstad, *Hydrometallurgy*, 90, 213, (2008).
11. S. Diaz, J. Calderon, O. Barcia, O. Mattos, *Electrochim. Acta*, 53, 7426, (2008).
12. D. Gabe, *Trans. IMF*, 77, 213 (1999).

ЕЛЕКТРОХИМИЧНО ИЗВЛИЧАНЕ НА МЕД В ПРИСЪСТВИЕТО НА ВРЕДНИ ЗА ПРОЦЕСА ФЕРОЙОНИ

Г. А. Ходжаоглу

Институт по физикохимия „Акад. Р. Каишев"- Българска Академия на Науките (ИФХ-БАН) , ул. „Акад. Г. Бончев" Бл. 11, 1113 София, България

(Резюме)

Целта на това изследване е да се съберат конкретни електрохимични условия за разделно отлагане на мед от смесени медно-железни моделни електролити. Изследването е посветено за по-нататъшно използване на богати медни индустриални отпадъци. Съставът на изследваните електролити е съобразен с реалните твърди и излужени вторични отпадъци. Чрез потенциодинамични и галваностатични методи е осъществена електро- екстракцията на мед в присъствието на железни йони от кисели сулфатни електролити. Потенциодинамичното поведение на медта е тествано чрез добавяне на феройони към изследваната система. Получените експериментални резултати показват, че вредното въздействие на феройоните върху отлагането на медта може да бъде сведено до минимум чрез увеличаване на медната компонента. Железните йони могат да бъдат разделени от медните йони в потенциодинамичен режим чрез ограничаване на обхвата на потенциала на сканиране. Във всички случаи, наличието на железни йони намалява анодните пикове на разтваряне на медта. В галваностатичен режим се наблюдава рязко намаляване на добива по ток с увеличаване концентрация на феро- йоните. При висока концентрация на медните йони този важен параметър е по-висок от 90% и на практика е независим от присъствието на железни йони. Получените медни покрития от еднакво смесени мед-желязо електролити са тъмно червени на цвят, рехави и прахообразни. При по-високо съотношение на мед-желязо 5: 1, покритията са светло червени на цвят, гладки и блестящи. От проведените СЕМ и прахово-дифракционен анализ се вижда, че покритията съдържат единствено метална мед.

Corrosion resistance of electroless deposited Ni-P coatings on polymer (ABS) substrate

V. Chakarova[*], M. Georgieva, M. Petrova

Institute of Physical Chemistry, Bulgarian Academy of Sciences,
Acad. G. Bonchev Str., Bl. 11, 1113 Sofia, Bulgaria

Nickel-phosphorus and composite nickel-phosphorus coatings with dispersed diamond particles (with 14-20 µm particles size) are produced by electroless deposition onto an Acrylonitrile-Butadiene-Styrene (ABS) substrate. The influence of deposition time and solution acidity on the deposition rate, phosphorus content and microhardness of the obtained coatings is investigated. The corrosion resistance of coatings deposited at two different pH values of the electrolyte is evaluated by Neutral Salt Spray (NSS) tests and the potentiodynamic investigations are carried out in a model corrosive medium 0.5 M Na_2SO_4 solution with pH 5.9. Scanning electron microscopy (SEM) is employed to examine the morphology of the deposites before and after the corrosion resistance test, and the changes in elemental composition of the coatings are determined by X-ray diffraction analysis (XRD). The results of these tests and analyses show that incorporation of diamond particles in the Ni-P coatings is advantageous for forming better passive films with improved corrosion resistance.

Keywords: electroless deposition, composite coatings Ni-P, diamond particles, microhardness, corrosion resistance, SEM, XRD

INTRODUCTION

The electroless coatings are mainly applied for wear resistance and corrosion resistance operations [1-6]. The properties of the electroless nickel-phosphorus alloy (Ni-P) strongly depend on the phosphorus content [2]. The P content can be changed by varying certain conditions of plating, such as composition and pH of the plating bath used. Typically, higher pH values yield lower phosphorus content in the deposit, while lower ranges produce high phosphorus deposits. Several studies have shown that Ni-P alloys provide good anticorrosive coatings. In general, electroless Ni-P is a barrier coating, protecting the substrate by sealing it off from the corrosive environments, rather than by sacrificial action [7]. The high resistance was a result of the amorphous nature and passivity of the Ni-P deposits. The corrosion resistance of electroless Ni-P coatings is a function of composition. Most deposits are naturally passive and very resistant to corrosion attack in most environments. Their degree of passivity and corrosion resistance, however, is greatly affected by their phosphorus content. Alloys containing more than 10 mass % P are more resistant to attack than those with lower phosphorus content in neutral or acidic environments. Alloys containing low phosphorus content (3 to 4 mass % P) are more resistant to strong al kaline envi ronment than high phosphorus deposits [3]. It is believed that anodic dissolution is accompanied by preferred dissolution of nickel and phosphorus enrichment to the surface [8].

To further enhance the properties of the Ni-P deposits, second phase particles have been introduced into the Ni-P matrix. The characteristics of Ni-P composite coatings depend on phosphorus content of the Ni-P matrix and on certain properties of the particles such as type, shape and size [9]. Incorporation of particles improves the mechanical and tribological properties of the Ni-P deposits [1, 9-12], but there is a disagreement among researchers regarding the corrosion resistance of the electroless composite coatings [9, 13].

The choice of appropriate particles is very important for the simple production of functional composite coatings with specific characteristics. A great number of studies have been devoted to the production of Ni-P composite coatings with incorporated diamond particles of various sizes [9, 13-20]. The obtained results have demonstrated that Ni-P/nano-diamond composite coatings exhibit better performances than Ni-P coatings and also optimum deposition of Ni-P/nano-diamond shows more desirable characteristics of corrosion properties rather than as deposited Ni-P coatings [9, 13, 15, 17].

The aim of the present work is to study the corrosion behaviour of Ni-P and composite Ni-P coatings with dispersed 14-20 µm diamond particles. The coatings are deposited onto acrylonitrile-butadiene-styrene (ABS) samples to eliminate the influence of the substrate.

---

* To whom all correspondence should be sent:
E-mail: vchakarova@ipc.bas.bg

Table 1. Technological scheme of the processing samples of ABS

Operation	Substance	Concentration, g.l^{-1}	Time, min	Temperature,$^{\circ}$C
Etching	CrO$_3$	367	15	65
	H$_2$SO$_4$	253		
Pre-activation	HCl	3M	3	20
Activation	PdCl$_2$	0.8	5	20
Acceleration	NaOH	1M	5	20
Chemical metalization		In Table 2		

Table 2. Chemical compositions and operating conditions of the plating bath

Substance	Concentration
NiSO$_4$.7H$_2$O, g.l^{-1}	25
NaH$_2$PO$_2$.H$_2$O, g.l^{-1}	22
CH$_3$COONa, g.l^{-1}	20
Lactic acid, g.l^{-1}	20
Stabilizer 2 (a commercial product of TU-Sofia), mg.l^{-1}	1
NaLS, g.l^{-1}	0.01
Operating condition	
pH	4.6 - 4.8
Temperature, ($^{\circ}$C)	82

EXPERIMENTAL

The nickel coatings were deposited onto samples of ABS (Novodur PM/2C, Bayer, Germany) with a working area of 0.2 dm^2. The employed technological scheme is presented in Table 1.

The composition of the Ni-P bath is presented in Table 2.

Diamond particles with particle size of 14-20 µm (D) were added to the solution for chemical deposition in concentration of 5 g.l^{-1}. The conditions of electroless deposition of Ni-P and composite Ni-P (Ni-P/D) coatings are described in earlier papers [20, 21].

The deposition rate, expressed in terms of the amount of deposited nickel, resp. the relative thickness of the obtained coating (δ, µm), was determined gravimetrically as the difference in sample mass before and after deposition of the composite coating:

$$\delta = \Delta m.10^4 / \rho.S, [\mu m]$$

where, ρ - density of nickel in [g.cm^{-3}]; S - working area in [cm^2]; Δm - mass of the deposited coating.

The coatings were tested for corrosion resistance employing a Neutral Salt Spray test (NSS) (5% NaCl, pH 6.6-7.2) (VSN 1000, Vötsch Industrietechnik GmbH), comprising three test cycles of 24 hours each. The corrosion damage was determined gravimetrically based on mass loss. The microhardness of the coatings was measured by the Vickers method at a load of 50 p (Durimet, Ernst Leitz GmbH).

Open circuit potential (OCP)-time transients were plotted in 0.5 M Na$_2$SO$_4$ solution with pH 5.9. Potentiodynamic polarization was applied to study the anodic dissolution of the coatings. A potential scan rate of 1 mV.s^{-1} was applied by starting from a potential 250 mV more cathodic than the OCP and scanned in anodic direction. The investigations were performed in a three-electrode cell with a volume of 50 ml, Hg/Hg$_2$SO$_4$ reference electrode, working electrode with surface area of 0.2 cm^2 and Pt counter electrode. All electrochemical experiments were carried out using a potentiostat/galvanostat model 263A (EG&G Princeton Applied Research, USA) and SoftCorr II software. The polarization resistance (R$_P$) and the corrosion current density (j$_{corr}$) were calculated from data collected during the potentiodynamic polarization.

The structures of the produced thin films were characterized by X-ray diffraction (XRD) using a PANalytical Empyrean equipped with a multichannel detector (Pixel 3D) using (Cu Kα 45 kV-40 mA) radiation in the 10–100 2θ range, with a scan step of 0.01 for 24 s.

The morphology and structure of the obtained coatings, as well as the distribution of the dispersoid particles on their surface, were examined by a Metallographic Microscope (AMPLIVAL$^{\circledR}$ pol u Carl Zeiss JENA, Germany) and by Scanning Electron Microscopy (SEM) (JEOL JSM 733, Japan). The average amount of co-deposited particles per square centimeter (N.cm^{-2}) was determined based on the number of particles, counted on the surface of the composite coating by SEM (the counting was done in three arbitrarily chosen zones at a magnification 200x). Energy Dispersive Spectroscopy (EDS/INCA) was used to determine the elemental chemical composition of the coatings.

RESULTS AND DISCUSSION

Characterization of Ni-P and Ni-P/D coatings

Hypophosphite reduces nickel ions at electrolyte pH values higher than 3. The rate of hypophosphite oxidation and of nickel deposition increases with increase of solution pH, but at pH values above 5.5, the electrolyte stability decreases. Therefore, two pH values were selected within the range 3.0-5.5 for electroless deposition of Ni-P coatings and investigation of the deposition rate and microhardness tests of the obtained coatings. The obtained results are summarized in Table 3.

For the same deposition time, the thickness of the coating deposited in electrolyte with pH 3.8 is twice smaller than that obtained at pH 4.8. With increase of the electrolyte pH the P content of the coating decreases, but its microhardness increases.

Table 3. Influence of the pH of the electrolyte on the thickness and microhardness of Ni-P coatings on $\tau = 30$ min.

pH	3.8	4.8
δ, (μm)	4.8	10.2
HV_{50}, (kg.mm^{-2})	275	640
P, (mass %)	14.9	6.4

The significantly lower microhardness of the coating deposited at pH 3.8 is not related to its thickness. Similar microhardness values were also measured for samples with a thickness of 30-35 μm. These results made us initiate deposition tests in the electrolyte with pH 4.8 but for different deposition times. It was established that the microhardness of the coatings increased but slightly with increase of coating thickness (Fig. 1).
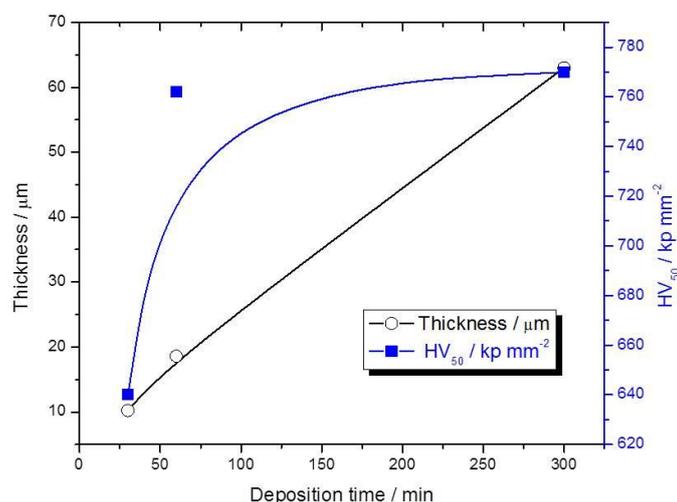
Fig. 1. Influence of deposition time on the thickness and microhardness of Ni-P coatings. Electrolyte pH 4.8

(a)   (b)
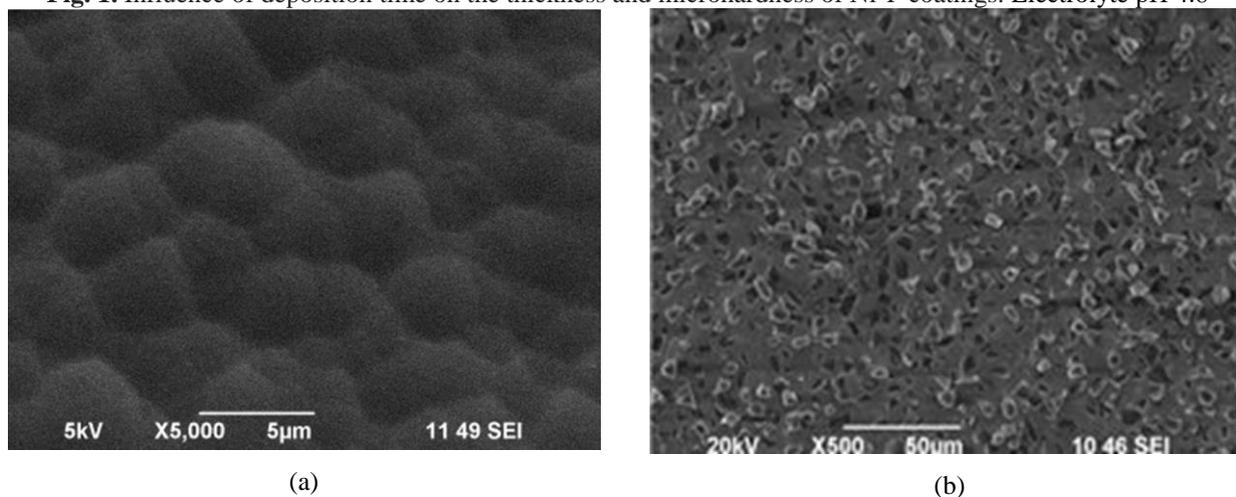
Fig. 2. SEM image of: a) Ni-P coating; b) Ni-P/D coating, $\tau = 30$ min.
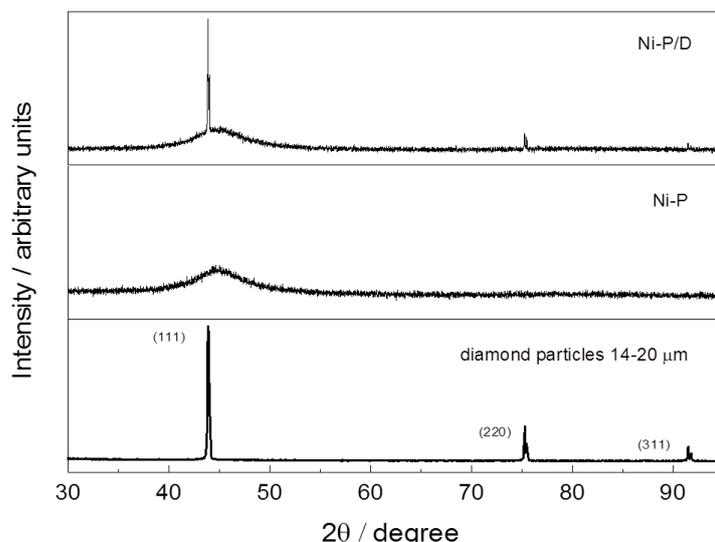
Fig. 3. XRD pattern of as deposited Ni-P, Ni-P/D coatings and diamond particles with size of 14-20 μm.

Composite coatings were deposited with addition of diamond particles to the solution for chemical deposition in concentration of 5 g.l^{-1}. The number of incorporated particles is of the order of 150 000 – 200 000 N.cm^{-2}. Figure 2 shows the morphology of such a coating.

The microhardness tests of the Ni-P/D coatings were not conducted, because of the great number and size of incorporated particles.

XRD analysis of Ni-P and Ni-P/D coatings

Figure 3 shows the XRD patterns of the obtained Ni-P and Ni-P/D coatings. Both coatings have amorphous structure. For comparison, the X-ray diffractogram of diamond particles is also presented and it indicates that the reflexes for the composite coating come from the incorporated particles.

Corrosion resistance tests of in a NSS chamber

Three samples from each type of coatings were prepared for testing in the corrosion chamber. The samples were with sizes 5 X 10 cm. The thickness of the coatings was in the range of 20-25 μm. The coatings were not evaluated visually or by optical methods because there were no visible signs of corrosion damage on their surface. The mass loss values for the respective coatings after the NSS test are presented in Table 4.

Table 4. Weight loss for the Ni-P and Ni-P/D coatings after 72 hours in a neutral salt spray chamber.

pH	Weight loss, mg	
	Ni-P	Ni-P/D
3.8	3.8	10.1
4.8	3.3	8.3

All coatings lose mass with prolonged time of stay in the chamber, the measured mass loss being more substantial for the composite coatings with incorporated particles. This is, probably, due to localized corrosion around the particles, which leads eventually to their shedding off the coating. Figure 4 shows the morphology of the specimens after the NSS test.

Electrochemical corrosion performance of Ni-P and Ni-P/D coatings

Figure 5 presents the potentiodynamic polarization curves of dissolution of the Ni-P and Ni-P/D coatings in model corrosive environment: 0.5 M Na$_2$SO$_4$, pH 5.9. The indifferent substrate used allowed plotting of polarization curves up to potentials sufficiently positive for oxygen evolution. On grounds of the obtained results it can be concluded that incorporation of diamond particles in the coating improves its corrosion behavior as compared to that of the deposit on pure Ni-P matrix. The corrosion potential of the composite coating deposited at pH 3.8 shifts to more positive values and the corrosion rate is much lower within a wide potential range. A plateau appears at about -600 mV which, according to literature data, is related to saturation of the surface layer with phosphorus resulting in impeded coating dissolution [8]. The curve for the composite coating deposited at pH 4.8 features an even broader passivation plateau and hence lower corrosion rate.

The corrosion potential (E$_{corr}$), corrosion current density (j$_{corr}$) and polarization resistance (R$_p$) of the different coatings, determined from the respective potentiodynamic polarization curves, are presented in Table 5.

Passivation of the remaining coating layer is recorded at about +600 mV in the curves for all samples. On completion of the potentiodynamic measurements, the remaining coating layer on the surface of all specimens has an average thickness of the order of 1 μm (Table 6).

33

**Table 5.** Corrosion characteristics of Ni-P and Ni-P/D coatings deposited at pH 4.8 in model corrosive environment.

	E_{corr}, (mV)	j_{corr}, (μA.cm^{-2})	R_p, (kΩ.cm^2)
Ni-P	-870	2.1	24
Ni-P/D	-890	1.0	35

Table 6. Influence of electrochemical treatment according Fig. 5 on the thickness of the Ni-P and Ni-P/D coatings.

	δ, (μm)	
	Ni-P	Ni-P/D
Before potentiodynamic polarization	12.5	9.2
After potentiodynamic polarization	1.1	1.9
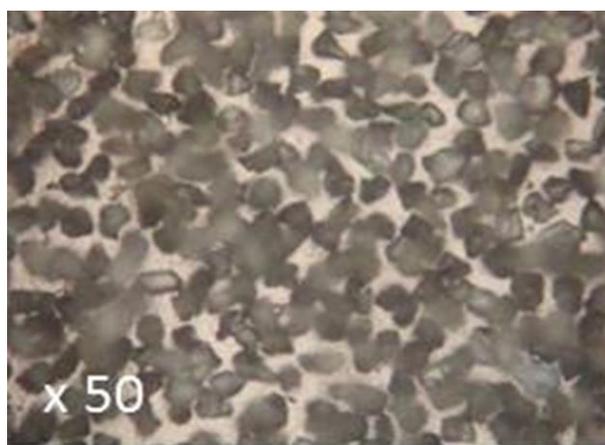
Fig. 4. Optical imaging of coatings after 72 hours in neutral salt spray chamber: a) Ni-P; b) Ni-P/D.
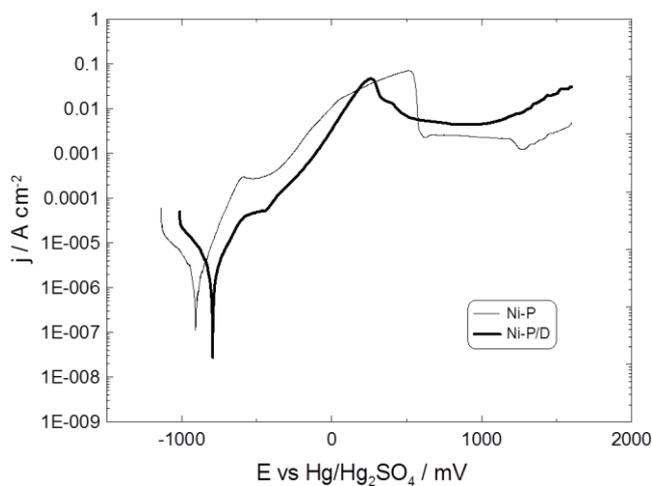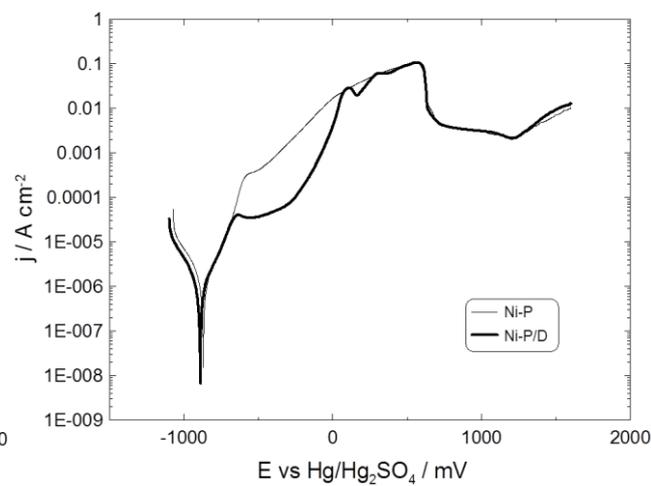
Fig. 5. Potentiodynamic polarization curves in model corrosive environment of Ni-P and Ni-P/D coatings deposited in electrolyte with a pH: a) 3.8; b) 4.8.

The SEM images in Fig. 6 compare the surface of the coatings without (Fig. 6a) and with (Fig. 6b) incorporated diamond particles after the potentiodynamic tests. The composite Ni-P/D coating dissolves more uniformly than the Ni-P coating. The latter features general thinning in the central work area and dissolves completely in the peripheral zones (Fig. 6a).

(a)   (b)
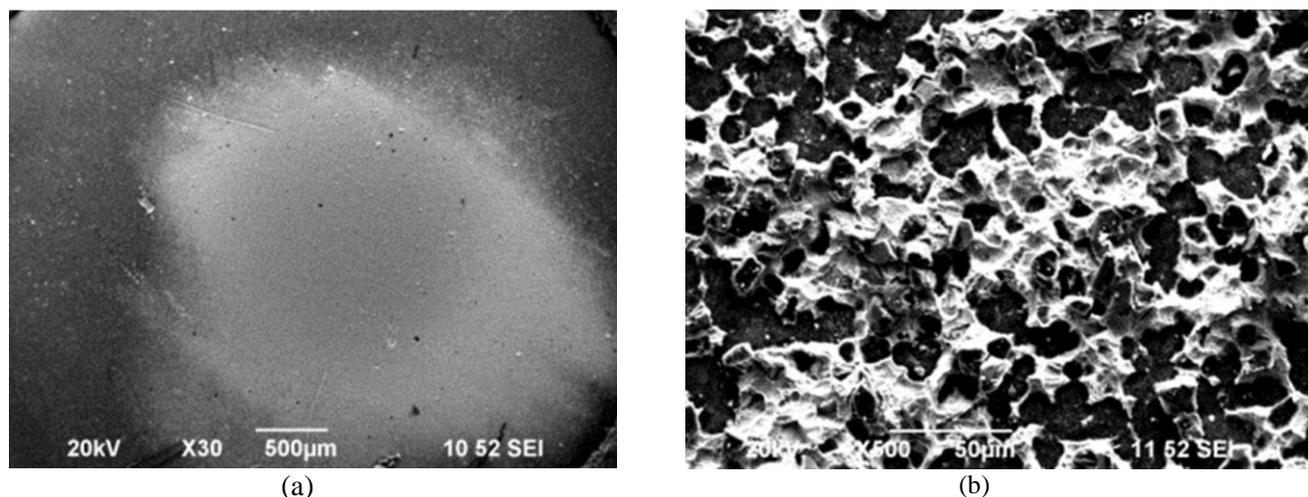
Fig. 6. SEM images of coatings (deposited at pH 4.8) after anodic potentiodynamic dissolution:
a) Ni-P; b) Ni-P/D.
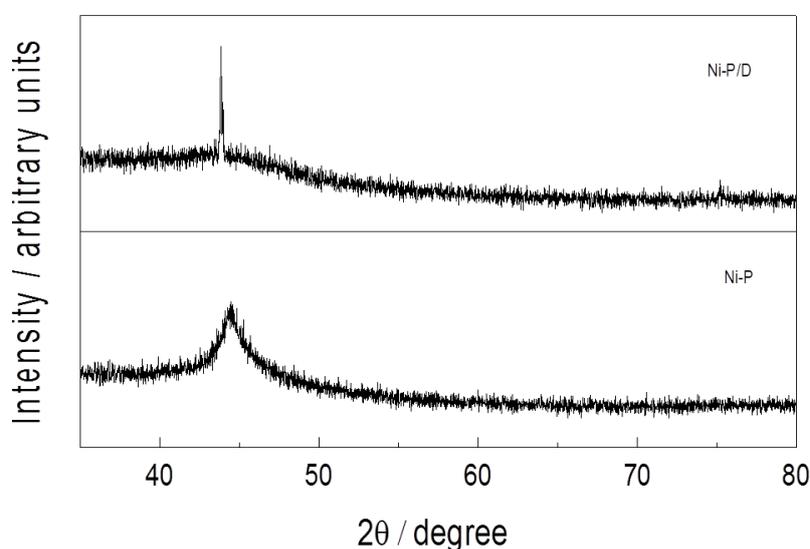
Fig. 7. XRD pattern of Ni-P and Ni-P/D coatings (deposited at pH 4.8) after anodic potentiodynamic dissolution according Fig. 5.

The XRD spectra show that both the Ni-P and Ni-P/D coatings have preserved their amorphous structure after the electrochemical test (Fig. 7). The results of the X-ray microanalysis indicate that the percent P content is preserved, too. The recorded reflexes evidence the incorporated particles in the coatings, irrespective of their low thickness, which is an indication of their good adhesion to the matrix.

CONCLUSIONS

Ni-P and composite Ni-P/D coatings with diamond particles sized 14-20 μm are produced by electroless deposition in electrolytes with two pH values: 3.8 and 4.8.

With increase of the electrolyte pH the thickness and microhardness of the Ni-P coatings increase, but the P content decreases.

A slight increase in microhardness of the Ni-P coatings with deposition time is observed when they are deposited at electrolyte pH 4.8.

With increase of the time of stay in the neutral salt spray chamber the coatings lose mass, more notably when they contain incorporated diamond particles.

On anodic polarization in sulfate medium up to the potential of oxygen evolution, the coatings do not dissolve completely. The composite Ni-P/D coatings dissolve more uniformly than the Ni-P deposits, they preserve their amorphous structure and exhibit lower corrosion rate.

REFERENCES

1. M. M. Mirza, E. Rasu, A. Desilva, *Amer. Chem. Sci. J.,* **13,** 1 (2016).
2. C.A. Loto, *Silicon,* **8, 177** (2016).

3. K. Hari Krishnan, S. John, K. N. Srinivasan, J. Praveen, M. Ganesan, P.M. Kavimani, *Metall. Mater. Trans.,* **37,** 1917 (2006).

4. C. Larson, J. R. Smith, G. J. Armstrong, *Trans. Inst. Metal Finishing,* **3,** 120 (2013).

5. B. W. Zhang, S. Z. Liao, H. W. Xie, H. Zhang, *Trans. Inst. Metal Finishing,* **6,** 310 (2013).

6. X. Shu, Y. Wang, J. Peng, P. Yan, B. Yan, X. Fang, Y. Xu, *Int. J. Electrochem. Sci.,* **10,** 1261 (2015).

7. T. Rabizadeh, S. Reza Allahkaram, *Mater. Design*, **32,** 133 (2011).

8. I. V. Petukhov, N. A. Medvedeva, I. R. Subakova, V. I. Kichigin, *Protctn Metals & Phys. Chem. Surfaces*, **50,** 875 (2014).

9. J. N. Balaraju, T. S. N. Sankara Narayanan, S. K. Seshadri, *Journal of Applied Electrochemistry,* **33** (2003) 807–816.

10. A. Sharma, A. K. Singh, *J. Materials Eng. Performance,* **22,** 176 (2013).

11. M. Islam, M. R. Azhar, N. Fredj. T. D. Burleigh, O. R. Oloyede, A. A. Almajid, S. I. Shah, *Surface Coatings Technol.,* **261,** 141 (2015).

12. P. Makkar, R.C. Agarwala, V. Agarwala, *J Mater Sci,* **50,** 2813 (2015).

13. H. Xu, Z. Yang, M.-Ke Li, Y.-Li Shi, Y. Huang, H.-Lin Li, *Surface Coatings Technol.,* **191**, 161 (2005).

14. V.V.N. Reddy, B. Ramamoorthy, P. Kesavan Nair, *Wear,* **239,** 111 (2000).

15. Y. L. Shi, Z. Yang, H. Hu, M. K. Li, H. L. Li, *J. Materials Sci.*, **39,** 5809 (2004).

16. X.T. Huang, G.Y. Cai, *Appl. Mech. Materials*, **26-28,** 843 (2010).

17. H. Mazaheri, S. Reza Allahkaram, *Appl. Surface Sci.*, **258,** 4574 (2012)..

18. S.R. Allahkaram, H. Mazaheri, *Iranian J. Materials Sci. Eng.,* **11,** 18 (2014).

19. C.K. Lee, C.L. Teng, A.H. Tan, C.Y.Yang, S.L. Lee, *Key Eng. Materials*, **656-657,** 51 (2015).

20. M. Petrova, M. Georgieva. V. Chakarova, E. Dobreva, *Arch. Metall. Mater.*, **61,** 493 (2016).

21. M. Georgieva, M. Petrova, V. Chakarova, *Bulg. Chem. Commun.,* **45,** 116 (2013).

КОРОЗИОННА УСТОЙЧИВОСТ НА БЕЗТОКОВИ Ni-P ПОКРИТИЯ ПОЛУЧЕНИ ВЪРХУ ПОЛИМЕРНА ПОДЛОЖКА (ABS)

В. Чакърова, М. Георгиева, М. Петрова

Институт по физикохимия - Българска академия на науките
София, 1113, ул. „Акад. Г. Бончев", бл.11
секция „Електрохимия и корозия"

(Резюме)

По метода на безтоково отлагане са получени Ni-P и композитни Ni-P покрития с диамантени частици с размер 14-20 µm върху подложка от акрилонитрил бутадиен стирол. Изследвано е влиянието на времето на отлагане и киселинността на разтвора върху скоростта на отлагане, съдържанието на фосфор и микротвърдостта на покритията. Корозионни изпитания на покрития, получени при две стойности на pH на електролита са проведени в камера за неутрална солена мъгла, а потенциодинамични криви са снети в моделна корозионна среда - 0.5M Na$_2$SO$_4$ solution with pH 5.9. С помощта на сканираща електронна микроскопия е изследвана морфологията на покритията преди и след изпитанията, а чрез рентгенов микроанализ са определени измененията в елементния състав. Резултатите показват, че включването с на диамантени частици в Ni-P покритие се образуват пасивни филми с добра корозионна устойчивост.

Electroless deposition of silver on poly(3,4-ethylenedioxythiophene) obtained in the presence of polystyrene sulfonate or dodecyl sulfate ions – effect of polymer layer thickness

V.I. Karabozhikova, V.Ts.Tsakova*

Institute of Physical Chemistry, Bulgarian Academy of Sciences,1113 Sofia, Bulgaria

Poly(3,4-ethylenedioxythiophene) (PEDOT) layers are electrochemically synthesized in the presence of excess of perchlorate ions and either polystyrene sulfonate (PSS) or dodecyl sulfate (DDS) as co-doping ions. Electroless deposition of silver is studied in two silver plating solutions containing Ag^+ cations or $[AgEDTA]^{3-}$ anion complexes. The electroless reduction of metal ions occurs at the expense of oxidation of mildly pre-reduced PEDOT/PSS and PEDOT/DDS layers with different thickness. It is established that the amount of deposited silver, Q_{Ag} depends linearly on thickness with steeper dependence obtained in solution of silver anion complexes in comparison to silver cations. At constant thickness, Q_{Ag} depends on the type of PEDOT layers with PEDOT/DDS providing higher Q_{Ag}, especially in $[AgEDTA]^{3-}$ solution. The results are discussed in terms of limited diffusion of $[AgEDTA]^{3-}$ ions inside the polymer structure, possible switching of the rate determining step from diffusion (in the Ag^+ case) to charge transfer across the polymer layer (in the $[AgEDTA]^{3-}$ case), and expected organic ions-induced difference in the internal PEDOT structure. SEM images reveal the possibility to affect markedly the number, size and size distribution of the metallic particles. In terms of homogeneous surface coverage with small monodisperse silver particles best results are obtained with thin PEDOT/PSS|Ag^+ and thick PEDOT/DDS|$[AgEDTA]^{3-}$ layers.

Keywords: electroless deposition, silver, PEDOT, polystyrene sulfonate, dodecyl sulfate

INTRODUCTION

Conducting polymers (CP) are often used as supporting materials for metal particles deposition due to their high electrical conductivity, well developed surface and opportunities for using different chemical and electrochemical deposition techniques to obtain well dispersed metal phase (see [1-6] and literature cited there in). Along with the conventional chemical deposition approach based on metal ions reduction occurring at the expense of oxidation of dissolved reductant species, CPs present another opportunity to drive electroless metal deposition in a way that is close to the immersion techniques for chemical deposition [2, 6]. This method is based on the intrinsic ability of CPs to occupy different interconvertible oxidation states and couples, following reactions:

$$Me^{n+} + ne^- \rightarrow Me^0 \qquad (1)$$
$$CP^{m+} \rightarrow CP^{(m+n)+} + ne^- \qquad (2)$$

where *n* is the number of electrons exchanged for reducing a single metal ion and *m* denotes the extent of initial oxidation of the CP material. For instance, if pre-reducing polyaniline (PANI) in the leucoemeraldine state and immersing it in solution of metal ions with positive enough equilibrium potential, such as silver or palladium, PANI will undergo oxidative transition to the emeraldine state. This oxidative transition will go in parallel with reduction of the corresponding metal ions. Apart from complete transition between two chemically different oxidation states, electroless metal deposition may occur also in the potential region, where CPs show only pseudo-capacitive behavior characterized with different amount of oxidized monomeric units within one and the same formal oxidation state. In any case the amount of deposited metal phase is limited by the available intrinsic redox charge of the CP layers and depends on the extent of CP initial reduction and the amount of the polymer material. In general, smaller amounts of intrinsic CP redox charge are involved in electroless metal deposition when working in the pseudo-capacitive potential region and thus, smaller amounts of metal become dispersed in the CP material.

Silver-modified CP-based electrodes have been recently intensively investigated for various applications, such as solar cells [7, 8], electrochromic devices [9], sensing applications [10, 11], Surface Enhanced Raman Spectroscopy (SERS) substrates [12], etc. Silver is considered also as an antimicrobial agent that becomes easily combined with polymeric materials [13, 14]. For all these applications the way of dispersing the silver phase is of utmost importance. Silver electroless

deposition at the expense of CP oxidation was studied mainly for PANI [15-25] and polypyrrole [17, 25-30]. Few studies address silver electroless deposition on polythiophenes, such as polyalkylthiophenes [31, 32] and poly(3,4-ethylenedioxythiophene) (PEDOT) [30, 33], although the latter is one of the most studied CP material. The investigations so far performed concern PEDOT layers obtained in aqueous solutions containing either perchlorate or nitrate ions. It is known that PEDOT is very often synthesized in the presence of organic anions such as polystyrene sulfonate (PSS) or dodecyl sulfate (DDS) which act as both surfactant and doping species and affect markedly the CP properties.

The aim of the present investigation is to study the dependence of the amount and type of electroless deposited silver on the thickness of PEDOT layers, synthesized in the presence of PSS or DDS ions. A further goal concerns the comparison between electroless deposition from plating solutions containing two different silver ionic species - silver cations and silver complex anions. In all cases, before immersion in the silver plating solution, PEDOT is subjected to mild reduction in the pseudocapacitive potential region for this polymer, in order to limit the amount of deposited silver. This investigation is a further extension of a series of studies [34-37] trying to elucidate the effect of the co-doping organic anions, used in the course of synthesis of PEDOT, for various characteristics of the polymer layers, such as surface morphology, electroanalytical sensitivity and selectivity with respect to oxidation of organic species and electrochemical and electroless metal deposition.

EXPERIMENTAL

The electrochemical experiments were carried out by means of Autolab PGSTAT 12 potentiostat/galvanostat equipped with GPES software (Eco Chemie, Utrecht, the Netherlands). A three electrode set-up was used with glassy carbon disk as working electrode (with surface area $S = 0.08$ cm^2) and a platinum plate as counter electrode. The reference electrode was saturated mercury/mercury sulfate (Hg/Hg$_2$SO$_4$/0.5 M K$_2$SO$_4$) electrode (MSE). $E_{MSE} = 0.66$ V *vs* standard hydrogen electrode. All potentials in the text and figures refer to MSE. Argon gas was used to remove dissolved oxygen from the electrolyte solutions before electrochemical measurements.

Electrochemical polymerization of EDOT was performed at constant potential $E_a = 0.38$ V in aqueous solutions of 10 mM EDOT, 0.5 M LiClO$_4$

and 34 mM organic anionic dopants - sodium PSS or sodium DDS. The PEDOT coatings obtained in the presence of the organic dopants will be further denoted by PEDOT/PSS and PEDOT/DDS, respectively. The thickness of the PEDOT layers was varied by using different polymerization times and fixing the polymerization charges at Q_{poly}=1, 2 or 4 mC.

Electroless deposition of silver was carried out at pre-reduced PEDOT layers. The electrochemical reduction was accomplished in supporting electrolyte (0.4 M HClO$_4$) at constant potential (-0.62 V for 15 min), corresponding to the high conducting state of PEDOT. The reduced PEDOT-coated electrodes were transferred in the silver plating solution consisting of either 10 mM AgNO$_3$ and 0.4 M HClO$_4$, or 10 mM AgNO$_3$, 0.02 M Na$_2$C$_{10}$H$_{14}$O$_8$N$_2$ (NaEDTA) and 0.5 M KNO$_3$. In the latter solution the silver species form [AgEDTA]$^{3-}$ anionic complexes [16]. The equilibrium potentials of silver in these solutions are $E^0 = -0.002$ V vs MSE for Ag$^+$ and $E^0 = -0.040$ V vs MSE for [AgEDTA]$^{3-}$. The time for silver electroless precipitation was set at 50 s. After each silver deposition experiment silver was dissolved in 0.4 M HClO$_4$ by applying voltammetric scans (at 5 mV s^{-1}) at potentials more positive than the equilibrium potential of Ag. The amount of silver was calculated by integrating the dissolutions peaks registered within the first two scans. The presented data for the amount of silver deposited under each set of experimental conditions (i.e. polymerization charge, type of layer and type of silver ionic species) is the average of three deposition/dissolution experiments. Within individual experiments at otherwise fixed experimental conditions the amount of the silver dissolution-related charge varied within 15 % of the average value.

The surface morphology of the various Ag-precipitated PEDOT layers was examined by scanning electron microscope JEOL 6390 equipped with Inca Oxford EDX analyzer.

RESULTS AND DISCUSSION

Fig. 1 shows open circuit potential (OCP) transients measured in the course of electroless silver deposition from Ag$^+$ and [AgEDTA]$^{3-}$ solutions at PEDOT/PSS and PEDOT/DDS layers obtained at different polymerization charges. For all transients a steep OCP drop is observed within the first few seconds followed by a gradual establishment of steady state OCP values. The final OCP values are in all cases more negative than the equilibrium potential of Ag in the respective silver

plating solutions, indicating the establishment of mixed potentials affected by the redox potential of the PEDOT layers themselves. With increasing Q_{poly} the transients measured at PEDOT/DDS do not show a strong thickness effect (Fig. 1 b and d). A stronger effect with thickness on OCP transients is observed for PEDOT/PSS layers (Fig. 1 a and c).
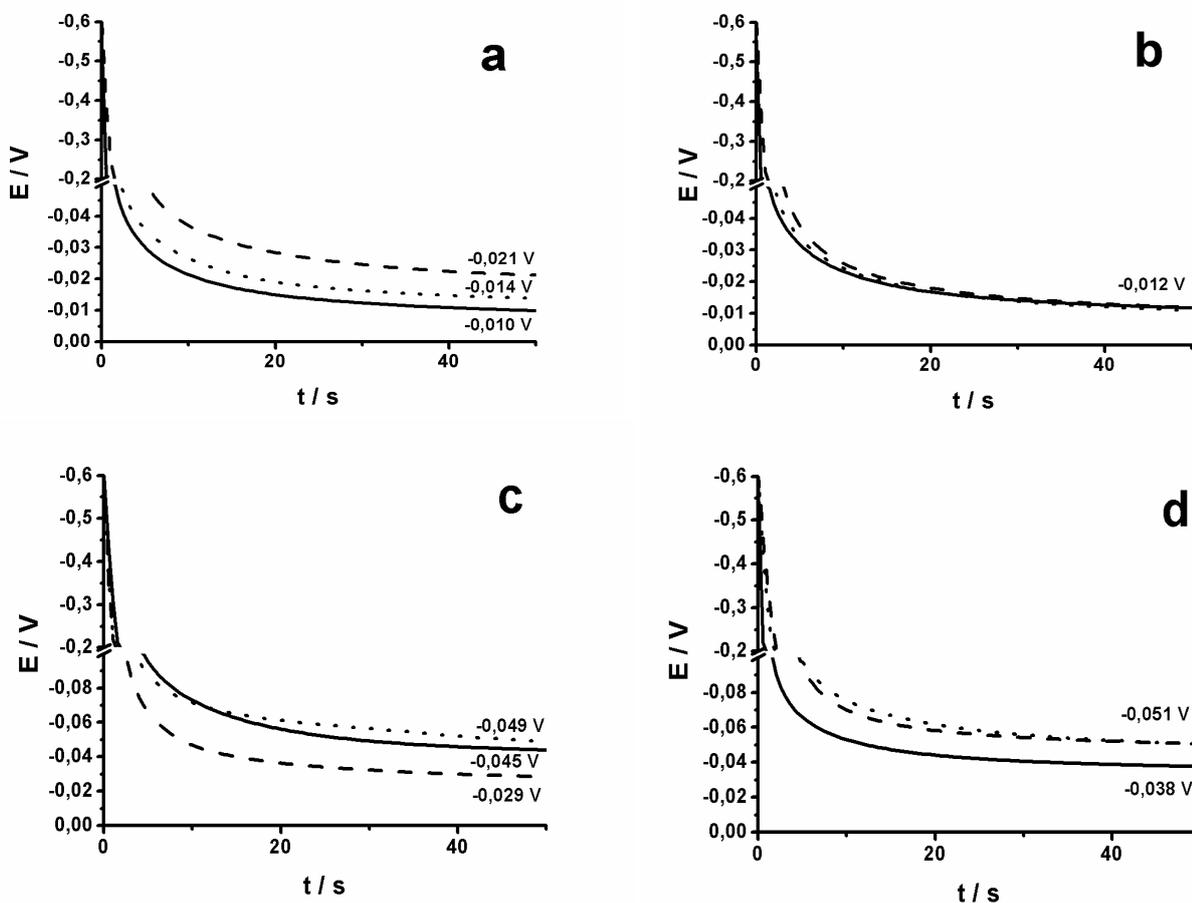

Figure 1. OCP transients obtained in Ag^+ (a, b) and $[AgEDTA]^{3-}$ (c, d) solutions at PEDOT/PSS (a, c) andPEDOT/DDS (b, d) layers with different amounts of polymerization charge: 1 mC (dashed line), 2 mC (dotted line), 4 mC (full line).
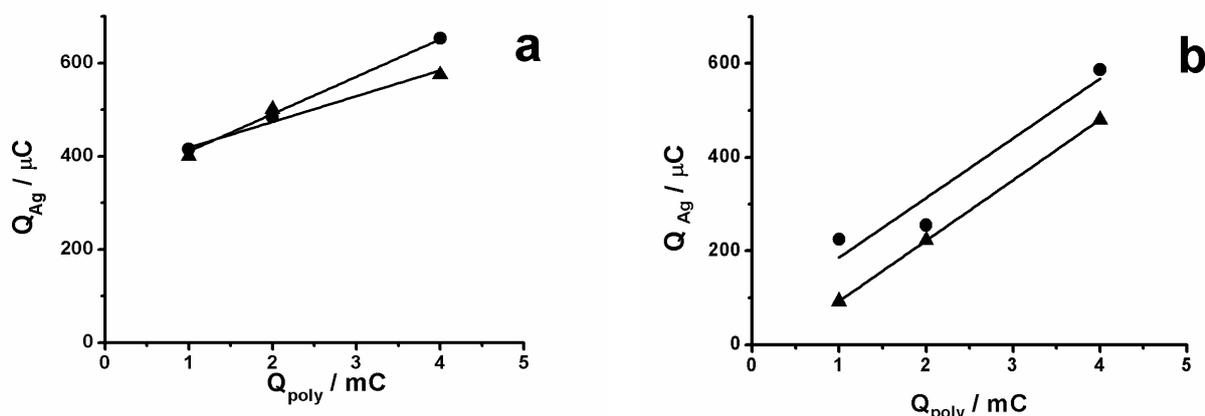
Figure 2. Amount of deposited silver from Ag^+ (a) and $[AgEDTA]^{3-}$(b) solutions at PEDOT/PSS (▲) and PEDOT/DDS (●) layers with different polymerization charge.

In this case, the final OCP value shifts to more negative potentials for Ag^+ solution, and to more positive values for $[AgEDTA]^{3-}$ solution, pointing to establishment of different mixed potential equilibria depending on PEDOT/PSS thickness. Comparison of the OCP transients obtained in Ag^+

and [AgEDTA]$^{3-}$ solution for the thickest PEDOT/PSS layers show that the final OCP values coincide irrespective of the type of depositing silver ions. This result, together with the shift in OCP with increasing PEDOT layer thickness, may be considered as indications for possible PSS-induced Ag complex formation. The possibility for formation of Ag/PSS complex species was considered in [38]. Formation of a complex of Ag with another polysulfonic acid was also discussed in the context of polysulfonic-acid-doped polypyrrole [39]. It can be suggested that with increasing Q_{poly}, the amount of PSS involved in doping of the PEDOT increases, and gives rise to complexation of silver. The latter may affect the establishment of a mixed potential in the PEDOT/PSS|Ag systems.

The amount of deposited silver obtained in the course of electroless deposition in the two silver plating solutions is presented in Fig. 2. The comparison shows a much steeper thickness dependence of Q_{Ag} in the presence of silver complex ions, than in the presence silver cations. At doubled polymerization charge Q_{poly}, the silver amount increases by a factor of 1.25 for Ag$^+$ solution and by a factor of about 2 in the [AgEDTA]$^{3-}$ solution. There is also a difference in the amount of silver depending on the type of PEDOT with PEDOT/DDS layers, providing larger amounts of silver in the [AgEDTA]$^{3-}$ plating solution.

To discuss these results let us consider the individual steps that may affect the overall rate for electroless metal deposition under OCP conditions [30]: i/ ions transport from bulk solution to the polymer surface; ii/ ions mass transfer within the polymer phase; iii/ inter and intra electronic charge transfer across the polymer chains and iv/ charge transfer between the metal ions and the polymer phase. Phase formation phenomena (i.e. metal nucleation and growth) may additionally complicate the situation. Obviously, one or several of these steps are affected by the type of silver ions involved in the electroless deposition process. Bulk diffusion of Ag$^+$ is faster than bulk diffusion of [AgEDTA]$^{3-}$. Ionic transport within the PEDOT structure should be easier for Ag$^+$ than for the bulky [AgEDTA]$^{3-}$ ions, which means that Ag$^+$ should have faster and easier access to both external and internal polymer phase surface. This may be in the origin of the large amounts of silver deposited even at low polymerization charges. The somewhat lower amount of Q_{Ag}, observed for the thickest PEDOT/PSS layer, should be attributed to the fact that equilibrium is established at a more negative potential. The latter corresponds to less oxidized PEDOT which predetermines the deposition of smaller amount of metal.

In general, the charge transfer between a conducting electrode and a metal anion complex is expected to be slower, and to require more negative potentials than the charge transfer of the corresponding cationic species. Electrodeposition in metal ion complex solutions requires usually higher overpotentials. According to the OCP transients in both solutions, the electroless deposition process occurs in the same range of potentials, which corresponds formally to lower overpotentials in the silver anion complex solution case. The role of the [AgEDTA]$^{3-}$ species should be considered also from another point of view. Diffusion of these relatively large anionic species inside the polymer structure will be impeded in comparison to cationic silver. On the other hand, anionic species are involved in the doping of PEDOT occurring in the course of oxidation. However, bearing in mind the large excess of nitrate ions present in the silver plating solution, this should occur at the expense of these inorganic anions. Thus, electroless deposition in the [AgEDTA]$^{3-}$ solution is expected to take place at the polymer/solution interface, rather than inside the polymer structure, which means that the transfer of charge across the polymer layer may become the rate determining step of the overall process. This transfer will definitely depend on the polymer layer thickness and specific internal polymer structure. The latter is expected to be influenced by the doping ions used in the course of synthesis. Thus, the difference in the behavior of PEDOT/DDS and PEDOT/PSS layers, established in [AgEDTA]$^{3-}$ solution, could be attributed to a different internal structure affecting the charge transfer across the polymer phase. Although, it is difficult to study and reveal the polymer structure, especially inside the polymer phase, SEM studies of PEDOT/PSS and PEDOT/DDS layers give evidence for a difference in the surface morphology of these two materials [35].

SEM observations of the silver deposit, carried out for the various PEDOT layers (Fig. 3), give additional evidence in support of the above considerations. The micrographs demonstrate that both the type of PEDOT layer and the type of the silver species used for deposition affect the number, size and size distribution of the metallic particles. It is readily seen that use of silver complex anions results in a narrow size distribution of smaller crystals and homogeneous coverage of the whole surface (Fig. 3 e and f). This is an expected effect of metal anionic complexes in metal deposition that

40

was demonstrated in studies on silver plating in the presence of EDTA [40]. Thin and thick PEDOT layers (compare Fig. 3a and 3b with Fig. 3c and 3d) behave in different ways depending on the type of organic dopant used for their synthesis. With increasing thickness the silver deposit on the electrode surface becomes more homogeneous (smaller size distribution and larger number of crystals) in the PEDOT/DDS case. On the opposite, a more homogeneous silver deposit is found on the PEDOT/PSS layer with smaller thickness (Fig. 3 a). These different trends should relate again to organic dopants-induced difference in the PEDOT structure.
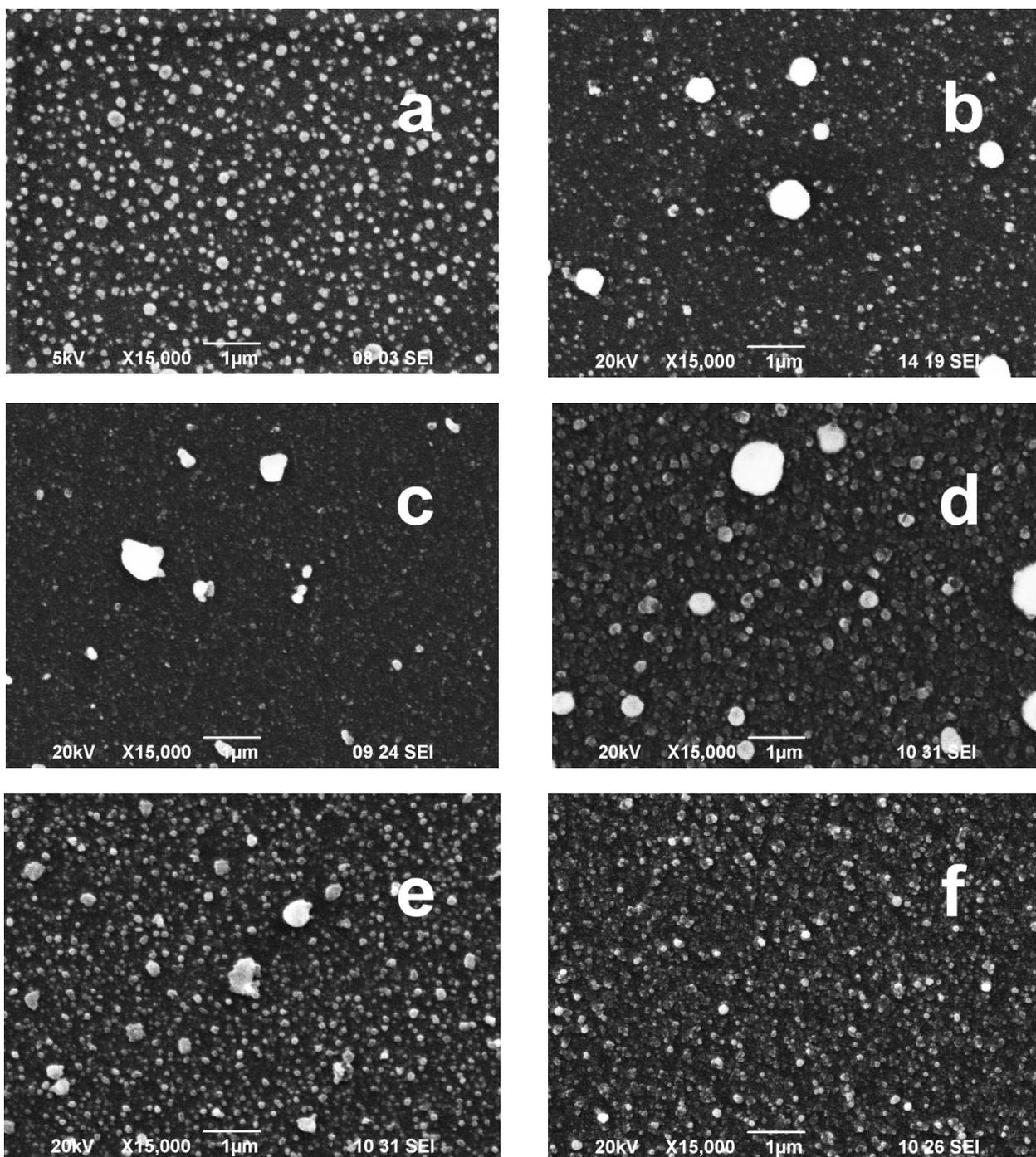
Figure 3. SEM of Ag-modified polymer layers with Q_{poly}=2 mC (a, c, e) and Q_{poly}=4 mC (b, d, f) obtained at PEDOT/PSS (a, b) and PEDOT/DDS (c, d, e, f) in Ag$^+$ (a, b, c, d) and [AgEDTA]$^{3-}$(e, f) solutions.

41

CONCLUSIONS

The present study shows that electroless deposition of silver on PEDOT is a process that depends markedly on several parameters, such as polymerization charge, type of organic ions used in the course of synthesis, and type of the depositing metal ions (cations or complex anions). Varying these parameters provides the opportunity to obtain not only different amounts of silver, but also completely different number, size and size distribution of the metallic phase. The type of the metal ion provides the opportunity to affect the diffusion inside the polymer phase, and to complete the process by involving both internal and external or, alternatively, mainly external polymer interface. Thus, the rate determining step becomes very probably affected, and limiting diffusion becomes replaced by limiting charge transfer across the polymer phase. As far as internal polymer structure is determining for this process, organic doping ions-induced properties of PEDOT start playing a decisive role.

The results presented so far reveal also the possibility to affect the electroless deposition by metal-complex formation at the expense of the doping ions used in the course of CP synthesis. Indications in this respect are obtained in the PEDOT/PSS|Ag$^+$ case. This opportunity should be studied in further details by exploring PEDOT layers obtained in the presence of PSS alone, without addition of inorganic anions, in order to reveal better this effect.

Finally, from a practical point of view, the opportunity to obtain a highly homogeneous monodisperse surface distribution of metal particles as provided by thin PEDOT/PSS|Ag$^+$ and thick PEDOT/DDS|[AgEDTA]$^{3-}$ layers is important and supports various applications of the Ag-modified PEDOT material.

REFERENCES

1. V. Tsakova, *J. Solid State Electrochem.*, **12**, 1421 (2008).
2. V. Tsakova, in:, Nanostructured Conductive Polymers, A. Eftekhari (ed), Ch. 7, John Wiley&Sons, Chichester, 2010, p. 289.
3. C. Janaky, C. Visy, *Anal. Bioanal. Chem.*,**405**,3489 (2013).
4. G. Ciric-Marjanovic, *Synth. Met.*,**170**,31 (2013).
5. R. Seeber, F. Terzi, C. Zanardi, in: Monographs in Electrochemistry, F. Scholz (ed), Springer, Berlin, 2014.
6. V. Kondratiev, V. Malev, S. Eliseeva, *Russ. Chem. Rev.*, **85**, 14 (2016).
7. A. Iwan, B. Boharewicz, I. Tazbir, A. Sikora, B. Zboromirska-Wnukiewicz, *Int. J. Photoenergy*, **2015**, 1 (2015).
8. H. Kim, G. Veerappan, D. H. Wang, J. H. Park, *Electrochim. Acta*, **187**, 218 (2016).
9. M.A.G. Namboothiry, T. Zimmerman, F. M. Coldren, J. Liu, K. Kim, D. L. Carrol, *Synth. Met.*, **157**, 580 (2007).
10. A. Balamurugan, S. M. Chen, *Electroanal.*, **21**, 1419 (2009).
11. E. Park, O. S. Kwon, S. J. Park, J. S. Lee, S. You, J. Jang, *J. Mater. Chem.*, **22**, 1521 (2012).
12. Ü. Dogan, M. Kaya, A. Cihaner, M. Volkan, *Electrochim. Acta*, **85**, 220 (2012).
13. P. Dallas, V. K. Sharma, R. Zboril, *Adv. Colloid Interface Sci.*, **166**, 119 (2011).
14. Z. Kucekova, V. Kasparkova, P. Humpolicek, P. Sevcikova, J. Stejskal, *Chem. Pap.*, **67**, 1103 (2013).
15. Q. Zhang, C. Q. Cui, J. Y. Lee, F. C.Loh, *J. Electrochem. Soc.*, **142**, 1097 (1995).
16. S. Ivanov, V. Tsakova, *Electrochim. Acta*, **50**, 5616 (2005).
17. R. Dimeska, P. S. Murray, S. F. Ralph, G. G. Wallace, *Polymer*, **47**, (2006) 4520.
18. H. L. Wang, W. Li, Q. X. Jia, E. Akhadov, *Chem. Mater.*, **19**, 520 (2007).
19. J. Stejskal, M. Trchova, J. Kovarova, J. Prokes, M. Omastova, *Chem. Pap.*, **62**,181 (2008).
20. J. Stejskal, M. Trchova, L. Brožová, J. Prokeš, *Chem. Pap.*, **63**, 77 (2009).
21. J. Stejskal, J. Prokes, I. Sapurina, *Mater. Lett.*, **63**, 709 (2009).
22. S. Bouazza, V. Alonzo, D. Hauchard, *Synth. Met.*, **159**, 1612 (2009).
23. N. Mack, J. Bailey, S. Doorn, C.-A. Chen, H.-M. Gau, P. Xu, D. Williams, E. Akhadov, H.-L. Wang, *Langmuir,* **27**, 4979 (2011).
24. V. Lyutov, V. Tsakova, *J. Solid State Electrochem.,* **15**, 2553 (2011).
25. J. Stejskal, *Chem. Pap.*, **67**,814 (2013).
26. F.-Y. Song, K.-K. Shiu, *J. Electroanal. Chem.*, **498**, 161 (2001).
27. C. Visy, E. Pinter, T. Fulei, R. Patakfalvi, *Synth. Met.*, **152**, 13 (2005).
28. E. Pinter, R. Patakfalvi, T. Fulei, Z. Gingl, I. Dekany, C. Visy, *J. Phys. Chem. B*, **109**, 17474 (2005).
29. V. Jovanovic, S. Terzic, A. Dekanski, *J. Serb. Chem. Soc.*, **70**, 41 (2005).
30. M. Ocypa, M. Ptasinska, A. Michalska, K. Maksymiuk, E.A.H. Hall, *J. Electroanal. Chem.*, **596**, 157 (2006).

31. M. Lebedev, M. Lauritzen, A. Curzon, S. Holdcroft, *Chem. Mater.*, **10**, 156 (1998).
32. E. Pinter, Z. Fekete, O. Berkesi, P. Makra, A. Patzko, C. Visy, *J. Phys. Chem. C*, **111**, 11872 (2007).
33. E.G. Tolstopyatova, N.A. Pogulyaichenko, V.V. Kondratiev, *Russ. J. Electrochem.* **50**, 510 (2014).
34. D. Filjova, G. Ilieva, V. Tsakova, *Bulg.Chem.Commun.*, **45**, 196 (2013).
35. V. Tsakova, G. Ilieva, D. Filjova, *Electrochim. Acta*, **179**, 343 (2015).
36. V. Karabozhikova, V. Tsakova, *Bulg.Chem. Commun.*, **48A**, 71 (2016).
37. V. Karabozhikova, V. Tsakova, *Chem. Pap.*, accepted for publication.
38. F. Vaslow, G. E. Boyd, *J. Phys. Chem.*, **70**, 2295 (1966).
39. M. Ignatova, D. Labaye, S. Lenoir, D. Strivay, R. Jerome, C. Jerome, *Langmuir*, **19C**, 8971 (2003).
40. G.M. de Oliveira, L.L. Barbosa, R.L. Broggi, I.A. Carlos, *J. Electroanal. Chem.*, **578**, 151 (2005).

БЕЗТОКОВО ОТЛАГАНЕ НА СРЕБРО ВЪРХУ ПОЛИ(3,4-ЕТИЛЕНДИОКСИТИОФЕН), ПОЛУЧЕН В ПРИСЪСТВИЕ НА ПОЛИСТИРЕНСУЛФОНАТНИ ИЛИ ДОДЕЦИЛСУЛФАТНИ ЙОНИ – ЕФЕКТ НА ДЕБЕЛИНАТА НА ПОЛИМЕРНОТО ПОКРИТИЕ

Василена И. Карабожикова, Весела Ц. Цакова*

Институт по физикохимия, БАН, 1113 София, България

(Резюме)

Поли(3,4,етилендиокситиофен) (ПЕДОТ) е синтезиран електрохимично в присъствие на излишък от перхлоратни йони и на полистиренсулфонатни (ПСС) или додецилсулфатни (ДДС) ко-дотиращи йони. Безтоково отлагане на сребро е изследвано в два разтвора на сребърни йони, катиони и [AgEDTA]$^{3-}$ анионни комплекси. Безтоковата редукция на металните йони се осъществява за сметка на окисление на предварително редуцирани слоеве от ПЕДОТ/ПСС и ПЕДОТ/ДДС с различна дебелина на полимерното покритие. Установено е, че количеството на отложеното сребро, Q_{Ag} зависи линейно от дебелината на полимерния слой като зависимостта е много по-стръмна при използване на разтвор на сребърни анионни комплекси в сравнение със сребърни катиони. При постоянна дебелина на полимерното покритие, Q_{Ag} зависи от вида на ПЕДОТ като слоевете от ПЕДОТ/ДДС осигуряват по-високи стойности на Q_{Ag}, особено в разтвор на [AgEDTA]$^{3-}$. Резултатите са обсъдени от гледна точка на ограничена дифузия на анионните комплекси на среброто във вътрешността на полимерната структура, възможна промяна на скоростоопределящата стъпка на процеса от дифузия (в случая на Ag$^+$) към пренос на заряд през полимерното покритие (в случая на [AgEDTA]$^{3-}$), както и очаквана, свързана с ко-дотиращите органични йони, структурна разлика на двата вида покрития от ПЕДОТ. Микроскопски снимки разкриват възможността да се влияе съществено върху броя, размера и разпределението по размер на металните частици в зависимост от вида и дебелината на полимерното покритие, както и на типа на отлагащия се метален йон. Най-добри резултати от гледна точка на хомогенно покритие на полимерната повърхност с малки монодисперсни сребърни частици са получени в случая на тънки ПЕДОТ/ПСС|Ag$^+$ и дебели ПЕДОТ/ДДС|[AgEDTA]$^{3-}$слоеве.

Novel polymer-based nanoporous carbon adsorbent for removal of pentachlorophenol from water

I.G. Stoycheva[1]*, B.G. Tsyntsarski[1], B.N. Petrova[1], T.K. Budinova[1], A. Popova[1], N.V. Petrov[1], B. Nagel[2], U. Szeluga[2]

[1]*Institute of Organic Chemistry with Centre of Phytochemistry, Bulgarian Academy of Sciences, Acad. G. Bonchev str., Bl. 9, 1113 Sofia, Bulgaria*

[2]*Center of Polymer and Carbon Materials, Polish Academy of Sciences, M. Sklodowskiej-Curie 34, 41-819 Zabrze, Poland*

Polyolefin material - polyolefin wax, a by-product from industrial production of polyethylene at low pressure - was used for preparation of nanoporous activated carbon. The adsorbent surface characterization revealed well-developed surface area and presence of high amount of surface functional groups, capable of binding the adsorbate molecules. The results suggest a possible use of polymer waste as a suitable precursor for production of nanoporous activated carbon, thus lowering the cost of wastewater treatment processes. The obtained activated carbon was applied for adsorption of pentachlorophenol (PCP) from aqueous solution. Batch adsorbing experiments were performed under different conditions, i.e. concentration of pentachlorophenol, pH, contact time, etc. The adsorption of pentachlorophenol was found to follow Langmuir equation, as well as Freundlich equation.

Keywords: Adsorption, activated carbon, pentachlorophenol, water purification, polymer waste

INTRODUCTION

Chlorinated phenols are widely used as flame retardants, solvents, herbicides, insecticides and fungicides [1]. Effluents from polymeric resin production and oil refining, steel, petroleum, paint, pharmaceutic, paper industries also contain chlorophenolic compounds [2]. Pentachlorophenol (PCP) is one of the seven industrially produced chlorophenols [1]. PCP is accumulated in sediments and aquatic systems, however it has slow biodegradation rate [1]. Pentachlorophenol is toxic and mutagenic for microorganisms and mammals; as it is an inhibitor of oxidative phosphorylation [2]. PCP uncouple oxidative phosphorylation via making cell membranes permeable to protons, resulting in dissipation of trans-membranes proton gradients and consequential electrical potentials [3]. Maximal PCP discharge concentration in industrial effluents is limited down to $1 - 2$ mg/l. [1].

There are several methods for PCP removal - oxidation, biological degradation, membrane filtration, ion exchange, reverse osmosis, photocatalytic degradation [4]. Adsorption is a simple and effective method and it has been widely applied for the removal of different organic and inorganic pollutants. Activated carbons (AC) are considered to be efficient adsorbents, however the industrial anthracite-based activated carbon are expensive. In the last years there is a special attention towards production of low-cost activated carbons from different waste materials - biomass (agricultural by products, different sources of plants, etc.), coal by-products, polymers wastes, etc.

Polymer by-products from production of different polymer materials are very promising raw materials for synthesis of activated carbons, due to their availability at a low price. Thermo-chemical conversion of plastic by-products has received attention of the researchers, which is connected with the potential of these materials to produce energy as well as activated carbon with very good characteristics [5-8].

There are some reports for PCP removal by different adsorbents – bentonite [9], activated sludge biomass, [2] spent mushroom compost [3], pine bark [10], almond shell residues [1], coal fly ash [11] and fungal biomass [12]. Till now activate carbons from waste polymers have not found suitable application. It is possible to use them for removal of different organic pollutants, especially different substituted phenol compounds like PCP, which is one of the aims of this research paper.

In the present paper, novel carbon adsorbent was synthesizes from polymer waste (a by-product at the producing of polyethylene at low pressure) by carbonization with sulfuric acid and subsequent hydro-pyrolysis.

Surface area, porosity and structural properties of obtained activated carbon were characterized in

* To whom all correspondence should be sent:
E-mail: racheva89@abv.bg

details. The adsorption of activated carbons towards pentachlorophenol was investigated.

EXPERIMENTAL AND THEORETICAL METHODS
Synthesis of activated carbon

The initial raw materials for synthesis of activated carbon are polyolefin wax and phenol-formaldehyde resin. Polyolefin wax is a waste material, obtained as a by-product from production of polyethylene at low pressure. The mixture of polyolefin wax and phenol-formaldehyde resin (50:50%) was heated up to the melting temperature (150ºC) and then concentrated sulfuric acid was added until solidification. The solid product was cooled down and washed with water, then dried at 150ºC, and carbonized at 600 ºC in a covered silica crucible with a heating rate of 10 ºC min^{-1} under nitrogen atmosphere. The obtained carbonizate product was subjected to hydro-carbonization at 800ºC in a stainless steel vertical reactor for 1 h.

Surface measurements

Textural characterization was carried out by measuring the N_2 adsorption isotherms at -196 ºC using Quantachrome NOVA 1200 apparatus. Prior to the adsorption measurements the samples were outgassed under vacuum at 300ºC overnight, to remove any adsorbed moisture and gases. The isotherms were used to calculate specific surface area S_{BET} and total pore volume V_t.

Micropore and mesopore volumes were obtained by applying the DFT model to the N_2 adsorption data, assuming a slit-shaped pore geometry [43].

Oxygen functional groups

The content of oxygen-containing functional groups with acidic character on the carbon surface was determined applying the Boehm method by neutralization with bases of increasing strength: water solutions of $NaHCO_3$, Na_2CO_3, NaOH and sodium ethoxide. About 0.5 g (the same quantity is used for all the basic solutions) of the activated carbon sample was put in contact with 100 ml of 0.05 N water base solutions in sealed flasks. The suspensions were shaken at least 16 h, and then filtered. The excess of base remaining in the solution was determined from back-titration after adding an excess of standard HCl water solution. It was assumed that $NaHCO_3$ was capable of neutralizing all carboxylic groups, Na_2CO_3 - carboxylic and lactonic groups, NaOH - carboxylic, lactonic and phenolic groups, and sodium ethoxide was assumed to neutralize all acidic groups [14]. The total number of basic sites was determined by titration with 0.05 N HCl [15]. The procedure is the same as above mentioned, as back-titration of the excess of HCl was performed using titration with 0.05 N NaOH water solution.

The point zero charge (pH_{pzc}) was determined by inserting six portions of 50 ml 0.1 M NaCl solutions in six closed Erlenmeyer flasks. The pH of the solutions (pH_0) in each flask was adjusted to values 2, 4, 6, 8, 10 and 12, respectively, by adding 0.1M HCl or 1 M NaOH solutions. Furthermore six portions of 0.2 g adsorbent were added and agitated in a shaker for 1 h, and allowed to stay for 48 h (with intermittent manual shaking) to reach equilibrium. Then, the final pH vaues (pH_f) of supernatant liquids were measured [16]. The value of pH_{pzc} is determined in the case when $pH_0 = pH_f$.

The infrared measurements were performed by *Bruker Tensor 27* FTIR Spectrometer in the range 4000 - 400 cm^{-1} with a resolution of 1 cm^{-1} by means of reflection technique using an *MIRacle-Diamond/ZnSe Crystal Plate* ATR accessory (Pike technology).

pH determination

The following procedure was carried out: 4.0 g of carbon was put into a 250 cm^3 beaker and 100 cm^3 of distilled water was added. The beaker was covered with a watch glass and heated to a boiling temperature for 5 min. The mixture was then set aside and the supernatant liquid was poured off at 60°C. The decanted portion was cooled down to room temperature and measured to the nearest 0.1 pH value [17].

Adsorption measurements

The adsorption capacity of the carbon toward PCP was determined by the following procedure: 0.1 g portions of the activated carbon were added to four aqueous solutions (50 cm^3) of PCP with different concentrations - 0.01, 0.02, 0.025, 0.03 g/l, respectively. The initial and equilibrium concentrations of the PCP in the solution were determined spectrophotometrically by UV spectrophotometer Pharo 300 at 305 nm. The effect of pH on PCP removal was studied using 0.1 g activated carbon and 0.03 g/l water solution of PCP. The pH is adjusted by HCl and NaOH water solutions.

RESULTS AND DISCUSSION
Chemical characterization

The chemical analysis of activated carbon is presented in Table 1. The results show that hydro-pyrolysis increases carbon and oxygen content. The activated carbon sample has very low ash content and high hydrogen content, whereas sulfur content decrease two times during hydro-pyrolysis.

Table 1. Chemical characterization of activated carbon.

Sample	W^a wt.%	A^d wt.%	C wt.%	H wt.%	N wt.%	S wt.%	O wt.%
AC	2.02	2.78	84.54	2.18	1.65	0.02	11.52

W^a – water content, ash free basis; A^d – ash content, dry basis

Textural characterization

Porosity has strong effect on the adsorption properties of activated carbon. The pore structure of obtained activated carbon was investigated by N_2 gas adsorption. Textural characterization was carried out by measuring the N_2 adsorption isotherms at −196°C. The nitrogen adsorption isotherms of the activated carbon are presented in Fig. 1. Analysis of nitrogen adsorption data shows that activated carbon from mixture of polymer waste and phenol-formaldehyde resin has high surface area (S_{BET}) and well-developed pore structure. The part of the isotherms in the range of the relatively lower pressures has a steep increase with a tendency for saturation, which is typical for microporous adsorbents. The obtained N_2 adsorption isotherms correspond to IV type, according to Brunauer classification at low pressure [13]. The main textural parameters of the prepared carbon, obtained from the analysis of the nitrogen adsorption isotherms, are complied in Table 2.

Our results show that using precursor mixture of polyolefin wax and phenol-formaldehyde resin (containing oxygen) leads to activated carbon with high surface area. The pore volume analysis show that this activated carbon has prevailing content of micropores.
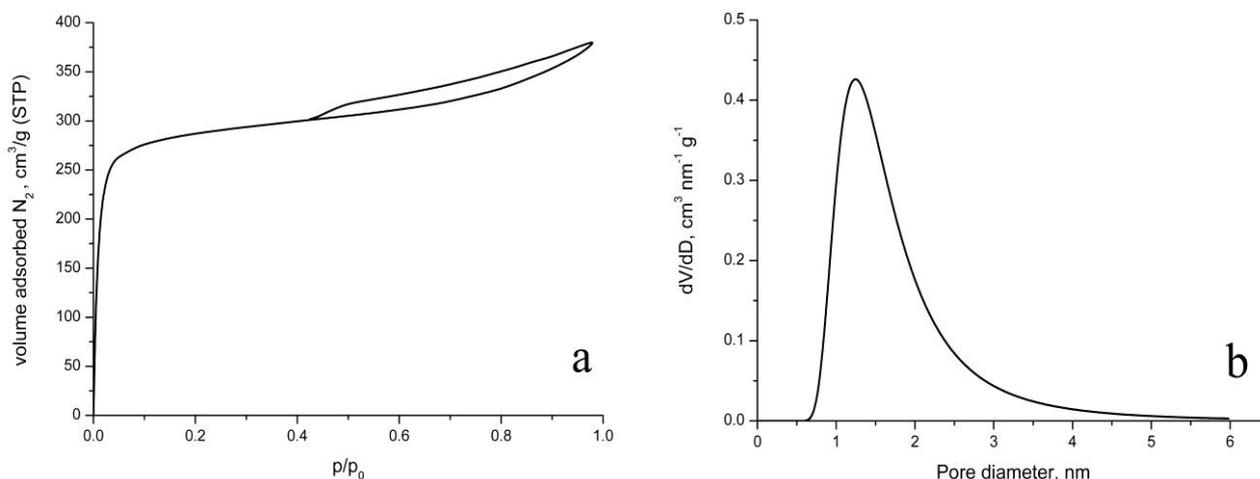
Fig.1. N_2 adsorption isotherm (a) and pore size distribution (b) of activated carbon at 196 ºC.

Table 2. Physico-chemical characteristics of the activated carbon.

Sample	BET surface area S_{BET}, m^2/g	Microporous surface area S_{mi}, m^2/g	External surface area S_{ext}, m^2/g	Total pore volume V_t, cm^3/g	Total pore volume V_{mi}, cm^3/g	Average pore diameter D_{av}, nm
AC	870	729	141	0.59	0.38	2.7

Oxygen-containing groups

The chemical character of the surface of the activated carbon was investigated by determining the amount of oxygen functional groups, and also by pH measurements and IR spectra. The oxygen-containing functional groups are very important specific characteristics of the activated carbon, because they have strong effect on its adsorption properties. The identification and quantification of the oxygen groups for the investigated carbon sample are shown in Table 3. The Boehm titration reveals that various oxygen-containing groups with different chemical properties are present on the activated carbon surface.

A large amount of carbonyl groups are detected on the surface of activated carbon, prepared from the mixture of polyolefin wax and phenol-formaldehyde resin. The activation with water

Table 3. Quantification of oxygen groups on carbon surface (mEquiv/g)

Sample	Carboxylic groups	Lactonic groups	Phenolic groups	Carbonyl groups	Basic groups	pH
	NaHCO$_3$	Na$_2$CO$_3$	NaOH	EtONa	HCl	
AC	0.050	0.047	0.050	2.021	0.4	8.31

vapor leads to considerable increase of the amount of basic groups, which is in a good agreement with the pH measurements. It should be mentioned that this distribution of the amount of different oxygen groups is logical, because in principle the application of the hydro-pyrolysis leads to formation of activated carbon with basic character of the surface.

IR spectroscopy

The IR spectroscopy results confirm the presence of oxygen-containing groups on the surface, which increase the adsorption properties of activated carbon.

IR spectra of the activated carbon sample are presented in Fig. 2. Stretch vibrations of associated –OH groups around 3400–3230 cm^{-1} were detected. The bands at 3000- 2800 cm^{-1} are due to aliphatic stretching vibrations. C-H stretching vibrations in the region of 3000– 2800 cm^{-1} are related to aliphatic structures. The band at 1709 cm^{-1} could be related to the stretching of C=O in linear aliphatic aldehydes, ketones and carboxyls [18, 19]. The bands around 1660 cm^{-1} cannot be interpreted unequivocally. They could be due to: 1) aromatic ring stretching coupled to highly conjugated carbonyl groups (C=O); 2) stretching vibrations of C=C bonds in aromatic structures; 3) OH groups [18, 19]. The bands in the region of 1200–1000 cm^{-1} are due to C–O in complex ethers and ring structures.
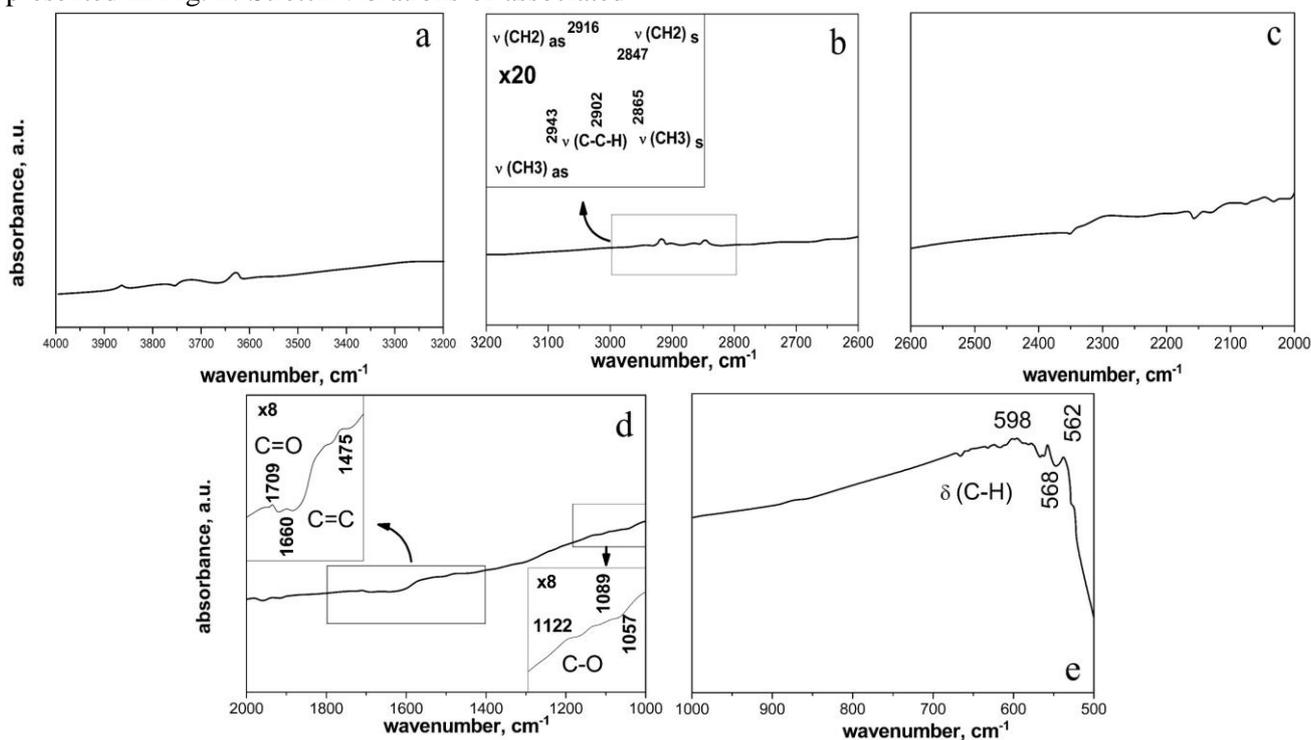
Fig. 2. IR spectrum of activated carbon: 4000-3200 cm^{-1} (a); 3200-2600 cm^{-1} (b); 2600-2000 cm^{-1} (c); 2000-1000 cm^{-1} (d); 1000-500 cm^{-1} (e).

Adsorption of PCP from water solution. Adsorption kinetics

The kinetic curves in Fig. 3 show the adsorption behavior of PCP on the synthesized activated carbon from water solution with PCP concentrations of 0.01–0.03 g/l. PCP adsorption increases sharply at short contact time. The adsorption process is quite fast and efficiently illustrates that the adsorption of PCP is completed almost on the whole surface of activated carbon. Furthermore, the adsorption capacity increases slowly and the adsorption equilibrium is established within 10 min. The removal curves are smooth and continuous, leading to saturation, suggesting the possibility of formation of monolayer coverage of PCP on the surface of the adsorbent [20]. However, the low amount of basic functional groups and saturation of less accessible adsorption sites could lead to delay of the adsorption process.
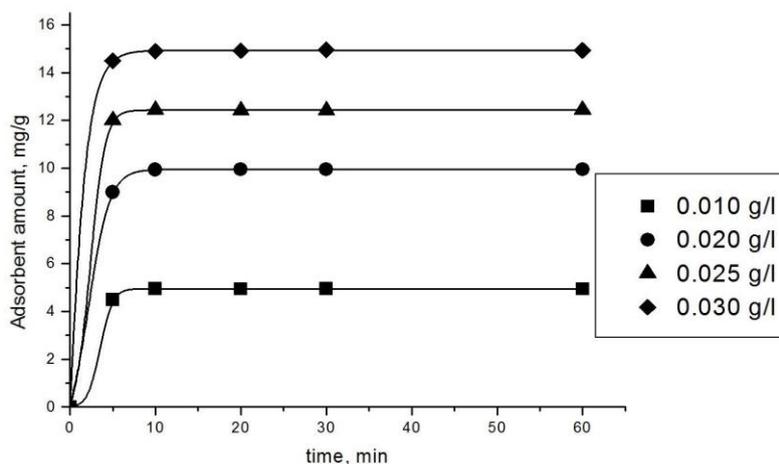
Fig. 3. Effect of treatment time and initial PCP concentration on the adsorption of PCP. Conditions: activated carbon amount - 0.1 g per 50 ml solution; PCP concentrations - 0.01, 0.02, 0.025, and 0.03 g/l.

Adsorption of PCP from water solution. Adsorption isotherms

The isotherms are obtained using a similar procedure as for the adsorption experiments previously mentioned. The adsorption capacity was investigated for different initial concentrations (0.01-0.03 g/l) for PCP for 60 min (Fig. 4). The adsorption isotherm for PCP was described by the well-known adsorption isotherm models of Langmuir and Freundlich. The Langmuir model isotherm based on monolayer adsorption is expressed as follows [21]:

$$C_e/q_e = C_e/q_m + 1/(b\ q_m) \qquad (1)$$

where q_e is the equilibrium PCP concentration on the adsorbent (mg/g), C_e - the equilibrium PCP concentration in the solution (mg/l), q_m - the monolayer adsorption capacity of the adsorbent (mg/g), and b is the Langmuir adsorption equilibrium constant (l/mg), related to the free energy and the affinity of adsorption.

Freundlich isotherm for sorption on a heterogeneous surface is expressed as follows:

$$\log Q_e = \log K_f + (1/n)\log C_e \qquad (2)$$

where K_f is a constant related to the adsorption capacity, and n is an empirical parameter, corresponding to adsorption intensity, which depends on adsorbent homogeneity (Fig. 5).

The values of the applied equations of the models are presented in Table 4.

The maximum adsorption capacity calculated from Langmuir equation is 29 mg/g, which is the highest value in comparison with other activated carbons, obtained from different raw materials [25, 26].

Table 4. Data for PCP adsorption obtained from Langmuir and Freundlich plot

Model	Parameters	R (linear regression coefficient)
Langmuir	Q_o = 29 mg/g ; b = 4.74 l/mg	0.97144
Freundlich	K_f = 63.68; n = 0.9143	0.98261
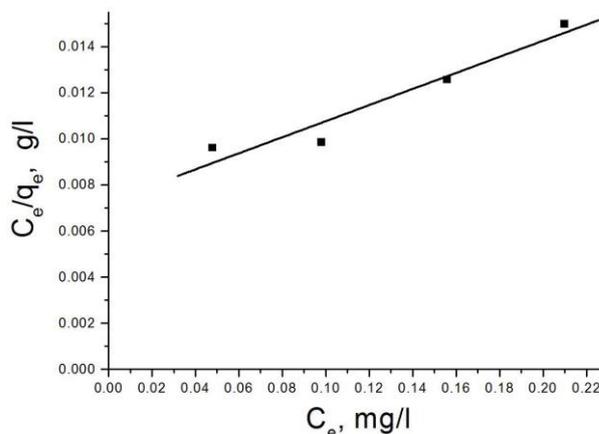
Fig. 4. Langmuir plot for PCP adsorption on activated carbon. Conditions: PCP concentrations - 0.01, 0.02, 0.025, 0.03 g/l; 60 min contact time; activated carbon amount - 0.1 g per 50 ml solution.

Effect of pH on adsorption

The pH of the solution is related to the surface chemistry of adsorbent and chemistry of adsorbate. In order to find optimum pH for maximum PCP removal onto activated carbon, the experiments were performed in the pH range from 2 to 10, using adsorbent amount of 0.1 g activated carbon and 0.03 g/l PCP water solution. The pH is adjusted by addition of hydrochloric acid and NaOH. The results are presented in Fig. 6.
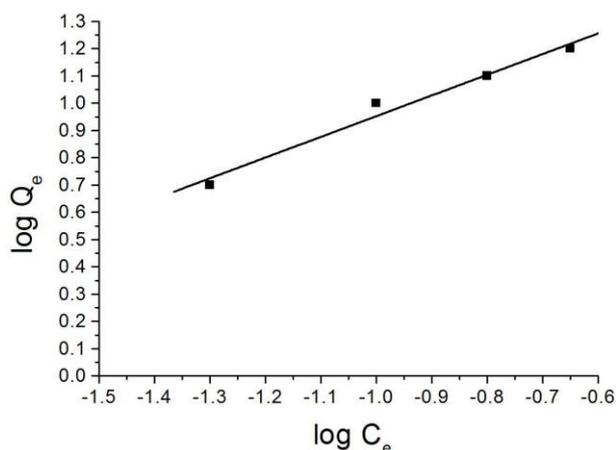
Fig. 5. Freundlich isotherm of PCP adsorption. Conditions: activated carbon amount 0.2-0.8 g; time of treatment 60 min.
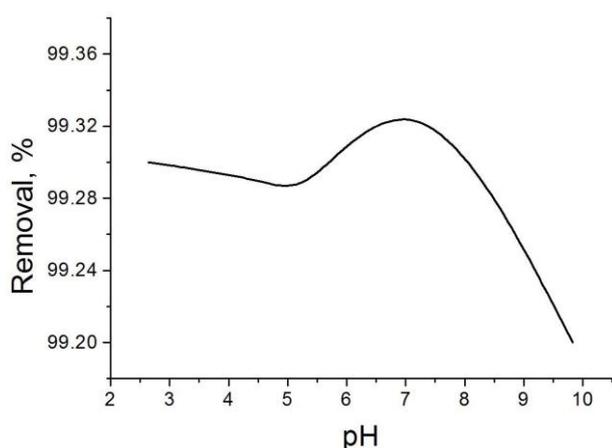
Fig. 6. Effect of pH on PCP removal. Conditions: time of treatment - 60 min, activated carbon amount - 0.1 g per 50 ml solution; PCP concentration - 0.03 g/l.

The effect of pH on PCP removal by the activated carbon can be explained by the surface chemistry of the adsorbent and the chemistry of PCP in solution. The carbon surface is positively charged at pH < pH_{pzc} and negatively charged at pH > pH_{pzc} [22]. It is also important to mention that PCP is the strongest acid among phenol derivates, with pKa value of 4.75 [23]. Thus, PCP in water solution will be mainly in protonated form at pH < pK_a, and in deprotonated form at pH > pK_a [22].

As can be seen from Fig 6, the maximum uptake of PCP by activated carbon was achieved at pH = 7. At pH = 7 PCP is dominantly in deprotonated form. Therefore attraction forces appear between PCP ions and the adsorbent surface. According to [24], at pH ~7 the adsorbent will tend to adsorb preferably cations, due to the cooperative effect of the net negative surface charge.

At pH values lower than adsorbent pH_{pzc}, the removal of PCP by activated carbon was minimal because of the repulsive forces existing between the positively charged activated carbon surface and the PCP present in water solution in its protonated

form. The removal of PCP by activated carbon decreased sharply at pH > 7. This observation was attributed to the fact that at pH values higher than pHpzc, the adsorbent surface will be negatively charged. At the same time, PCP in the water solution exists entirely in the anionic form at neutal and basic pH. Therefore electrostatic repulsion between the negatively charged adsorbent surface and the anionic form of PCP in water solution will appear at lower adsorption.

CONCLUSIONS

Activated carbon prepared from polymer waste (polyolefin wax) and phenol-formaldehyde resin has been successfully used as adsorbent for the removal of PCP from aqueous solution. The adsorption of PCP attains equilibrium in a short time of 10 minutes. The adsorption was found to follow Langmuir and Freundlich equations, as the Langmir model showed better fit to the experimental data. The maximum adsorption capacity calculated from Langmuir equation is 29 mg/g, which is the highest value in comparison with other reported activated carbons obtained from different raw materials.

REFERENCES

1. B. Estevinho, N. Ratola, A. Alves, L. Santos, *J. Hazard. Mater.,* **137**,1175 (2006).
2. W. Jianlog, Q. Yi, N. Horan, E. Stentiford, *Biores. Technol.,* **75**, 157 (2008).
3. W. Law, W. Lau, K. Lo, S. Lai, S. Chiu, *Chemosphere,* **52**, 1531 (2003).
4. J. Dominguez-Vergas, J. Navarro-Rodriguez, J. de Beltran Heredia, E. Cuerda-Correa, *J. Hazard. Mater.,* **169**, 302 (2009).
5. G. San Miguel, G.D. Fowler, C.J. Sollars, *Carbon,* **41**, 1009 (2003).
6. B. Tsyntsarski, B. Petrova, T. Budinova, N. Petrov, D. Teodosiev, A. Sarbu, T. Sandu, M. Ferhat Yardim, A. Sirkecioglu, *Desalin. Water Treat.,* **52**, 3445 (2014).
7. I. Stoycheva, B. Tsyntsarski, B. Petrova, T. Budinova, N. Petrov, *Desalin. Water Treat.,* **57**, 15435 (2016).
8. I. Stoycheva, B. Tsyntsarski, B. Petrova,T. Budinova , N. Petrov , B. Nagel, U. Szegula, *NanoSci. Nanotechnol.,* **15**, 29 (2015).
9. T. Vivarghavan, K. Slough, *Chemosphere,* **39**, 1487 (1999).
10. I. Bras, L. Lemos, A. Alves, M. Pereira, *Chemosphere,* **60**, 1095 (2005).
11. B. Estevinho, I. Martins, N. Ratola, A. Alves, L. Santos, *J. Hazard. Mater.,* **143**, 535 (2007).

49

12. T. Mathialagan, T. Viraraghavan, *Bioresour. Technol.*, **100**, 549 (2009).
13. R. Bansal, M. Goyal, Activated Carbon Adsorption, Taylor & Francis, Boca Raton, USA, 2005.
14. H.P. Boehm, in: Advances in catalysis and related subjects, D.D. Eley, H. Pines, P.B.Weisz (Eds), vol. 16, Academic press, New York, 1966, p. 179-191.
15. E. Papier, S. Li, J-B. Donnet, *Carbon,* **25**, 243, (1987).
16. N. Abdel Ghani, G. EI-Chaghaby, F. Helal, *Desalin. Water Treat.*, **51**, 3558 (2013).
17. J. Visser, Summary of Methods for Testing Norit Activated Carbons on Specifications, Norit Standard, Netherlands, 1977.
18. J. Zawadzki , B. Azambre, O. Heintz, A. Krzton, J. Weber, *Carbon*, **38**, 509 (2000).
19. J. Zawadzki, M. Wisniewski, J. Weber, O. Heintz, B. Azambre, *Carbon*, **39**, 187 (2001).
20. C. Giles, T. MacEwan, S. Nakhwa, D. Smith, Studies in adsorption. Part XI. A system of classification of solution adsorption isotherms, and its use in diagnosis of adsorption mechanisms and in measurement of specific surface, p. 3973 (1960).
21. S. Greg, K. Sing, Adsorption, Surface Area and Porosity, Academic Press, London, 1982.
22. Q-S. Liu, T. Zheng, P. Wang, J-P. Jiang, N. Li, *Chem. Eng. J.*, **157**, 348 (2010).
23. K. Schellenberg, C. Leuenberger, R. Schwarzenbach, *Envir. Sci Technol.*, **18**, 652 (1984).
24. R. Leyla-Ramos, L. Bernal-Jacome, J. Mendoza-Barron, M. Hernandez-Orta, *J. Taiwan Inst. Chem. Engineers,* **40**, 622 (2009).
25. N. Abdel-Ghani, G. El-Chaghaby, E. Zahran, *Int. J. Envir. Sci. Technol.,* **12**, 211 (2015).

НОВ НАНОПОРЕСТ ВЪГЛЕРОДЕН АДСОРБЕНТ НА ОСНОВАТА НА ПОЛИМЕР ЗА ОТСТРАНЯВАНЕ НА ПЕНТАХЛОРФЕНОЛ ОТ ВОДИ

И. Г. Стойчева[1]*, Б. Г. Цинцарски[1], Б. Н. Петрова[1], Т. К. Будинова[1], А. Д. Попова[1], Н. В. Петров[1], Б. Нагел[2], У. Шелуга[2]

[1]Лаб. "Химия на твърдите горива", Институт по органична химия с Център по фитохимия, Българска академия на науките, ул. Акад. Г. Бончев, бл. 9, 1113 София, България
[2]Център за полимерни и въглеродни материали към Полската академия на науките, ул. Мария Склодовска-Кюри 34,41-819 Забже, Полша

(Резюме)

Полиолефинов материал - полиолефинов восък, страничен продукт от производството на полиетилен при ниско налягане - бе използван за получаването на нанопорест активен въглен. Повърхностните характеристики на адсорбента демонстрират добре развита повърхност и наличие на много повърхностни функционални групи, склонни да свързват молекулите на адсорбата. Резултатите показват възможност за използване на полимерния отпадък като подходящ прекурсор за производството на нанопорест активен въглен, като по този начин се намаляват разходите за пречистване на отпадните води. Полученият активен въглен бе използван като адсорбент на пентахлорфенол от воден разтвор. Адсорбционните експерименти бяха проведени при различни условия: концентрация на пентахлорфенола, pH, време на контакт, и др. Резултати от адсорбцията на пентахлорфенола съвпадат много добре с изотермите на Лангмюир и Фройндлих.

Silver and quercetin loaded nanostructured silica materials as potential dermal formulations

I. Trendafilova[1]*, D. Momekova[2], A. Szegedi[3], G. Momekov[2], D. Zgureva[4], S. Boycheva[4], M. Popova[1]

[1]*Institute of Organic Chemistry with Centre of Phytochemistry, Bulgarian Academy of Sciences, 1113 Sofia, Bulgaria*
[2] *Faculty of Pharmacy, Medical University of Sofia, 2 Dunav Str., 1000 Sofia, Bulgaria*
[3] *Research Centre for Natural Sciences, Institute of Materials and Environmental Chemistry, Hungarian Academy of Sciences, 1117, Budapest Magyar tudósok krt. 2, Hungary*
[4] *Department of Thermal and Nuclear Power Engineering, Technical University of Sofia, 8 Kl. Ohridsky Blvd., 1000 Sofia, Bulgaria*

In this study it was demonstrated for the first time that the application of silver modified nanoporous silica as a carrier of natural flavonoid quercetin leads to the formation of efficient dermal formulation. By direct or post synthesis methods finely dispersed silver nanoparticles can be stabilized in the channels or on the outer surface of nanoporous silica support. High quercetin loading capacity (over 40 wt. %) could be achieved on the parent and Ag-containing MCM-41 samples. The in vitro release process at pH=5.5 showed slower quercetin release from Ag-modified MCM-41 samples compared to the parent one. The cytotoxic experiments evidenced that quercetin encapsulated in Ag-modified silica carriers has superior antineoplastic potential against HUT-29 cells compared to free drug.

Keywords: silver, quercetin, nanoporous silica, spherical MCM-41.

INTRODUCTION

In the recent years several efficient nanoporous silica based drug delivery systems have been developed [1,2]. Nanoporous silica carriers (SBA-15 or MCM-41) are biocompatible materials and have the capability both to load nanosized metal particles into the channels and to be functionalized with organic groups [3,4]. The functionalization of the silica surface (inside the channels and/or the outer surface) not only can enhance the adsorption of drug molecules but give opportunities to modify the release properties. The effect of modified drug release can be combined with the antibacterial effect of metallic nanoparticles, such as silver. From antiquity silver has been used as a disinfectant and for the treatment of burns, ulcerations and bacterial infections. The silver nanoparticles are widely explored and applied because their toxicity to human cells is quite lower than to bacteria and they had broad spectrum of antimicrobial activity and low propensity to induce bacterial resistance [5]. Silver nanoparticles can be stabilized in the channels or on the outer surface of mesoporous silica supports, and besides the empty channels can be loaded by biologically active molecules.

Flavonoids are natural pigments found in many plants and fruits and they possess high antioxidative and antiradical activities. Quercetin (2-(3,4-dihydroxyphenyl)-3,5,7-trihydroxy-4H-chromen-4-one, Fig. 1) is the most widespread flavonoid with the highest antioxidant activity among flavonoids. It was chosen in our study due to its interesting biological and pharmacological effects, such as anti-inflammatory, antiallergenic, antiviral, antibacterial and anticancer [6]. Biological activity of the quercetin is characterized by multiple mechanisms, including scavenging reactive oxygen species (ROS) [7], inhibition of lipid peroxidation [8], and chelating metal ions [9].

Due to their potential beneficial effects in the prevention of oxidative stress, antioxidants are studied not only for oral administration but also for dermal applications for protection against UV radiation damage [10,11] or for prevention of skin cancer [12,13]. Their use as pharmaceutical agents is extremely limited by their low water solubility and high instability in a neutral and alkaline medium [14]. To overcome this major hurdle and to increase quercetin's bioavailability, quercetin was loaded in delivery systems on the basis of mesoporous silica materials.

In this study silver nanoparticle containing mesoporous silica MCM-41 carriers, prepared by direct synthesis or post synthesis method, were loaded with quercetin. *In vitro* release profiles of quercetin from parent and Ag modified mesoporous silica particles were studied in respect of their possible application as dermal formulations against

---

* To whom all correspondence should be sent:
E-mail: ivtrendafilova@gmail.com

cutaneous T-cell lymphoma. The cytotoxic potential of non-loaded and quercetin loaded particles was investigated against two types of human cells, including HUT-29 cells as a model of CTCL *in vitro*.
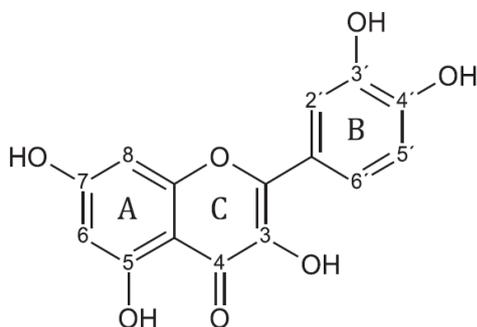

Figure 1 Molecular structure of quercetin.

EXPERIMENTAL
Materials

Cetyl trimethyl ammonium bromide (CTAB), Quercetin (>99.5%) and tetraethyl orthosilicate (TEOS) were purchased by Aldrich.

Synthesis of siliceous MCM-41 material

Spherical nanosized (100 nm) MCM-41 particles were prepared according to the procedure of Huh et al. [15]. This sol-gel procedure is carried out at 80°C in water solution with NaOH as a catalyst. The silica source was tetraethyl orthosilicate (TEOS), and hexadecyltrimethyl-ammonium bromide (C_{16}TMABr) was applied as template. The relative molar composition of the reaction mixture was: 1 TEOS: 0.12 C_{16}TMABr: 0.31 NaOH: 1190 H_2O. The formed gel was aged at 80°C for 2 h, than washed with distilled water until neutral pH, and dried at ambient. Template was removed by heat treatment in air at 450°C for 5h with a heating ramp of 1°C/min.

Direct synthesis of Ag-MCM-41

Silver nanoparticles were loaded to the silica carrier by the template ion-exchange method of Gac et. al.[**Error! Bookmark not defined.**]. The template containing MCM-41 material was ion-exchanged by refluxing it at 80°C with 0.036 M $AgNO_3$ solution (50 ml/g MCM-41) for 20 h, and then filtered on 0.2 μm membrane filter, and washed with distilled water. The ion-exchanged material was heat treated in air at 550°C for 5 h with a heating rate of 1°C/min. Silver containing MCM-41 sample prepared by template ion-exchange method was designated as Ag-MCM-41(DS).

Post synthesis modification of MCM-41 with Ag

Modification of MCM-41 with $AgNO_3$ by incipient wetness impregnation technique was

applied for loading of 2, 4 and 5.5 wt. % silver. In a typical experiment silver nitrate – 9.45 mg, 18.9 mg and 25.9 mg for 2, 4 and 5.5 wt. % silver, respectively, was dissolved in 1 ml ethanol (99.9%) and 300 mg of mesoporous support (MCM-41) were added. The functionalization was performed at room temperature. Samples were calcined in air at 450°C for 3 hours and designated as xAgMCM-41(PS) where x= 2,4 or 5.5 wt.% Ag.

Loading of quercetin on silver modified nanoporous MCM-41 materials

Ag modified materials and quercetin in ratio 1:1 were stirred in 1 ml ethanol (99.9%) and then dried at 50°C till the total evaporation of the solvent. The quercetin loaded MCM-41 formulation was designated as AgMCM-41(DS)Qu, and xAgMCM-41(PS)Qu, where *x*= 2, 4 and 5.5 Ag wt.%.

Characterization of the samples

X-ray patterns were recorded by a Philips PW 1810/3710 diffractometer with Bregg-Brentano parafocusing geometry applying monochromatized CuKα (λ=0.15418 nm) radiation (40 kV, 35 mA) and a proportional counter.

Nitrogen physisorption measurements were carried out at 77 K using TriStar II surface area analyzer, Micrometrics. The specific surface area was calculated applying BET (Brunauer–Emmett–Teller) method to the monolayer adsorption region on the isotherms observed in the range of relative pressures p/p_o from 0.02 to 0.1. The pore-size distribution was calculated from desorption branch of the isotherms with the BJH (Barrett-Joyner-Halenda) method. Silica samples were pre-treated at 200°C, whereas drug loaded materials at 80°C for 5 h before measurements [17,18].

TEM images were taken by using a MORGAGNI 268D (100 kV; W filament; point-resolution = 0.5 nm) electron microscope. Samples were suspended in small amount of ethanol and a drop of suspension was deposited onto copper grid covered by carbon supporting film and dried at ambient.

Thermogravimetric measurements were performed with a Setaram TG92 instrument with a heating rate of 5 °C/min in air flow.

In-vitro release study

An in-vitro quercetin release study was performed in buffer (pH = 5.5) at 37°C. The drug-loaded particles (2 mg) were incubated in 200 ml phosphate buffer with pH=5.5 at 37°C under stirring (300 rpm). At appropriate time intervals, 3 ml samples were withdrawn from the release

medium and analyzed with UV-Vis spectroscopy at a wavelength of 367 nm. The concentration of the released quercetin was calculated according to the standard curves prepared in pH=5.5 solution (r>0.9993).

Cell lines and culture conditions

The cell lines HEK-293 (human embryonal kidney cells) and HUT-78 (cutaneous T-cell lymphoma - CTCL) were supplied by DSMZ GmbH, Germany. Cells were cultured routinely in a controlled environment: 37°C in 5% CO_2 humidified atmosphere. All cell lines were maintained in RPMI 1640 supplemented with 2 mM L-glutamine and 10% fetal calf serum. The cell lines were subcultured biweekly to maintain continuous logarithmic growth.

Cytotoxicity assay

Cell survival was evaluated by using the standard MTT-dye reduction assay (Mosmann, 1983) with slight modifications (Konstantinov et al., 1999). The method is based on the ability of viable cells to metabolize a yellow tetrazolium salt to a violet formazan product which is detected spectrophotometrically at 527 nm. Exponentially growing cells were plated in 96-well sterile plates at a density of 10^4 cells/ well in 100 μL of medium and were incubated for 24 h. Thereafter the quercetin and the tested mesoporous silica particles were applied for 72 h, whereby for each concentration a set of 8 wells was used. After a 72-h continuous exposure period, 10 μL aliquots from a 5 mg/ml MTT solution were added to each well and the plates were further incubated for 4 h at 37°C in a humidified 5 % CO_2 atmosphere. The

formazan crystals yielded were solubilized by addition of a 5% solution of HCOOH in isopropanol. The MTT-formazan absorbance was read on a microprocessor controlled multiplate reader (Labexim LMR-1). The cell survival data were normalized as percentage of the untreated control (set as 100% viability) and were fitted to sigmoidal dose response curves and the corresponding IC_{50} values (concentrations causing 50% suppression of cellular viability) were calculated.

RESULTS AND DISCUSSION

Material characterization

Low and high angle XRD powder patterns of pure silica and silver containing MCM-41 materials, and their Qu loaded varieties are shown in Fig. 1. AgMCM-41 samples prepared by template ion-exchange method or post synthesis modification show the typical patterns of highly ordered hexagonal phase. The intensity of (100) reflection is lower than that of parent silica material indicating some decrease of structure ordering after modification with Ag. More significant intensity decrease and broadened reflections are observed for the functionalized and quercetin loaded mesoporous samples, indicating some loss of structure ordering or pore filling (not shown).

Reflection characteristic of the crystalline form of Ag could be observed only for AgMCM-41 prepared by direct synthesis and 5.5AgMCM-41 prepared by post synthesis method. For other samples containing lower amount of Ag, crystalline Ag was not registered (Fig.1 A).
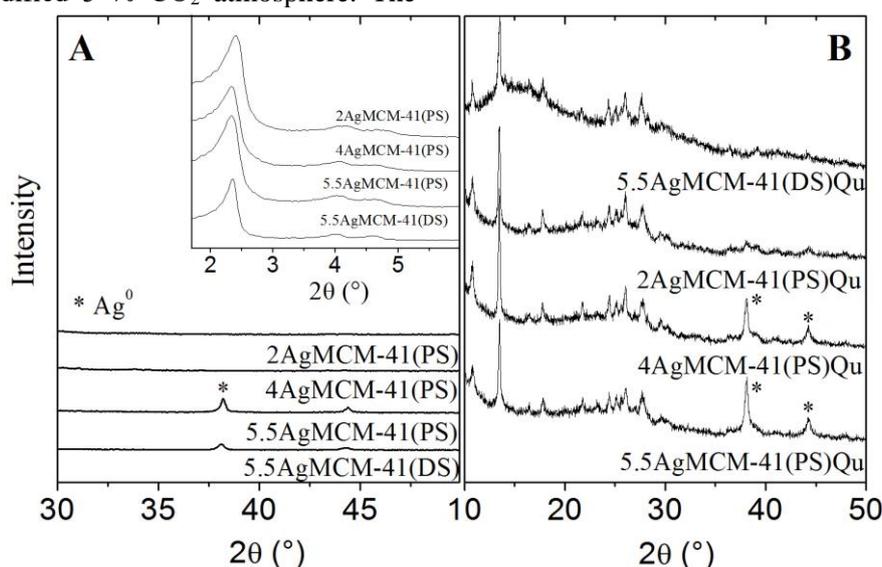
Fig. 1 XRD patterns of silver containing nanoporous pure silica and silver modified silica samples (A) and their Qu loaded varieties (B).

High angle XRD patterns of quercetin loaded parent and silver modified silica carriers are shown in Fig. 1 B. Reflections of quercetin can be observed on all samples. This is evidence that quercetin is not only contained in the pore channels, but can be found on the outer surface of the small nanoparticles or in the voids among the particles. Quercetin can be found in its anhydrous form after loading due to its recrystallization in the ethanolic media.
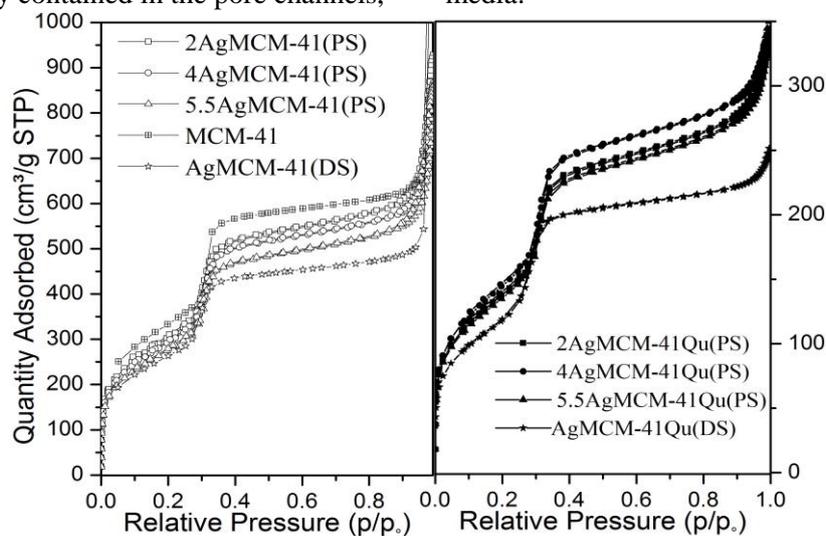
Fig. 2 N_2 physisorption isotherms of pure silica, silver containing and quercetin loaded varieties of nanoporous silica materials.
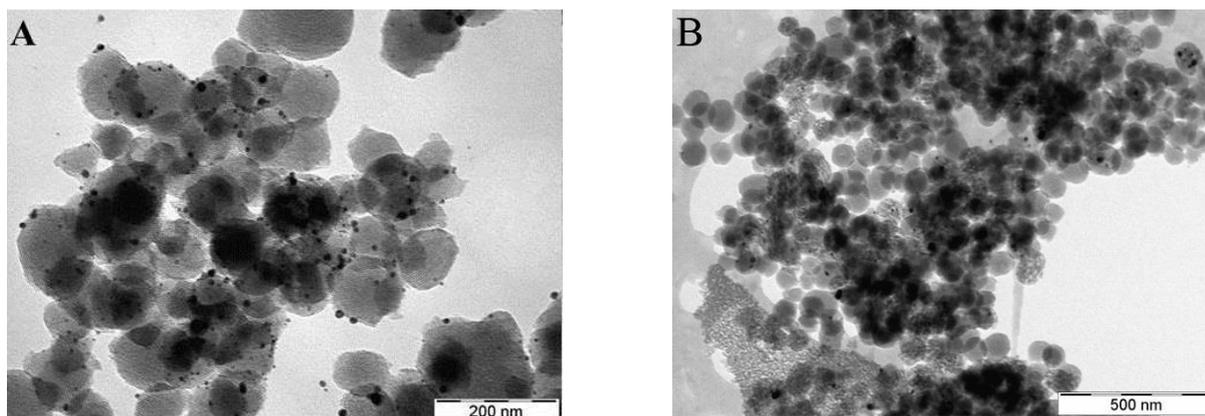
Fig. 3 TEM images of 5.5AgMCM-41(DS) (A) and 4AgMCM-41(PS) (B) samples

The above observations were supported also by the N_2 adsorption data (Fig. 2). Textural parameters are summarized in Table 1. The isotherms of pure silica and silver modified MCM-41 materials exhibited a sharp increase at a relative pressure of $p/po = 0.2$-0.4, which was associated with capillary condensation in the channels and narrow pore size distribution (Fig. 2). The isotherms of the MCM-41 samples were reversible and did not show any hysteresis loop. Specific surface area and the total pore volume of Ag-modified MCM-41 sample are slightly lower in comparison with the parent material. However, after quercetin loading textural parameters of the samples show a significant decrease in the surface area and total pore volume, due to the macrovoid filling revealed by the slower adsorption at high p/p_o.

The modification by silver does not influence the original morphology of MCM-41 material as evidenced by TEM investigations (Fig. 3). AgMCM-41 and 5.5AgMCM-41 (Fig.3) show the typical 100 nm spherical particles and the channel system is well preserved. Silver nanoparticles with different dispersity, among 5-20 nm, can be observed on the images. These results are in accordance with XRD results showing the presence of separate silver phase on the outer side of the particles.

Diffuse reflectance UV-Vis spectroscopic investigation evidenced the formation of Ag nanoparticles and incorporation of Ag into the silica matrix. UV-Vis spectra of the parent and the silver modified silica carriers can be seen in Fig. 4. The spectra of the samples prepared by post synthesis method show an intensive peak at around 400 nm

which is due to the formation of Ag nanoparticles [19, 20]. The registered peak at 280 nm in the spectrum of AgMCM-41 can be assigned to the presence of silver ions [19].
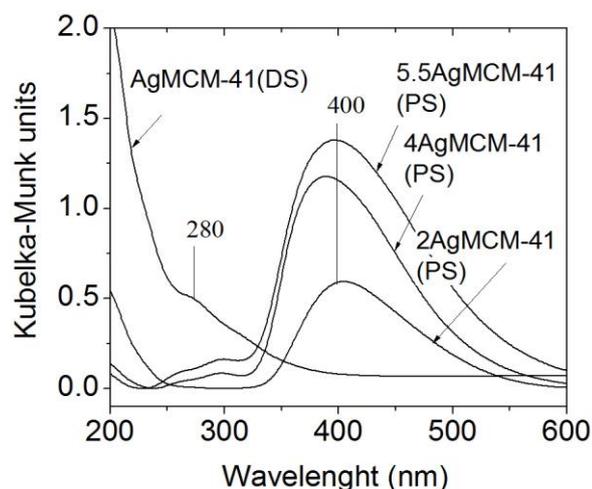
Fig.4 UV Vis spectra of the studied silver containing MCM-41 samples.

Adsorption of quercetin

Quercetin was adsorbed on silver containing samples by dissolving it in ethanol (99.9%). Qu penetrated into the channels of silica carrier and partial pore filling was achieved, evidenced by the N_2 physisorption data (Fig 2, Table 1). However,

according to the XRD patterns of the Qu loaded silica materials (Fig. 1 B) some amount of Qu can be found as a separate phase in the sample as well. The amount of quercetin loaded in the mesopores of Ag-modified MCM-41 was quantified using thermogravimetry (TG, Fig 5). TG data are presented in Table 1. The studied samples showed high loading capacity of quercetin (44 -50 wt. %) The loaded amount of quercetin is higher for the silver modified sample prepared by direct synthesis (50 wt.%).
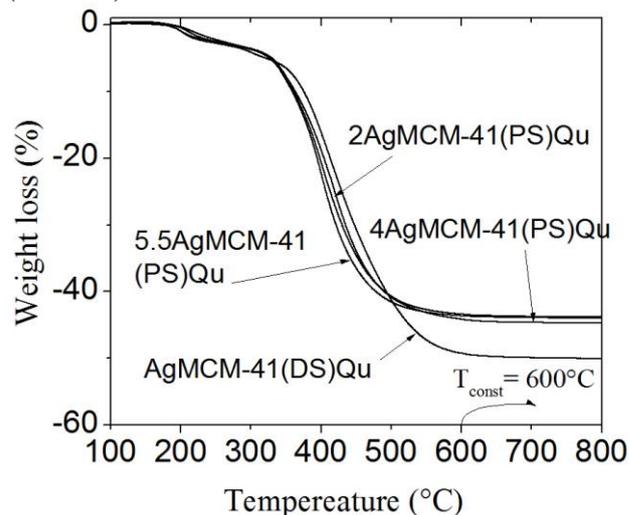
Fig. 5 Thermogravimetric curves of Qu loaded silver MCM-41 samples.

Table 1. Composition and textural properties of the studied samples.

Samples	a_0^a (nm)	Qu content (mg/g)	BET surf. area (m²/g)	Total pore vol. (cm³/g)	PD[b] (nm)
MCM-41	4.4	-	1175	0.970	2.7
AgMCM-41(DS)	4.3	-	927	0.760	2.6
2AgMCM-41(PS)	4.2	-	1170	0.820	2.7
4AgMCM-41(PS)	4.3	-	1162	0.790	2.7
5.5AgMCM-41(PS)	4.3	-	1097	0.750	2.8
AgMCM-41(DS)Qu	4.3	50.0	430	0.371	2.6
2AgMCM-41(PS)Qu	4.2	44.0	539	0.380	2.8
4AgMCM-41(PS)Qu	4.2	44.7	568	0.400	2.8
5.5AgMCM-41(PS)Qu	4.1	44.0	530	0.370	2.8

[a] Unit cell parameter ($a_0 = 2d_{100}(3)^{-1/2}$).
[b] Mean pore diameter calculated by the BJH method.
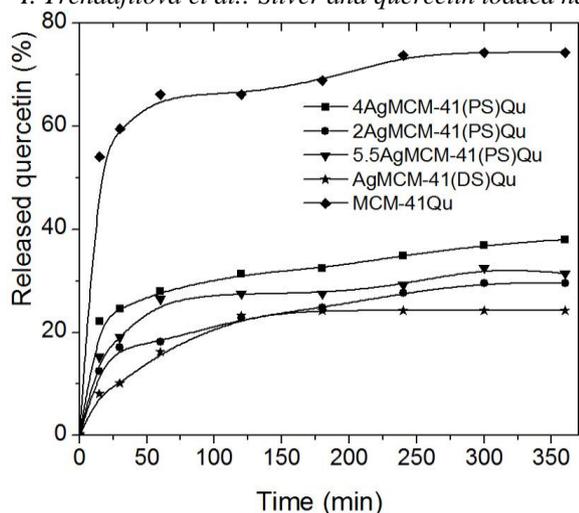
Fig. 6 *In vitro* release of quercetin from parent and Ag-modified MCM-41 carriers.

In vitro release of quercetin

The *in vitro* release of Qu from all samples was investigated in a phosphate buffer (pH=5.5). The latter pH value is widely applied for *in vitro* experiments for dermatological formulations. The drug release profiles are presented in Fig. 6. As evident from the presented data the parent mesoporous MCM-41 silica are characterized with burst quercetin release where over 60 % of the encapsulated quercetin is released within 30 minutes. Contrary, the silver-modified silica formulations' showed slower drug release and thus within 6 h the Qu release reached not more the 36 %. Probably the main part of quercetin remains in the pores of the silica carrier.

Cytotoxicity assessment

The cytotoxicity potential of mesoporous silica non-modified or Ag-modified nanoparticles was determined in two human cell lines with different cell type and origin, namely non-malignant HEK-293 and malignant HUT-78. The two cell lines were chosen in order to discriminate between the growth inhibitory potential of tested systems against non-tumorigenic and malignant cell lines, as the lack of toxicity is an important requirement for all materials used in preparation of drug delivery systems. In addition a comparative evaluation of the cytotoxic effect of quercetin loaded system vs. free drug (ethanol solution) in the above mentioned cell lines was performed. HEK-293 cells represent non-cancerous epithelial cells, whereas HUT-78 are a suitable model for cutaneous T-cell lymphoma.
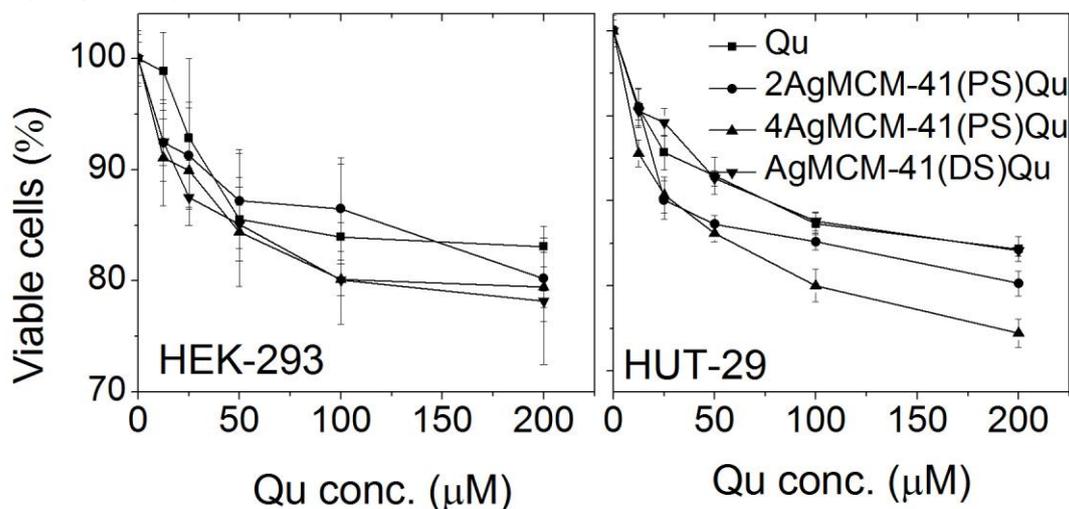
Fig. 7. The concentration-response curves determined by the MTT-dye reduction assay after 72 hours continuous exposure. Concentration range of 25-200 μM quercetin corresponds to 0.2-1 mg/ml of mesoporous silica particles. Each data point represents the arithmetic mean ± SD of 8 separate experiments.

Table 2 Equieffective concentrations of tested quercetin formulations, *vs.* the free drug.

Cell line	IC_{50} (μM)			
	Quercetin (Qu)	2AgMCM-41Qu (PS)	4AgMCM-41Qu (PS)	AgMCM-41Qu (DS)
HEK-293	n.d.	n.d.	n.d.	n.d.
HUT-78	174.8	105.53	59.6	68.4

The growth inhibitory concentration-response curves are presented in Fig. 7 and the corresponding equieffective IC 50 values are summarized in Table 2. Evident from the growth inhibitory concentration-response curves shown in Fig. 7, the non-loaded silica particles, as well as their quercetin loaded counterparts and quercetin itself, failed to induce any significant decrease in

cell viability of non-malignant HEK-293 cells even at the highest dose of 200 μM and furthermore in the whole tested concentration range IC_{50} were not reached (Table 2). In contrast in malignant HUT-78 cells all tested formulations exerted clear concentration dependent cytotoxic effect. These findings show that the tested compounds are characterized with high selectivity against malignant cells and are non-harmful for normal cells. In addition to their selectivity quercetin loaded mesoporous silica nanoparticles were superior in terms of cytotoxic activity as compared to the free drug. The concentration-response curves were shifted to the lower concentrations and respectively the IC_{50} values were app. two folds lower as compared to those of free quercetin, applied as an ethanol solution. This effect was more pronounced in quercetin loaded 4AgMCM-41 particles prepared by direct synthesis, causing more than 60 % eradication of viable cells at the highest concentration.

CONCLUSIONS

In this study it was shown that silver modified MCM-41 materials are suitable carriers for bioflavanols, such as quercetin, to design dermal delivery systems. It was found that nanoporous silica materials can be easily modified by direct or post-synthesis methods to prepare silver nanoparticles inside the channels or on the outer surface of the particles. Incipient wetness impregnation method was used for quercetin loading on parent and Ag-modified mesoporous carriers. High quercetin loading capacity (over 40 wt. %) was registered on all samples. The in-vitro release process at pH=5.5 showed lower and incomplete quercetin release for silver modified samples in comparison with the parent MCM-41 possibly due to the formation of complex between quercetin and Ag. High quercetin loading and controlled release indicate that the obtained delivery systems are promising for dermal application. The cytotoxic experiments show that quercetin encapsulated in Ag-modified silica carrier (4 wt. % Ag) prepared by post synthesis proved to exert superior antineoplastic potential against HUT-29 cells compared to free drug.

REFERENCES

1. M. Vallet-Regi, A. Ramila, R.P. del Real, J. Perez-Pariente, *Chem. Mater.* **13**, 308 (2001).
2. Sh. Wang, *Micropor. Mesopor. Mater.* **117**, 1 (2009).
3. A.Szegedi, M. Popova, I. Goshev, Sz. Klébert, J. Mihály, *J. Solid State Chem.* **194**, 257 (2012).
4. M. D. Popova, Á. Szegedi, I. N. Kolev, J. Mihály, B. S. Tzankov, G. Tz. Momekov, N. G. Lambov, K. P. Yoncheva, *Int. J. Pharm.* **436**, 778 (2012).
5. M. Rai, A. Yadav, A. Gade, *Biotechnol. Adv*. **27**, 76 (2009).
6. M. Zhang, S.G. Swarts, L. Yin, C. Liu, Y. Tian, Y. Cao, M. Swarts, S. Yang, S.B. Zhang, K. Zhang, Oxygen Transport to Tissue XXXII, Springer, 283 (2011).
7. V. Krishnamachari, L.H. Levine, P.W. Paré, *J. Agric. Food Chem.*, **50**, 4357 (2002).
8. O. Dangles, C. Dufour, G. Fargeix, *J. Chem. Soc.*, **2**, 1215 (2000).
9. Z. Jurasekova, A. Torreggiani, M. Tamba, S. Sanchez-Cortes, J. Garcia-Ramos, *J. Mol. Struct.*, **918**, 129 (2009).
10. R. Casagrande, S.R. Georgetti, W.A. Verri Jr., D.J. Dorta, A.C. dos Santos, M.J.V. Fonseca, *J. Photochem. Photobiol.*, **B 84**, 21 (2006).
11. D. Liu, H. Hu, Z. Lin, D. Chen, Y. Zhu, S. Hou, X. Shi, *J. Photochem. Photobiol.,* **B 127**, 8 (2013).
12. M.M. Heinen, M.C. Hughes, T.I. Ibiebele, G.C. Marks, A.C. Green, J.C. van der Pols, *Eur. J. Cancer* **43**, 2707 (2007).
13. J.S. Reis, M.A. Corrêa, M.C. Chung, J.L. dos Santos, *Bioorg. Med. Chem*. **22**, 2733 (2014).
14. A.J. Smith, P. Kavuru, L. Wojtas, M.J. Zaworotko, R.D. Shytle, *Mol. Pharm.* **8,** 1867 (2011).
15. S. Huh, J. Wiench, J.-Ch Yoo, M. Pruski, V.S.-Y. Lin, *Chem. Mater.* **15**, 4247 (2003).
16. W. Gac, A. Derylo-Marczewska, S. Pasieczna-Patkowska, N. Popivnyak and G. Zukocinski, *J. Mol. Catal. A: Chem.*, **268**, 15 (2007).
17. A. Szegedi, M. Popova, I. Goshev, J. Mihaly, *J. Solid State Chem.* **184**, 1201 (2011).
18. A.Szegedi, M. Popova, K. Yoncheva, J. Makk, J. Mihaly, P. Shestakova, *J. Mater. Chem. B* **2**, 6283 (2014).
19. L. Jia, S. Zhang, F. Gu, Y. Ping, X. Guo, Z. Zhong, F. Su, *Microporous Mesoporous Mat.* **149**, 158 (2012).
20. W. Zhu, Y. Han, L. An, *Microporous Mesoporous Mat.* **80,** 221 (2005).

МОДИФИЦИРАНИ СЪС СРЕБРО НАНОСТРУКТУРНИ СИЛИКАТНИ МАТЕРИАЛИ, НАТОВАРЕНИ С КВЕРЦЕТИН, КАТО ПОТЕНЦИАЛНИ ДЕРМАЛНИ ПРЕПАРАТИ

Ив. Трендафилова[1]*, Д. Момекова[2], А. Сегеди[3], Г. Момеков[2], Д. Згурева[4], С. Бойчева[4], М. Попова[1]

[1]Институт по органична химия с Център по фитохимия, БАН
[2] Фармацевтичен факултет, Медицинска академия, София
[3]Изследователски център по природни науки, Институт по материали и химия на околната среда, Унгария
[4] Катедра топлотехника и ядрена енергетика, Технически университет, София

(Резюме)

В настоящото изследване за първи път модифициран със сребро MCM-41 силикат е използван, като носител на природния флавоноид кверцетин и на негова основа е разработена ефикасна лекарствена форма. Чрез директен синтез или постсинтезен метод са получени и стабилизирани финно дисперсни сребърни наночастици в порите или върху външната повърхност на нанопорестия силикат. Постигната е висока степен на натоварване с кверцетин (над 40%) както при изходните, така и при сребро-съдържащи образци. In-vitro тестовете при pH=5.5 показват забавено освобождаване на кверцетина от модифицираните със сребро MCM-41 проби, в сравнение с немодифицирните. Цитотоксичните експерименти показват, че кверцетинът натоварен в модифицирани със сребро силикатни носители има по-висок антинеопластичен потенциал срещу HUT-29 клетки в сравнение с чистото вещество.

Low temperature preparation of nanosized LiFePO$_4$ by molten salt reactions

T. Boyadzhieva, R. Stoyanova, E. Zhecheva, V. Koleva*

Institute of General and Inorganic Chemistry, Bulgarian Academy of Sciences, 11, G. Bonchev Str., 1113 Sofia, Bulgaria

Molten salt reactions between dittmarite-type NH$_4$FePO$_4$.H$_2$O and different lithium eutectic compositions are systematically investigated in order to obtain at low temperature olivine-type LiFePO$_4$ which is valuable electrode material for lithium-ion batteries. Nanosized LiFePO$_4$ powder is successfully prepared by topotactic reactions using LiCl-LiOH eutectic compositions at 277–325 ºC for short reaction time of 60−90 min. It is well crystallized with a preferred crystallite orientation along *a*-crystallographic axis. The prepared LiFePO$_4$ is characterized by a plate-like morphology inherited from the iron precursor. The micrometer LiFePO$_4$ plates are composed of nanosized spherical particles with dimensions about 50 nm which is favorable for further electrochemical performance.

Keywords: LiFePO$_4$, Phospho-olivine, Molten salts reactions, Lithium-ion batteries

INTRODUCTION

The iron-based compounds are very desirable as electrode materials in alkaline-ion batteries since they meet in largest extend the increasing environmental and economic requirements for usage of low-cost nontoxic metals. Among the iron-based polyanion compounds, LiFePO$_4$ is the most attractive electrode material already found application in high-power batteries for hybrid electric vehicles [1,2]. It belongs to phospho-olivine family, LiMPO$_4$ (M^{2+} = Fe, Mn, Co, Ni) that is characterized by a stable crystal structure based on three-dimensional phosphate framework. The phospho-olivine structure presents one-dimensional edge-sharing LiO$_6$ octahedra which define an energetically favorable pathway for Li$^+$ intercalation. LiFePO$_4$ exhibits remarkable electrochemical storage properties in terms of excellent safety due to the intrinsic lattice and thermal stability in both lithiated and delithiated states, long cycle life and reasonable energy density [1,2].

One of the electrochemical characteristics of LiFePO$_4$ electrodes needed to be improved is the low rate capability owing to low electron and ion conductivity. One of the prerequisites for overcoming the problem is that phospho-olivines have to be prepared as nanosized materials [3,4]. In this regard "soft chemistry" routes are particularly recommended [3]. More recently, we have demonstrated that manganese compounds MMnPO$_4$.H$_2$O (M$^+$ = K, NH$_4$) having a dittmarite-type structure can be effectively used as structure-directed precursors for low temperature synthesis (200-270 ºC) of both lithium and sodium manganese phospho-olivines [5-8]. Due to the same topology of M^{2+}–PO$_4^{3-}$ layers in the dittmarite structure (along *b*-axis) and olivine structure (along *a*-axis) [9,10], the transformation of dittmarite- into olivine-type structure follows a topotactic pathway by direct ion exchange of K$^+$ or NH$_4^+$ for Li$^+$ (accordingly Na$^+$). In present paper we have extended our studies on the preparation of LiFePO$_4$ by ion exchange in molten lithium salts using dittmarite-type NH$_4$FePO$_4$.H$_2$O. This precursor is cheap, easily obtained, remains stable and retains the Fe^{2+} state for long time.

There are only few reports on successful use of NH$_4$FePO$_4$.H$_2$O as a reagent for the preparation of LiFePO$_4$. Ellis *et al.* [11] have obtained LiFePO$_4$ with a unique tablet-shaped morphology at hydrothermal conditions using NH$_4$FePO$_4$.H$_2$O and LiOH. Solid state reaction between NH$_4$FePO$_4$.H$_2$O and Li$_2$CO$_3$ in the presence of sugar at temperatures between 600 and 850 °C for 12h also yields LiFePO$_4$ [12].

EXPERIMENTAL

Precursor preparation

The precursor NH$_4$FePO$_4$.H$_2$O is prepared by a precipitation reaction between aqueous solutions of (NH$_4$)$_2$Fe(SO$_4$)$_2$ (120 ml 0.65M solution) and (NH$_4$)$_2$HPO$_4$ (200 ml 2M

---

solution). To prevent the oxidation of the Fe^{2+} sulphate were added to the iron solution. The precipitation was performed at temperature higher than 70 °C in order to avoid the crystallization of $NH_4FePO_4.6H_2O$ having a struvite-type structure. So that, both solutions were preliminary heated to about 75 °C before mixing. The precipitate is left in the mother solution for 3-4h to achieve a better crystallinity of $NH_4FePO_4.H_2O$. Then, it is filtered, washed and dried at room temperature.

LiFePO$_4$ preparation

The reactions between $NH_4FePO_4.H_2O$ and molten lithium salts are examined following, in general, the synthetic procedure already developed in the case of manganese dittmarites [5-8]. $NH_4FePO_4.H_2O$ and lithium salts are thoroughly ground, the reaction mixture is rapidly heated in an argon flow to the given reaction temperature (in the case melting point of the lithium salts). After definite reaction time, the product is cooled to room temperature, washed thoroughly with water and ethyl alcohol (96 %) to remove the biproducts and unreacted salts, filtered and dried in air for about 5–6 h. We have performed experiments with three different lithium eutectic compositions having low melting points between 270 and 325 °C. Based on our previous experience [5,8] we have used small excess of the lithium salts for very short reaction times of 60 and 90 min. The detailed description of the experimental conditions and sample labeling are given in Table 1. Thus prepared samples are additionally annealed at 500 °C for 10 h in argon flow and these samples are briefly designated as LFP2-500, LFP3-500, LFP4-500 and LFP5-500 (the numbers 2, 3, 4 and 5 correspond to the synthesis parameters according to Table1). All reagents used are of analytical grade.

Methods of characterization

The XRD patterns are recorded on a Bruker Advance 8 diffractometer using CuKα radiation. The lattice parameters are calculated by WinPlotr programme. The TG-DTA analysis of $NH_4FePO_4.H_2O$ is performed using LABSYS^{TM} Evo apparatus (SETARAM) in an argon flow at a heating rate of 5 °C/min up to

ions, several milligrams of hydrazine 700 °C. The infrared (IR) spectra are measured on a Fourier transform Nicolet Avatar-320 instrument using KBr pellets (resolution < 2 cm^{-1}). The SEM images of the precursor and LiFePO$_4$ powders are obtained by JEOL (JSM-5510) scanning electron microscope.

RESULTS AND DISCUSSION
Precursor characterization

The prepared $NH_4FePO_4.H_2O$ is well-crystallized and free of impurities as revealed by its XRD pattern (Fig. 1) where all diffraction peaks match completely these in the reference pattern. Moreover, the XRD pattern shows a preferred crystallites orientation along *b*-crystallographic axis which is evident by the much higher intensity of the (010) diffraction peak than that in the reference pattern. This is a result of the plate-like morphology of the salt (see further) which is consistent with the layered dittmarite-type structure [9]. The calculated unit cell parameters are: *a* = 5.6605(3) Å, *b* = 8.8178(3) Å, *c*= 4.8254(2) Å (space group *Pmn2$_1$*) and they coincide very well with the reported values from neutron diffraction data [9].

In accordance with our previous findings [5-8] the topotactic transformation of $NH_4FePO_4.H_2O$ into LiFePO$_4$ should include a direct ion exchange of NH_4^+ from the precursor with Li^+ from the molten salts in the framework of the dittmarite structure, followed by fast release of water of crystallization. For a successful synthesis this mechanism suggests that the dehydration of the precursor would be better to take place with a maximum rate at temperatures close to the reaction temperature. In this regard we have examined the thermal behaviour of $NH_4FePO_4.H_2O$ in Fig. 2.

The TG curve shows two steps: the first one finishes at 315 °C and the second one is between 315 and 550 °C (Fig. 2). The course of DTA curve is consistent with that of the TG curve exhibiting two endothermic effects with peak temperatures 256 and 448 °C (Fig. 2). As in the case of $NH_4MnPO_4.H_2O$ [8] the first step is due to simultaneous release of H_2O and NH_3 resulting in formation of an intermediate $FeHPO_4$ at 315 °C (18.64 % mass loss *vs* calculated 18.73 %). Above 315°C a

dehydration-condensation process takes and $Fe_2P_2O_7$ is a final product at 550 °C (4.52 % mass loss *vs* calculated 5.93 %). The small exothermic effect observed immediately after this process at 546 °C is most probably due to the crystallization of $Fe_2P_2O_7$. From obtained

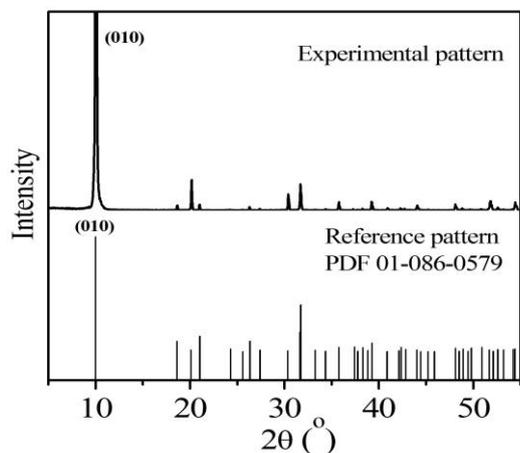data one can conclude that the water molecule is released from the iron precursor at temperature that will favor the successful transformation of dittmarite- into olivine-type structure.
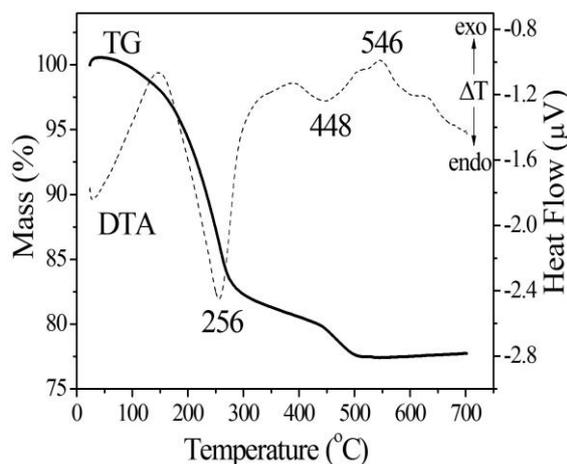

Fig. 1. Experimental and reference XRD patterns of $NH_4FePO_4.H_2O$. In the plot of the experimental pattern, the scale range of vertical *y* axis is much extended for better view of the diffraction peaks.

Fig. 2. TG and DTA curves for $NH_4FePO_4.H_2O$

Characterization of LiFePO₄

The XRD patterns of the reaction products between $NH_4FePO_4.H_2O$ and three lithium eutectic compositions are presented in Fig. 3. The phase analysis showed that $LiCl:LiNO_3$ eutectic composition (LFP1-270) is not appropriate because of the complete oxidation of Fe^{2+} to Fe^{3+}, although the inert atmosphere, with formation of mixture from $\alpha\text{-}Li_3Fe_2(PO_4)_3$ (about 75 wt %) and $\alpha\text{-}Fe_2O_3$ (about 25 wt%) (Fig. 3). The replacement of $LiNO_3$ by LiOH in other eutectic compositions (Table 1) gave a positive effect and in all next experiments the major product is the target LiFePO₄ (Fig. 3). Thus, in the XRD pattern of the sample obtained in molten LiOH:LiCl at 325 ºC for 90 min (LFP2-325) only a weak peak from admixture Li_3PO_4 can be seen. The annealing at 500 ºC (LFP2-500) improves the crystallinity of all reaction products, and now the presence of biproducts Li_3PO_4 (4.5 wt %) and $\alpha\text{-}Fe_2O_3$ (3.5 wt %) becomes visible (Fig. 3). In order to increase the purity of the target olivine phase in the next experiments we have slightly decreased either the excess LiCl-LiOH (LiFP3-325 in Table 1) or the reaction time to 60 min (LFP4-325 in Table 1). The XRD

patterns of LFP3-325 (Fig. 3) and LFP4-325 (XRD pattern not given) are the same and both
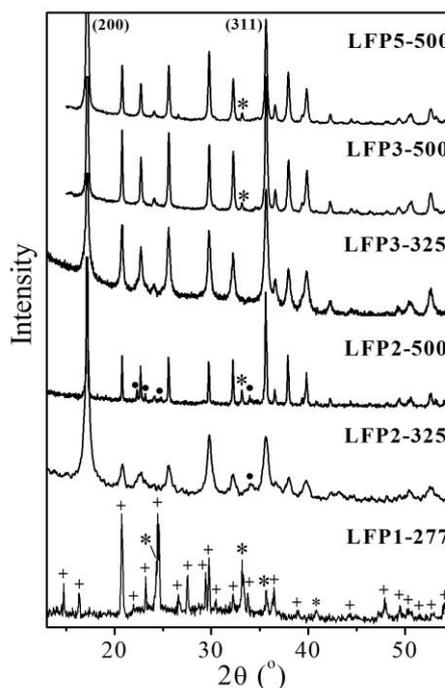
Fig. 3. XRD patterns of: LFP1-270; LFP2-325; LFP2-500; LFP3-325; LFP3-500 and LFP5-500. Symbols: * denotes $\alpha\text{-}Fe_2O_3$ (PDF 01-073-0603); + denotes $Li_3Fe_2(PO_4)_3$ (PDF 00-047-0107) and ● denotes Li_3PO_4 (PDF 00-15-760). The diffraction peaks without symbols correspond to olivine-type LiFePO₄.

Table 1. Description of the synthesis parameters and sample labeling.

Sample labeling	Lithium eutectic compositions	T, °C	Mole ratio Li-salts:Precursor	Reaction time, min
LFP1-270	LiCl–LiNO₃ (0.12:0.88)	270	2:1	90
LFP2-325	LiCl:LiOH (0.3:0.7)	325	2:1	90
LFP3-325	LiCl:LiOH (0.3:0.7)	325	1.5:1	90
LFP4-325	LiCl:LiOH (0.3:0.7)	325	2:1	60
LFP5-277	LiCl:LiOH (0.35:0.65)	277	1.5:1	90

exhibit diffraction peaks only due to LFePO₄ [10]. The annealed samples at 500 °C (LFP3-500 and LFP4-500), however, contain a small amount of α-Fe₂O₃ (about 2 wt %) according to the XRD data. As an illustration, Fig. 3 displays the XRD pattern of LFP3-500, while the IR spectrum of LFP4-500 is included in Fig. 4b. We have also probed another LiCl-LiOH eutectic composition having melting point at 277 °C (LFP5-277 in Table 1). The result obtained is the same as in the two previous experiments which is evident from the XRD pattern of the annealed sample at 500 °C (LFP5-500 in Fig. 3). In our opinion the formation of small amount of α-Fe₂O₃ during the ion exchange synthesis of LiFePO₄ most probably arises from the presence of residual oxygen in the argon flow. The calculated lattice parameters of LiFePO₄ obtained at 325 °C are: $a = 10.3271(8)$ Å, $b = 5.9912(8)$ Å, $c = 4.6953$ Å (space group *Pnma*). These values are very close to the reported data for single crystal grown by hydrothermal method [10] as well as for "defectless" LiFePO₄ powders obtained by other methods [13-15]. It should be mentioned that LiFePO₄ crystallites exhibit preferred orientation along the *a*-crystallographic axis which is clearly manifested by the much higher intensity of the (200) diffraction peak than that of (311) peak. In the case of random crystallite orientation the (311) peak is the strongest peak in the XRD pattern of LiFePO₄ [10,13-15]. This crystallite orientation is inherited from the dittmarite precursor (the difference in the space groups of the dittmarite and olivine-type structures switches *a* and *b* axes) [9,10].

The formation of LiFePO₄ by ion exchange reactions is further supported by IR spectroscopy (Fig. 4). All IR spectra are dominated by the strong absorbance related to the fundamental vibrations of the PO_4^{3-} ions: P–O stretching vibrations in the 1137-947 cm⁻¹ region and OPO asymmetric bending vibrations in the 651-546 cm⁻¹ region. The two bands at 500 and 447 cm⁻¹ are mainly related to
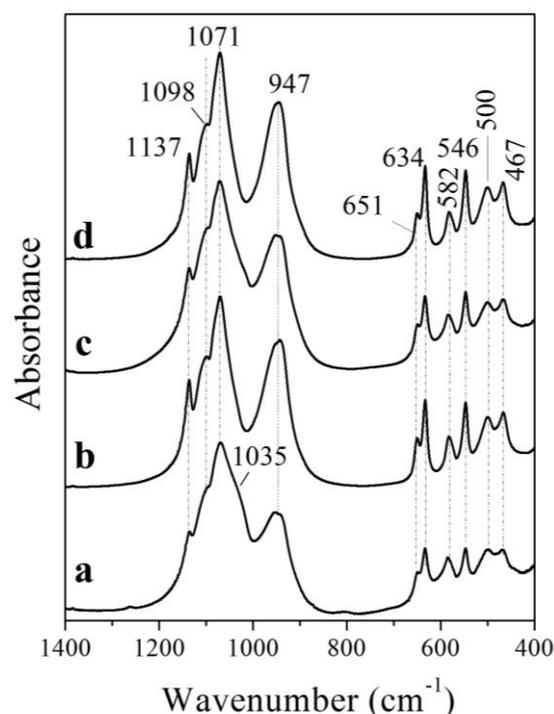
Fig. 4. IR spectra of: (a) LFP2-500; (b) LFP4-500; (c) LFP3-325; (d) LFP3-500

the Li⁺ translations but a mixing with the OPO symmetric bending mode was also supposed [16,17]. The positions of the IR vibrational bands agree with these previously reported for well-crystallized olivine phase LiFePO₄ [16,17]. In the IR spectrum of LFP2-500 (Fig. 4a), however, additional shoulder at 1035 cm⁻¹ appears and it most probably originates from Li₃PO₄ present in this sample according to its XRD pattern (Fig. 3c). In the IR spectrum of Li₃PO₄ the band at 1040 cm⁻¹ due to P–O stretching vibrations is the strongest one [16]. It is important that the IR spectrum of LiFePO₄ obtained at 325 °C for 90 min is identical to that after annealing at 500 °C for 10h (Fig. 4 c and d). This is an additional evidence that our method ensures well-crystallized olivine phase LiFePO₄ which remains stable upon further annealing, although the low synthesis temperature and very short reaction time of 60-90 min.

Moreover, the absence of any pyrophosphate phases gives further support that the ion exchange between NH_4^+ and Li^+ occurs very quickly in the framework of the dittmarite structure before the precursor decomposition. This ion exchange process is immediately followed by the H_2O release, so that the dittmarite structure is easily transformed in the olivine structure by a topotactic pathway.
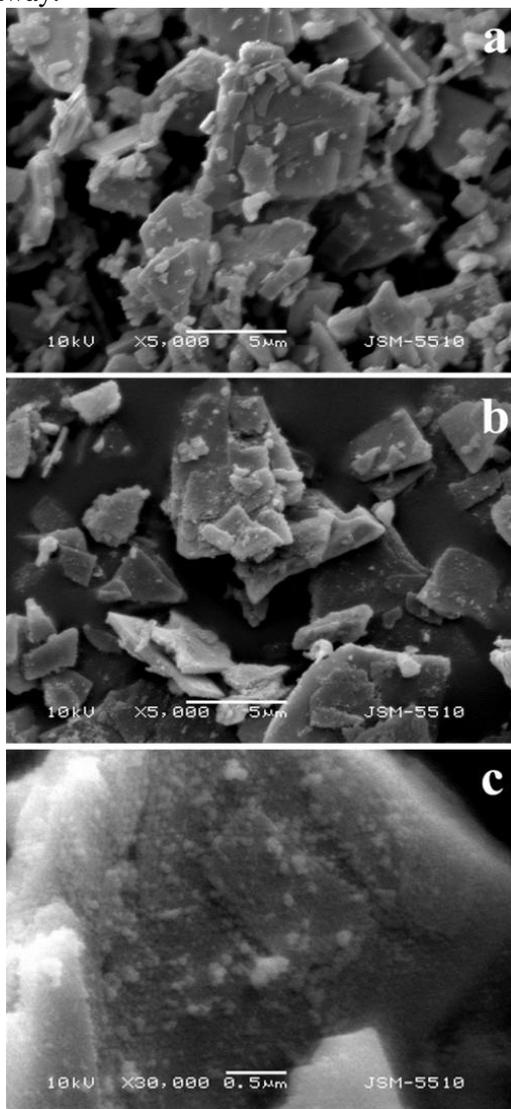
Fig. 5. SEM images: (a) $NH_4FePO_4.H_2O$; (b, c) LiFePO$_4$ obtained at 325 °C.

The topotactic transformation is manifested by the SEM images of $NH_4FePO_4.H_2O$ and obtained LiFePO$_4$ (Fig. 5). Evidently, the plate-like morphology of the precursor is preserved in the reaction product. In both SEM images (Fig. 5a, b) plates with basal dimensions of 2−7 μm are clearly visible. At higher magnification (Fig. 5c) one can see that micrometer plates of LiFePO$_4$ are composed of spherical particles with sizes about 50 nm. The SEM particle dimensions are slightly larger as compared to the crystallite dimensions (30

nm) determined by Scherrer equation from XRD line broadening. This fact again evidences for the good crystallinity of as-prepared LiFePO$_4$ powder although the rapid low-temperature synthesis.

CONCLUSIONS

The present study confirms that the dittmarite-type compounds are very effective precursors for fast, low-temperature synthesis of crystalline lithium iron and lithium manganese phospho-olivines, LiMPO$_4$ (M^{2+} = Fe, Mn). In both cases the reactions between dittmarite precursors $NH_4MPO_4.H_2O$ (M^{2+} = Fe, Mn) and lithium salts follow a topotactic pathway. This is manifested by the plate-like morphology and preferred crystallite orientation of prepared LiMPO$_4$ which are inherited from the used dittmarite-type precursors.

REFERENCES

1. Z. Gong, Y. Yang, *Energy Environ. Sci.*, **4,** 3223 (2011).
2. C. Masquelier, L. Croguennec, *Chem. Rev.,* **113**, 6552 (2013).
3. C. Delacourt, P. Poizot, S. Levasseur, C. Masquelier, *Electrochem. Solid-State Lett.,* **9**, A352 (2006).
4. S. Ferrari, R. L. Lavall, D. Capsoni, E. Quartarone, A. Magistris, P. Mustarelli, P. Canton, *J. Phys. Chem. C,* **114**, 12598 (2010).
5. V. Koleva, E. Zhecheva, R. Stoyanova, *Dalton Trans.,* **40**, 7385 (2011).
6. V. Koleva, T. Boyadzhieva, E. Zhecheva, D. Nihtianova, S. Simova, G. Tyuliev, R. Stoyanova, *Cryst. Eng. Comm.,* **15**, 9080 (2013).
7. T. Boyadzhieva, V. Koleva, R. Stoyanova, *Bulg. Chem. Commun.,* **45B,** 208 (2013).
8. V. Koleva, R. Stoyanova, E. Zhecheva, D. Nihtianova, *Cryst. Eng. Comm.,* **16**, 7515 (2014).
9. G. Carling, P. Day, D. Visser, *Inorg. Chem.,* **34,** 3917 (1995).
10. V.A. Streltsov, E.L. Belokoneva, V.G. Tsirelson, N.K. Hansen, *Acta Cryst.,* **B49**, 147 (1993).
11. B. Ellis, W.H. Kan, W.R.M. Makahnouk, L.F. Nazar, *J Mater. Chem.,* **17,** 3248 (2007)
12. N. W. Li, J. Gao, J. Ying, C. Wan, C. Jiang, *J. Electrochem. Soc.,* **153,** F194 (2006).
13. F. Gao, Zh. Tang, J. Xue, *Electrochim. Acta* **53** 1939 (2007).
14. D. Choi, P. N. Kumta, *J. Power Sources* **163**, 1064 (2007).
15. V. Koleva, E. Zhecheva, R. Stoyanova, *J. Alloys Compd.,* **476** 950 (2009).
16. A. A. Salah, P. Jozwiak, K. Zaghib, J. Garbarczyk, F. Gendron, A. Manger, C.M. Julien, *Spectrochim. Acta* **65A,** 1007 (2006).
17. C. M. Burba, R. Frech, *Spectrochim. Acta* **65A,** 44 (2006).

НИСКОТЕМПЕРАТУРНО ПОЛУЧАВАНЕ НА НАНОРАЗМЕРЕН LiFePO₄ ЧРЕЗ РЕАКЦИИ В СТОПИЛКА

Т. Бояджиева, Р. Стоянова, Е. Жечева, В. Колева*

Институт по обща и неорганична химия, Българска академия на науките
Ул. Акад. Г. Бончев, бл.11, 1113 София, България

(Резюме)

Реакции в стопилка между дитмаритен-тип NH₄FePO₄.H₂O и различни литиеви евтектични състави са систематично изследвани с цел нискотемпературно получаване на оливинов-тип LiFePO₄, който е ценен електроден материал за литиево-йонни батерии. Наноразмерен LiFePO₄ е успешно синтезиран чрез топотактични реакции използвайки LiCl-LiOH евтектични състави при температури 277–325 ºC за много кратко реакционно време 60–90 мин. Фосфо-оливиновата фаза е добре изкристализирала с предпочитана ориентация на кристалитите по *a*-кристалографска ос. Прахообразният LiFePO₄ се характеризира с плочковидна морфология, унаследена от железния прекурсор. Микрометърните плочковидни агрегати на LiFePO₄ са изградени от наноразмерни сферични частици с размери около 50 нм, което е благоприятен фактор за по-нататъшно електрохимично приложение.

Slice selective NMR approach for investigation of distribution phenomena in biphasic samples

Y.N. Mitrev*

Institute of Organic Chemistry with Centre of Phytochemistry, Bulgarian Academy of Sciences, Acad. G. Bontchev Str., Bl. 9, 1113 Sofia, Bulgaria

Distribution phenomena in biphasic systems using slice selective NMR measurements are discussed. Two quantification strategies are compared, demonstrating, that reliable data for the systems $D_2O/CDCl_3$ are easily obtained, even on low field spectrometer.

Keywords: Slice selection, NMR, biphasic samples, quantification

INTRODUCTION

Slice-selective NMR is a relatively new technique, allowing registration of spectral information from different parts of the sample. The idea of spatially resolved spectroscopy is not new and numerous examples can be found in the literature, using specialized equipment [1-3]. In the last years its application on standard NMR equipment is drawing increasing attention due to its easier implementation. It is successfully used to study diverse systems, where the sample composition varies along the NMR tube, including diffusion in polystyrene [4,5] agar gels [6] and ionic liquids [7].

Surprisingly, little is done on its application on biphasic samples. In 2000, Kozminski demonstrates the possibility to record high resolution NMR spectra in the system $D_2O/CDCl_3$ [8]. More recent papers investigate D_2O/olive oil [9] and D_2O/octanol systems [10], but in all cases, no attempt to derive quantitative information is made.

As a continuation of previous investigations, this paper discusses the possibility to quantify biphasic samples from the type chloroform/water and tries to provide guidelines for performing that type of analysis, using the distribution of vanillin as an example.

THEORY AND METHODS

1. Introduction to slice selection

Slice selection is achieved by the simultaneous use of frequency selective pulses and pulsed field gradients (PFG). Applying a gradient with strength G in the direction of the external magnetic field (B_o) induces linear variations in the local magnetic fields, depending on their position (z):

$$B(z) = B_0 + G*z \qquad (1)$$

Following the resonance condition, this results in encoding of the spatial position of the spins in their resonance frequencies:

$$\nu(z) = \nu_0 + G*z*\gamma \qquad (2)$$

where ν_0 is the resonance frequency in the static field and gamma is the gyromagnetic ratio. Applying a frequency selective pulse during the gradient will then affect only those resonances, which fulfil Eq. 2. When the bandwidth is large enough to cover the whole spectrum of the compound under investigation, this results in the selection of spins from a discrete region of the sample (slice), with thickness Δz, proportional to the ratio of the bandwidth (BW) and the gradient strength:

$$\Delta z = \frac{BW}{G*\gamma}$$

Changing the offset of the selective pulse allows to "scan" different parts of the sample along the direction of the applied gradient (Figure 1).

* To whom all correspondence should be sent:
E-mail: yavor@orgchm.bas.bg
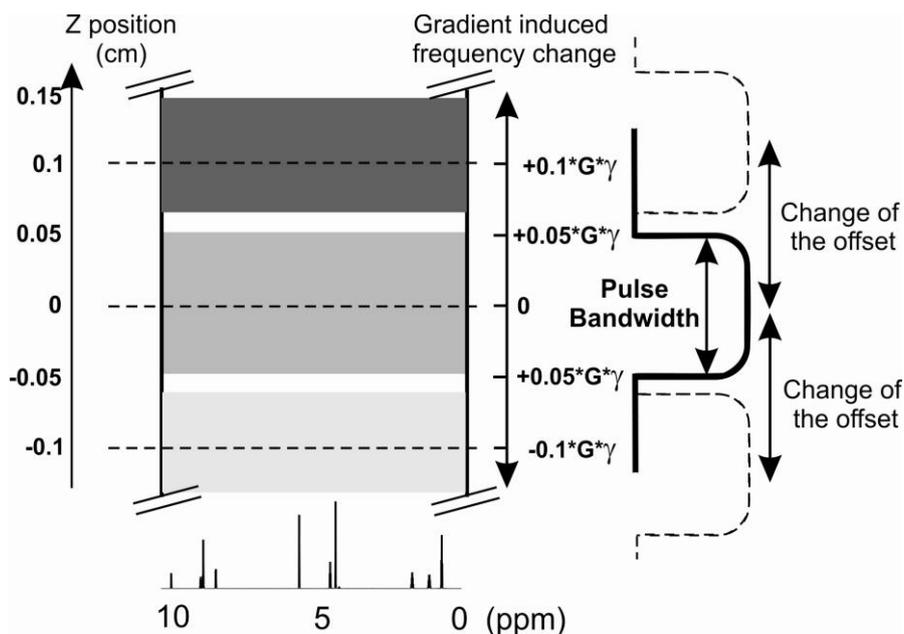
Figure 1. Principal scheme of slice selective NMR. The pulse bandwidth is 0.1*G*γ, resulting in 1 mm slice thickness.

The fact, that only part of the sample is observed marks the main drawback of the slice selection approach – its lower sensitivity, proportional to the thickness of the slice. However, this also offers the opportunity to record series of quantitative spectra at greatly reduced times, using interleaved schemes of acquisition [6,11], making the technique particularly suitable for quantification of systems which change in time.

2. Choice of pulse sequence

The use of interleaved acquisition requires only part of the sample to be irradiated at a time, which is usually the case, when only frequency selective pulses are used. In this respect, the slice selective

excitation is often the experiment of choice. Consisting of only one pulse, it offers the best sensitivity with minimum signal losses due to diffusion or transversal relaxation processes. However, when applied to biphasic samples, it leads to the presence of artefacts, often observed in the magnetic resonance imaging when change in the magnetic susceptibility is present (Figure 2) [12]. Spectra with much higher quality are acquired when using a slice selective version of the spin echo. The presence of a refocusing pulse flanked by two spoil gradients effectively supresses the susceptibility artefacts, yielding clean spectra with excellent phase and baseline properties.
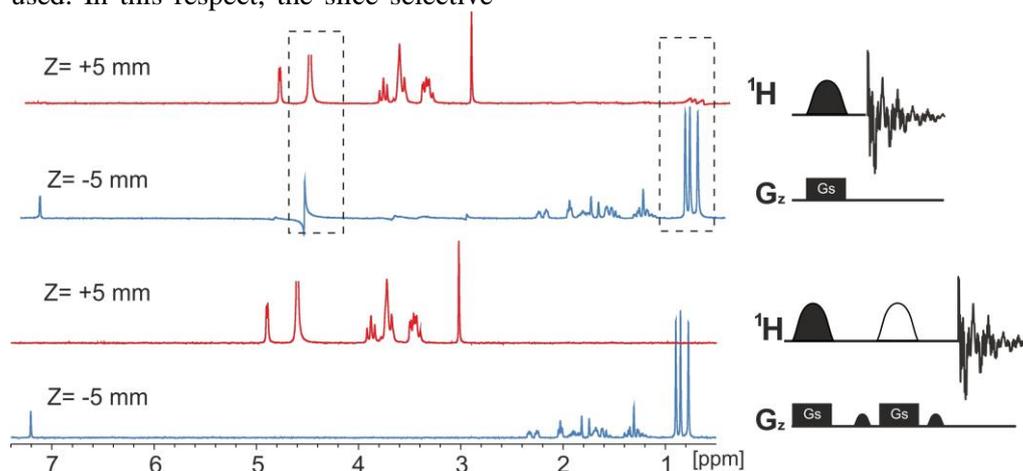
Figure 2. Comparison between slice selective excitation (top) and spin echo (bottom). The corresponding pulse sequences are shown on the right with filled and open shapes corresponding to excitation and refocussing pulses. The used sample is 20 mM α-cyclodextrin in D$_2$O, layered on 50 mM camphor in CDCl$_3$.

A drawback of the spin echo is the lower signal to noise ratio, compared to the excitation scheme, as the signal intensity depends on transverse relaxation properties of the system and the two spoil gradients also add possible diffusion losses [13]. To minimize those unwanted effects, the echo time is set to 1 ms, resulting in decrease of the sensitivity by approximately 50%, compared to the excitation experiment. Attempting to obtain higher sensitivity, two additional approaches were also examined – a mixed scheme, consisting of slice selective excitation element, flanked by two nonselective 180° pulses, [14] and the LOCSY experiment [9]. In both cases susceptibility artefacts were observed, which limits the choice to the spin echo.

3. Quantification strategies

Commonly, quantification in the slice selective NMR is done by conversion of the measured absolute integral values in concentrations using calibration curves. With samples of known concentration, series of spectra with identical experimental parameters are acquired and separate curves for each slice are built. Although time consuming, this method gives excellent precision, as it accounts for possible diffusion and/or relaxation processes during the experiment.

The presence of two different phases suggests that separate calibration curves for each of the solvents are needed. This is true for high-field spectrometers, which are usually more sensitive to solvent change. In this case, however, the optimal 90° pulse is practically the same - 14.1 μs for D_2O and 14.0 μs for $CDCl_3$, resulting in identical intensity profiles (Figure 3).

The excellent agreement allows us to use single calibration curve in the current study, but performing that type of measurements on high-field

instruments may require separate quantification for each solvent.
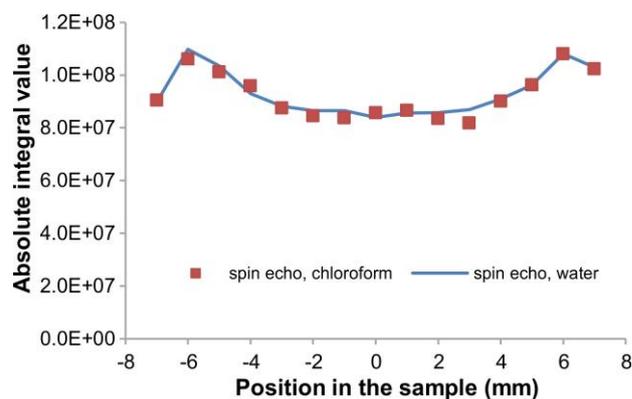
Figure 3. Intensity profiles, obtained for 40 mM vanillin samples in D_2O and $CDCl_3$.

An alternative approach, that could greatly simplify the quantification process in such cases, is the internal standardization. It relies on the assumption, that the measured ratio of two compounds is independent on the experimental parameters, if no signal losses, due to diffusion or relaxation are present. Additionally, when biphasic samples are studied, care should be taken to homogeneously spread the standard in both phases, or, preferably, different standards for each phase should be used. In this respect, hexamethyldisloxane (HDMSO) and tetramethylammonium bromide (TMAB), commonly used for chemical shift referencing, present good compounds for quantification. They have relatively long T2 relaxation times and diffusion coefficients, similar to vanillin, ensuring minimal signal loss during the spin echo experiment (Table 1).

Table 1. Diffusion and relaxation parameters of vanillin, HDMSO and TMAB.

Concentration (mM)	Chloroform sample		D_2O sample	
	Vanillin	HDMSO	Vanillin	HDMSO
D (m^2/s) $*10^{-10}$	13.5	15.2	5.7	8.7
T1 (s)	4.23*	2.32	1.52*	7.45
T2 (s)	3.76*	2.06	1.38*	6.31

* Values for the CH_3O- group

RESULTS AND DISCUSSION

Following the already mentioned considerations, biphasic sample, containing 40 mM vanillin in the D_2O layer was prepared, and its distribution between the two phases is measured. Preliminary investigations revealed that the opposite approach is not practical, as the higher solubility of vanillin in chloroform [15] results in much slower diffusion

in the water phase. To ensure good temperature stability, the sample is kept in the magnet for the time of all measurements. Figure 4 summarizes the results, which prove that both methods - using calibration curve and using internal standard yield satisfactory agreement, with difference in the calculated concentrations of approximately 5 %.

Significant dependence of the vanillin distribution from the air flow, used to maintain the sample temperature is observed (Figure 5). This result is unexpected, as it is known, that increasing the airflow results in better temperature stability, at least in the active volume of the coil [16]. However, recent study demonstrate, that often the sample temperature at the bottom of the tube differs from the one in the observable volume, thus promoting convection flows along the tube [17].
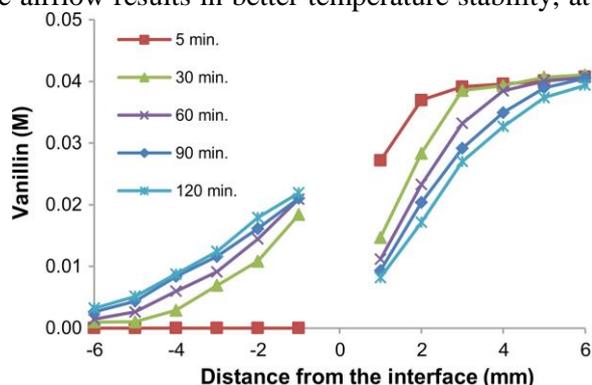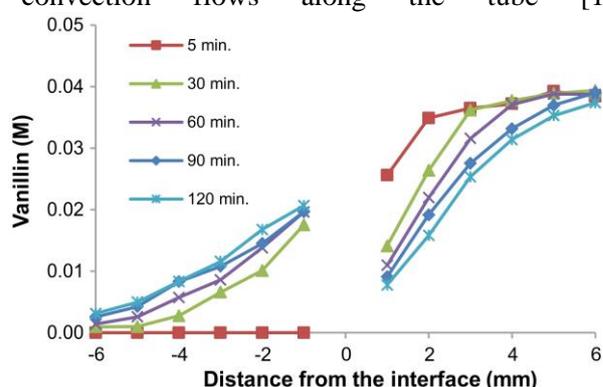

Figure 4. Concentration profiles of vanillin in $D_2O/CDCl_3$ sample at different times. The concentrations are calculated, using calibration curve (left) and internal standard (right). The initial solution was 40 mM vanillin in D_2O. Due to signal broadening, data for the slice, containing the interface is not shown.
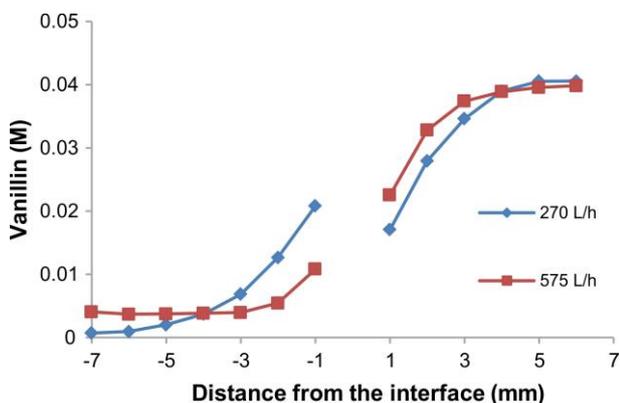
Figure 5. Comparison between the distribution of 40 mM vanillin in $D_2O/CDCl_3$ after 30 min. Air flows of 270 and 575 L/h were used.

EXPERIMENTAL

All experiments were conducted on Bruker DRX 250 spectrometer (5.87 T magnet), operating at 250 MHz ^{1}H frequencies, equipped with 5 mm BBO probe with z-gradient coil. The temperature was maintained at 298 K, using Bruker B-VT 2000 temperature unit with airflow of 270 L/h. All spectra were referenced against tetramethylammonium bromide (TMAB, 3.15 ppm) and hexamethyldisoloxane (HDMSO, 0 ppm) for water and chloroform, respectively.

Slice selection is performed, using 2088.5 µs G4 Gauss-Cascade [18] excitation pulse and 621.7 µs RSnob [19] for refocusing, both of them with bandwidth of 3751 Hz. Combined with gradient strength of 8.81 G/cm they produce 1 mm slices. Changing the frequency offset for those pulses from 22506 Hz to -22506 Hz with a step of 3751 Hz, results in 13 adjacent slices. The strength of the

spoil gradients used in the spin echo sequence is 16.05 G/cm. The spectra are acquired with 4 scans in interleaved mode of acquisition for a total experimental time of 4 min.

Typical samples were prepared by using 250 µl of chloroform, containing HDMSO in standard 5 mm NMR tube. 250 µl D_2O solution of vanillin (40 mM) was carefully layered on top of it so that both layers remain separated. The volume of both solvents was chosen so that the interface appears in the center of the coil as determined by the Bruker sample depth gauge.

CONCLUSIONS

Slice-selective NMR experiments on $D_2O/CDCl_3$ biphasic samples provide a quick and easy technique to obtain quantitative data on distribution processes. On low field instruments, quantification is relatively simple, as no significant difference between the NMR behaviour of the two solvents is observed. As a proof of principle it is shown, that the use of internal standard can be a good alternative to the calibration curve method, which could simplify the quantification on high-field instruments, which are usually more sensitive to changes in the solvent.

REFERENCES

1. J. Tritt-Goc, J. Kowalczuk, N. Pislewski, *Appl. Magn. Reson.*, **29**, 605 (2005).
2. J. Lambert, R. Hergenroder, D. Suter, V. Deckert, *Angew. Chem. Int. Ed.,* **48**, 6343 (2009).
3. C. García-Aparicio, I. Quijada-Garrido, L. Garrido, *J. Colloid Interface Sci.* **368**, 14 (2012).
4. T. Niklas, D. Stalke, M. John, *Chem. Commun.*, **51**, 1275 (2015).
5. A. Poppler, S. Frischkorn, D. Stalke, M. John, *ChemPhysChem*, **14**, 3103 (2013).
6. Y. Mitrev, S. Simova, D. Jeannerat, *Chem. Commun.*, **52**, 5418 (2016).
7. J. Allen, K. Damodaran, *Magn. Reson. Chem.*, **53**, 200 (2015).
8. W. Kozminski, *Polish J. Chem.*, **74**, 1185 (2000).
9. C. Mantel, P. Bayle, S. Hediger, C. Berthon, M. Bardet, *Magn. Reson. Chem.*, **48**, 600 (2010).
10. B. Martin, G. Chingas, O. McDougal, *J. Magn. Reson.*, **218,** 147 (2012).
11. J. Kind, C. Thiele, *J. Magn. Reson.,* **260**, 109 (2015).
12. K. Krupa, M. Bekiesinska-Figatowska, *Pol. J. Radiol.*, **80**, 93 (2015).
13. E. Stejskal, J. Tanner, *J. Chem. Phys.*, **42**, 288 (1965).
14. B. Sathyamoorthy, D. Parish, G. Montelione, R. Xiao, T. Szyperski, *ChemPhysChem*, **15**, 1872 (2014).
15. N. Singh T. Henningsen, E. Metz, R. Hamacher, E. Cumberledge, R.H. Hopkins, R. Mazelsky, *Mater. Lett.*, **12**, 270 (1991).
16. N. Loening, J. Keeler, *J. Magn. Reson.*, **139**, 334 (1999).
17. I. Swan, M. Reid, P. Howe, M. Connell, M. Nilsson, M. Moore, G. Morris, J. Magn. Reson., **252**, 120 (2015).
18. L. Emsley and G. Bodenhausen, *Chem. Phys. Lett.*, 165 (1990).
19. E. Kupce, J. Boyd, I. Campbell, *J. Magn. Res. B.*, **106**, 300 (1995).

ПРОСТРАНСТВЕНО СЕЛЕКТИВНА ЯМР СПЕКТРОСКОПИЯ ЗА ИЗСЛЕДВАНЕ НА ПРОЦЕСИ НА РАЗПРЕДЕЛЕНИЕ В ДВУФАЗНИ СИСТЕМИ

Я. Н. Митрев

Институт по органична химия с Център по фитохимия, Българска академия на науките, ул. Акад. Г. Бончев, бл. 9, 1113 София

(Резюме)

Статията разглежда процеси на разпределение в двуфазни системи, изследвани с помощта на пространствено селективна ЯМР спектроскопия. Сравнение между две стратегии за получаване на количествени данни показва, че получаването на надеждни данни за системи от типа $D_2O/CDCl_3$ е лесно, дори на спектрометър с ниска работна честота.

Layer by layer deposition of chitosan/xanthan thin films studied *in situ* by QCM

S. A. Yaneva[1*], G. E. Alexieva[2], T. S. Velinov[2]

[1]University of Chemical Technology and Metallurgy, Department of Fundamentals of Chemical Technology, 8, Kliment Ohridksi Blvd, 1756 Sofia, Bulgaria.
[2]Sofia University, Department of Solid State Physics and Microelectronics, 5, James Bourchier Blvd, 1164 Sofia, Bulgaria

The layer by layer (LbL) technique was used to obtain a layered film consisting of two natural polyelectrolytes: chitosan (CHI) and xanthan (X). The buildup of the film was monitored by a quartz crystal microbalance (QCM). The obtained films showed exponential growth and, besides, some of the accumulated mass was washed away by the buffer. This was attributed to the "free" CHI molecules which penetrate the entire film because of the initial difference of the chemical potential in and out the film. When glutaraldehyde was added as a crosslinking agent substantial differences in the film growth were observed. First, the crosslinked CHI layers become impermeable for "free" molecules and thus each layer interacts only with its two adjacent layers. This leads to a linear growth of the polyelectrolyte films. Second, crosslinking makes the outer layers stable enough to resist to dissolution during deposition of subsequent layers.

Keywords: QCM, chitosan, xanthane, thin films, drugs release.

INTRODUCTION

The Layer-by-layer self-assembly technique is a powerful tool for production of polyelectrolyte multilayer thin films that are widely used in drug delivery [1], biosensors [2], food science [3] and tissue engineering [4]. Among the polyelectrolytes, the natural-based polymers received many applications due to their excellent biological performance, similarity with the extracellular matrix and good chemical flexibility [5]. Most of natural polyelectrolytes are polysaccharides such as hyaluronan, chitosan and xanthan [6-8]. CHI is a biodegradable, non-toxic and biocompatible material which seems to be the only important polysaccharide that charge positively in a suitable water based solution. Due to its porous structure and amine groups, chitosan is well-suited for attachment of biomolecules and the chitosan films are commonly used to elaborate selective coatings for biosensors [9]. Another successful medical application of CHI is its use for delivery container where various vesicles could be filled with drugs for controlled release after its degradation under low pH [9].

Many of CHI properties are explained by the presence of primary amine groups in its molecule. At pH lower than 6.5, this amines are positively charged and chitosan is soluble. At pH higher than 6.5 the amines are more deprotonated, and CHI becomes insoluble [9]. Thus, the deposited CHI films must be kept at a pH above 6.5 to prevent them from dissolving. The ionic strength and pH of the solution also influence the charge density of the adsorbed and adsorbing layers which in turn plays an important role in the LBL processing of the weak polyelectrolytes.

Xanthan gum is a commercially important polysaccharide that has various applications in diverse fields of food and pharmaceutical industries. It is a polysaccharide produced as a secondary metabolite in biotechnological fermentation process based on cultivation under aerobic conditions of the microorganism *Xanthomonas campestris*. Many microorganisms are able to metabolize high molecular polysaccharides, but X gum is the only bacterial polysaccharide obtained in larger industrial conditions. X has gelling nature which determines its ability in retarding drug release and potential of entrapping the drug within the gel [10].

Despite of several publications concerning properties of CHI/X gel complexes or focused on the controlled drug release potential of the system [12-14], data about building the CHI/X multilayer system using a QCM microfluidic system appear as not yet reported. Tablets of CHI/X were prepared by direct compression method [15]. The samples were made by mixing solutions of the two electrolytes and then stirring [12, 16]. The precipitates are separated either by ultracentrifugation or by filtration. The same method is used to obtain a gel for enzyme immobilization [17, 18]. The rheological and structural characteristics of a hydrogel spheres

---

* To whom all correspondence should be sent:
E-mail: sp_yaneva@uctm.edu

composed of CHI and X, and obtained by adding small drops of xanthan in chitosan solution were studied [19]. The same method was used for studying the influence of the pH solutions and the polymer concentration on the crosslinking between CHI and X, and to obtain a matrix for controlled drug released [8, 14]. A LbL method combined with dipping technique was used to obtain multilayered CHI/X films and the influence of pH and ionic strength on the films formation were studied by optical methods [20].

A film consisting of alternating layers of these two natural polyelectrolytes seems a good candidate for delivery and retarded release of drugs. CHI will be the carrier while the gelling nature of X layers will make the drug diffusion and/or film degradation slower. Luckily, the two polyelectrolytes charge oppositely in water based solutions and thus electrostatic attraction can be used to perform the LbL deposition technique. QCM is a sensitive technique for measuring mass changes on the quartz resonator [11] and when it is incorporated in a microfluidic platform it allows the building of the multilayer system to be monitored in real time. The aim of this research was to study the influence of different factors as pH of the rinsing buffer solution, air flow and crosslinking reagent on the formation of CHI/X structure obtained by LbL technique. The deposition of multilayer structures was performed by using a fluidic system to deliver the solutions to a quartz crystal microbalance.

EXPERIMENTAL
Reagents

Chitosan with medium molecule weight and 75-85% degree of deacetylation, Xanthan (from *Xanthomonas campestris*), NaOH p.a. (99%), Glutaraldehyde, and Acetic acid were obtained from Sigma-Aldrich. $NaH_2PO_4*2H_2O$, p.a. was purchased from Valerus Co.

LbL assembly of the multilayered structure

Solutions of 0.1% w/v chitosan and 0.05 % w/v xanthan in 0.1 M sodium acetate buffer (pH 4.0) were made. In order to remove the excess polymers after each deposition of polysaccharides a rinsing procedure was performed with 0.1 M sodium phosphate buffers having different pH: pH 7.0 and pH 7.5. A 2.5 % v/v glutaraldehyde in 0.1 M phosphate buffer with pH=7.0 was used as a crosslinking reagent. The first deposited layer in our experiments was always CHI. Often, in order to improve the attachment of the CHI molecules to gold, the latter is first modified, for example with cysteamine [21]. To keep things as simple as

possible, and also, in view of future medical applications we didn't modify the gold surface. Deionized water was first introduced in the fluidic system until the QCM data stabilized and then the CHI solution was applied directly.

LbL characterization
Scanning electron microscopy

The morphology of the obtained structures was observed with a dual beam scanning electron/focused ion beam system LYRA I XMU, TESCAN after being coated with a conductive thin gold film.

QCM experiments

A quartz crystal microbalance with a nominal resonance frequency of 10 MHz was used for in situ monitoring the formation of polyelectrolyte layers. Sensor chips from Attana A100 (Attana AB, Sweden) were used. The cell volume was approximately 4 μl and the electrode surface – 16 mm^2. Multilayer films were fabricated on the gold electrode of quartz AT-cut resonators. These resonators oscillate in a thickness-shear mode with a displacement vector parallel to the plate surface. According to Sauerbrey equation [22] there is a linear relationship between the deposited onto the quartz plate mass Δm and the frequency change Δf: Δm = - CΔf provided that this additional mass is less than 2% of the quartz plate mass. In our case, the constant C is 0.7 ng/Hz. The frequency was recorded every second from the beginning of the introduction of the liquid flow in the cell by a frequency counter and then stored in a computer and displayed on the computer screen for convenience. All of the reported experiments were repeated three times and the repeatability was good.

RESULTS AND DISCUSSION

With regard to future medical applications of the CHI/X films we first varied the pH of the buffer but in all cases it was kept near that of pure water. Then, in another set of experiments, an air was introduced in the fluidic system in order to make the layers more compact and resilient to the shear forces that fluids exert on the attached to the QCM layers. Finally, the influence of a cross-linker, namely, glutaraldehyde, on the film growth was investigated.

The surface of obtained LbL thin films was investigated by SEM (Fig. 1). The SEM images confirmed that there is CHI/X films formed onto the quartz resonators. Fig. 1a shows the surface of a film without added glutaraldehyde while in Fig. 1b a film with glutaraldehyde added as a cross-linker is presented. Both films show uneven surfaces. However, a difference can be seen – the film

without glutaraldehyde has a flake like structure whilst the surface of the film in Fig. 1b appears to have continuous and smoother structure. This difference in the structures may be in the origin of the obtained results which are discussed later in the text.
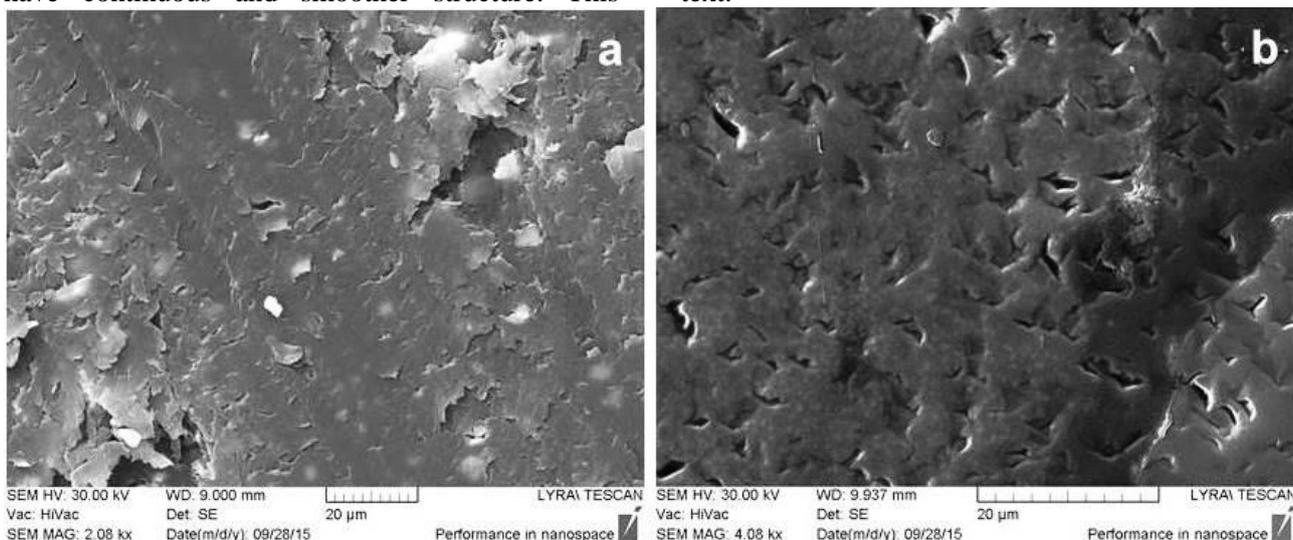

Fig. 1. SEM images of a sample without glutaraldehyde (a) and with glutaraldehyde (b) added as a crosslinking agent.
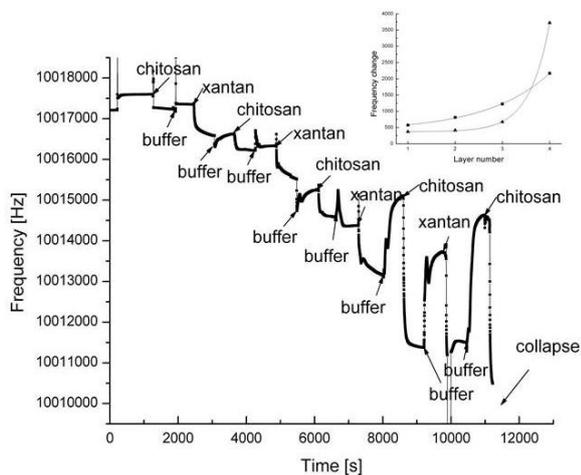

Fig. 2. Raw signal obtained from CHI/X layers at pH=7.0. Arrows show polyelectrolyte or buffer injection. In the inset the frequency shift after each CHI layer (■) and X layer (▲). Lines are an exponential fit to the corresponding symbols.
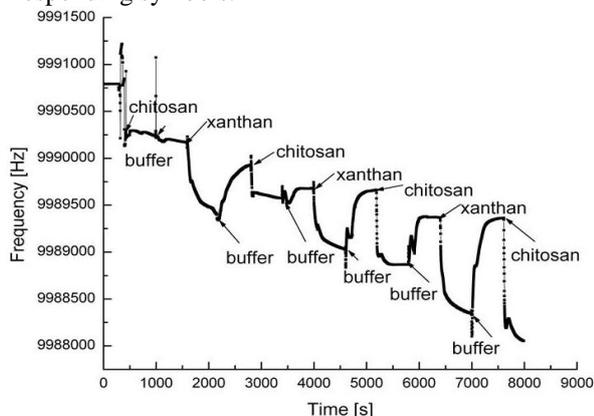
Fig. 3. Raw signal obtained from CHI/X layers at pH=7.5. Arrows show polyelectrolyte or buffer injection.

The QCM results of the use of 0.1 M phosphate rinsing buffers with different pH are presented in Figure 2 and 3. The order of the stages of each cycle of depositions was chitosan - buffer - xanthan - buffer. It is seen that the frequency shifts associated with depositions of polymers increases after each cycle but at the same time more mass is washed away by the phosphate buffer from the layers with the increment of the cycle number.

In the first experiment, (Fig. 2) four complete cycles were performed before the resonator stopped oscillating. The final frequency shift (Δf) was about 6,900 kHz. In the second procedure, shown in Fig. 3, three complete cycles of depositions were realized and then the oscillator stopped. The final frequency shift (Δf) was about 2,250 kHz meaning that the increased pH of the buffer resulted in about three times less polyelectrolyte mass deposited onto the substrate. This could be attributed to a reduction of the positive charges in CHI molecules as a result of the higher alkalinity of the buffer. Furthermore, the higher the effective charge density of X chains is the more the free COO^- groups along the X chains repel each other to make the chains with more extended conformations, which does not favor the X adsorption.

In both experiments, however, the frequency shift was unusually high compared to other structures with polysaccharides. For example the formation of chitosan – hyaluronan was studied by QCM and the frequency change was about 400 Hz at the fundamental frequency after deposition of four bilayers using high molecular weight CHI [23]. This change corresponds to about 1600 Hz in our case because the fundamental frequency of the

QCM we use is 10 MHz compared to 5 MHz [23]. The high frequency change can be attributed to the non-homogeneous structure of our layers which, in case of films without glutaraldehyde has a flake-like structure as can be seen from the scanning electron microscopy image (Fig. 1a). Such a structure favors the entrapment of water because CHI is hygroscopic and forms hydrogen bonds with water. This bonded water becomes a part of the film and contributes to the frequency change. Also, apart from CHI molecules bound electrostatically to the X chains in the process of the film building, another type of CHI chains, called "free chains" can diffuse from the surface into the volume [23, 24]. Their existence is explained by the different initial chemical potential of CHI molecules in the solution and the film. As a result, these molecules diffuse into the film until the chemical potentials in and out the film equalize or the electric potential barrier becomes high enough to prevent "free chains" crossing the interface between the solution and the film. In the next stage, however, when the structure is washed by a buffer these "free" molecules diffuse back in the solution. In principle, same arguments may hold true for the polyanion molecules but in our case the X molecules are much less mobile. Such an explanation of the rapid increase of the mass deposited onto the resonator is also consistent with the results obtained when glutaraldehyde is introduced in the system as a crosslinking agent. These results are discussed later in the paper together with the details on the film growth.

In order to optimize the deposition conditions for the multilayered system and stabilize the polymer layers, in another set of experiments we introduced air into the flow system after each deposition of CHI (results not shown). Usually, when polyelectrolyte films are exposed to air they become more compact and rigid, and we hoped that this would reduce the mass decrement during washing steps. Unfortunately, the results were not very different from the ones shown in Fig.2 and Fig. 3. Crucially, the tendency for washing away some material from the film after rinsing with phosphate buffer remained.

Many polyelectrolyte films can be crosslinked with reagents such as phenols, DTBP or glutaraldehyde making them more chemically resistant and physically harder [9]. In our next experiments we used glutaraldehyde as a crosslinking agent. The aldehydes groups of glutaraldehyde molecule bind covalently to CHI amine groups of different CHI molecules (or the same one), therefore establishing a strong link between them and forming polymer network. In our

case, the crosslinking stages were carried out with using a glutaraldehyde water solution. The same buffer but without glutaraldehyde was used for rinsing. The sequence of deposition was as follows: chitosan solution - glutaraldehyde solution - buffer solution - xanthan solution - buffer solution. The time for each stage was 5 min. The results are presented on Fig. 4. The total frequency shift here is about 6.3 kHz, and, as can be seen from Fig. 4, the tendency of washing away the last layer after introducing buffer in the fluidic system isn't observed. We can draw the conclusion that the stable decrease of the resonant frequency of the QCM after the introduction of glutaraldehyde reflects the improvement of the stability of the polymer films.
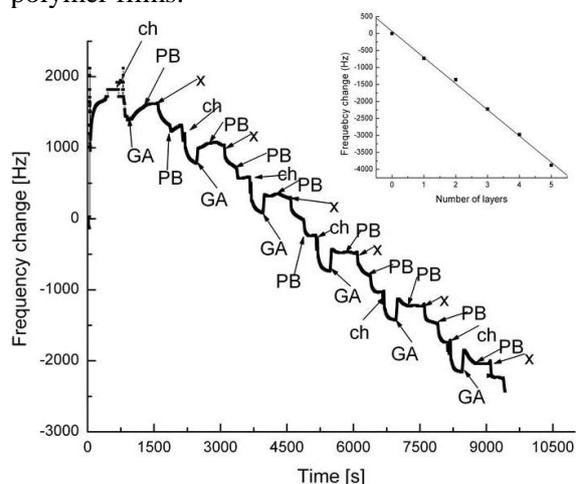
Fig. 4. Raw signal obtained from CHI/X layers at pH=7.01 with glutaraldehyde added after each CHI layer. Arrows show chitosan (ch), xanthan (x) buffer with glutaraldehyde (GA) or pure phosphate buffer (PB) injection. In the inset data for the frequency change after each double layer (CHI/X) deposition are shown together with a linear fit.

Another striking difference is the frequency change after every cycle with and without added glutaraldehyde. In the inset of Fig. 2 the change of the resonant frequency before introducing the buffer into the fluidic system is presented for CHI and X layers separately. It is seen that this change is exponential, presumably reflecting the exponential growth of the layers. Such an exponential growth isn't surprising since most of the polysaccharides films are known to grow exponentially when LbL technique is used [23]. This behavior is attributed to the mobile CHI chains (in this case) that can penetrate not only into the adjacent layers but the whole system. Thus, such type of growth relies on the diffusion of "free" chains in and out of the whole structure during each deposition step. This explanation is consistent with the decrement of the deposited mass onto the quartz resonator during the

washing stage. Such a decrement is observed also in [23] for the system chitosan/hyaluronan although on a much smaller scale. In view of the large decrement of the QCM resonant frequency, it seems that in our case some dissolution of the films due to not strong enough electrostatic attraction is also a plausible explanation. The added glutaraldehyde binds the different CHI molecules of one and the same layer and this seems to have two major effects. First, the crosslinked CHI layers become impermeable for "loose" molecules and thus each layer interacts only with its two adjacent layers. This leads to a linear growth of the polyelectrolyte films [23]. In the inset of Fig. 3 this linear growth is emphasized by showing the film thickness after each deposition of a double layer CHI/X and the best linear fit with linear correlation coefficient (r) 0.998. Second, crosslinking makes the outer films stable enough to resist to any possible dissolution.

CONCLUSIONS

In this short communication, we report the results of the study of CHI/X multilayers formation on gold substrates. The recording of the QCM resonant frequency every second allows monitoring of the film formation under different conditions in real time. Without a crosslinking agent the growth of the film is exponential. Besides, after a few layers a part of film is washed away by the buffer. These two phenomena are attributed to the diffusion of "free" CHI molecules throughout the entire film which may be is the reason of partial dissolution of the last layer. However, the addition of glutaraldehyde as a crosslinker after deposition of each CHI layer seems to limit the diffusion of CHI chains to the neighboring layers. This results in linear growth of the film and, more importantly, in the formation of stable films - the first step towards a study of potential applications of the system consisting of chitosan / xanthan layers as a carrier of drugs and their controlled release.

REFERENCES

1. V. Gunjkar, S. Patwekar and S. Dhage, *WJPPS* **4**, 216 (2015).
2. M. Yin, B. Huang, S. Gao, A. P. Zhang and X. Ye, *Biomed. Opt Express*, **7**, 2067 (2016).
3. E. Poverenov, S. Danino, B. Horev, R. Granit, Y. Vinokur and V. Rodov, *Food and Bioprocess Tech*. **7**, 1424 (2014).
4. C. Detzel, A. Larkin, P. Rajagopalan, *Tissue Eng: Part B Rev.*, **17** 101(2011).
5. J. F. Mano, G. A. Silva, H. S. Azevedo, P. B. Malafaya, R. A. Sousa, S. S. Silva, L. F. Boesel, J. M. Oliveira, T. C. Santos, A. P. Marques, N. M. Neves, R. L. Reis, *J. R. Soc. Interface* **4**, 999 (2007).
6. D. Wu, T. Delair, *Carbohydrate Polymers*, **119**, 149 (2015).
7. W. Yuan, H. Dong, C. M. Li, X. Cui, L. Yu, Z. Lu, Q. Zhou, *Langmuir*, **23,** 13046 (2007).
8. S. Argin-Soysal, P. Kofinas, Y. Martin Lo, *Food Hydrocolloids*, **23**, 202 (2009).
9. S. T. Koev, P. H. Dykstra, X. Luo, G. W. Rubloff, W. E. Bentley, G. F. Payne, R. Ghodssi, *Lab Chip*, **10**, 3026 (2010).
10. I. S. Benny, V. Gunasekar, V. Ponnusami, *Int.J. PharmTech Res.*, **6**, 1322 (2014).
11. K. A. Marx, *Biomacromolecules*, **4**, 1099 (2003).
12. A. Martínez-Ruvalcaba, E. Chornet, D. Rodrigue, *Carbohydr. Polym.*, **67**, 586 (2007).
13. F. Ahmadi, Z. Oveisi, S. Mohammadi Samani, Z. Amoozgar, *Res. Pharm. Sci.*, **10**, 1 (2015).
14] N. Popa, O. Novac, L. Profire, C. Lupusoru, M. Popa, *J. Mater. Sci.: Mater. Med.*, **21**, 1241 (2010).
15. T. Phaecham.d, *TJPS*, **3**, 1 (2008).
16. Mohamed Hassan G Dehghan*a*, Marzuka Kazi*b*, *Iran. J. Pharm. Res.*, **13**, 769 (2014).
17. S. Dimitriu, P. Magny, D. Montané, P.F. Vidal, E. Chornet, *J. Bioact. Compat. Polym*, **9**, 184 (1994).
18. S. Dimitriu, E. Chornet, P.F. Vidal C. Moresoli, *Biotechnol. Tech*., **9**, 833 (1995).
19. D. Magnina, J. Lefebvreb, E. Chorneta, S. Dumitriu, *Carbohydr. Polym.*, **55**, 437 (2004).
20. A. Viraneva, M. Marudova, S. Sotirov, I. Bodurov, B. Pilicheva, Y. Uzunova, G. Exner, Ts. Grancharova, I. Vlaeva, T. Yovcheva, *AIP Conf. Proc.*, **1722**, 220025 (2016).
21. Y. Liu, Y. Li, S. Liu, J. Li, S. Yao, *Biomaterials,* **25**, 5725 (2004).
22. G. Sauerbrey, *Z. Für Phys*., **155**, 206 (1959).
23. L. Richert, P. Lavalle, E. Payan, X. Z. Shu, G. D. Prestwich, JF Stoltz,| P. Schaaf, JC Voegel, C. Picart, *Langmuir*, **20**, 448 (2004).
24. P. Lavalle, C. Picart, J. Mutterer, C. Gergely, H. Reiss, JC. Voegel, B. Senger, P. Schaaf, *J. Phys. Chem. B*, **108,** 635 (2004).

In situ ИЗСЛЕДВАНЕ НА ОТЛАГАНЕТО СЛОЙ ПО СЛОЙ НА ТЪНКИ ПОКРИТИЯ ОТ ХИТОЗАН/КСАНТАН ЧРЕЗ КВАРЦОВО КРИСТАЛНА МИКРОВЕЗНА

Сп. А. Янева[1], Г. Е. Алексиева[2], Цв. С. Велинов[2]

[1]Химикотехнологичен и металургичен университет, Катедра "Основи на химичната технология", бул. „Св. Климент Охридски, 8, 1756, София, България.
[2]Софийски университет, Катедра "Физика на твърдото тяло и микроелектроника", бул. Джеймс Баучер 5, 1164, София, България.

(Резюме)

За получаване на многослойни филми от природните полиелектролити хитозан и ксантан е използвана техниката „слой по слой". Нарастването на филма се регистрира чрез кварцово кристална микровезна. При формиране на многослойните структури се наблюдава експоненциално нарастване като при това част от натрупаната маса се отмива от буфера. Това се обяснява с наличието на „свободни" хитозанови молекули, които проникват в целия многослоен филм, в следствие на разликата в химичния потенциал в и извън филма.

При включването на глутаров алдехид като омрежващ агент се наблюдават значителни разлики при нарастването на филма. Първо, омрежените хитозанови слоеве стават непроницаеми за „свободните" молекули. По този начин всеки слой взаимодейства само с двата му съседни слоя, а филмът нараства линейно. Също така омрежването прави филмите достатъчно стабилни, за да не бъдат отмивани при отлагането на следващите слоеве.

Electronic polarizability, optical basicity and chemical bonding of zinc oxide-barium oxide-vanadium oxide glasses

T. R. Tasheva*, V. V. Dimitrov

Department of Silicate Technology, University of Chemical Technology and Metallurgy,
8, Kl. Ohridski Blvd., Sofia 1756, Bulgaria

Glasses with compositions $xZnO.(35-x)BaO.65V_2O_5$ (x= 1, 3, 5, 7, 10, 15 and 20 mol%) were prepared using a conventional melt quenching method. XRD, DTA and DSC analysis were performed. The results of XRD analysis confirm amorphous nature of the samples. The ternary glasses possess low glass transition temperatures T_g and crystallization temperatures T_x. The measured density decreases with increase of ZnO content from 3.974 g/cm^3 to 3.245 g/cm^3. The theoretical refractive index, electronic oxide ion polarizability and optical basicity of the glasses were calculated by Lorentz-Lorenz equation. The glasses were found to possess high refractive index (2.112-2.421), high electronic oxide ion polarizability (2.692-2.725 $Å^3$) and high optical basicity (1.050-1.057). The third order nonlinear optical susceptibility $\chi^{(3)}$ was determined by generalized Miller's rule. It was established that $\chi^{(3)}$ is high in the 0.58-2.24x10^{-12} esu range. The average single bond strength B_{M-O} and interaction parameter $A(n_o)$ were calculated. The bond strength was found to vary from 251 to 253 kJ/mol and interaction parameter was in the 0.049-0.053 $Å^{-3}$ range, thus suggesting the presence of weak chemical bonds. Such bonds, namely Ba$^{...}$O=V, V-NBO (nonbridging oxygen), V-O-Zn and V-O-V were confirmed by IR-spectra of the glasses. The high polarizability of the oxide ions in these bonds accounts for the observed linear and nonlinear optical properties of the glasses. A structural model of glasses containing VO_5, VO_4 and ZnO_4 groups is proposed.

Keywords: oxide glasses, refractive index, electronic polarizability, optical basicity, chemical bonding, IR spectra, nonlinear optical materials

INTRODUCTION

One of the most important properties of materials, which is closely related to their applicability in the field of optics and electronics, is the electronic polarizability of ions. It demonstrates the ease of deformation of their electronic clouds by the application of an electromagnetic field. It is closely related to interionic interactions as well as to many properties of the materials such as refraction, conductivity, electro-optical effect, ferroelectricity, optical basicity along with optical nonlinearity [1-4]. An estimate of the state of polarization of ions is obtained using the so-called polarizability approach based on the Lorentz-Lorenz equation [5]. The polarizability approach was systematically developed in our recent investigations concerning the origin of electronic ion polarizability and optical basicity of numerous simple oxides and oxide glasses [6-8].

According to the pioneering studies of Duffy and Ingram [9], the bulk optical basicity, Λ, of an oxide medium is a numerical expression of the average electron donor power of the oxide species constituting the medium and can be a measure of the acid-base properties of oxides, glasses, alloys, slags, molten salts, etc.

V_2O_5 containing oxide glasses are non-conventional group vitreous materials and their electronic conductivity and semiconducting properties are well known [10, 11]. Recently, the optical properties of vanadate glasses have attracted much attention because of possible application in the field of nonlinear optics. The nonlinear optical properties of V_2O_5 thin film and TeO_2-V_2O_5 bulk glasses have been investigated and high values of the third order nonlinear optical susceptibility $\chi^{(3)}$ have been obtained [12, 13]. Also recently, $\chi^{(3)}$ of BaO-V_2O_5, Fe_2O_3-BaO-V_2O_5, B_2O_3-BaO-V_2O_5 and TiO_2-BaO-V_2O_5 glasses has been predicted [14-16]. The obtained values of $\chi^{(3)}$ based on experimental data and predicted data are rather large, indicating that such glasses are interesting materials for non-linear optical devices.

On the other hand ZnO possess interesting mechanical, thermal, electrical and optical properties. That is why today ZnO-based materials and devices including magnetic semiconductors, light emitting devices, photodiodes, metal-isulator-semiconductors, transparent thin-film transistors and nanostructures are very attractive [17]. Simultaneously, the oxide glasses containing high ZnO content seem also promising materials from

* To whom all correspondence should be sent:
E-mail: tina.tasheva@gmail.com

optical nonlinearity point of view. For example, Ticha et al. have reported high values of nonlinear refractive index for $PbO-ZnO-P_2O_5$ glasses [18]. Recently, Zawadzka et al. have measured second and third harmonic generation of ZnO thin film for NLO applications and obtained high values for nonlinear optical susceptibility [19].

That is why it is of scientific and practical interest to check the together influence of V_2O_5 and ZnO on the optical properties of the glasses. In this connection the purpose of the present study is to investigate the electronic oxide ion polarizability that is optical basicity, interaction parameter and average single bond strength of $ZnO-BaO-V_2O_5$ glasses and have looked for some intrinsic relationship between them and predicted third order nonlinear optical susceptibility. The correlation with the structure of the glasses has been also estimated.

EXPERIMENTAL

Glasses with composition of $xZnO.(35-x)BaO.65V_2O_5$ (x= 1, 3, 5, 7, 10, 15 and 20 mol %) were prepared by using a conventional melt-quenching method. Chemical powders of reagent grade ZnO, V_2O_5 and $BaCO_3$ were mixed together and melted in a porcelain crucible at 900 – 950℃ in an electric furnace for 15 min. The melts were poured onto an aluminum plate and pressed to thickness of 1-2 mm by another copper plate.

Densities of the glasses at room temperature were determined by pycnometer using distilled water as immersion liquid. The IR-spectra of glasses were recorded in the 2000 – 400 cm^{-1} range by using FT-IR spectrometer Varian 600-IR. The samples for these measurements were prepared as KBr – discs. The precision of the absorption maxima was ± 3 cm^{-1}. DSC curves were made at 10 ℃/min using STA PT 1600 TG-DTA/DSC LINSEIS Messgerate GmbH calorimeter. The glass transition temperature T_g and crystallization temperature T_x were estimated from the DSC curves. The amorphous nature of the samples was identified using X-Ray diffractometer Philips APD15 Cu k_α graphite monochromator.

RESULTS AND DISCUSSION

Density, X-ray diffraction and DSC/DTA analysis

The obtained results of the density of the glass samples are presented at Table 1, column 2. As can be seen with increasing ZnO content the density decrease from 3.974-3.245 g/cm^3.

X-ray diffraction investigation of the studied glasses reveals no diffraction peaks and the results indicate that the prepared samples were of high quality glasses. An example of X-ray diffraction

pattern of $5ZnO.30.BaO.65V_2O_5$ glass is presented in Fig. 1.

The values and compositional dependence of the glass transition temperature T_g and the crystallization temperature T_x of $ZnO-BaO-V_2O_5$ glasses were similar to each other. The glasses possess low glass transition temperatures T_g of 262° – 303 ℃ and crystallization temperatures T_x of 315° – 372℃. For example the DTA and DSC curves of glass with composition $5ZnO.30BaO.65V_2O_5$ are shown in Fig. 2. As can be seen T_g is 299 ℃ and sharp exo effect corresponding to Tx exist at 372 ℃. At the same time the difference $\Delta T = T_x - T_g$ is small in the 50 - 73 ℃ range which indicates for low thermal stability of $ZnO -BaO-V_2O_5$ glasses. Recently, similar results were obtained for $B_2O_3-BaO-V_2O_5$ and $TiO_2-BaO-V_2O_5$ glasses [15,16].
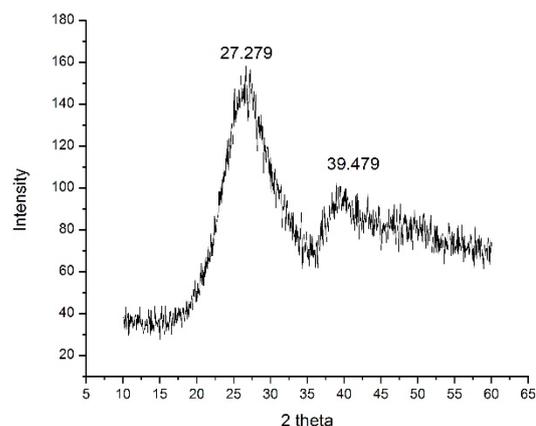
Fig. 1. XRD pattern of glass with composition $5ZnO.30BaO.65V_2O_5$.
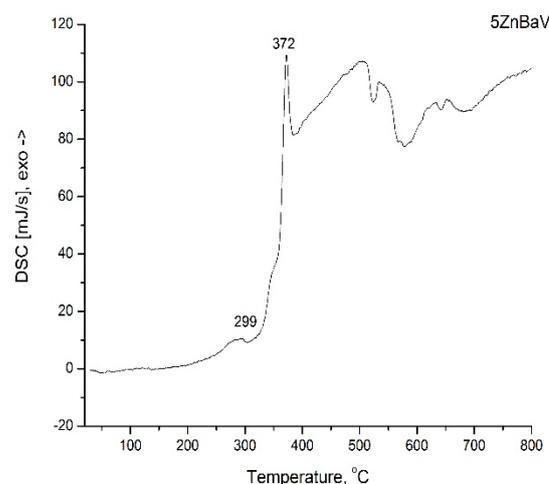
Fig. 2. DSC curve of glass with composition $5ZnO.30BaO.65V_2O_5$.

Table 1. Composition, density d, molar mass M, molar volume V_m , optical basicity Λ_{th}, electronic oxide ion polarizability αo^{2-} and molar refractivity R_m of ZnO-BaO-V_2O_5 glasses

Composition	d, g/cm^3	M, g/mol	V_m	Λ_{th}	αo^{2-}, Å^3	R_m
1ZnO.34BaO.65V_2O_5	3.974	171.17	43.07	1.057	2.725	26.63
3ZnO.32BaO.65V_2O_5	3.928	169.73	43.21	1.056	2.721	26.56
5ZnO.30BaO.65V_2O_5	3.852	168.29	43.69	1.056	2.718	26.50
7ZnO.28BaO.65V_2O_5	3.591	166.86	46.47	1.055	2.714	26.43
10ZnO.25BaO.65V_2O_5	3.415	164.70	48.23	1.054	2.709	26.33
15ZnO.20BaO.65V_2O_5	3.337	161.10	48.28	1.052	2.701	26.17
20ZnO.15BaO.65V_2O_5	3.245	157.51	48.54	1.050	2.692	26.00

Application of polarizability approach to ZnO-BaO-V_2O_5 glasses

Electronic polarizability and optical basicity of ZnO-BaO-V_2O_5 glasses

Determination of electronic oxide ion polarizability is an object of so called polarizability approach. Polarizability approach in glass science is based on the Lorentz-Lorenz equation which relates molar refraction R_m to refractive index n_o and molar volume V_m of the substance by,

$$R_m = \frac{n_0{}^2-1}{n_0{}^2+2}.V_m \qquad (1)$$

$$R_m = 2.52(\sum\alpha_i + N\alpha_{O^{2-}}) = 2.52\,(a.\,\alpha_{Zn^{2+}} + b.\,\alpha_{Ba^{2+}} + c.\,\alpha_{V^{5+}} + N.\,\alpha_{O^{2-}}) \qquad (3)$$

where $\sum\alpha_i$ denotes molar cation polarizability, $\alpha_{Zn^{2+}}$, $\alpha_{Ba^{2+}}$ and $\alpha_{V^{5+}}$ are cation polarizabilities of Zn^{2+}, Ba^{2+} and V^{5+} respectively, $\alpha_{O^{2-}}$ is electronic oxide ion polarizability, *a, b, c* are numbers of cations and *N* is number of oxide ions in one molecule of glass. According to [6] the cation polarizabilities are: $\alpha_{Zn^{2+}} = 0.283$ Å^3 ; $\alpha_{Ba^{2+}}= 1.595$ Å^3 ; $\alpha_{V^{5+}} = 0.122$ Å^3.

The electronic oxide ion polarizability $\alpha_{O^{2-}}$ which participate in Eq. 3 we have calculated from theoretical optical basicity Λ_{th} of ZnO-BaO-V_2O_5 glasses in accordance with the approach proposed by Duffy and Ingram [20]:

$$\Lambda_{th} = X_{ZnO}\Lambda_{ZnO} + X_{BaO}\Lambda_{BaO} + X_{V_2O_5}\Lambda_{V_2O_5}, \qquad (4)$$

where X_{ZnO}, X_{BaO} and $X_{V_2O_5}$ are equivalent fractions based on the amount of oxygen contributed by each oxide to the overall glass stoichiometry, Λ_{ZnO}, Λ_{BaO} and $\Lambda_{V_2O_5}$ are optical basicities of individual oxides (Λ_{ZnO}=1.08; Λ_{BaO}=1.22 and $\Lambda_{V_2O_5}$=1.04 [7,21]).

On the basis of an intrinsic relationship between electronic polarizability of the oxide ions $\alpha_{O^{2-}}$ and

This equation gives the average molar refraction of isotropic substances, i.e., for liquids, glasses and cubic crystals. R_m can be expressed as a function of molar polarizability α_m. With α_m in (Å^3) the following equation can be used,

$$R_m = 2.52\alpha_m \qquad (2)$$

Assuming that molar polarizability α_m of a glass is additive quantity, it follows that for ternary oxide glass with general molar formula xZnO.(0,35-x)BaO.0,65V_2O_5 the molar refraction could be presented as follows,

optical basicity of the oxide medium Λ, proposed by Duffy [22] the oxide ion polarizability can be calculated by using this equation:

$$\alpha_{O^{2-}} = \frac{1,67}{1,67-\Lambda} \qquad (5)$$

Using the obtained basicity data with Eq. (4) the oxide ion polarizability $\alpha_{O^{2-}}$ of ZnO-BaO-V_2O_5 glasses was determined my means of Eq. (5). On the basis of the data for oxide ion polarizability the molar refraction R_m of the glasses was calculated using Eq. (3). The molar volume V_m was estimated on the basis of the molar mass and density of the glasses. The data for molar volume V_m, theoretical optical basicity Λ_{th}, oxide ion polarizability $\alpha_{O^{2-}}$ and molar refraction R_m are listed in Table 1. It is seen that the glasses possess high optical basicity (~1) and high electronic oxide ion polarizability (2.725 - 2.692 Å^3) which indicate for their basic nature.

Refractive index of ZnO-BaO-V_2O_5 glasses

According to the Lorentz-Lorenz equation the refractive index n_o of the substance can be presented as,

$$n_0 = \sqrt{\frac{V_m + 2R_m}{V_m - R_m}} \qquad (6)$$

We have estimated the theoretical refractive index of ZnO-BaO-V_2O_5 glasses using Eq. 6. The data are listed in Table 2, column 2. As can be seen the glasses possess high values of refractive index in the 2.421-2.112 range. The results shown in Table 2 are in good agreement with experimental data for refractive index of thin films of V_2O_5 (n_o=2.59) [12] as well as crystalline ZnO (n_o=2.008) [6].

Chemical bonding of the glasses

Average single bond strength of the glasses

Based on Sun's fundamental condition of glass formation [23] Dimitrov and Komatsu [24] proposed an approach for calculation of average single bond strength B_{M-O} of oxide glasses using values of single bond strength B_{M-O} for corresponding simple oxides and taking into account the molar part of each oxide in the glass composition. The bond strength of different glasses such as phosphate, silicate,

germanate, tellurite and bismuthate glasses has been estimated [24, 25]. In the case of ZnO-BaO-V_2O_5 glasses the following equation can be used,

$$B_{M-O}= xB_{Zn-O} + yB_{Ba-O} + (1-x-y) B_{V-O} \qquad (7)$$

where B_{Zn-O}, B_{Ba-O} and B_{V-O} are single bond strength of M-O in the corresponding individual oxide (138 kJ/mol for BaO, 151 kJ/mol for ZnO and 313 kJ/mol for V_2O_5 (see Ref. 26)). We have determined the average single bond strength B_{M-O} of the glasses by means of Equation (7). The obtained data are presented in Table 2, column 3. It is seen that with increasing ZnO and decreasing BaO content the single bond strength show small increase from 251.2 to 253.7 kJ/mol. These values of B_{M-O} suggest predominantly ionic character of the bonds in the glass structure. Probably V-NBO, V-O-Zn along with V-O-V chemical bonds are formed in their structure. Similar type of bonds namely Te-NBO, Te-O-Te, Bi-O-M (M=B, P, Si and Ge) and Bi-O-Bi with high ionic contribution are formed in the structure of tellurite and bismuthate glasses [24, 25].

Table 2. Composition, refractive index n_0, single bond strength B_{M-O}, interaction parameter A and third-order nonlinear optical susceptibility $\chi^{(3)}$ of ZnO-BaO-V_2O_5 glasses.

Composition	n_0	B_{M-O}, kJ/mol	A, Å^{-3}	$\chi^{(3)}$ (n_0). 10^{-12}, esu
$1ZnO.34BaO.65V_2O_5$	2.421	251.2	0.049	2.24
$3ZnO.32BaO.65V_2O_5$	2.406	251.5	0.050	2.11
$5ZnO.30BaO.65V_2O_5$	2.372	251.8	0.050	1.84
$7ZnO.28BaO.65V_2O_5$	2.227	252.0	0.050	0.99
$10ZnO.25BaO.65V_2O_5$	2.147	252.4	0.051	0.68
$15ZnO.20BaO.65V_2O_5$	2.133	253.1	0.052	0.64
$20ZnO.15BaO.65V_2O_5$	2.112	253.7	0.053	0.58

Interaction parameter of the glasses

Yamashita and Kurosawa [27] have proposed a general theory of the dielectric constant of simple ionic crystals based on quantum-mechanical treatment of the electronic structure of constituent ions in order to take into account the effect of charge overlapping between neighboring ions. A quantitative measure of this complex interaction is given by the so-called interaction parameter *A*, which in fact for a chosen cation-anion pair represents the charge overlapping of the oxide ion with its nearest positive neighbor. Dimitrov and Komatsu have proposed approach for calculation of the interaction parameter in the case of oxide glasses

[8,26]. According to this approach the interaction parameter of ZnO-BaO-V_2O_5 glasses was calculated by us using the following equation, where X_{ZnO}, X_{BaO} and X_{V2O5} are equivalent fractions based on the amount of oxygen each oxide contributes to the overall glass stoichiometry, α_{O2-} is oxide ion polarizability in the glass and α_{Zn}^{2+}, α_{Ba}^{2+}, and α_{V}^{5+} are cation polarizabilities. Pauling's value of 3.921 Å^3 for the electronic polarizability of the free oxide ion is used. The calculated data of interaction parameter of ternary ZnO-BaO-V_2O_5 glasses are given in Table 2, column 4. The glasses possess small values of the interaction parameter in

$$A = X_{ZnO} \frac{(3{,}921 - \alpha_{O^{2-}})}{2(\alpha_{Zn^{2+}} + 3{,}921)(\alpha_{O^{2-}} + \alpha_{Zn^{2+}})} + X_{BaO} \frac{(3{,}921 - \alpha_{O^{2-}})}{2(\alpha_{Ba^{2+}} + 3{,}921)(\alpha_{O^{2-}} + \alpha_{Ba^{2+}})}$$
$$+ X_{V_2O_5} \frac{(3{,}921 - \alpha_{O^{2-}})}{2(\alpha_{V^{5+}} + 3{,}921)(\alpha_{O^{2-}} + \alpha_{V^{5+}})}$$

$$(8)$$

the 0.049-0.053 Å^{-3} range. Small interaction parameter means week interionic interactions resulting in large unshared electron density at one averaged oxide ion. Since both interaction parameter $A(n_0)$ and average single bond strength B_{M-O} are assigned to an average chemical bond M-O in the glass structure, it is of scientific interest to investigate the correlation between them. For that purpose we have plotted the data of interaction parameter A against the data of single bond strength B_{M-O} of ZnO-BaO-V$_2$O$_5$ glasses in Fig. 3. A systematic increase in the interaction parameter with composition corresponds to a systematic increase in the average single bond strength. Simultaneously, the average single bond strength and interaction parameter of the ternary vanadate glasses are close to these of pure V$_2$O$_5$ (B_{V-O}=313 kJ/mol and $A(n_o)$=0.057 Å^{-3}) which means that the interaction along V-O bonds in ternary glasses have significant effect [26].

IR spectra of ZnO-BaO-V$_2$O$_5$ glasses

The IR-spectra of ZnO-BaO-V$_2$O$_5$ are presented in Fig 4. Three well defined maxima at 910 cm^{-1}, 796-774 cm^{-1} and 658 cm^{-1} are outlined in the IR spectra of the glasses with small ZnO (1-5 mol%). A
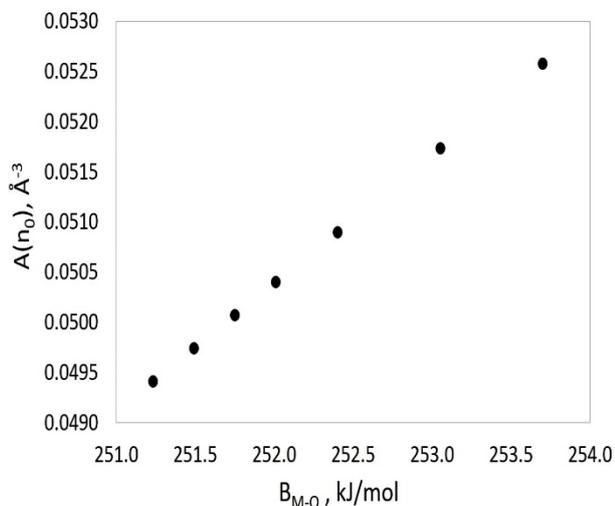
Fig. 3. Interaction parameter as a function of single bond strength of the glasses.

shoulder appears at 972-969 cm^{-1} and the band at 796-774 cm^{-1} disappears in the spectra of glasses containing 7-20 mol% ZnO. At the same time, the intensity of the band at 910 cm^{-1} decreases and the band is shifted to lower frequencies up to 896 cm^{-1}. The assignment of these bonds could be made on the basis of large number of previous results on IR spectra of crystalline and vitreous phases [28-33]. On this basis the band at 910 cm^{-1} is assigned to

symmetrical stretching vibrations $\nu_{VO_2}^s$ of free VO$_2$ groups of the VO$_4$ tetrahedra from (VO$_3$)$_n$ chains
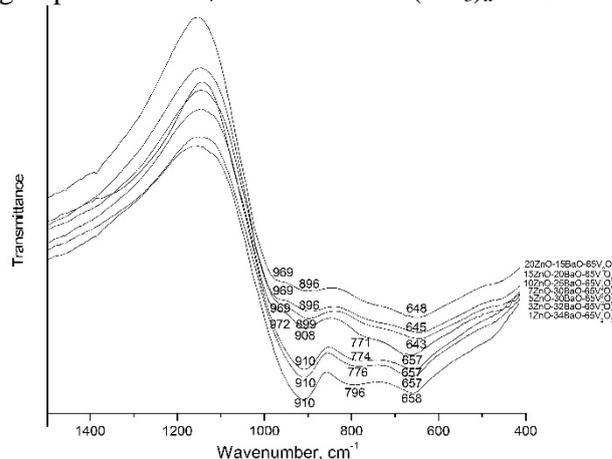
Fig. 4. IR spectra of ZnO-BaO-V$_2$O$_5$ glasses.
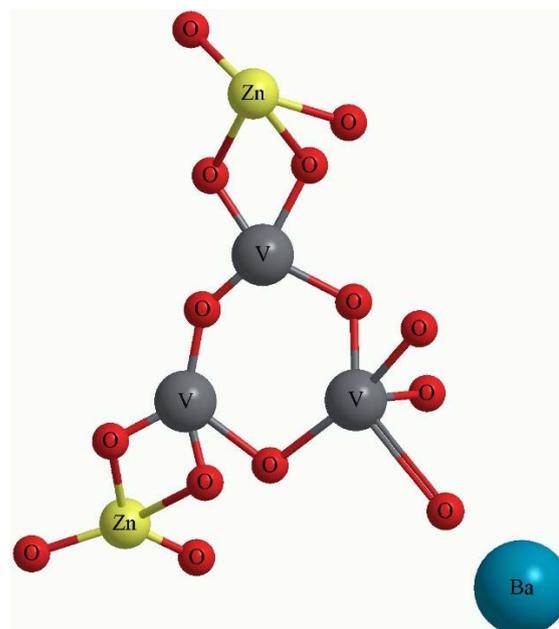
Fig. 5. Structural model for glass with high ZnO content.

while the band at 796-774 cm^{-1} could be attributed to asymmetrical stretching vibrations $\nu_{VO_2}^{as}$ of these groups. The appearance of the shoulder at 972-969 cm^{-1} could be connected with the transformation of part of VO$_4$ tetrahedra into VO$_5$ trigonal bipyramids. VO$_5$ groups are formed in the structure of crystalline and vitreous V$_2$O$_5$. Their IR spectra show band at 1020 cm^{-1}, assigned to the vibrations of isolated V=O bonds in VO$_5$ trigonal bipyramids [28]. According to the mechanism suggested in Ref. 28 Ba^{2+} ions occupy a position between V-O-V layers. This is why they have a direct influence on the isolated V=O bonds of the VO$_5$ groups according to the scheme:

$$Ba^{2+}\cdots O=V^{5+}$$
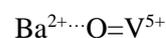
This leads to an elongation of the affected V=O bonds and a drop in the frequency down to 972-969

cm^{-1}. The shift of the band at 910 cm^{-1} to lower frequencies up to 896 cm^{-1} could be explained with formation of V-O-Zn bridging bonds created by the influence of Zn^{2+} ion on non-bridging oxygen from VO$_2$ groups. According to Ref. 33 the band at 658-648 cm^{-1} could be assigned to asymmetrical stretching vibrations ν^{as}_{V-O-V}. At the same time the shift to lower frequencies with increase of ZnO content is probably due to Zn-O vibrations of tetrahedral ZnO$_4$. Such vibrations in the spectra of glasses were reported in the range of 550-400 cm^{-1} [34]. On the basis of obtained IR spectral results we presented in Fig 5 possible structural model of glass with high ZnO content. VO$_4$, VO$_5$ and ZnO$_4$ groups participating in the model. V-O-V, V-O-Zn and Ba$^{2+\cdots}$O=V^{5+} chemical bonds are formed between the groups.

Third order nonlinear optical susceptibility of the glasses

The third order nonlinear susceptibility $\chi^{(3)}$ of ZnO-BaO-V$_2$O$_5$ glasses was estimated by generalized Miller's rule,

$$\chi^{(3)} = \left[\chi^{(1)}\right]^4 . \, 10^{-10}, \, esu \qquad (9)$$

where $\chi^{(1)}$ is linear optical susceptibility, calculated by,

$$\chi^{(1)} = \frac{n_0{}^2 - 1}{4\pi} \qquad (10)$$

The obtained data are presented in Table 2, column 5. ZnO-BaO-V$_2$O$_5$ glasses show high values of the third order nonlinear optical susceptibility in the 0.58-2.24 x 10^{-12} esu range, which is about 100 times larger than that of pure silica glass (2.8x10^{-14} esu). The obtained results are in good agreement with the experimental data obtained by Hashimoto and Yoko [12] for the third order nonlinear optical susceptibility of thin films of V$_2$O$_5$ ($\chi^{(3)}$=1.1x10^{-11} esu). This means that ZnO-BaO-V$_2$O$_5$ glasses are probably good candidates for nonlinear optical applications. Recently, detailed analysis was made on the relationship between electronic oxide ion polarizability and third nonlinear optical susceptibility of different binary oxide glasses [35]. It was established that third nonlinear optical susceptibility $\chi^{(3)}$ of the glasses increases with increasing electronic oxide ion polarizability, that is optical basicity. This is associated with the high electron donor ability of the oxide ion and the high refractive index. In this connection we have plotted the data of the third order nonlinear optical susceptibility $\chi^{(3)}$ as a function of refractive index n$_o$ of ZnO-BaO-V$_2$O$_5$ glasses in Fig. 6. It is seen that $\chi^{(3)}$ increases with increasing the refractive index. The high values of the third order nonlinear optical

susceptibility of ZnO-BaO-V$_2$O$_5$ could be attributed to the presence of V-O-Zn, V-O-V and Ba$^{2+\cdots}$O=V^{5+} bonds in their glass structure. Such bonds were confirmed by the IR spectra. Probably, the high electronic polarizability of the oxide ions in these bonds is responsible for high optical nonlinearity of the glasses.
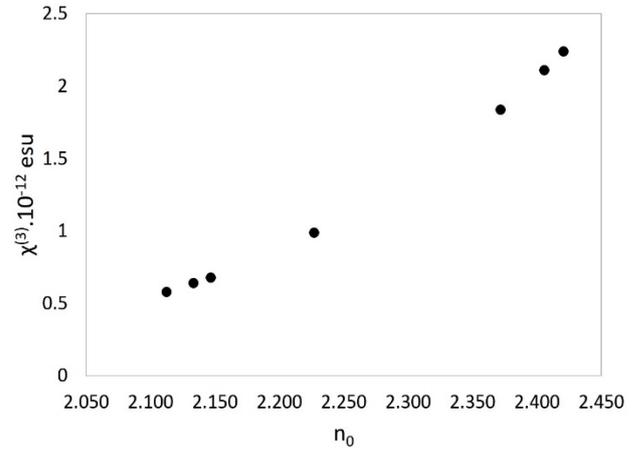
Fig. 6. Third order nonlinear optical susceptibility as a function of refractive index of the glasses.

CONCLUSIONS

Ternary ZnO-BaO-V$_2$O$_5$ glasses have been investigated by means of XRD, DTA and DSC analysis. XRD analysis confirmed amorphous nature of the samples. DTA and DSC analysis show that the glasses possess low glass transition temperatures T$_g$ of 262° – 303 ℃ and crystallization temperatures T$_x$ 315° – 372℃. The experimental density was found to be in 3.974-3.245 g/cm^3 range. The polarizability approach based on Lorentz-Lorenz equation has been applied to ZnO-BaO-V$_2$O$_5$ glasses. With a view to elucidate theoretical refractive index, electronic ion oxide polarizability and optical basicity of the glasses was calculated. It was established that the glasses possess high refractive index (2.421-2.112), high electronic ion polarizability (2.725 - 2.692 Å^3) and high optical basicity (1.050-1.057). The theoretical third order nonlinear optical susceptibility $\chi^{(3)}$ was determined and it was found that the glasses possess high values of $\chi^{(3)}$ in the 0.58-2.24 x10^{-12} range. It was established that the glasses have small single bond strength and interaction parameter, thus suggesting the presence of weak chemical bonds. Such bonds, namely V-O-Zn, V-O-V and Ba$^{2+\cdots}$O=V^{5+} where confirmed by IR spectral analysis of the glasses. The high polarizability of oxide ions in these bonds accounts to the observed linear and nonlinear optical properties of the glasses. Structural model of glass with high ZnO content containing VO$_4$, VO$_5$ and ZnO$_4$ groups is proposed.

REFERENCES

1. C. A. Wert and R. M. Thomson, Physics of Solids, McGraw-Hill, New York, 1964.
2. A. Yarif and P. Yeh, Optical Waves in Crystals, Wiley, New York, 1984.
3. A. R. West, Solid State Chemistry and Applications, Wiley, New York, 1984.
4. M. Yamane, Y Asahara, Glasses for Photonics, Cambridge, University Press, 2000.
5. W. A. Weil, E. G. Marboe, The Constitution of Glasses, Wiley, New York, 1962
6. V. Dimitrov, S. Sakka, *J. Appl. Phys.,* **79**, 1736 (1996).
7. V. Dimitrov, T. Komatsu, *J. Solid State Chem.* **163**, 100 (2002).
8. V. Dimitrov, T. Komatsu, *J. Solid State Chem.* **178**, 831 (2005).
9. J. A. Duffy, M. D. Ingram, *J. Non-Cryst. Solids* **21**, 373 (1976).
10. M. Sayer, A. Mansingh, *Phys. Rev.*, **B6**, 4629 (1972).
11. C. H. Chung, J. Mackenzie, *J. Non-Cryst. Solids*, **42**, 357 (1980).
12. T. Hashimoto, T. Yoko, *Appl. Opt.*, **34**, 2941 (1995).
13. S. H Kim, T. Yoko, *J. Am. Ceram. Soc.*, **78**, 1061 (1995).
14. A. Haralampieva, I. Simeonova-Lozanova, V. Dimitrov *J. Univ.Chem. Technol. Metallurgy*, **47**, 392 (2012).
15. T. Tasheva, V. Dimitrov, *J. Chem. Technol. Metallurgy*, **50 (4)**, 441 (2015).
16. T. Tasheva, V. Dimitrov, *J. Chem. Technol. Metallurgy,* **51 (5)**, 525 (2016).
17. Ü. Özgür, Ya. I. Alivov, C. Liu, A. Teke, M. A. Reshchikov, S. Doğan, V. Avrutin, S.-J. Cho, and H. Morkoç – *J. Appl. Phys.*, **98**, 041301, (2005).
18. H. Ticha, J. Schwarz, L. Tichy, R. Mertens, *J. Optoel. Adv. Mater.* **6(3)**, 747 (2004)
19. A. Zawadzka, P.Plociennik, J. Strzelecki, B. Sahraoui, *Opt. Mater.* **37**, 327 (2014).
20. J.A. Duffy, M.D. Ingram, in Optical Properties of Glass, Eds. D. Uhlman, N. Kreidl, Am. Ceram. Soc., Westervill, 1991.
21. V. Dimitrov, T. Komatsu, *Phys. Chem. Glasses: Eur. J. Glass Sci. Technol. B*, **47**, 638 (2006).
22. J.A. Duffy, *Phys. Chem. Glasses,* **30**, 1, (1989).
23. K. H. Sun, *J. Am. Ceram. Soc.*, *30*, 277 (1947).
24. V. Dimitrov, T. Komatsu, *Phys. Chem. Glasses: Eur.J.Glass Sci. Technol. B,* **46**, 521 (2005).
25. V. Dimitrov, T. Komatsu, *J. Non-Cryst. Solids*, **382**, 218 (2013).
26. V. Dimitrov, T. Komatsu, *J. Univ. Chem. Technol. Metallurgy*., **45**, 219 (2010).
27. J. Yamashita, T. Kurosawa, *J. Phys. Soc. Japan*, **10**, 610 (1955).
28. Y. Dimitriev, V. Dimitrov, M. Arnaudov, D. Topalov, *J. Non-Cryst. Solids*, **57**, 147 (1983).
29. V. Dimitrov, *J. Non-Cryst. Solids* **192&193**, 183 (1995).
30. S. Mandal, SW. Hazra, D. Das, A. Goswh, *J. Non-Cryst. Solids* **183**, 1995, 315-319.
31. R. Punia, R. S. Kundu, J. Hooda, S. Dhankhar, S. Dahiya, NJ. Kishore, *J. Appl. Phys.*, **110**, 033527 (2011).
32. H. R. Panchal, *Turk. J. Phys.* **38**, 136 (2014).
33. Y. Saddeek, E. R. Shaaban, K. A. Aly, I. M. Sayed, *J. Alloys Comp.* **478**, 447 (2009).
34. C. Ruvalcaba-Cornejo, Ma. E. Zayas, S. J. Castillo, R. Lozada-Morales, M. Perez-Tello, C. C. Diaz, J. Ma. Rincon, *Opt. Mat.* **33**, 823 (2011).
35. V. Dimitrov, T. Komatsu, *J. Non-Cryst. Solids* **249**, 160 (1999).

ЕЛЕКТРОННА ПОЛЯРИЗУЕМОСТ, ОПТИЧЕСКА ОСНОВНОСТ И ХИМИЧЕСКО СВЪРЗВАНЕ НА ЦИНК-БАРИЙ-ВАНАДАТНИ ОКСИДНИ СТЪКЛА

Т. Р. Ташева*, В. В. Димитров

Катедра „Технология на силикатите", Химикотехнологичен и металургичен университет, бул. Кл. Охридски 8, София 1756, България

(Резюме)

Стъкла със състави $xZnO.(35-x)BaO.65V_2O_5$ (x= 1, 3, 5, 7, 10, 15 и 20 мол %) бяха синтезирани посредством рязко охлаждане на стопилки. Пробите бяха анализирани посредством рентгеноструктурен и термичен анализ. Резултатите от рентгеноструктурния анализ доказаха аморфната природа на образците. Трикомпонентните стъкла притежават ниски температури на застъкляване T_g и кристализация T_x. Измерената плътност намалява с увеличаване съдържанието на ZnO от 3.974 g/cm^3 до 3.245 g/cm^3. Теоретичния показател на пречупване на светлината, кислородната електронна поляризуемост и оптическата основност на стъклата беше изчислена посредством уравнението на Лорентц-Лоренц. Стъклата притежават висок показател на пречупване (2.112-2.421), висока кислородна електронна поляризуемост (2.692-2.725 $Å^3$) и висока оптическа основност (1.050-1.057). Нелинейната оптическа възприемчивост от трети порядък $\chi^{(3)}$ беше определена посредством Милеровото правило. Беше установено, че стъклата притежават високи стойности за $\chi^{(3)}$ (0.58-2.24x10^{-12} esu). Средната здравина на химичната връзка B_{M-O} и параметъра на междуйонно взаимодействие $A(n_o)$ също бяха изчислени. Здравината на химичната връзка варира в граници от 251 до 253 kJ/mol , а параметъра на междуйонно взаимодействие от 0.049 до 0.053 $Å^{-3}$, което предполага наличието на слаби химични връзки. Такива връзки, а именно Ba…O=V, V-NBO (немостови кислород), V-O-Zn и V-O-V бяха потвърдени с инфрачервена спектроскопия. Високата поляризуемост на кислородните йони в тези връзки е причината за наблюдаваните линейни и нелинейни оптични свойства на стъклата. Предложен е структурен модел на стъкла съдържащи VO_5, VO_4 и ZnO_4 групи.

Assembling and test of a system for determination on site of acid dew point of exhaust flue gas from power steam boilers

K.Ts. Todorov*, R.A. Asenov, A.N. Asenov

Technical University of Sofia, Departament of Thermal and Nuclear Power Engineering, 8 Kl. Ohridski Blvd, 1000 Sofia, Bulgaria

Acid dew point occurs due to decreasing of the temperature of exhaust flue gas from steam boiler in thermal power plant. From other point of view the lower temperature is the main requirement for higher boiler efficiency. When the temperature of flue gasses up to the value of acid dew point, the part of streams are saturated consistent and the acidic gases form liquid acid. This temperature is the thin limit between efficiency and stable operation. Its determination is important to achieve best performance of thermal power plants. Theoretical prediction of acid due point is complicate and includes validation with additional laboratory test. Aim of this study it to assemble system for determination acid dew point, which can be used on site on different power steam boilers. After choosing the appropriate components and their assembling, the system was tested in laboratory condition. The achieved result of 56°C was compared to the data received from three different equations for theoretical prediction of acid dew point. The data comparison proved that the assembled system can operate reliable.

Key words: thermal power plants, performance test, flue gas, acid dew point

INTRODUCTION

As a result, from the combustion process in power steam boilers, are generated exhaust flue gas, which contain mainly carbon dioxide (CO_2), water vapor (H_2O), nitrogen (N_2) and excess oxygen (O_2) remaining from the combustion air. There are few additional gases compounds as carbon monoxide (CO), nitrogen oxides (NOx), sulfur dioxide (SO_2) and sulfur trioxide (SO_3), which has smaller concentrations but bigger environmental impact. At the saturation temperature of the exhaust gas, the acidic gases interact together with the oxygen and the condensed water vapor to compose liquid acids [1, 2] as shown below:

$$SO_2 + H_2O \leftrightarrow H_2SO_3 \qquad (1)$$
$$H_2SO_3 + O_2 \rightarrow H_2SO_4 \qquad (2)$$
$$2SO_2 + O_2 \rightarrow 2SO_3 \qquad (3)$$
$$SO_3 + H_2O \rightarrow H_2SO_4 \qquad (4)$$
$$2NO + SO_2 \rightarrow N_2O + SO_3 \qquad (5)$$
$$NO_2 + SO_2 \rightarrow NO + SO_3 \qquad (6)$$

$$4NO_2 + 2H_2O + O_2 \rightarrow 4HNO_3 \qquad (7)$$
$$NO_2 + SO_2 + H_2O \rightarrow H_2SO_4 + NO \qquad (8)$$
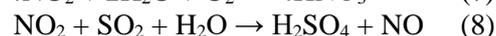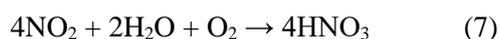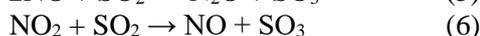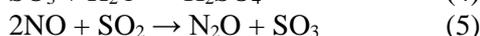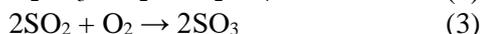
All those reactions lead to a very complex gaseous system. From other point the particular composition of the flue gas depends on the organization of the combustion process, which is preconditioned by the combustion system and fuel properties.

There are a lot of studies for theoretical prediction of acid dew point of exhaust flue gas. The five equations below were developed from different authors with the aim to determine theoretically flue gas acid point:

According Ohtsuka [3]

$$t_D = 20 \lg V + A \qquad (9)$$

A : constant depending on moisture content (°C) - 184 at 5 %, 194 at 10 %, 201 at 15 %.

Neubauer's equation [4]

$$t_D = t_S + (290.54 - 30.79 p_{H2O})\, p_{SO_2}^{\left(0.0959 + 0.143 p_{H2O} - 0.1669 p_{H2O}^2\right)} \qquad (10)$$

According Mueller [5] / Pierce [6] / Okkes [7]:

$$t_D = 203.25 + 27.6 \lg(p_{H2O}) + 10.83 \lg(C\, p_{SO2}) + 1.06\{\lg(C\, p_{SO2}) + 8\}^{2.19} \qquad (11)$$

Verhoff & Banchero [8] relation for acid dew point prediction:

$$T_D = 10000 / [15.13 - 0.2943 \ln(p_{H2O}) - 0.858 \ln(C\, p_{SO2}) + 0.062\,\{6.633 - \ln(C\, p_{SO2})\}\,\{6.633 - \ln(p_{H2O})\}] \qquad (12)$$

---

* To whom all correspondence should be sent:
E-mail: krum.ts.todorov@gmail.com

Haase and Borgmann [9] equation for acid dew point:

$$t_D = [255 + 27.6\,\lg(p_{H2O}) + 18.7\,\lg(C\,p_{SO2})] \quad (13)$$

where:

- T_D : Dew-point temperature (K)
- t_D : Dew-point temperature (°C)
- t_S : Saturation temperature of water at total pressure of exhaust flue gas (°C)
- C : Conversion rate of SO_3 from SO_2 by volume
- p_{SO2} : mole fraction of SO_2, equivalent to partial pressure (in atm) with the mixture of gases at standard atmospheric pressure (101.325 kPa)
- p_{H2O} : mole fraction of water, equivalent to partial pressure (in atm) with the mixture of gases at standard atmospheric pressure (101.325 kPa)
- V : H_2SO_4 concentration (vol %)

According to above equations there are cases where the results for acid dew point evaluated by them have difference of 20° K [2]. This shows that theoretical determination of temperature of acid dew point depends on many factors as: exhaust flue gas content and conditions in the duct, even from fuel quality and combustion process organization. So the proved way to evaluate acid dew point of flue gas is to assembly a measuring system, which may be used on site at different boilers, independently of the fuel used and the combustion process organization.

EXPERIMENTAL

Assessment of acid dew point of flue gas requires measurement of the temperature of a cooled surface at the moment when a liquid aced appears over it. Measuring principle of the constructed sensor is demonstrated on Figure 1.
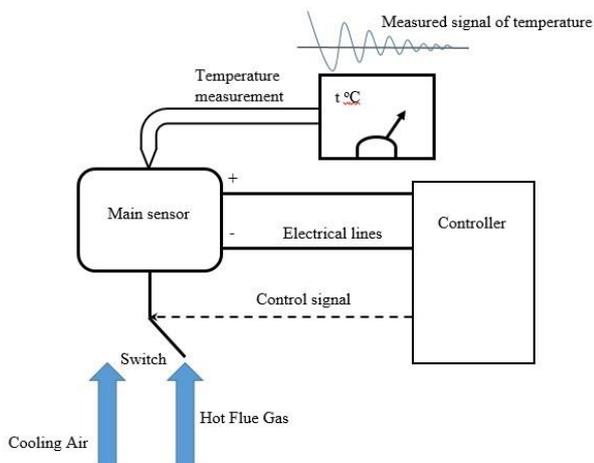
Fig. 1 Principle of measurement of acid dew point.

The main sensor gives two signals. The first is for the temperature measurement and the second is for existence of liquid acid. The signal of acid appearance is registered from a controller, which switch the main flow to hot flue gas pass over the sensor if it is necessary to increase temperature or switch to ambient air – to cool the sensor from the outside. The result of this regulatory process is temperature deviation around the acid dew point to the moment of achieving stable value.

Main elements of the acid dew point measuring system are presented on Figure 2. The operational principle of the system, is sampling exhaust flue gas from the duct and analyzing it to determine the acid dew point.
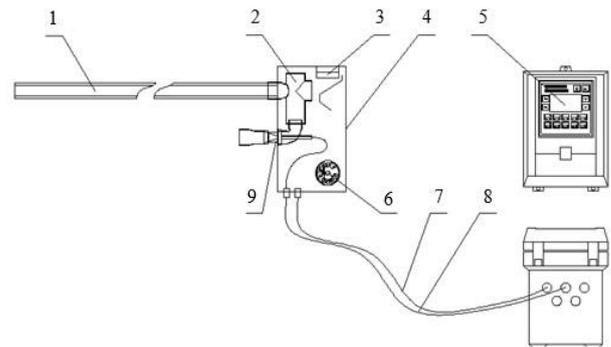
Fig. 2 Acid dew point measurement system: 1 – Ceramic sampling probe, 2 – Ceramic conductive sensor, 3 – Cooling fan,4 – Sensor's unit, 5 – Control unit, 6 – Transmitter TMT 181, 7 – Air supply line, 8 – Electrical line, 9 – Pneumatic ejector.
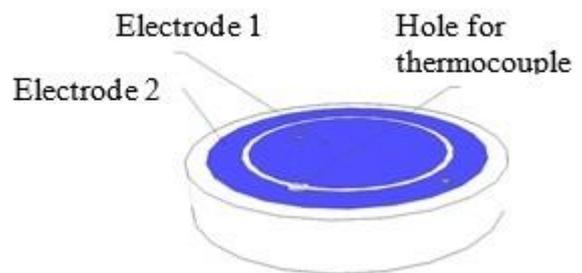
Fig. 3 Ceramic sensor.

The acid dew point measuring system includes a ceramic pad with metal overlay - Fig. 3, which forms two electrodes. Ceramic sensor (2) is attached tight to a metal tube with good seal to prevent leakage of ambient air. There is a small hole, 1mm in diameter, into the pad for mounting the thermocouple, and seal it with clay. Outer surface of the pipe is thermally isolated, except the back side of the sensor, because it has to be cooled by the cooling fan (3).

For the purpose of this system is used an FTW 325 electrical unit [10], which is very sensitive to condensate formation. It can detect condensation, which is not visible for the human eye. The electrical unit provides AC with frequency of 20 Hz, which prevents electrodes destruction.

Temperature measurement is assured by a J-type thermo-electrical thermometer. This thermocouple can measure temperature in the range -200…1200°C. The thermocouple is connected to a TMT 181 temperature transmitter, produced by E&H [11]. Its role is to convert the raw signal from thermometer to a unified electrical signal of 4…20mA.

To increase the accuracy of the measuring system it is important to select a thermo-sensitive element with small inertia. In other case, there is a risk to read data different from the real temperature of the sensor.

In assembled system was used programmable logical controller – Vision 120-R1 [12]. It is responsible for reading both the temperature sensor and condensation detector, and manages the PID regulator, which controls the temperature of the ceramic pad, by switching on and off the cooling fan.
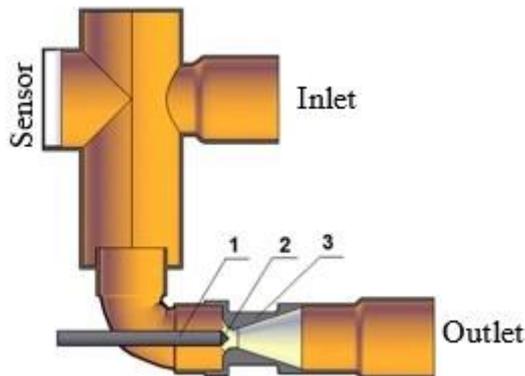
Fig. 4 Sampling unit.

One of the main components of the system is the sampling unit - Fig. 4. It contains an ejector, by which part of the exhaust flue gas is directed toward the ceramic sensor.

The ejector works with compressed air, provided by a compressor, external to the sampling unit. The air enters the pipe (1), through a nozzle (2) and is lead into a Laval nozzle (3). The high speed of the air flow expires within the Laval nozzle result to static pressure drop. Obtained by Laval nozzle dilution in necessary to compensate linear and local pressure loses through sampling system. The quantity of the collected flue gas depends on the compressed air flow rate. So compressor operation is managed by a Vision 120-R1 controller.

The assembled flue gas acid dew point measuring system gas was tested in the laboratory for Heat and Gas Supply - Fig.5 in department "Thermal and Nuclear Power Engineering" in Technical University of Sofia.

For the test was used RIELLO gas boiler with 24 kW thermal power. The combustion chamber and the burner, which are responsible for organization of the combustion process, are shown on Fig. 5b.

The acid dew point test is conducted ten times, at different setting for the hysteresis cycle of gas sampling and sample cooling, controlled by Vision 120-R1. Received data are statistically analyzed and an average value for acid dew point is estimated.

RESULTS AND DISCUSION

After conducting tests for determination of acid dew point of exhaust flue gas from laboratory boiler, achieved result was compared with data from equations 10, 12 and 13, for theoretical prediction of the same temperature. Other two equations 9 and 11 are not used, because they are appropriate for flue gas with high sulphur concentration. Comparison of the results from the test and the one calculated by the equations are shown above in Table 1.

Table 1. Comparison between laboratory test and theoretical equations.

Method	Lab. test	Haase&Borg.	Verh.&Banch.	Neubauer
Value	56°C	41°C	48°C	68°C

After the analysis of compared data from Table 1, the conclusion is that the assembled measurement system for determination of acid dew point of exhaust flue gas works properly. This fact proves that it can be used to provide determination on site of acid dew point.

Outlook

To achieve on site tests at different power steam boilers, with different fuels, respectively different combustion process conditions and flue gas content.

REFERENCES

1. S. Boycheva, System and Devices for Environmental Protection, ISBN: 978-954-438-895-9, Technical University of Sofia Press, 2011.
2. IAPWS Certified Research Need – ICRN 23, Dew Point for Flue gas of Power-Plant Exhaust, 2012.
3. T. Ohtsuka, 1961: CRIEPI report, Chemical 61001.
4. W. Gumz, Kurzes., 1962: Handbuch der Brennstoff- und Feuerungstechnik, Heidelberg, Springer-Verlag.
5. P. Mueller, *Chemie-Ing-Techn.*, **31**, 345 (1959).
6. R.R. Pierce, *Chem. Eng.*, **84**, 125 (1977).

7. A.G. Okkes, *Hydrocarbon Processing*, **66**, 53 (1987).
8. F.H. Verhoff, J.T. Banchero, *Chem. Eng. Prog*., **70**, 71 (1974).
9. R. Haase, H.W. Borgmann, *Korrosion*, **15**, 47 (1981).
10. Technical Information, TI 373F/00/en, http://www.endress.com;
11. Technical Information, TI00070R/09/en, http://www.endress.com
12. Vision 120 Graphic Operator Panel & Programmable Logic Controller, User Guide, V120-21-G1, http://unitronicsplc.com/vision-series-vision120/

АСЕМБЛИРАНЕ И ТЕСТВАНЕ НА СИСТЕМА ЗА ОПРЕДЕЛЯНЕ НА МЯСТО ТОЧКАТА НА РОСАТА НА ИЗХОДЯЩИ ДИМНИ ГАЗОВЕ ОТ ЕНЕРГИЙНИ ПАРОГЕНЕРАТОРИ

Кр. Ц. Тодоров*, Р. А. Асенов, Ас.Н. Асенов

Технически университет – София, катедра „Топлоенергетика и ядрена енергетика“, бул. „св. Кл. Охридски“ №8, София 1000, България

(Резюме)

Кондензацията на водните пари и газообразните киселини резултат от горивния процес при енергийни парогенератори настъпва при понижаване на температурата на отпадните димни газове. Нуждата от по-ниски температури е продиктувана от стремежа за повишаване на ефективността на котлите. Точката на росата представя температурата, при която започва формирането на киселини в течна фаза. Тази температура представлява тънката граница между ефективност и надеждна експлоатация. Нейното определяне е необходимо за да се постигне оптимална работа, на една ТЕЦ. Определянето на точката на росата чрез теоретични зависимости е сложно и включва провеждане на допълнителни лабораторни тестове за доказване на получените резултати. Целта на настоящото изследване е да се асемблира система за определяне точката на росата, която да може да бъде използвана на място при различни енергийни парогенератори. След като бяха избрани подходящи елементи за асемблиране, системата беше тествана в лабораторни условия. Полученият резултат от 56ºC беше съпоставен с данни от различни теоретични зависимости за определяне точката на росата. Сравнението на данните доказа, че асемблираната система може да работи надеждно.

Optimization of optical and sensing properties of sol-gel oxides through zeolite doping

K. Lazarova[1]*, H. Awala[2], J. El Fallah[2], M. Vassileva[1], S. Mintova[2], T. Babeva[1]

[1]Institute of Optical Materials and Technologies ''Acad. J. Malinowski'', Bulgarian Academy of Sciences, Acad. G. Bonchev str., bl. 109, 1113 Sofia, Bulgaria.

[2]Laboratoire Catalyse et Spectrochimie, Normandie Université, ENSICAEN, CNRS, 6 boulevard Maréchal Juin, 14050 Caen, France

The modification of the optical and sensing properties of Nb_2O_5 and SiO_2 oxides thin films through doping with nanosized zeolite crystals with MFI and EMT- types framework was studied. Thin films of pure oxides and oxo-zeolite composites consisting of oxide matrix embedded with zeolites were deposited by spin-coating method using pre-synthesized metal sols and colloidal stable zeolite suspension mixed at the desired ratios and subjected to post-deposition annealing. The surface morphology of the films and their optical properties were investigated by SEM and UV-VIS-NIR spectroscopy, respectively. The sensing behavior was studied by measuring the reflectance spectra before and after exposure to probe molecule (acetone vapors) and successive calculation of the changes in effective refractive index due to vapor condensation in the porous films. The potential of the developed materials for optical sensing applications is discussed.

Keywords: sol-gel materials; nanosized zeolites; films; optical properties; optical sensing.

INTRODUCTION

Enhanced performance, low manufacturing cost, simple processing and possibility for integration in different devices are essential preconditions for novel materials to be used in advanced technologies. In this context, the solution processed metal oxides have increasingly attracted scientific interest due to their potential applications for improving the performance of different devices such as Bragg gratings, optical filters, photonic crystals, sensors etc. [1-3].

Among these applications, the optical sensing is highly promising and it has also been intensively studied [4,5]. The idea behind the sensing is the change of refractive index of the oxide due to capillary condensation of vapors inside the pores. Therefore the generation of well-defined and interconnected pore system inside the oxide film is essential for its sensing application. Two general approaches have been reported in the open literature for porosity creation, each one with its pros and cons. In the first approach, porosity has been generated using sacrificing organic template which after its removal through an appropriate annealing or chemical treatment leaves interconnected or closed pores inside the films [6]. Alternatively, thin films with different porosity have been fabricated using suspensions of nanoparticles in different aggregation states [7].

In this paper, a different approach for porosity generation via using zeolites nanocrystals as dopants for dense metal oxide matrix is applied. The approach is similar to the one already used for preparing meso-structured silica films containing nanosized zeolite [8] and silica / zeolite composites [9]. Since zeolites are crystalline materials with well-defined ordered micropore structure on the molecular scale it is expected that their intrinsic microporosity will introduce additional porosity in the sol-gel oxide thus improving oxide-sensing properties. Besides, due to the low refractive index of zeolites [10] it is anticipated that the effective refractive index of oxo-zeolite composite can be tuned in wide range when matrix with high refractive index such as Nb_2O_5, V_2O_5 oxides is used [11, 12]. This will allow production of multilayered structures such as Bragg stacks where the same material with different doping level, i.e. different porosity can be used for achieving significant optical contrast instead of alternation of different materials thus overcoming the incompatibility issues.

Herein we report the optimization of optical sensing properties of Nb_2O_5 and SiO_2 oxides films through doping with EMT and MFI-type zeolite nanocrystals. Pre-synthesized metal sols and colloidal stable zeolite suspension were mixed together at the desired volume ratios and used for the preparations of thin films by spin-coating method. The optical and sensing properties are studied by measuring of reflectance spectra. The potential of the developed materials for optical

---

* To whom all correspondence should be sent:

E-mail: klazarova@iomt.bas.bg

sensing applications is demonstrated.

EXPERIMENTAL

Nb-sol was prepared by a sonocatalytic method using 0.40 g $NbCl_5$ (99%, Aldrich) as a precursor, 8.3 ml ethanol (98%, Sigma-Aldrich) and 0.17 ml distilled water [11, 13]. The solution was subjected to sonication for 30 min and aged for 24 h at ambient conditions prior to deposition. The Si-sol was prepared using 2.2 ml tetraethyl orthosilicate (TEOS) as a precursor dissolved in 4.6 ml H_2O and 11.8 ml ethanol and magnetically stirred for 4 h at 50 ºC. Pure silica MFI-type zeolite (Si-MFI) was synthesized according to the procedure described before; the synthesis was performed at 90 °C for 3 days. [14]. While the synthesis of nanosized EMT-type zeolite with particle size of 10-15 nm was performed according to the procedure published in [15]. The synthesis was performed at 35 °C for 36 h. Both zeolites were extracted *via* high-speed centrifugation (20 000 rpm, 60 min) followed by re-dispersion in double distilled water; this procedure was repeated several times until the final colloidal suspensions reached pH of 8.5.

The doping of metal oxides with zeolites was realized in liquid phase by adding different volumes of zeolites solutions to the already prepared metal sols thus achieving doping levels from 0% (pure metal oxide film) to 100 % (pure zeolite films) in the film. It should be noted here that in the case of Si-sol the highest doping levels were 60 % and 70 % for Si-MFI and EMT zeolites, respectively. Further doping deteriorated the film's optical quality and resulted in increased scattering. Prior to mixing, the zeolites and sols were sonicated for 30 minutes in order to redispersed the aggregated particles.

Oxo-zeolites thin films were prepared by pouring of 0.3 ml of sol / zeolite mixture on preliminary cleaned silicon substrates and spinning at a rate of 3000 rpm for 30 s. A post deposition annealing was applied to all films for 30 min at 320 ºC with temperature ramp of 10 ºC / min. Our additional experiments have shown that further annealing at 320 ºC did not modify the samples properties.

The aqueous cellulose solution (1.5 wt.%) is added to zeolite suspension in order to improve the adhesion of zeolite film on silicon substrate. The surface morphology of the films and their structures were characterized by Philips 515 scaning electron microscope. The refractive index (n) and extinction coefficient (k) along with the thickness (d) of the films were determined from reflectance spectra of the films measured at normal light incidence by UV-VIS-NIR spectrophotometer Cary 05E (Varian, Australia) using non-linear curve fitting method [16]. The experimental errors for n, k and d were 0.005, 0.003 and 2 nm, respectively. The vapor sensing measurements on films were conducted by measuring reflectance spectra prior to and after vapor exposure using Cary 05E spectrophotometer equipped with a homemade bubbler system for generation of vapors from liquids with controlled concentrations [17].

RESULTS AND DISCUSSIONS
Thin films of Nb_2O_5 doped with Si-MFI type zeolites

Fig. 1 shows the surface morphology of the Nb_2O_5 films doped with Si-MFI zeolites with different volume ratio from 0 to 100 %. It is seen that the pure oxide film has a very smooth and featureless surface, while the pure zeolite film exhibits rough surface with grainy morphology. The surface morphology of the oxo-zeolite composites is dependent on the fraction volume between zeolites and oxides. The results show an increase of the surface roughness as the concentration of zeolite crystals increased (see Fig. 1c).
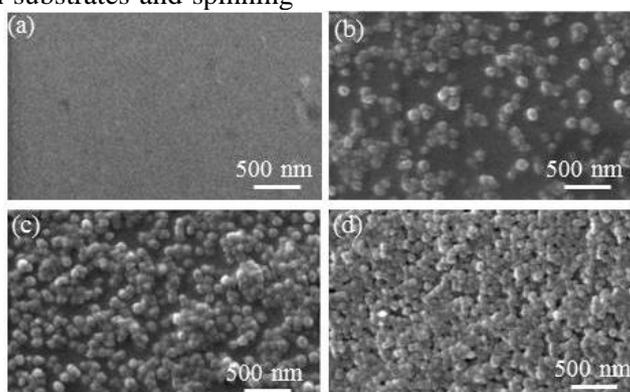
Fig. 1. SEM images of the surface of films (a) pure Nb_2O_5, (b) 50% Nb_2O_5:50% Si-MFI, (c) 25% Nb_2O_5:75% Si-MFI and (d) 100% Si-MFI.
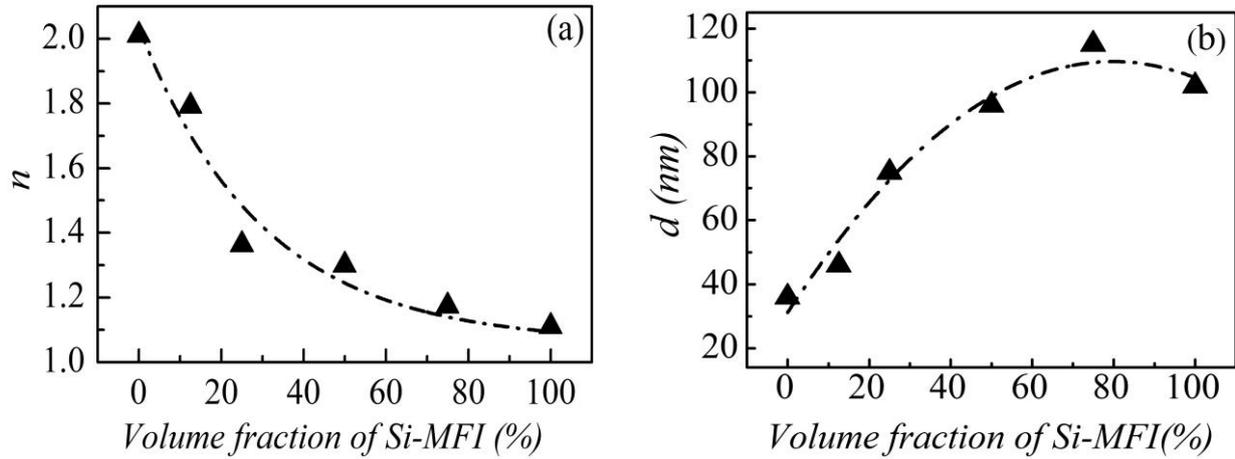
Fig. 2. (a) Refractive index and (b) thickness of the Nb_2O_5 films doped with Si-MFI zeolite.
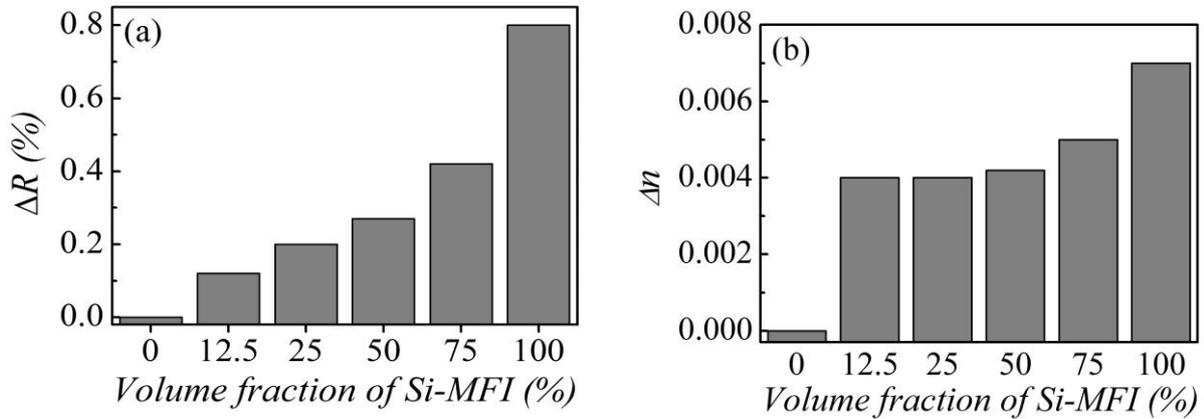
Fig. 3. Absolute change of (a) the reflectance and (b) effective refractive index of Nb_2O_5 films.

The variation of the refractive index (*n*) and thickness (*d*) of Nb_2O_5/Si-MFI films as a function of the volume fraction of zeolites is shown in Fig. 2. For determination of the optical properties of the films, reflectance spectra of all samples were measured and their thicknesses and refractive indices were calculated according to [16]. It is seen from Fig. 2 that by increasing of the doping level of zeolite, the refractive index of the composite decreases exponentially from 2.02 for undoped film to 1.11 for 100 % doped film (pure Si-MFI film). The thickness for pure Nb_2O_5 and Si-MFI-zeolite films is 36 nm and 102 nm, respectively, while the thickness of the composites changes exponentially with increasing the doping level. Since the refractive index of zeolites is lower than oxides [10], the reduction of *n* can be expected due to the increase of zeolite volume fraction in the oxo-zeolite composites, which leads to a decrease of the effective refractive index of the films. Due to the small size of zeolite crystals (30 - 40 nm) there is no significant increase of optical losses due to

scattering for doped samples as compared to the pure Nb_2O_5 films.

The results presented (Fig. 2) are very useful when materials with specific optical characteristics are required for certain applications. For example, this approach can be used for production of rugate filters that exhibit sine profile of the refractive index across the film thickness [18] because a wide range of refractive index values can be covered simply by doping of Nb_2O_5 films with zeolites.

We have already shown [10] that Si-MFI zeolite films change their effective refractive index when exposed to analytes due to adsorption and condensation of vapors in their micro- and meso-pores. To the contrary, no changes are observed for pure Nb_2O_5 films. However, when Nb_2O_5 film is doped with zeolites it may be expected the formation of mesoporosity in addition to the microporosity of the zeolites inside the films. In order to clarify the results, we studied the sensing properties of the films through measurements of reflectance spectra of the samples before (R_{air}) and after exposure to acetone vapors (R_{ac}), and the

change in effective refractive index (Δn) is calculated. The absolute changes in reflectance, ΔR ($= |R_{air} - R_{ac}|$) and refractive index, Δn, are displayed in Fig. 3. The calculation of Δn is performed using already measured values of ΔR and it is explained in details elsewhere [19].

As can be seen (Fig. 3a), with increasing of the volume fraction of zeolites, ΔR increases gradually from 0 % for undoped film to 0.27 % for 50 % doped one and reaches the value of 0.82 % for pure zeolite film. The total pore volume increases with doping of the films with zeolite, since the vapor penetrates more easily and condense in the pores due to the capillary condensation. As a result the effective refractive index increases with 0.004 -

0.005 for doped films to 0.007 for pure zeolite film (Fig. 3b). Thus doping of the Nb_2O_5 layers with Si-MFI zeolites improves their sensing properties and allows control of the optical characteristics.

Thin films of SiO_2 doped with Si-MFI and EMT-types zeolites

The same approach for preparing SiO_2-based oxo-zeolite composites was applied where thin films of SiO_2 was used as a matrix for incorporation of Si-MFI and EMT-type zeolites with different volume fractions (Fig. 4). The pure silica surface is not shown in Fig. 4 because it is very similar to the surface of pure Nb_2O_5 (Fig. 1a).
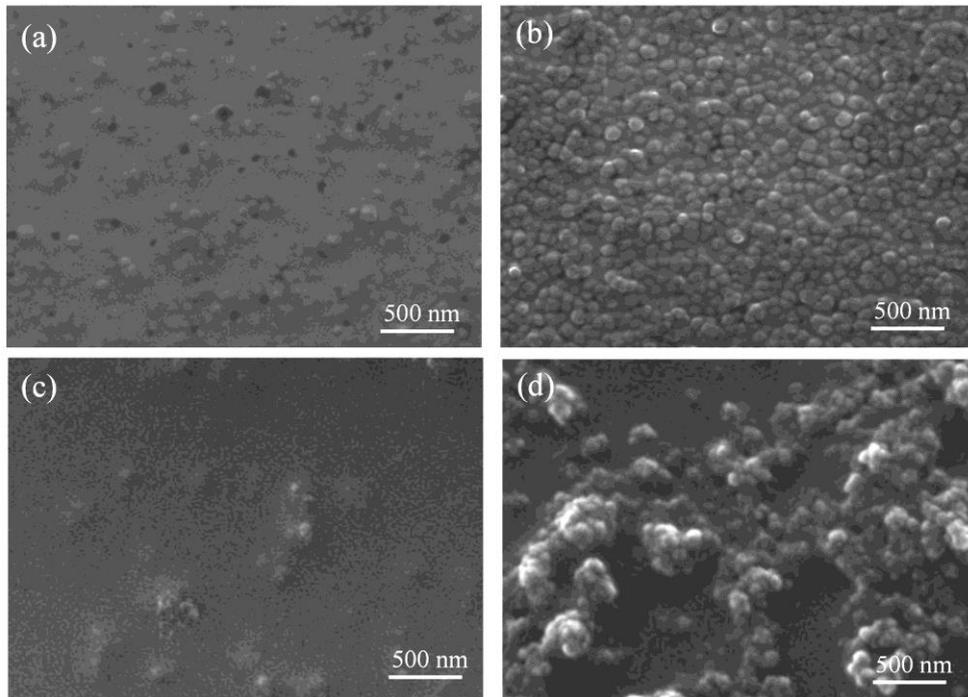
Fig. 4. SEM images of the surface of SiO_2 films doped with Si-MFI (a, b) and EMT (c, d) type zeolites with a volume fraction of 17 % (a, c) and 60 % (b, d).
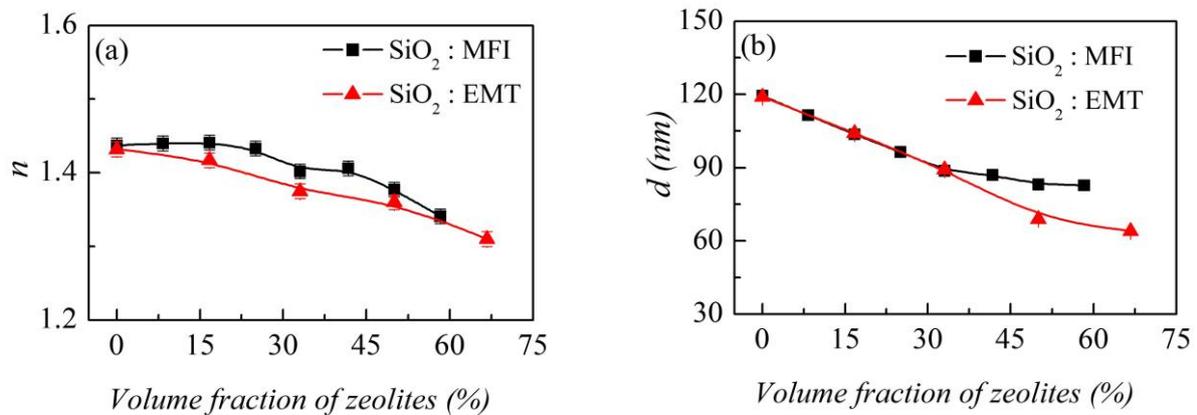
Fig. 5. Dependence of (a) the effective refractive index (n) and (b) thickness (d) of SiO_2 based oxo-zeolites films on the volume fractions of zeolite crystals.

With increasing the doping level, the smooth oxide surface changes to a granular one where the

Si-MFI zeolites are distributed almost homogeneously on the surface in comparison with

the EMT-type zeolite crystals. It should be noted that the addition of zeolites in the volume fraction greater than 60% and 70 % in the cases of Si-MFI and EMT, respectively, leads to films with strong scattering and it is practically impossible to be realized.

The optical properties of the oxo-zeolite composites were studied, i.e., the refractive index and extinction coefficient were calculated from the reflectance spectra. Fig. 5 shows the refractive index (n) and thickness (d) of SiO_2 doped with Si-MFI and EMT-types zeolites. It is seen that the influence of zeolites on the effective refractive index of the film is similar in both cases: n decreases from 1.43 to 1.34 for Si-MFI-type zeolite and to 1.31 for EMT-type zeolite, when the volume fractions vary from 0 to 60% and from 0 to 70 %, respectively. The smaller values of n could be due to the existence of bigger empty spaces between the EMT-type zeolites in comparison with Si-MFI-type zeolite as dopants (Fig. 4 (b) and 4 (d)). According to the thickness dependences, the difference in thickness values of oxo-zeolite composites prepared using different zeolite types is stronger for volume fractions higher than 30 % while for small amount of zeolites added to the matrix, the d-values are very similar in both cases (Fig. 5b). The similar film morphologies for small doping levels and significantly different surface status for higher doping (Fig. 4) may explain the observed dependences.
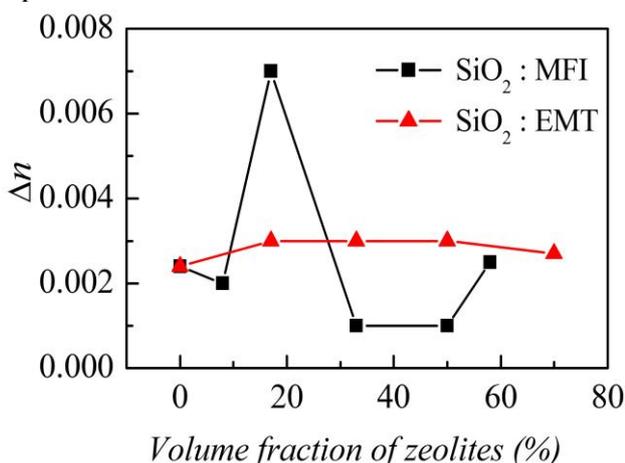
Fig. 6. Refractive index change of SiO_2 films doped with different volume fraction of Si-MFI and EMT-zeolites exposed to acetone vapors at partial pressure p/p_0=0.15 (p_0 is the saturated vapors pressure at 0ºC)

To check whether there is an improvement of sensing properties of oxo-zeolite composites in comparison with pure silica matrix, the reflectance spectra of the films are measured prior to and after exposure to acetone vapors with partial pressure p/p_0=0.15 (p_0 is the saturated vapors pressure at 0

ºC). The changes in reflectance are used further for calculation of the refractive index (Δn) shown in Fig. 6. For EMT composites there is a weak enhancement of sensitivity that is independent of the volume fraction of added zeolites. The refractive index of EMT/SiO_2 composites changes with 0.003 after exposure to acetone vapors, while for pure silica the change is 0.002. In addition EMT-type zeolite is highly hydrophilic, which decreases its selectivity and adsorption toward acetone vapors. However, when hydrophobic Si-MFI type zeolite is used as dopant, there is a significant improvement of the sensing properties of the composite with zeolite volume fraction around 20 % where the increase in sensitivity is more than 3 times. The achieved change in n is comparable with Δn for pure zeolite film (Fig. 3b).

The supplementary advantage of the SiO_2/MFI film is the smoother surface and higher refractive index, both are very important if the films are used as building blocks of vapor responsive Bragg stacks. The first one will guarantee smooth interfaces between the layers in the stack thus leading to the stronger reflectance band. The higher value of n for the composite (1.43) as compared to 1.11 for zeolite film will allow an omnidirectional reflectance to be achieved because the condition of refractive index higher than 1.2-1.30 for one of the stack's constituents will be fulfilled [20].

Interestingly, for the rest of composites there is no improvement of Δn, even weaker changes are obtained as compared to SiO_2 matrix. Previously, we have shown that the surface hydrophobicity and tension mainly influence the adsorption strength [21]. We can speculate that there is an optimal value of MFI volume fraction where the interplay between these two parameters intensifies their positive impact on adsorption thus leading to the highest optical response.

For further increase of the sensitivity, the SiO_2/Si-MFI composite can be used as a building block of Bragg stack along with an appropriately chosen material with high refractive index (doped Nb_2O_5 for example). Our additional calculations have shown that the reflectance changes of 0.14% for single film can be increased to 0.7%, 1.6 % and 2.6 % using 3, 5 and 7 layered stacks, respectively.

CONCLUSIONS

The fabrication of oxo-zeolite composites comprising SiO_2/Nb_2O_5 matrix doped with Si-MFI and EMT-type zeolites was demonstrated. It was shown that in the case of Nb_2O_5 matrix the refractive index of the resulting composite can be tune in a wide range from 2.02 to 1.11, while for

SiO$_2$ the refractive index varies from 1.43 to 1.34 and 1.31 for MFI and EMT zeolites, respectively. Besides, the highest possible volume fraction of zeolites inserted in SiO$_2$ matrix depends on zeolite type, and it is 60 % and 70 % for zeolites with MFI and EMT-types frameworks, respectively. Further increase of the doping level leads to deterioration of the optical quality of the films and increased scattering.

A significant improvement of sensing properties was observed for the Nb$_2$O$_5$ composites where there is no change for pure oxide: the effective refractive index of composites increases with 0.004 - 0.005 after exposure to the probe molecules (acetone vapors) that is very close to the change obtained for pure zeolite films (0.007). The reason is the porosity induced in the oxide matrix through doping with zeolites. The increase in sensitivity more than 3 times was achieved for SiO$_2$ film doped with Si-MFI zeolites with volume fraction around 20%.

Although the obtained changes in refractive index are comparable with these for pure Si-MFI films the composites have the supplementary advantages of smoother surface and higher refractive index, both opening the pathway of using them in vapor responsive Bragg stacks.

REFERENCES

1. A. Cusano, A. Iadicicco, D. Paladino, S. Campopiano, A. Cutolo, M. Giordano, *Opt. Fiber Techn.*, **13**, 291 (2007).
2. W. F. Ho, M. A. Uddin, H. P. Chan, *Polym. Degrad. Stab.*, **94**, 158 (2009).
3. G. Kang, J. Yoo, J. Ahn, K. Kim, *Nano Today,* **10**, 22 (2015).
4. M. Ghazzal, O. Deparis, J. De Coninck, E. Gaigneaux, *J. Mater. Chem. C*, **1**, 6202 (2013).
5. O. Dalstein, D. R. Ceratti, C. Boissière, D. Grosso, A. Cattoni, M. Faustini, *Adv. Funct. Mater.*, **26**, 81 (2016).
6. M. N. Ghazzal, O. Deparis, A. Errachid, H. Kebaili, P. Simonis, P. Eloy, J. P. Vigneron, J. De Coninck, E. M. Gaigneaux, *J. Mater. Chem.*, **22**, 25302 (2012).
7. D. Lee, M. F. Rubner, R. E. Cohen, *Nano Lett.*, **6**, 2305 (2006).
8. N. Petkov, S. Mintova, B. Jean, T. H. Metzger, T. Bein, *Chem. Mater.*, **15**, 2240 (2003).
9. T. Bein, K. Brown, *J. Am. Chem. Soc.*, **111**, 7640 (1989).
10. T. Babeva, H. Awala, M. Vasileva, J. El Fallah, K. Lazarova, S. Thomas, S. Mintova, *Dalton Trans.*, **43**, 8868 (2014).
11. T. Babeva, K. Lazarova, M. Vasileva, B. Gospodinov, J. Dikova, *Bulg. Chem. Comm.*, **45**, 28 (2013).
12. K. Lazarova, R. Georgiev, M. Vasileva, B. Georgieva, M. Spassova, N. Malinowski, T. Babeva, *Opt. Quant. Electron.*, **48**, 310 (2016).
13. N. J. Arfsten, J. F. Gavlas. USpatent 6811901B1 (2004).
14. S. Mintova, N. H. Olson, J. Senker, T. Bein, *Angew. Chem.*, **41**, 2558 (2002).
15. E.-P. Ng, D. Chateigner, T. Bein, V. Valtchev, S. Mintova, *Science*, **335**, 70 (2012).
16. B. Gospodinov, J. Dikova, S. Mintova, T. Babeva, *J. Phys.: Conf. series,* **398**, 012026 (2012).
17. K. Lazarova, H. Awala, S. Thomas, M. Vasileva, S. Mintova, T. Babeva, *Sensors*, **14**, 12207 (2014).
18. B. Bovard, *Appl. Opt.*, **32**, 5427 (1993).
19. R. Georgiev, B. Georgieva, M. Vasileva, P. Ivanov, T. Babeva, *Adv. Cond. Matt. Phys.*, **2015**, 403196 (2015).
20. S. H. Kim, C. K. Hwangbo, *Appl. Opt.* **41**, 3187 (2002).
21. T. Babeva, R. Todorov, B. Gospodinov, N. Malinowski, J. Fallah, S. Mintova, *J. Mater. Chem.*, **22**, 18136 (2012).

ОПТИМИЗИРАНЕ НА ОПТИЧНИТЕ И СЕНЗОРНИ СВОЙСТВА НА ОКСИДИ, ПОЛУЧЕНИ ПО ЗОЛ-ГЕЛ МЕТОДА, ЧРЕЗ ДОТИРАНЕ СЪС ЗЕОЛИТИ

К. Лазарова[1]*, Х. Авала[2], Дж. Ел Фаллах[2], М. Василева[1], С. Минтова[2], Цв. Бабева[1]

[1]*Институт по оптически материали и технологии ''Акад. Й. Малиновски'', Българска Академия на Науките, ул. Акад. Г. Бончев бл.109, 1113 София, България.*
[2]*Лаборатория по катализ и спектрохимия, Нормандски университет, ENSICAEN, CNRS, бул. Маршал Жуен 6, 14050 Каен, Франция*

(Резюме)

В настоящото изследване е изучено модифицирането на оптичните и сензорни свойства на тънки слоеве от Nb_2O_5 и SiO_2 чрез дотиране с наноразмерни зеолити MFI и EMT - тип. Тънките филми от чисти оксиди и оксо-зеолитни композити, съдържащи оксидна матрица с вградени зеолити, са получени чрез центрофужно нанасяне и последващо загряване, използвайки предварително синтезиран зол и стабилизирани колоидни разтвори на зеолити, смесени в различно съотношение. Повърхностната морфология на филмите и техните оптични свойства са изследвани съответно чрез SEM и UV-VIS-NIR спектроскопия. Сензорните свойства са изучени чрез измерване на спектъра на отражение преди и след излагането на филмите на тестваните молекули (ацетонови пари) и пресмятане на промените на ефективния показател на пречупване, вследствие на кондензацията на парите в порите на филма. Дискутиран е потенциалът на разработените материали за оптични сензорни приложения.

Efficiency of ZnO photocatalysts doped with La and Ag

K. I. Milenova[1]*, K. L. Zaharieva[1], I. D. Stambolova[2], V. N. Blaskov[2], A. E. Eliyas[1]

[1]*Institute of Catalysis, Bulgarian Academy of Sciences, Acad. G. Bonchev St., bl. 11, 1113 Sofia, Bulgaria*
[2]*Institute of General and Inorganic Chemistry, Bulgarian Academy of Sciences, Acad. G. Bonchev St., Bl. 11, 1113 Sofia, Bulgaria*

The photocatalytic efficiency of Ag and La doped ZnO materials, obtained using the impregnation followed by thermal treatment, was studied and compared in the reaction of oxidative degradation of RB5 dye as model contaminant in aqueous solutions under UV irradiation. The structure, phase composition, morphology and specific surface area of the non-doped and doped ZnO photocatalysts were investigated by Powder X-ray diffraction analysis, Scanning electron microscopy and BET method. The results indicated that the highest degree of degradation of RB5 dye (69%) after 120 minutes of illumination was achieved using La doped ZnO photocatalyst, comparing with the degree of degradation over the others samples - Ag doped ZnO (35%) and non-doped ZnO (20%). The apparent rate constants of RB5 dye degradation decrease in the following order: La-ZnO (9.2×10^{-3} min^{-1}) > Ag-ZnO (3×10^{-3} min^{-1}) > ZnO (1.4×10^{-3} min^{-1}) due to the interplay of La^{2+} and La^{3+} ion pair.

Keywords: ZnO, dopants, photocatalytic oxidation, Reactive Black 5.

INTRODUCTION

Developing effective and green methods for pollutants removal (among them dyes from textile industry) is important environmental hot topic of the day [1]. Heterogeneous photocatalysis using semiconductors has demonstrated its productivity in this aspect, especially in degrading persistent organics into CO_2 and H_2O or into easily biodegradable compounds [2, 3]. ZnO is among the most popular photocatalysts for dyes degradation due to its ability to absorb a wide solar spectrum [1, 4]. An effective approach for decreasing the recombination of photo-generated charge carriers and enhancing photoactivity is the modification of ZnO using doping with metals or nonmetals, metal deposition and coupling with other semiconductors [5].

The activities of Ag/ZnO samples were investigated by photodegradation of aqueous solution of Acid Blue 113, Rhodamine B, Basonyl Violet and Methylene Blue dyes under UV illumination [6-11]. Ag/ZnO photocatalysts were evaluated by the dye degradation also under direct sunlight [12-15]. Mechanism of photodegradation of Methyl Orange [16-18] and Methylene Blue dye on Ag/ZnO nanocomposites for UV and visible-light was studied [16, 17, 19]. ZnO nanosheets were hybridized with Ag_3PO_4 nanoparticles and their photocatalytic activity for the degradation of Rhodamine B dye under visible-light illumination was investigated [20]. The Fenton-like photocatalytic activity for the degradation of Rhodamine B and Methylene Blue in the mixed dye solution using Ag/ZnO hybrid samples was studied [21]. Photodegradation of dye mixtures of Methylene Blue and Methyl Orange by Ag/ZnO under UV-irradiation were performed in [22].

Mechanisms of the degradation of three different dyes on La doped ZnO photocatalyst using visible light was presented in [23]. The photocatalytic degradation of Reactive Black 5 dye in distilled and sea water using La/ZnO samples under UV-light irradiation was described in [24]. The photodegradation of the Metasystox, Paracetamol drugs, 2,4,6-trichlorophenol and Methyl Orange dye on La-doped ZnO powders were reported [25-28].

The aim of the present paper is to study comparatively the photocatalytic properties of non-doped and Ag- or La-doped-ZnO photocatalysts obtained by impregnation method for degradation of aqueous solution of Reactive Black 5 dye as model contaminant.

EXPERIMENTAL

The activated ZnO powder was prepared by procedure presented in Bulgarian Patent № 28915/1980 by Shishkov et al. (Cl. Index C 01 G 9/02) [29]. The commercial ZnO was dissolved in nitric acid and after that simultaneous treatment by adding NH_4OH and bubbling CO_2. The obtained precipitate $Zn(OH)CO_3$ was filtered, washed, dried at 110 °C and thermally treated at 400 °C for 4 h. ZnO powder was impregnated with definite amounts of the aqueous solutions of the $AgNO_3$ and $La(NO_3)_3$ (prepared by dissolving of La_2O_3 in nitric

acid). The concentrations of Ag and La metal dopants were so preset to give 1.5 wt% metal content with respect to Zn amount. The doped ZnO samples were calcined at 500 °C for 2 h in air atmosphere [30-32].

The powder X-ray diffraction analysis, scanning electron microscopy (SEM) and single point Brunauer-Emmet-Teller (BET) method were used to study the phase composition, morphology and specific surface area of the catalysts. The PXRD patterns were registered on a TUR M62 apparatus with PC control and data acquisition, using HZG-4 goniometer and CoKα radiation. The Scherrer's formula was used to calculate the crystallites size. The morphology of the ZnO photocatalysts surface were investigated by scanning electron microscope (SEM) JEOL, model JEM-200CX, scanning adaptor EM-ASID3D. The specific surface area of the samples was measured in a conventional volumetric apparatus Micromeritics FlowSorb II 2300 (USA) applying single point BET method and using nitrogen adsorption from a mixture 30% N_2+70% He at the boiling temperature of liquid nitrogen (77.4 K). Before determining the specific surface area the materials were degassed at 423 K for 30 min to liberate the entire surface from adsorbed impurities until the residual pressure became lower than 1.333×10^{-2} Pa. The nitrogen (N_2) monolayer formed was used to evaluate the specific surface area (A_{BET}) using the BET equation, whereupon He was the carrier-gas [30-32].

The photocatalytic degradation of Reactive Black 5 (RB5) dye as contaminant in aqueous solution under UV-A polychromatic illumination (18 W) was tested. The change of absorbance during the photocatalytic tests was monitored by UV-Vis absorbance spectrophotometer CamSpec M501 in the wavelength range from 200 to 800 nm, observing especially the wavelength maximum of absorbance at λ_{max} = 599 nm for RB5. The initial concentration of RB5 dye was 20 ppm. The studied systems were left in the dark for about 30 min before switching on the UV irradiation in order to reach adsorption-desorption equilibrium state. A semi-batch slurry photocatalytic reactor was used continuously feeding air flow creating large excess of O_2 compared to stoichiometry. The measurements were carried out by taking aliquot samples of the suspension out of the reaction vessel after regular time intervals. The powder was then separated from the aliquot solution by centrifugation before the UV–Vis spectrophotometrical measurements. After that, the aliquot solution, together with the photocatalyst

powder, were returned back quantitatively into the reaction vessel, which ensured the operation under constant volume and constant catalyst amount [30-32].

RESULTS AND DISCUSSION

On the Figure 1 the Powder X-ray diffraction patterns of the undoped and doped ZnO materials are displayed. The presence of ZnO wurtzite phase (PDF-36-1451) was registered in the spectra of the investigated samples. The low content of La and Ag is possible reason explaining the absence of their peaks on the X-ray diffractograms. The determined crystallites size of the studied samples is varying within the range 50÷57 nm (Figure 2). The results established smaller crystallites size of Ag and La doped ZnO (50 and 54 nm) compared to the non-doped ZnO sample (57 nm). The SEM images of the Ag and La doped ZnO materials are presented in Figure 3. The smaller size of the particles is observed for Ag doped ZnO than that in the case of La dopant. The aggregates consisting of nanosized particles with irregular shape can be seen on the Figure 3. The Ag-ZnO (32 m^2/g) and La-ZnO (30 m^2/g) doped photocatalyst samples possess somewhat higher specific surface areas compared to that of the pure ZnO (19 m^2/g) [30-32].
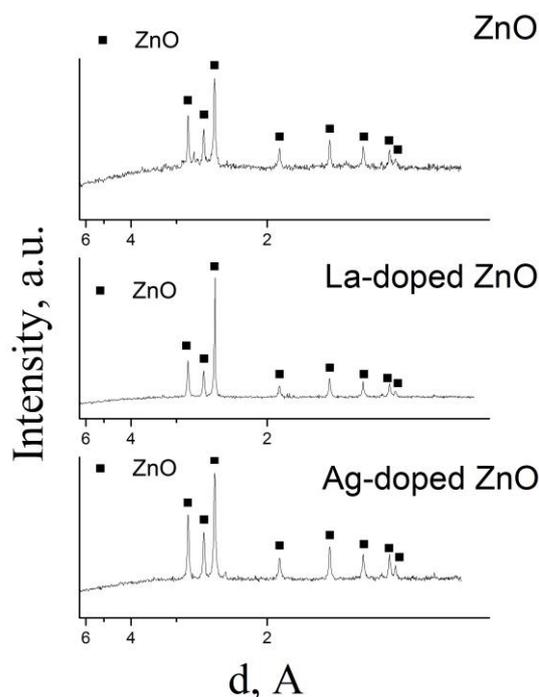
Fig. 1. PXRD patterns of studied non-doped and doped ZnO samples.

The adsorption capacities of non-doped and doped ZnO samples after 30 minutes dark period

(adsorption discoloration) were calculated by the equation:

$$Q = \frac{(C_0 - C).V}{m} \qquad (1)$$

where C_0 and C are the initial and after 30 minutes in the dark concentrations of the dye, V is the volume of the solution and m is the weight of the catalyst.
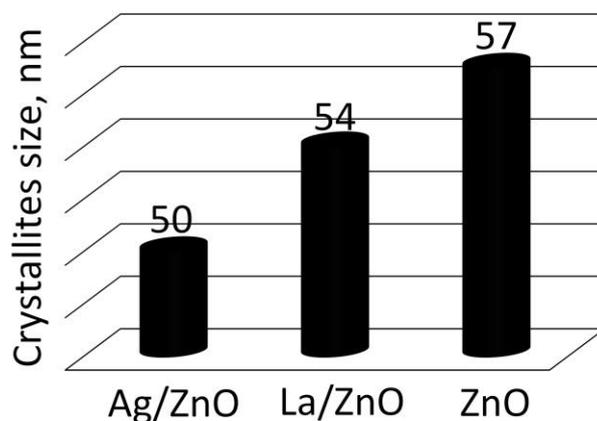
Fig. 2. Crystallites size of investigated non-doped and doped ZnO materials.
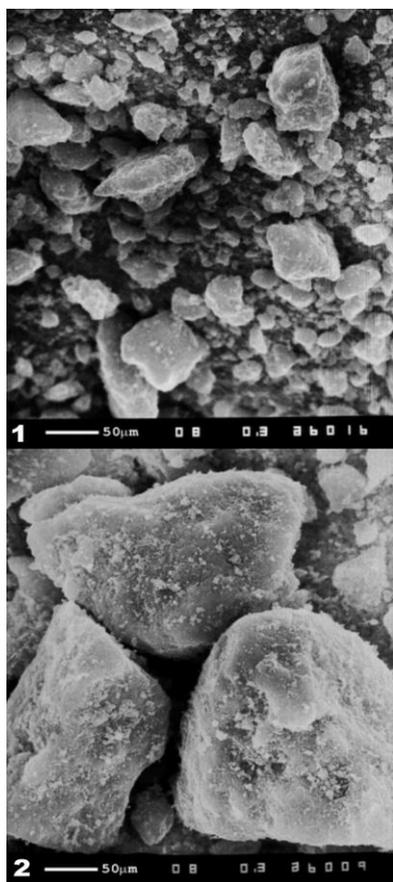
Fig. 3. SEM images of 1 - Ag doped ZnO and 2 - La doped ZnO photocatalysts

The adsorption capacities of the investigated samples decrease in the following order: ZnO (0.028 mg/g) > La-ZnO (0.025 mg/g) > Ag-ZnO (0.018 mg/g).

Figure 4 presents concentration changes of RB5 dye related to the surface area of the photocatalyst based on the changes in the intensity of the

maximal absorbance at 599 nm with time under UV irradiation. Photocatalytic degradation degree of RB5 dye on the studied samples are different for doped and undoped zinc oxide photocatalysts. We observed lower activity for ZnO, while doping with
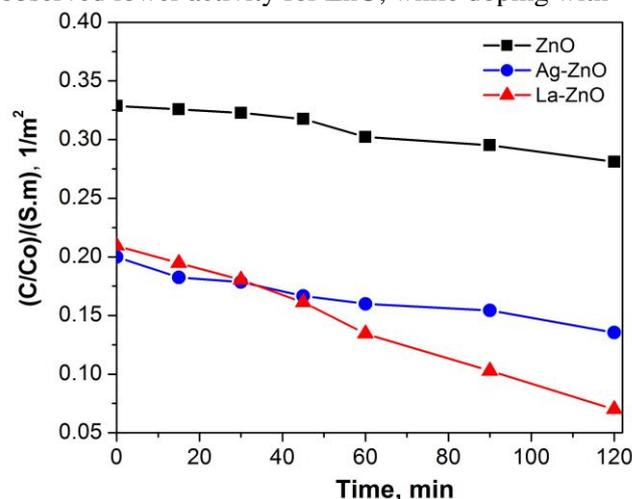
Fig. 4. Concentration changes of RB5 dye related to the surface area of the photocatalyst based on changes in the intensity of the maximal absorbance at 599 nm corresponding to the peak of the diazo bond (-N=N-) for RB5 respectively, with the course of time under UV-A irradiation

Ag and La improved it especially in the case of La-ZnO sample. Figure 5 illustrates the reaction course of dye degradation of investigated catalysts with the time of illumination. The results for degradation conversion degrees are in correlation with those of Figure 4 as they followed the order of activities: ZnO (20%)< Ag-ZnO (35%)< La-ZnO (69%). The degradation apparent rate constants (pseudo first order kinetics) have been calculated using logarithmic linear dependence of the concentrations
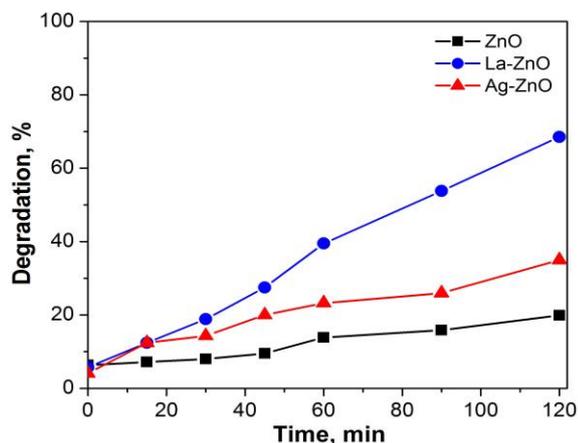
Fig. 5. Degradation of Reactive Black 5 dye calculated as $[(C_0-C)/C_0]x100,\%$ with the course of time under UV-A illumination at 599 nm absorbance maximum, attributed to the peak of the diazo bond (-N=N-) for RB5 using non-doped and Ag and La doped ZnO photocatalysts.

ratio on the time: $-\ln(C/C_0) = $ k.t. and they are represented in Figure 6. The highest photocatalytic activity is demonstrated by La doped ZnO photocatalyst. In comparison with our previous work on La-ZnO photocatalyst this new sample possesses higher value of the rate constant than those of Co, Mn, Ni or Cu doped ZnO samples [32].
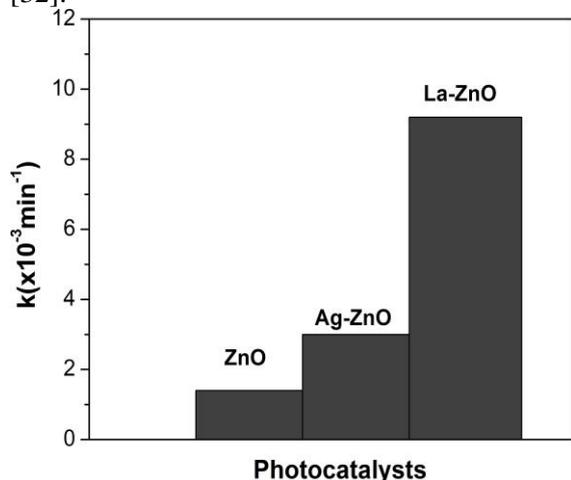
Fig. 6. Apparent rate constants of non-doped and Ag and La doped ZnO photocatalysts.

The enhanced photocatalytic activity in oxidative photodegradation of organic compounds is probably due to the decrease in rate of recombination of the photogenerated electron-holes, synergistic effect between dopant and ZnO [10], production of a large number of oxygen vacancies on doped ZnO, which strongly adsorb OH^- [27]. Among the lanthanides doped ZnO catalysts, La/ZnO shows the best photocatalytic activity because of: higher dark adsorption capacity, electron accepting ability, more OH radical production capability [28].

The doped photocatalysts have higher specific surface area than the non-doped ZnO. The higher photocatalytic efficiency of La-ZnO samples, compared to that of Ag/ZnO, can be explained in terms of differences in dark adsorption capacity and higher degree of crystallinity.

The superiority of the La/ZnO photocatalytic material is probably due to the interplay of the $La^{3+} \leftrightarrow La^{2+}$ ion pair representing an oxidation/reduction catalytic cycle, whereupon the reduction of La^{3+} ions into La^{2+} ions is caused by the photoexcited electrons, while the oxidation of La^{2+} into La^{3+} is caused by the oxygen molecules in large stoichiometric excess in comparison to the pollutant concentration in a semi-batch reactor feeding continuously air to the photoreactor (equation 2). This interplay of an ion couple is missing in the case of Ag/ZnO sample.

$$La^{2+} + O_2 \rightarrow La^{3+} + O_2^{\bullet-} \qquad (2)$$
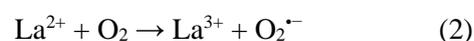
Similar supposition has been put forward by Okte [28]. The produced superoxide anion-radical $(O_2^{\bullet-})$ is responsible for the generation of highly reactive •OH radicals, due to their electrophilic nature.

In the meantime, photogenerated holes may react with H_2O molecules and produce •OH radicals. Thus, loading of lanthanum ions on the surface of ZnO matrix can suppress the recombination of photoinduced charge carriers either with only electron capture ability or with steps forward to produce •OH radicals.

CONCLUSIONS

The present study on the photocatalytic behavior of Ag and La doped ZnO materials in the oxidative degradation of aqueous solutions of RB5 dye under UV light, shows that the doping affects the photocatalytic activity, the crystallite size and the specific surface area of ZnO material. The Ag and La doping of ZnO lead to increase in the photocatalytic activity and specific surface area and decrease in the crystallite size, comparing with those characteristics of the non-doped ZnO material. Lanthanum doped ZnO photocatalyst exhibited higher efficiency in the oxidative degradation of RB5 dye than Ag doped ZnO samples due to the interplay between La^{2+} and La^{3+} ions, which effect is missing in the case of Ag dopant.

REFERENCES

1. K. M. Lee, C. W. Lai, K. S. Ngai, J. C. Juan, *Water Res.,* **88**, 428 (2016).
2. I. Daou, O. Zegaoui, A. Elghazouani, *C. R. Chimie*, **20**, 47 (2017).
3. N. Tripathy, R. Ahmad, H. Kuk, Y.-B. Hahn, G. Khang, *Ceram. Int.*, **42**, 9519 (2016).
4. S. Akir, A. Barras, Y. Coffinier, M. Bououdina, R. Boukherroub, A. D. Omrani*, Ceram. Int.*, **42**, 10259 (2016).
5. Y.-C. Weng, K.-T. Hsiao, *Int. J. Hydrogen Energ.*, **40**, 3238 (2015).
6. S. Mohammadzadeh, M. E. Olya, A. M. Arabi, A. Shariati, M.R. Khosravi Nikou, *J. Environ. Sci.*, **35**, 194 (2015).
7. Q. Huang, Q. Zhang, S. Yuan, Y. Zhang, M. Zhang, *Appl. Surf. Sci.*, **353**, 949 (2015).
8. J. Kaur, K. Gupta, V. Kumar, S. Bansal, S. Singhal, *Ceram. Int.*, **42**, 2378 (2016).
9. K. Saoud, R. Alsoubaihi, N. Bensalah, T. Bora, M. Bertino, J. Dutta, *Mater. Res. Bull.,* **63**, 134 (2015).
10. X. Hou, *Mater. Lett.*, **139**, 201 (2015).
11. H. Liu, Y. Hu, Z. Zhang, X. Liu, H. Jia, B. Xu, *Appl. Surf. Sci.*, **355**, 644 (2015).
12. H. Zhai, L.Wang, D. Sun, D. Han, B. Qi, X. Li, L. Chang, J. Yang, *J. Phys. Chem. Solid.*, **78**, 35 (2015).
13. R. Aladpoosh, M. Montazer, *Carbohydr. Polymer.*, **141**, 116 (2016).
14. S. S. Patil, M. G. Mali, M. S. Tamboli, D. R. Patil, M. V. Kulkarni, H. Yoon, H. Kim, S. S. Al-Deyab, S. S. Yoon, S. S. Kolekar, B. B. Kale, *Catal. Today*, **260**, 126 (2016).
15. H. Bouzid, M. Faisal, F.A. Harraz, S. A. Al-Sayari, A. A. Ismail, *Catal. Today*, **252**, 20 (2015).
16. D. Zhang, X. Pu, H. Li, Y. M. Yu, J. J. Shim, P. Cai, S. I. Kim, H. J. Seo, *Mater. Res. Bull.*, **61**, 321 (2015).
17. Q. Deng, H. Tang, G. Liu, X. Song, G. Xu, Q. Li, D. H. L. Ng, G. Wang, *Appl. Surf. Sci.*, **331**, 50 (2015).
18. R. Kumar, D. Rana, A. Umar, P. Sharma, S. Chauhan, M. S. Chauhan, *Talanta*, **137**, 204 (2015).
19. M. Khademalrasool, M. Farbod, A. Iraji zad, *J. Alloy Comp.,* **664**, 707 (2016).
20. J. Wang, Y. Xia, Y. Dong, R. Chen, L. Xiang, S. Komarneni, *Appl. Catal. B Environ.*, **192**, 8 (2016).
21. Y. I. Choi, H. J. Jung, W. G. Shin, Y. Sohn, *Appl. Surf. Sci.*, **356**, 615 (2015).
22. M. A. Chamjangali, G. Bagherian, A. Javid, S. Boroumand, N. Farzaneh, *Spectrochim. Acta Mo. Biomol. Spectros.*, **150**, 230 (2015).
23. W. Raza, M. M. Haque, M. Muneer, *Appl. Surf. Sci.*, **322**, 215 (2014).
24. N. Kaneva, A. Bojinova, K. Papazova, D. Dimitrov, *Catal. Today*, **252**, 113 (2015).
25. P. V. Korake, R. S. Dhabbe, A. N. Kadam, Y. B. Gaikwad, K. M. Garadkar, *J. Photochem. Photobiol. B:Biol.*, **130**, 11 (2014).
26. M. Shakir, M. Faraz, M. Asif Sherwani, S. I. Al-Resayes, *J. Lumin.*, **176**, 159 (2016).
27. M. Samadi, M. Zirak, A. Naseri, E. Khorashadizade, A. Z. Moshfegh, *Thin Solid Films*, **605**, 2 (2016).
28. A. Neren Ökte, *Appl. Catal. A:Gen.*, **475**, 27 (2014).
29. D. Shishkov, C. Velinova, N. Kassabova, C. Canov, D. Ivanov, D. Klissurski, V. Iordanova, I. Uzunov, Method of preparation of activated zinc oxide. Bulgarian Patent 28915/1980 (Classification Index C 01G 9/02) (in Bulgarian) (1980).
30. K. Milenova, A. Eliyas, V. Blaskov, I. Stambolova, S. Rakovsky, *Journal of International Scientific Publications: Materials, Methods & Technologies*, **8**, 259 (2014).
31. K. Milenova, A. Eliyas, V. Blaskov, I. Stambolova, B. Kunev, S. Rakovsky, *Journal of International Scientific Publications: Materials, Methods & Technologies*, **8**, 265 (2014).
32. K. Milenova, I. Avramova, A. Eliyas, V. Blaskov, I. Stambolova, N. Kassabova, *Environ. Sci. Pollut. Res.*, **21**, 12249 (2014).

ЕФЕКТИВНОСТ НА ZnO ФОТОКАТАЛИЗАТОРИ ДОТИРАНИ С Ag И La

К. И. Миленова[1]*, К. Л. Захариева[1], И. Д. Стамболова[2], В. Н. Блъсков[2], А. Е. Елияс[1]

[1]*Институт по катализ, Българска академия на науките, ул. „Акад. Г. Бончев“, бл. 11, 1113 София, България*
[2]*Институт по обща и неорганична химия, Българска академия на науките, ул. „Акад. Г. Бончев“, бл. 11, 1113 София, България*

(Резюме)

Фотокаталитичната ефективност на Ag и La дотирани ZnO материали, получени чрез импрегниране и последваща термична обработка, беше изследвана и сравнена в реакцията на окислително разграждане на Реактивно Черно 5 багрило (РЧ5) като моделен замърсител във водни разтвори под действието на УВ светлина. Структурата, фазовия състав, морфологията и специфичната повърхност на недотираните и дотираните ZnO фотокатализатори бяха изследвани чрез рентгенова дифракция, сканираща електронна микроскопия и БЕТ метод. Резултатите установиха, че най-висока степен на разграждане на РЧ5 багрило (69%) след 120 минути осветяване беше постигната използвайки La дотиран ZnO фотокатализатор в сравнение с другите проби - Ag дотиран ZnO (35%) и недотиран ZnO (20%). Скоростните константи на разграждане на РЧ5 багрилото намаляват в следния ред: La-ZnO (9.2×10^{-3} min^{-1}) > Ag-ZnO (3×10^{-3} min^{-1}) > ZnO (1.4×10^{-3} min^{-1}) дължащо се на обменно взаимодействие на La^{2+} и La^{3+} двойка йони.

Effect of the particle sizes on the thermoelectric efficiency of metal substituted LaCo$_{1-x}$Ni$_x$Fe$_x$O$_3$ perovskites and Zn$_{1-x}$Al$_x$O wurtzite

S.G. Harizanova[1*], E.N. Zhecheva[1], V.D. Valchev[2], M.G. Khristov, P.V. Markov[1], R.K. Stoyanova[1]

[1]Institute of General and Inorganic Chemistry, Bulgarian Academy of Sciences,
Acad. G. Bonchev Str., Bldg. 11, Sofia 1113, Bulgaria
[2]Faculty of Physics, University of Sofia, 1164 Sofia, Bulgaria

This contribution aims to assess the effect of the particle sizes on the thermoelectric efficiency of oxides. Two groups of oxides are studied: *p*-type semiconductor LaCo$_{1-x}$Ni$_x$Fe$_x$O$_3$ with a perovskite structure and *n*-type semiconductor Zn$_{1-x}$Al$_x$O with a wurtzite structure. The particle sizes are simply varied from 20 to 500 nm by increasing the annealing temperature from 400 to 900 ºC. Structural and morphological characterizations are carried out by powder XRD, SEM and TEM analysis. The thermoelectric efficiency of oxides is determined by the dimensionless figure of merit, calculated from the independently measured Seebeck coefficient, electrical resistivity and thermal conductivity. The results show that the particle dimensions affect mainly the electrical conductivity, while Seebeck coefficient and thermal conductivity remain unchanged.

Keywords: Thermoelectric oxides; cobalt-based perovskites and ZnO.

INTRODUCTION

Thermoelectric oxide materials are nowadays considered as a key factor for clean energy production of the future since they are able to generate electric energy by using waste, geothermal or solar heat as an energy source [1,2]. Since the first report on thermoelectric efficiency of layered sodium cobalt oxides in 1997 till now, there is a challenging research competition aimed at defining the most suitable oxide composition and structure having simultaneously a high Seebeck coefficient, a high electrical conductivity and a low thermal conductivity [1-3]. As a result, several groups of compounds have been proposed: *p*-type conducting materials including Co-based perovskites and misfit Ca$_3$Co$_4$O$_9$ oxides, as well as *n*-type conducting materials comprising metal doped Zn$_{1-x}$M$_x$O and SrTiO$_3$ [4]. The state-of-the-art research is mainly devoted to the enhancement of the thermoelectric efficiency of oxides by a single metal substitution or by a particle-size engineering [5,6].

Recently we have demonstrated that the multiple substitution for cobalt ions in the framework of the perovskite-type structure is an effective way to improve the thermoelectric performance of LaCoO$_3$-based ceramics [7-9]. The best thermoelectric efficiency is established for Ni, Fe-double substituted cobaltates LaCo$_{0.8}$Ni$_{0.1}$Fe$_{0.1}$O$_3$, which is an order of magnitude higher than that of LaCoO$_3$ at room temperature [7-9]. The improved performance is explained with a synergic effect of

Ni and Fe ions substituted for Co ions to reduce effectively thermal conductivity of cobaltates [7-9]. The strategy for the metal substitution is also fruitful for improving thermoelectric properties of ZnO semiconductor [10-12]. It has been found that substitution of aliovalent Al^{3+} ions for Zn^{2+} in regular lattice sites yields Zn$_{1-x}$Al$_x$O oxides (0<x≤0.005) with improved thermoelectric efficiency which is a consequence of the decreased electrical and thermal resistivity [10-12].

This contribution aims to examine the effect of the particle sizes on the thermoelectric efficiency of metal substituted LaCo$_{0.8}$Ni$_{0.1}$Fe$_{0.1}$O$_3$ perovskites and wurtzite-type Zn$_{0.995}$Al$_{0.005}$O. These two oxide compositions are chosen due to their high thermoelectric efficiencies reported early [7,12]. Both LaCo$_{0.8}$Ni$_{0.1}$Fe$_{0.1}$O$_3$ and Zn$_{0.995}$Al$_{0.005}$O oxides are prepared by thermal decomposition of homogeneous precursors such as freeze-dried LaCo$_{0.8}$Ni$_{0.1}$Fe$_{0.1}$ citrates and co-precipitated Zn$_{0.995}$Al$_{0.005}$ carbonate-hydroxides, respectively. The temperature of oxide formation is determined from TG and DTA analyses. The particle sizes are simply varied by increasing the annealing temperature. Structural and morphological characterizations are carried out by powder XRD, SEM and TEM analysis. The thermoelectric efficiency of the oxides is determined by the dimensionless figure of merit, calculated from the independently measured Seebeck coefficient (S), electrical resistivity (ρ) and thermal conductivity (λ).

* To whom all correspondence should be sent:
E-mail: sonya@svr.igic.bas.bg

EXPERIMENTAL

Perovskite $LaCo_{0.8}Ni_{0.1}Fe_{0.1}O_3$ is obtained from corresponding freeze-dried citrates following the procedure described elsewhere [7]. The thermal decomposition of the citrate-precursors was achieved at 400°C for 3 h in air. The obtained solid residue was annealed at 600 and 900 °C for 40 h in air, then cooled down to room temperature with a rate of 5°/min.

Wurtzite-type oxide $Zn_{0.995}Al_{0.005}O$ is prepared by co-precipitation from aqueous solution of $Zn(NO_3)_2.6H_2O$ and $Al(NO_3)_3.9H_2O$ with NH_4HCO_3. The details are given in details elsewhere [12]. The mixed hydroxide-carbonate precipitates are treated at 450 and 700 °C for 10h.

X-ray structural analysis is performed on a Brucker Advance 8 diffractometer with Cu Kα radiation. Step-scan recording for structure refinement is carried out using 0.02 °2θ steps of 5s duration. XRD patterns are analyzed by a structural model comprising rhombohedrally distorted perovskite-type structure (*R-3c* space group), as well as a model on the basis of wurtzite-type structure ($P6_3mc$ space group). The crystallite size of oxides was calculated by the Scherrer equation from the line width of the (012) and (024) perovskite reflection peaks, as well as of the (101) wurtzite peak: $D_{hkl} = \lambda /((\beta^2-\beta^2_o)^{1/2}cos\theta_{hkl})$ where λ is CuKα radiation, β is the peak width at the half height corrected with instrumental broadening and θ_{hkl} is the Bragg angle. The line width was determined by profile analysis using a WinPlotr program.

SEM images of pellets coated with gold are obtained by Zeiss DSM 962 microscope and Philips XL30 scanning electron microscope. The TEM investigations are performed by TEM JEOL 2100 at accelerating voltage of 200 kV. The specimens are prepared by grinding and dispersing them in ethanol by ultrasonic treatment for 6 minutes. The suspensions are dripped on standard holey carbon/Cu grids. The analysis was carried out by the Digital Micrograph software.

The thermal analysis (simultaneously obtained DTA, TG and DTG) of precursors is carried out by a combined LABSYS™ EVO DTA/TG system of the SETARAM Company, France, with a gas-analyser of the OmniStar™ type. The samples are investigated in air, a heating rate of 5 °C/min and sample mass of 10 mg.

The transport properties of the oxides are measured on pellets sintered at 600 and 900 °C for 40 hours. Pellet density was determined by Archimedes' method. The property was evaluated by comparison with the theoretical density of $LaCoO_3$ and ZnO.

Electrical resistivity (ρ), density and mobility of charge carriers were determined by MMR's Variable temperatures Hall System (k2500-5SLP-SP) using Van der Pauw method over a temperature range of 250 - 600 K. The benchtop permanent magnet (0.5T) is used. Thermal conductivity was determined at room temperatures on Thermal Conductivity Analyzer TCi (SETARAM). In order to compare the thermal conductivities of samples having different porosity, the thermal conductivity is normalized to 95% of the theoretical density (λ_t) using the following density correction [13]: $\lambda_t = \lambda(0.95^{1.5})/(1-P)^{1.5}$, where λ is the measured thermal conductivity and P is the fractional porosity of the pellet.

RESULTS AND DISSCUSIONS

Structure and morphology of $LaCo_{0.8}Ni_{0.1}Fe_{0.1}O_3$ and $Zn_{0.995}Al_{0.005}O$

The organic component has been shown to be an important factor determining the thermal properties of precursors [14,15]. Figure 1 compares the DTA, DTG and TG curves of freeze-dried $LaCo_{0.8}Fe_{0.1}Ni_{0.1}$ citrate and co-precipitated $Zn_{0.995}Al_{0.005}$ carbonate-hydroxide. For citrates, the DTA curves display two endothermic processes at 149 and 180°C, followed by strong exothermic process above 280 °C (Fig. 1a). According to the thermal properties of citrate complexes [14-16], the endothermic processes can be assigned to the dehydration and to the transformation of the citrate into aconitate, while the exothermic processes correspond to the combustion of the residual organics. The process is finished at around 380°C. The thermal decomposition of co-precipitated $Zn_{0.995}Al_{0.005}$ carbonate-hydroxide is accomplished at one endothermic peak at 246 °C, the process being completed up to 300 °C.

At 400 °C and short heating time of 3 hours, the product of thermal decomposition of freeze-dried citrate is a mixture of cobalt-based perovskite, spinel and $La_2O_2CO_3$, which agree with our previous data [12,13]. The well-crystallized single perovskite phase is only obtained by increasing the temperature from 400 to 600 °C, as well as by prolonging the heating time to 20 hours (Fig. 2). At these conditions, the XRD pattern consists only of rhombohedrally distorted perovskite phase $LaCo_{0.8}Fe_{0.1}Ni_{0.1}O_3$.
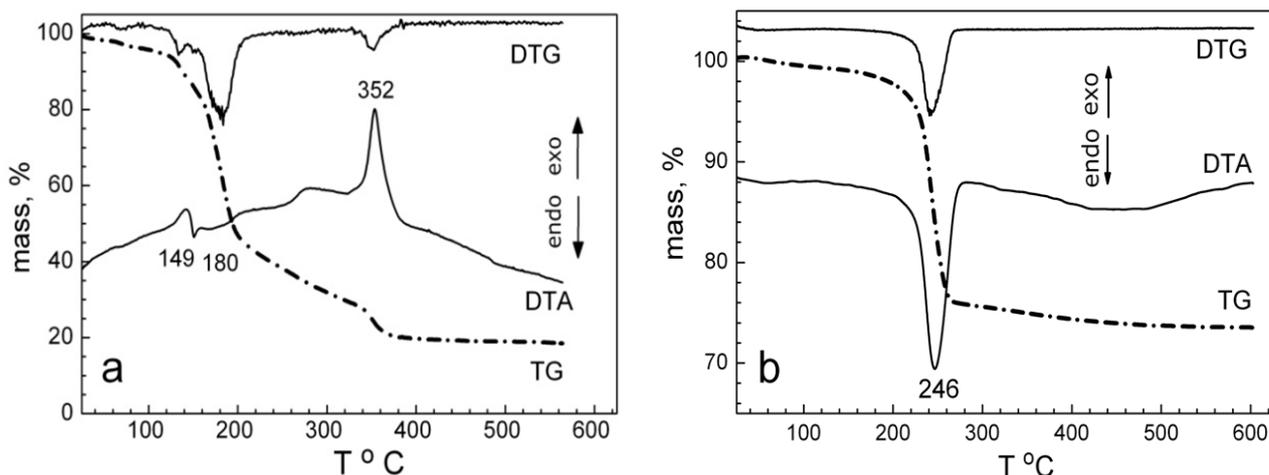
Figure 1. DTA, DTG and TG curves of freeze-dried $LaCo_{0.8}Fe_{0.1}Ni_{0.1}$ citrate (a) and co-precipitated $Zn_{0.995}Al_{0.005}$ carbonate-hydroxide (b).
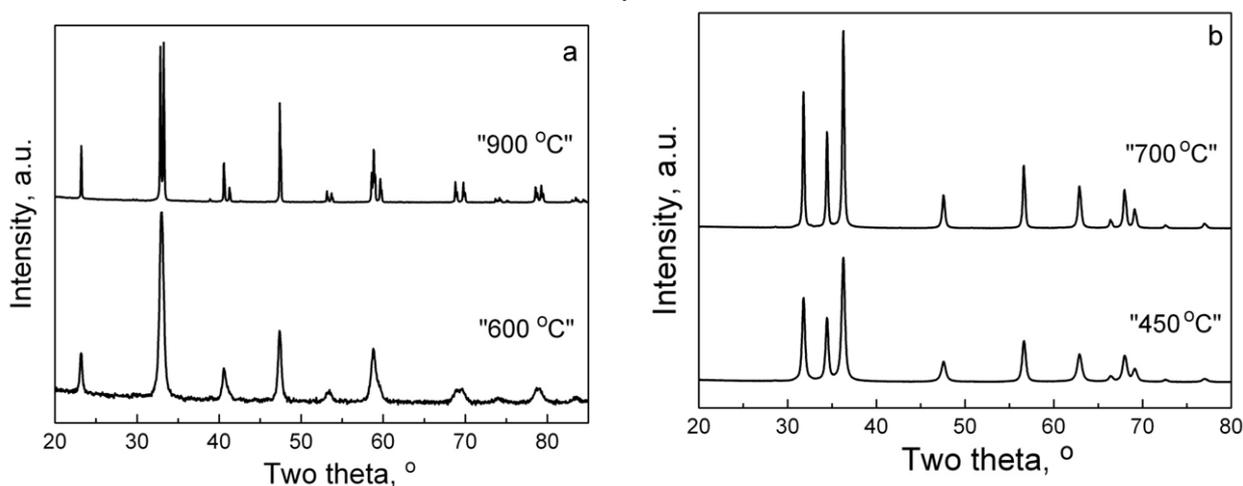
Figure 2. XRD patterns of $LaCo_{0.8}Ni_{0.1}Fe_{0.1}O_3$ (a) and $Zn_{0.995}Al_{0.005}O$ (b). The samples are annealed at 600 and 900°C for $LaCo_{0.8}Ni_{0.1}Fe_{0.1}O_3$, as well as at 450 and 700 °C for $Zn_{0.995}Al_{0.005}O$.

Table 1 Lattice parameters (*a, c, V*) and XRD crystallite sizes (r_{XRD}) for $LaCo_{0.8}Ni_{0.1}Fe_{0.1}O_3$ and $Zn_{0.995}Al_{0.005}O$.

Samples	Unit cell parameters			r_{XRD}, nm
	$a\pm0.0001$, Å	$c\pm0.0003$, Å	V, Å³	
$LaCo_{0.8}Ni_{0.1}Fe_{0.1}O_3$-600	5.4470	13.1752	338.54	37
$LaCo_{0.8}Ni_{0.1}Fe_{0.1}O_3$-900	5.4532	13.1191	337.86	131
$Zn_{0.995}Al_{0.005}O$-450	3.2505	5.2084	47.66	22
$Zn_{0.995}Al_{0.005}O$-700	3.2504	5.2062	47.64	36

This means that the multiple substitutions at Co sites proceed in the framework of the perovskite type structure. Further annealing of $LaCo_{0.8}Fe_{0.1}Ni_{0.1}O_3$ at 900 °C does not provoke any changes in the perovskite structure. Lattice parameters for $LaCo_{0.8}Fe_{0.1}Ni_{0.1}O_3$ annealed at 600 and 900 °C are listed on Table 1. The only parameter that is changed is the line width of the diffraction peaks. Using the correlation between the line width and the crystal size, Table 1 gives also the calculated crystallite sizes for the perovskite annealed at low and high-temperature. The result reveals a strong increase in the XRD crystallite sizes (more than 3 times) when going from 600 to 900 °C.

The same picture is observed for Al doped ZnO. The well-crystalline wurtzite-type oxide is formed at 400 °C. The lattice parameters are close to that of

undoped ZnO: a = 3.2486 and c = 5.2035 [12]. Further annealing at 700 $^{\circ}$C is related with an increase in the crystallite size of $Zn_{0.995}Al_{0.005}O$ without changing the lattice parameters (Table 1). The comparison shows that changes in the crystallite sizes are more restricted for $Zn_{0.995}Al_{0.005}O$ in comparison with that for the perovskite phase. Based on solid state ^{27}Al MAS NMR, we have established that aliovalent Al^{3+} ions substitute for Zn^{2+} in the wurtzite-type of structure when the samples are annealed in the temperature range of 400-700 $^{\circ}$C [12]. As a result, the temperature range of annealing of Al-doped ZnO is chosen between 400 and 700 $^{\circ}$C so that to ensure both the particle growth and the preservation of Al^{3+} ions inside the wurtzite structure. All XRD results reveal clearly that the perovskite and the wurtzite structures remain unchanged in the temperature range of annealing.
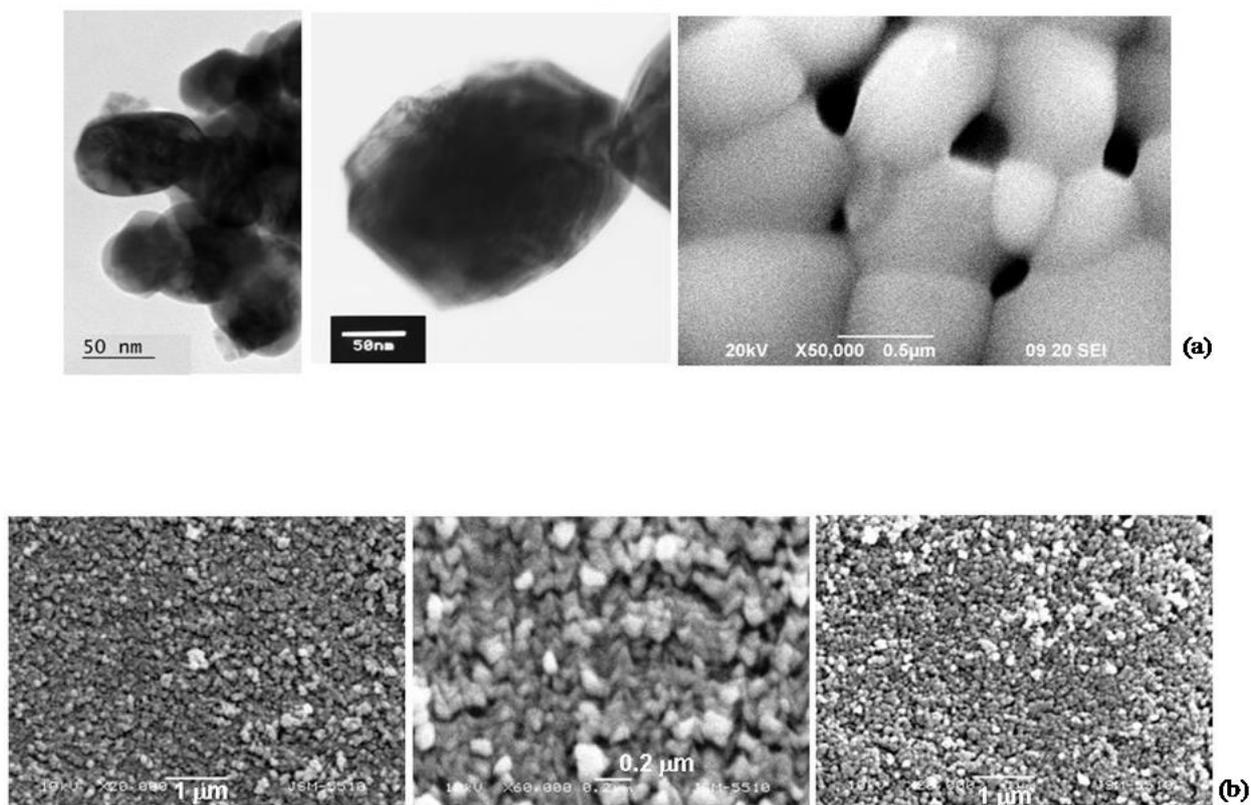
Figure 3. TEM and SEM images for $LaCo_{0.8}Ni_{0.1}Fe_{0.1}O_3$ (a) annealed at 600 and 900 $^{\circ}$C. SEM images of $Zn_{0.995}Al_{0.005}O$ (b) annealed at 450 and 700 $^{\circ}$C.

The morphology of the oxides is a critical parameter in order to fabricate the dense pellets suitable for electrical resistivity measurements. Therefore, Figure 3 compares the morphologies of $LaCo_{0.8}Ni_{0.1}Fe_{0.1}O_3$ and $Zn_{0.995}Al_{0.005}O$ having different particle dimensions. At low annealing temperature, $LaCo_{0.8}Ni_{0.1}Fe_{0.1}O_3$ displays well-shaped individual particles with a mean dimension of about 50 nm, while a significant crystal growth is observed at high annealing temperature: a mean particle size reaches a value of about 500 nm. The observed changes in the particle sizes during perovskite annealing are consistent with that established for the crystallite sizes calculated from XRD line width (Table 1). The temperature-induced changes in the morphology are less obvious for $Zn_{0.995}Al_{0.005}O$ (Fig. 3b), which is also in agreement with the calculated XRD crystallite sizes.

The important finding is the fact that both $LaCo_{0.8}Ni_{0.1}Fe_{0.1}O_3$ and $Zn_{0.995}Al_{0.005}O$ form dense pellets irrespective of the different particle dimensions. For the perovskite phase, well shaped particles fused one to another give rise to the pellet porosity varying between 20 – 25 %. Irrespective of the smaller particle sizes, the pellet porosity of

$Zn_{0.995}Al_{0.005}O$ is also close to 25 %. The similar pellet porosities allow us to compare the thermoelectric properties of samples having different particle dimensions.

Size-dependent transport properties of $LaCo_{0.8}Ni_{0.1}Fe_{0.1}O_3$ and $Zn_{0.995}Al_{0.005}O$

The performance of thermoelectric materials is usually characterized by the dimensionless figure of merit $ZT=S^2T/(\rho.\lambda)$ where S is the Seebeck coefficient, T is the absolute temperature, ρ is the electrical resistivity, and λ is the thermal conductivity. The improvement of their properties can be achieved by rational control of carrier density, electrical and thermal transport. All results on transport properties of the perovskite and the wurtzite phases are summarized on Figure 4 and Table 2.
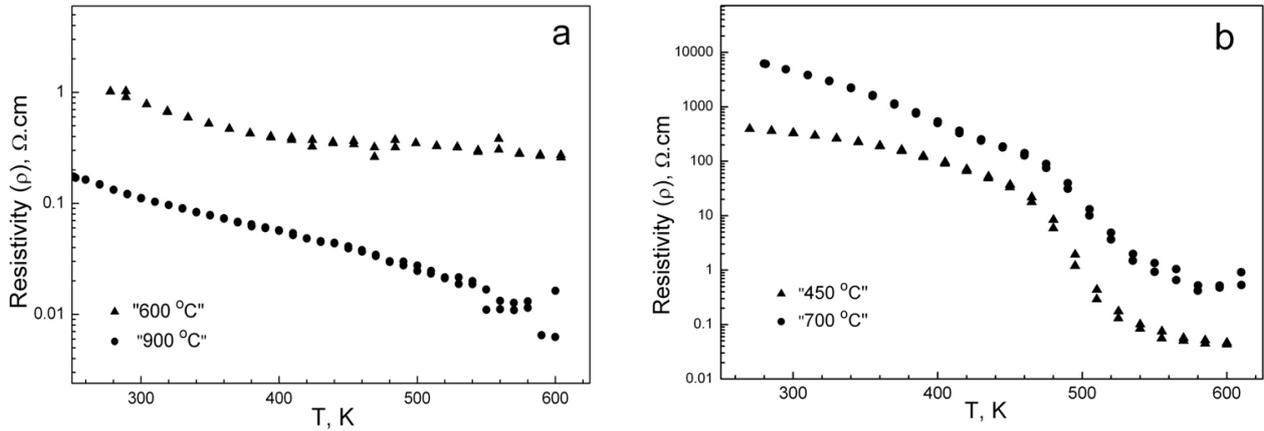
Figure 4. Temperature dependence of the electrical resistivity for $LaCo_{0.8}Ni_{0.1}Fe_{0.1}O_3$ (a) annealed at 600 and 900 °C, as well as for $Zn_{0.995}Al_{0.005}O$ (b) annealed at 450 and 700 °C.

Table 2. Electrical resistivity, carrier density (CD), carrier mobility (CM), Seebeck coefficient, thermal conductivity, power factor and figure of merit for $LaCo_{0.8}Ni_{0.1}Fe_{0.1}O_3$ annealed at 600 and 900 °C (P600, P900) and for $Zn_{0.995}Al_{0.005}O$ annealed at 450 and 700 °C, (W450, W700) respectively.

Samples	ρ, Ω.cm	CD, cm^{-3} x10^{18}	CM, cm^2/Vs	S, μV/K	λ, W/(m.K) ± 0.04	*PF*	*FM*
P600	0.793	2.9	2.5	+ 189	0.20	0.045	0.007
P900	0.072	8.6	2.7	+ 234	0.17	0.758	0.134
W450	333.5	1.5	0.01	- 259	0.33	2.0 x 10^{-4}	1.8 x 10^{-5}
W700	4570.1	0.05	0.03	-590	0.30	0.8 x 10^{-4}	0.8 x 10^{-5}

Figure 4 shows the temperature dependence of the electrical resistivity of $LaCo_{0.8}Ni_{0.1}Fe_{0.1}O_3$ and $Zn_{0.995}Al_{0.005}O$ having different particle dimensions. For all of the samples studied, the electrical resistivity decreases with raising the temperature from 250 to 600 K, thus indicating their semiconducting behaviour. While the electrical resistivity of the perovskite phase increases with decreasing the particle dimensions, the wurtzite phase displays an opposite trend: the electrical resistivity is higher for the sample having higher particle dimensions. It is worth mentioning that the changes in the resistivity of the wurtzite phase are more significant in comparison with that for the perovskite phase.

In accordance with our previous data, the temperature dependence of the electrical resistivity of $LaCo_{0.8}Ni_{0.1}Fe_{0.1}O_3$ annealed at 900 °C is describes by the model based on the nearest neighbors hopping of small polarons [$\rho=\rho_oTexp(-E_p/kT)$], the activation energy being 0.0909(5) eV [5]. It is noticeable that the same model can be used to describe most adequately the temperature dependence of the electrical resistivity of $LaCo_{0.8}Ni_{0.1}Fe_{0.1}O_3$ having one order smaller particle dimensions. Moreover, the activation energy for $LaCo_{0.8}Ni_{0.1}Fe_{0.1}O_3$ with smaller particles tends to that for $LaCo_{0.8}Ni_{0.1}Fe_{0.1}O_3$ with bigger particles: 0.093 eV. Contrary to the perovskite phase, the temperature dependence of the electrical resistivity for the wurtzite phase can not be described with one model in the temperature range of 250 – 600 K.

The observed changes in the resistivity for the perovskite and the wurtzite phases are related with the density and mobility of the charge carriers (Table 2). As one can see, for the perovskite phase the carrier density increases with an increase in the particle dimensions, while the carrier mobility remains the same. This means that the smaller the particle sizes, the lower the carrier density is. The observed dependence suggests that defects in the perovskite structure induced by the smaller particle

sizes destroy the charge carriers. Keeping the carrier mobility unchanged, the mechanism of the electrical conductivity stays insensitive towards the particle dimensions.

The wurtzite phase displays the opposite behavior. By increasing the particle dimensions, the charge carriers decrease. As in the case of the perovskite phase, the carrier mobility is insensitive towards the particle sizes. This indicates that size-induced defects in the wurtzite structure give rise to the charge carrier (Table 2).

The Seebeck coefficient is strongly dependent on the structure type (Fig. 8). All perovskites display positive sign of the Seebeck coefficient (S), thus indicating that the predominant mobile charge carriers are holes (*p*-type semiconductor). Contrary, the sign of the Seebeck coefficient is negative for the wurtzite phase, thus revealing that the predominant mobile charge carriers are electrons (*n*-type semiconductor). While the Seebeck coefficient remains size-independent for the perovskite phase, the wurtzite phase displays an increase in the Seebeck coefficient with particle dimensions.

The thermal conductivity is the next parameter that is independently determined for the perovskite and the wurtzite phases (Table 2). The results show that thermal conductivity does not undergo any measurable changes with variation of the particle sizes. This can be understood if we take into account the physical meaning of thermal conductivity. The thermal conductivity can be expressed by two terms due to the electronic and lattice contributions. For the oxides, the total the thermal conductivity is mainly governed by the lattice contribution. This means that the phonon scattering for the perovskite and the wurtzite structure is size-independent. The lattice contribution can be tentatively related with the carrier mobility, which is also size-independent parameter.

Taking into account the Seebeck coefficient and electrical resistivity data, the power factor is calculated: $PF=S^2/\rho$ (Table 2). In general, the comparison shows that PF is higher for the perovskite phase than the wurtzite phase. In addition, the highest PF is observed for the perovskite with bigger particle sizes. Contrary, the wurtzite phase with smaller particle sizes displays a high PF value.

In addition to PF, Table 2 gives also a calculated figure of merit. It appears that the perovskite phase with bigger particle sizes exhibits a highest thermopower activity, while the wurtzite phase with smaller particles has a better performance. This reveals that by a variation of the particle sizes it is possible to control the thermopower efficiency of the perovskite and the wurtzite phases in respect to their desired applications.

CONCLUSIONS

Two groups of compounds are studied in order to assess the effect of the particle dimensions on the thermoelectric efficiency: *p*-type semiconductor $LaCo_{0.8}Ni_{0.1}Fe_{0.1}O_3$ with a perovskite structure and *n*-type semiconductor $Zn_{0.995}Al_{0.005}O$ with a wurtzite structure. Although the bigger particles contribute to an increase in the thermopower activity of the perovskite phase, the wurtzite phase is better performed in the case when smaller particles dominate. The particle sizes affect mainly the density of charge carriers, while the carrier mobility, Seebeck coefficient and thermal conductivity are size-independents. The variation in the particle sizes has an opposite effect on the transport properties of the oxides in comparison with that of metal substitution: the metal additives reduce effectively the heat transport in the oxide matrices. This study demonstrates the capability to control the thermoelectric efficiency of oxides by rational combining of the type of crystal structure, the kind of metal dopants and sizes of the crystal particles.

REFERENCES

1. S. Hébert, D. Berthebaud, R. Daou, Y. Bréard, D. Pelloquin, E. Guilmeau, F. Gascoin, O. Lebedev, A. Maignan *J. Phys. Condensed Matter* **28** (1), (2015) art. no. 013001.
2. J. W. Fergus, *J. Europ. Ceram. Soc.*, **32,** 3, 525 (2012).
3. I. Terasaki, Y. Sasago and K. Uchinokura, *Phys. Rev. B*, **56,** 12685 (1997).
4. S. Hébert, W. Kobayashi, H. Muguerra, Y. Bréard, N. Ragavendra, F. Gascoin, E. Guilmeau and A. Maignan, *Phys. Status Solidi A*, **210,** 69 (2013).
5. R. Robert, L. Bocher, M. Trottmann, A. Reller, A. Weidenkaff, *J. of Solid State Chem.*, **179**, 3893 (2006).
6. B. T. Geraldine, C. Dewei, X. Xinrun, Li. Sean, *Current Phys. Chem.*, **4**, 256 (2014).
7. V. Vulchev, L. Vassilev, S. Harizanova, M. Khristov, E. Zhecheva, R. Stoyanova, *J. Phys. Chem. C*, **116,** 13507 (2012).
8. S. Harizanova, E. Zhecheva, V. Valchev, M. Khristov, R. Stoyanova, *Materials Today: Proceedings 2*, 4256 (2015).
9. S. Harizanova, E. Zhecheva, M. Khristov, V. Valchev, R. Stoyanova, *Bulg. Chem. Commun.*, **48,** 82 (2016).

10. Z. L. Wang, *J. Phys.: Condens. Matter*, **16,** R829 (2004).
11. T. Tsubota, M. Ohtaki, K. Eguchi, H.Arai, *J. Mater. Chem.*, **7**, 85 (1997).
12. S. Harizanova, E. Zhecheva, R. Stoyanova, V. Valchev and M. Khristov, *Materials and Technologies for Energy Efficiency*, (ISBN-10: 1-62734-559-0; ISBN-13: 978-1-62734-559-0), Publisher: BrownWalker Press, Editor: A. Méndez-Vilas, 475 (2015).
13. B. Schulz, *High Temp. High Press.* **13,** 649 (1981).
14. S. Ivanova, A. Senyshyn, E. Zhecheva, K. Tenchev, V. Nikolov, R. Stoyanova, H. Fuess, *J. Alloys and Comp.* **480**, 279 (2009).
15. S. Ivanova, A.Senyshyn, E.Zhecheva, K.Tenchev, R.Stoyanova, H. Fuess, *J. of Solid State Chem.*, **183**, 940 (2010).
16. M. M. Milanova, M. G. Arnaudov, M. M. Getsova, D. S. Todorovsky, *J. of Alloys and Comp.*, **264,** 95 (1998).

ЕФЕКТ НА РАЗМЕРА НА ЧАСТИЦИТЕ ВЪРХУ ТЕРМОЕЛЕКТРИЧНАТА ЕФЕКТИВНОСТ НА МЕТАЛ ЗАМЕСТЕНИ $LaCo_{1-x}Ni_xFe_xO_3$ ПЕРОВСКИТИ И ВЮРЦИТ $Zn_{1-x}Al_xO$

С. Г. Харизанова[1*], Е. Н. Жечева[1], В. Д. Вълчев[2], М. Г. Христов[1], П. В. Марков[1], Р. К. Стоянова[1]

[1]Институт по обща и неорганична химия, Българска академия на науките,
бул. Акад. Г. Бончев, бл. 11, София 1113, България
[2]Физически Факултет,Софийски Университет, 1164 София, България

(Резюме)

Проведеното изследване има за цел да оцени ефекта на размера на частиците върху термоелектричната ефективност на оксидни материали. Два класа от оксиди са изследвани: полупроводници от *p*-тип $LaCo_{1-x}Ni_xFe_xO_3$ с перовскитова структура и полупроводници от *n*-тип $Zn_{1-x}Al_xO$ с вюртцитна структура. Размера на частиците са варирани от 20 до 500 nm чрез увеличаване на температурата на отгряване в интервала 400 – 900 ºC. Структурното и морфологично охарактеризиране е проведено с използване на прахов рентгеново дифракционен анализ, SEM и TEM анализи. Термоелектричната ефективност е определена чрез безразмерната величина пресметната от независимо измерените коефициент на Зеебек, електрично съпротивление и термична проводимост. Резултатите показват, че размерът на частиците влияе основно върху електричната проводимост, докато коефициентът на Зеебек и термичната проводимост остават практически непроменени.

Preparation and characterization of palladium containing nickel-iron-cobalt perovskite catalysts for complete oxidation of propane

S. G. Stanchovska*, R. K. Stoyanova, E. N. Zhecheva, A. I. Naydenov

*Institute of General and Inorganic Chemistry, Bulgarian Academy of Sciences,
Acad. G. Bonchev Str., Bldg. 11, Sofia 1113, Bulgaria*

Palladium containing nickel-iron-cobalt perovskite catalysts $La(Co_{0.8}Ni_{0.1}Fe_{0.1})_{1-x}Pd_xO_3$ with x=0.05 and 0.15 were synthesized at 600 °C from citrate precursors obtained by freeze-drying. Structural and morphological characterization was carried out by XRD, BET surface measurements, TEM and XPS. The reduction properties of catalysts were examined by TPR with H_2 combined with *ex-situ* XRD measurements. The results obtained indicate formation of cobalt-based perovskite phases in which Pd ions are incorporated into the crystal structure. For the sample with the higher Pd content, traces of PdO and/or $La_2Pd_2O_5$ also appear. The oxide compositions are studied as catalysts for complete oxidation of propane as model substance of saturated hydrocarbons. The reaction parameters as light-off temperatures (for achievement of 50 % conversion, T_{50}), pre-exponential factors and the apparent activation energies were determined, internal diffusion effect being taken into account within the applied reactor model. The observed increase in the reaction rate constant when palladium is incorporated in into the perovskite structure is accordance with the concentration and forms of the palladium, exposed on the catalytic surface.

Key words: palladium, cobalt perovskites, propane, complete oxidation

INTRODUCTION

The catalytic combustion of volatile organic compounds (VOCs) is considered as one of the best methods for waste gases purification. Noble metals and transition metal oxides are intensively studied as catalysts for VOCs neutralization. The "classical" exhaust catalysts contain noble metals (Pd, Pt, Rh) for pollutant treatment. The high price of the noble metals and limited abundance, as well as their sintering ability and sensitivity to catalytic poisons, are the driving force for the development of new catalysts for VOCs neutralization. Perovskite-type oxides containing transition metals are considered to be a promising catalyst for pollution abatement because of their low cost, high activity and thermal stability, which makes them potential alternatives to noble metals. In 1972 Voorhove was the first who reported the high catalytic activity of perovskite oxides for heterogeneous oxidation [1]. These studies stimulated a lot of research that was related to exhaust control catalysts (see, for example refs. [2-4]. Perovskites are mixed oxides with general formula ABO_3, where A is usually a lanthanide ion and B is a transition metal ion. The B-site cation is surrounded octahedrally by oxygen, and the A site cation is located in the cavity made by these octahedra. Both A and B ions can be partially substituted, leading to a wide variety of mixed oxides. For complete oxidation reactions, cation B is responsible for the catalytic activity [4], while cation A, especially when partially substituted by a cation of different oxidation state, governs the stabilization of unusual oxidation states for B, leading to different catalytic performance [4-6]. It has been reported that the highest catalytic activity belongs with lanthanum as metal A and Co, Mn, Fe and Ni as metal B [2,7,8]. For oxidation of CO and hydrocarbons, $LaCoO_3$ is demonstrated to be one of the most active perovskites [9]. In the last decade the interest in the perovskite catalysts revived, due to the elaboration of the so-called "intelligent" three-way catalysts based on Pd-containing perovskite oxides [10, 11]. It was established that these catalysts display self-regenerative function under operating conditions through the interaction of Pd (or other platinum group metals) with the perovskite lattice. In response to the periodic reducing and oxidizing reaction conditions in stoichiometric engines fuelled by natural gas, Pd segregates and re-dissolve into ABO_3 lattice, thus preventing extensive particle sintering under prolonged operation at high temperature [10, 12, 13].

Generally, the catalytic activity of the "intelligent" catalysts is governed by the chemical state and redox behavior of Pd, which, on its turn, depends on the composition of the perovskite phase as well as on the feed stream composition and operating conditions. The preparation method is of crucial importance for the activity of these catalysts [14-17].

In this study we present data on the synthesis of a Pd-containing Co-based perovskite oxide and the

*   To whom all correspondence should be sent:
E-mail: stanchovska@svr.igic.bas.bg

impact of Pd additives on the catalytic oxidation of propane as model substance for saturated hydrocarbons. In the cobalt perovskite studied, Ni and Fe were partially substituted for Co, since, according to ref. [18], these compositions display improved catalytic activity as compared to pure $LaCoO_3$. In order to ensure homogeneous distribution of Co, Ni, Fe and Pd, the samples were prepared using the citrate precursor method.

EXPERIMENTAL

Homogeneous La-Co-Ni-Fe-Pd citrate precursors for the target perovskite compositions $La(Co_{0.8}Ni_{0.1}Fe_{0.1})_{1-x}Pd_xO_3$, x=0, 0.05 and 0.15, were obtained by the freeze-drying method. La-Co-Ni-Fe and La-Co-Ni-Fe-Pd citrates were prepared by adding $La(NO_3)_2.6H_2O$, $CoCO_3$, $NiCO_3$, $Fe(NO_3)_2.xH_2O$ and $Pd(NO_3).xH_2O$ 5M to a 0.1M aqueous solution of citric acid (CA). After stirring at 60 °C, a clear solution was obtained. After concentration to 0.5 M La, the solution was cooled to room temperature, then frozen instantly with liquid nitrogen and dried under vacuum at -20 °C in an Alpha-Christ freeze dryer. The thermal decomposition of the citrate precursors was achieved at 400 °C for 3h in air. The obtained solid residue was annealed at 600 °C for 3 h in air.

X-ray structural analysis was performed on a Bruker Advance 8 diffractometer with Cu Kα radiation. Step-scan recordings for structure refinement by the Rietveld method were carried out using 0.02° 2θ steps of 5 s duration.

The TEM investigations were performed on a TEM JEOL 2100 instrument at accelerating voltage of 200 kV. The specimens were prepared by grinding and dispersing them in ethanol by ultrasonic treatment for 6 min. The suspensions were dripped on standard holey carbon/Cu grids. The analysis was carried out by the Digital Micrograph software.

The XPS measurements were carried out in the UHV chamber of the electron spectrometer ESCALAB MkII (VG Scientific) using a AlKα excitation source. The spectra calibration was performed by using the C 1s line of adventitious carbon, centred at binding energy (BE) of 285.0 eV.

The specific surface area of the catalysts was determined by low temperature adsorption of nitrogen according to the BET method using Nova 1200 (Quantachrome) apparatus. Temperature programmed reduction (TPR) experiments were carried out in the measurement cell of a differential scanning calorimeter (DSC), model DSC-111 (SETARAM), directly connected to a gas chromatograph (GC), in the 300–973 K range at a 10 K/min heating rate in a flow of $Ar:H_2 = 9:1$, the total flow rate being 20 ml/min. A cooling trap between DSC and GC removes the water obtained during the reduction. To obtain the ex situ XRD patterns of the partially reduced oxides, the reduction process was interrupted at selected temperatures and then the samples were cooled down to room temperature in an $Ar:H_2$ flow followed by Ar treatment for 10 min.

The catalytic activity tests were carried out in a continuous-flow type reactor. The following testing conditions were applied: catalyst bed volume of 0.5 cm³, irregular shaped particles having an average diameter of 0.65 ± 0.15 mm, reactor diameter of 7.0 mm, quartz-glass (Dreactor/Dparticles ≥ 10). The gas hourly space velocity (GHSV) was fixed to 60 000 h^{-1}. The inlet concentration of propane was 0.1 vol. %, while the oxygen supply was kept at 20.9 vol.%. The gas mixture was balanced to 100 % with nitrogen (4.0). The gas analysis was performed using an on-line gas-analyzers of $CO/CO_2/O_2$ (Maihak) and THC-FID (total hydrocarbon content with a flame ionization detector, Horiba). For compensation of the adiabatic effect of the reaction, the catalyst bed temperature was maintained almost constant. The pressure drop of the catalytic bed was measured to be less than 2 kPa, and it was not taken into account. The axial dispersion effect was neglected as the catalyst bed is corresponding to a chain of more than 10 ideal-mixing cells along the reactor axis. Therefore the geometrical characteristics and the flow conditions of the catalytic reactor justify the conclusion that the reactor is close to the case of isothermal plug flow reactor (PFR) except for the effect of radial velocity profile inside the catalyst bed.

RESULTS AND DISSCUSIONS

Figure 1 displays the XRD diffraction patterns of $La(Co_{0.8}Ni_{0.1}Fe_{0.1})O_3$ and $La(Co_{0.8}Ni_{0.1}Fe_{0.1})_{1-x}Pd_xO_3$, x=0.05 and 0.15, obtained at 600 °C. The XRD peaks correspond to a rhombohedrally distorted perovskite phase (space group R-3c). No additional reflections are visible for $La(Co_{0.8}Ni_{0.1}Fe_{0.1})O_3$ and $La(Co_{0.8}Ni_{0.1}Fe_{0.1})_{1-x}Pd_xO_3$ with x=0.05. For $La(Co_{0.8}Ni_{0.1}Fe_{0.1})_{1-x}Pd_xO_3$ with x=0.15, additional low intensity peaks are observed which correspond to traces of impurity PdO and/or $La_2Pd_2O_5$ phases (inset of Fig. 1c).

The unit cell parameters of the perovskite phase for the three samples are listed in Table 1. The substitution of Pd for transition metal ions leads to a lattice expansion, which is in accordance with the

higher ionic radius of palladium ions (0.615 for Co^{3+} (low spin 0.545 Å), Ni^{3+} (low spin 0.56 Å, high spin 0.60 Å) and Fe^{3+} (0.645 Å).

The XRD results indicate the formation of perovskite phases in which Pd ions are incorporated

Pd^{4+} and 0.64 Å for Pd^{2+}) as compared to that of into the crystal structure. This underlines an effectiveness of the citrate-precursor method for the preparation of perovskite oxides.

Table 1. Unit cell parameters and specific surface area of La(Co$_{0.8}$Ni$_{0.1}$Fe$_{0.1}$)$_{1-x}$Pd$_x$O$_3$.

	a, Å	c, Å	V, Å^3	S, m^2/g
x=0	5.4482 (7)	13.1763 (22)	338.71 (8)	13
x=0.05	5.4479 (8)	13.1827 (23)	338.84 (9)	14
x=0.15	5.4576 (9)	13.2048 (31)	340.61 (11)	15

(a)

(b)

(c)
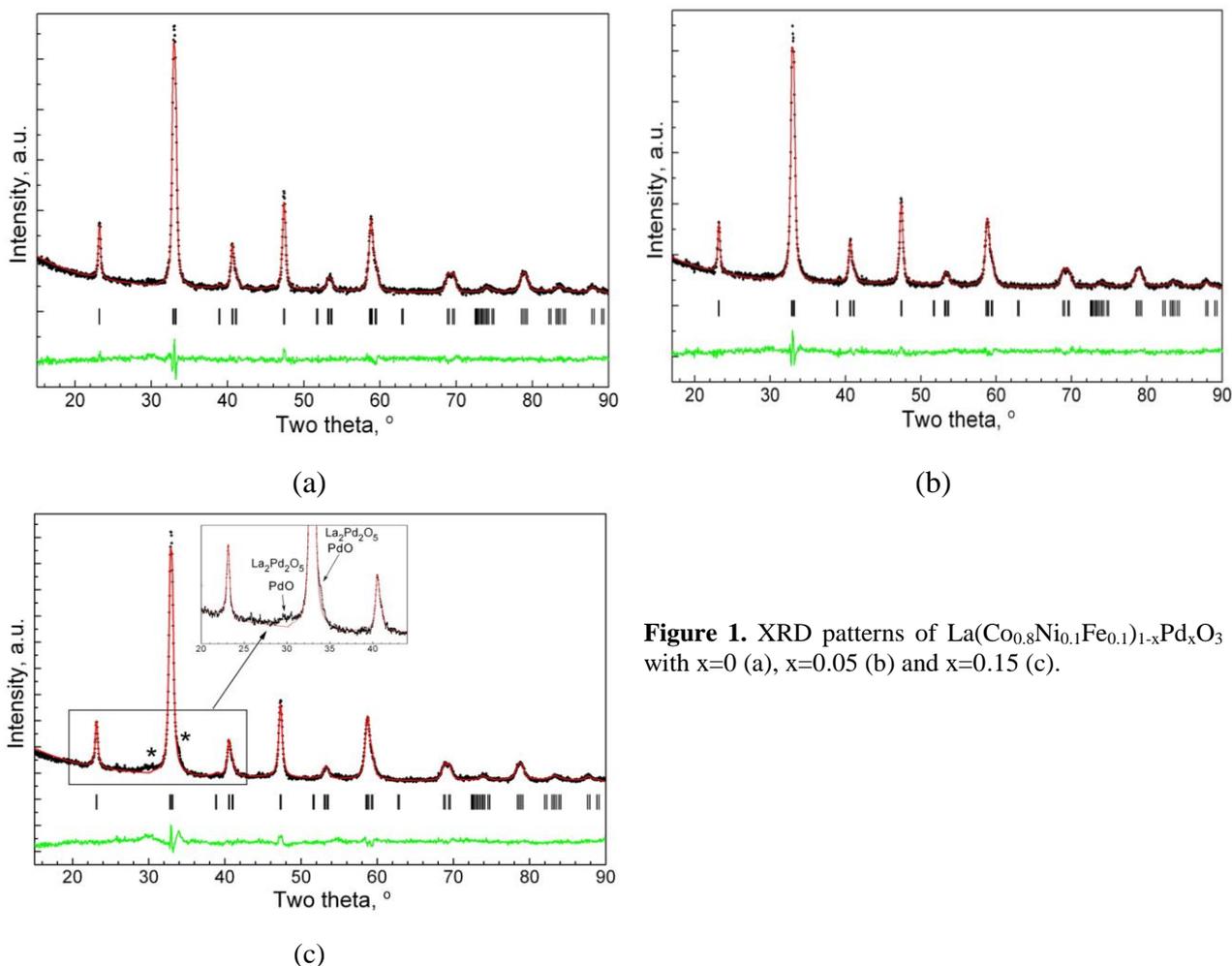
Figure 1. XRD patterns of La(Co$_{0.8}$Ni$_{0.1}$Fe$_{0.1}$)$_{1-x}$Pd$_x$O$_3$ with x=0 (a), x=0.05 (b) and x=0.15 (c).

Palladium additives poorly affect the morphology of the perovskite phase. The specific surface areas have close values (13-15 m^2/g) and the particle sizes are in the nanometer range (30-50 nm, Figs. 2a and 2b). Figures 2a and 2b show the electron diffraction images of La(Co$_{0.8}$Ni$_{0.1}$Fe$_{0.1}$)$_{1-x}$Pd$_x$O$_3$. It can be seen that both materials were polycrystalline with a rhombohedral perovskite as a main phase.

The oxidation states of Pd on the surface of the powder catalysts were analyzed by means of XPS. Figure 3 shows the Pd 3d3/2 and 3d5/2 core level spectra of La(Co$_{0.8}$Ni$_{0.1}$Fe$_{0.1}$)$_{1-x}$Pd$_x$O$_3$. For

La(Co$_{0.8}$Ni$_{0.1}$Fe$_{0.1}$)$_{0.95}$Pd$_{0.05}$O$_3$ the Pd 3d5/2 peak is located at 338.1 eV and appears symmetrical (Fig. 3a). For the sample with the higher Pd content x=0.15 the experimental spectrum of Pd 3d5/2 is asymmetrical and can be deconvoluted into two peaks centered at 338.1 and 337.2 eV, respectively (Fig. 3b). The XPS spectra of Pd in palladium-containing perovskite catalysts in their oxidized and reduced form are presented in several papers [19-21]. The unusual high Pd 3d5/2 peak observed for these catalysts at about 337.7-338.2 eV was ascribed to Pd^{3+} or Pd^{4+} species inserted in the B-site of the perovskite structure, whereas the peak

with the lower energy at 336.1-336.6 corresponds to Pd^{2+} in PdO [19-21].

This means that for the $La(Co_{0.8}Ni_{0.1}Fe_{0.1})_{0.95}Pd_{0.05}O_3$ sample Pd is mostly incorporated into the perovskite structure, whereas for $La(Co_{0.8}Ni_{0.1}Fe_{0.1})_{0.85}Pd_{0.15}O_3$ the palladium ions are distributed between the perovskite phase and a Pd-rich phase (PdO or $La_2Pd_2O_5$) , the ratio between these two Pd species being of about 2:1. The Pd concentration in the surface layer of the two samples is close to that in the bulk: 3.6 and 4.6 at. % Pd in the surface versus 1.7 and 5 at. % for the bulk composition.

The amount and the forms of Pd in $La(Co_{0.8}Ni_{0.1}Fe_{0.1})_{1-x}Pd_xO_3$ is related with their thermal reduction properties. Figure 4 compares the TPR curves with H_2 of pure $La(Co_{0.8}Ni_{0.1}Fe_{0.1})O_3$ and the Pd containing samples. The TPR profiles of $La(Co_{0.8}Ni_{0.1}Fe_{0.1})O_3$ shows two successive

(a)

(b)
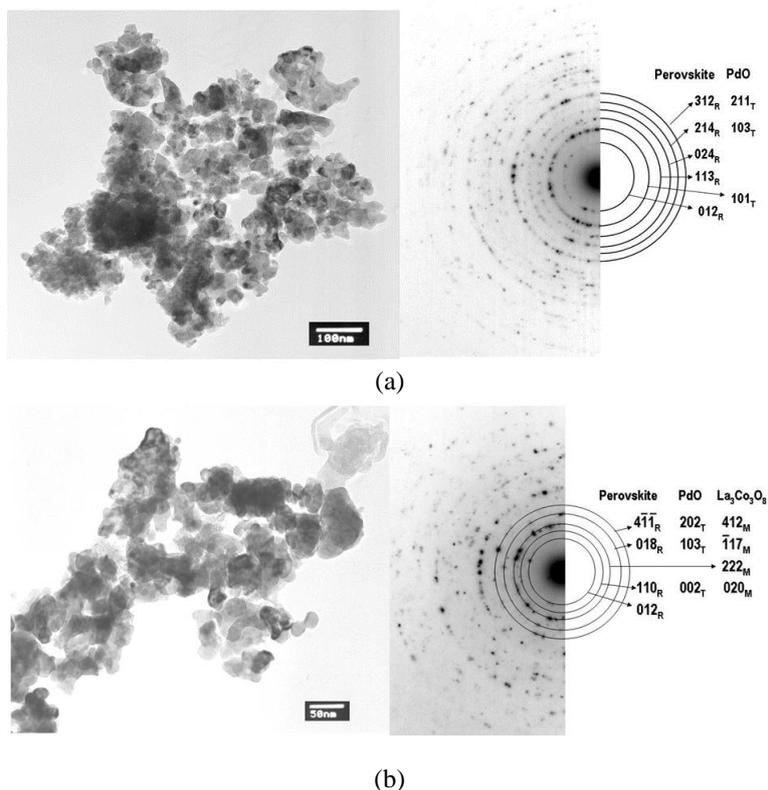
Figure 2. Bright field micrographs and polycrystalline electron diffractions of $La(Co_{0.8}Ni_{0.1}Fe_{0.1})_{0.95}Pd_{0.05}O_3$ (a) and $La(Co_{0.8}Ni_{0.1}Fe_{0.1})_{0.85}Pd_{0.15}O_3$ (b).
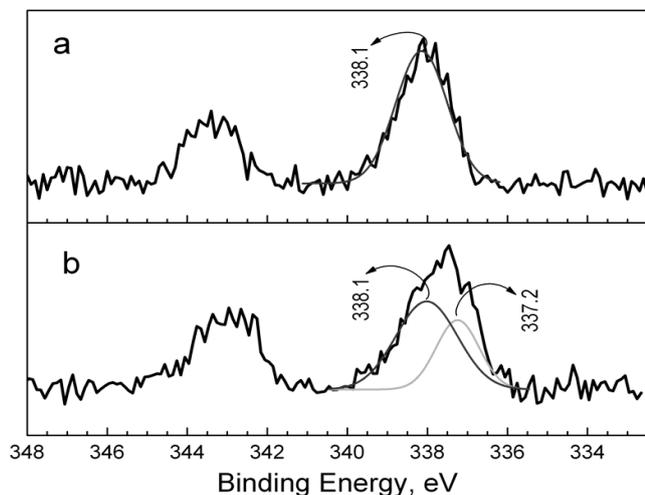
Figure 3. XPS spectra in the Pd 3d3/2 and Pd 3d5/2 regions for La $(Co_{0.8}Ni_{0.1}Fe_{0.1})_{0.95}Pd_{0.05}O_3$ (a) and La $(Co_{0.8}Ni_{0.1}Fe_{0.1})_{0.85}Pd_{0.15}O_3$ (b).

reduction peaks, the first one with T_{max}=420 ℃ and the other with T_{max}=570 ℃. It is well documented that the reduction of $LaCoO_3$ is a two-staged process including a reduction of $LaCoO_3$ to La_2O_3 and Co^0 via the formation of intermediate Brownmillerite-type phases containing Co^{2+} ions [22-25]. The presence of Pd in the catalysts shifts the reduction of the perovskite phase to lower temperatures [21, 26-29]. For $La(Co_{0.8}Ni_{0.1}Fe_{0.1})_{1-x}Pd_xO_3$ samples Pd affects only the first reduction stage: for the sample with x=0.05 the first reduction stage is shifted to significantly lower temperatures and the peak is split into three components with T_{max}=86, 155 and 209 ℃, respectively. For the sample with x=0.15 the reduction temperature is lowered remarkably, thus reaching values of T_{max} = 66 ℃ and 110 ℃, respectively (Fig. 4). It is interesting to note that for both samples the second

stage of the reduction process is not affected by the presence of Pd in the catalysts. This means that the perovskite-derived Brownmillerite phases do not contain Pd.

In the literature, the first low-temperature peak with a low-intensity appearing in TPR curves has been explained by the reduction of Pd oxide species into Pd metal whereas the other peaks have been assigned to the reduction of Co^{3+} to Co^0 via Co^{2+} [30]. It is suggested that Pd facilitates the reduction of cobalt due to spillover of the dissociated hydrogen atoms which were formed on the palladium particles [30].
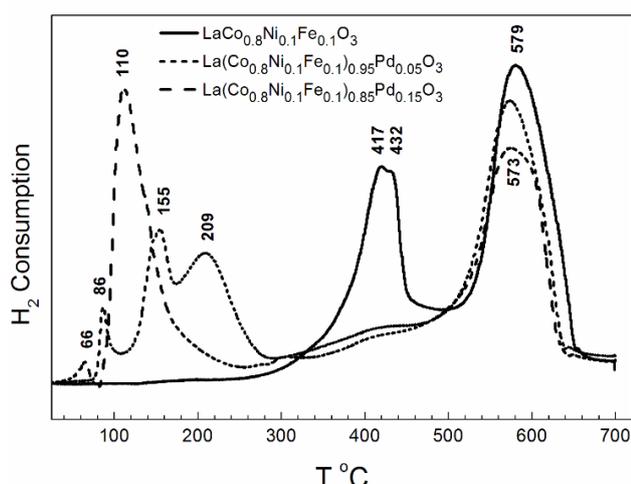
Figure 4. TPR curves for $La(Co_{0.8}Ni_{0.1}Fe_{0.1})_{1-x}Pd_xO_3$ perovskites.
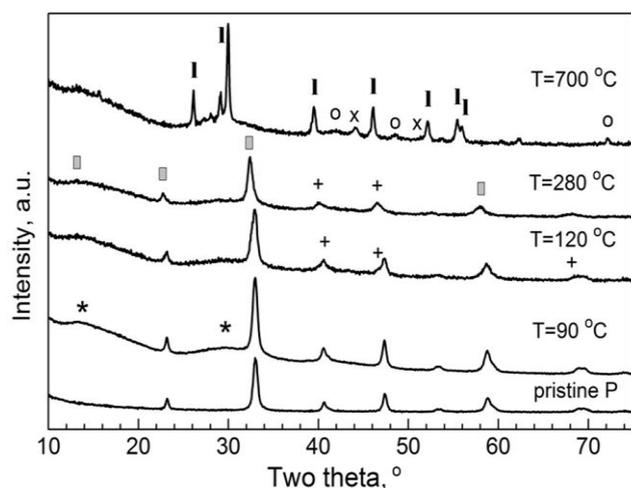
Figure 5. *ex-situ* XRD patterns of partially reduced $LaPd_{0.05}M_{0.95}O_3$. The symbols correspond to: * - $La_2Pd_2O_5$ or La_2PdO_4; + - Pd; ▣- $La_2Co_2O_5$, ❙ – La_2O_3; o – CoPd; x – Co/Ni.

To rationalize the observed difference in reducibility of $La(Co_{0.8}Ni_{0.1}Fe_{0.1})_{1-x}Pd_xO_3$, *ex-situ* XRD measurements of partially and completely reduced samples were undertaken. The reduced compositions were obtained after interrupting the reduction process at selected temperatures. The reduction of $La(Co_{0.8}Ni_{0.1}Fe_{0.1})_{0.95}Pd_{0.05}O_3$ starts below 100 °C with the separation of La-Pd oxide phases of the type $La_2Co_2O_5$ or La_2PdO_4 from the Co-perovskite matrix (Fig. 5). Reduction up to 120 °C leads to the formation of metallic Pd and oxygen-deficient perovskite phases, $LaMO_{3-\delta}$. At 280 °C, the reduction of Co^{3+} to Co^{2+} is completed and Co-brownmillerite is formed. The end products of the reduction of $La(Co_{0.8}Ni_{0.1}Fe_{0.1})_{0.95}Pd_{0.05}O_3$ are CoPd, Co/Ni metals and La_2O_3. Hence, in the case of Pd substituted perovskites, the reduction of the Pd species to metallic Pd is preceded by their separation from the perovskite phase, $La_2Pd_2O_5$ or La_2PdO_4 oxides containing Pd^{2+} being formed.

In order to examine the applicability of the synthesized materials as combustion catalysts, the reaction of complete oxidation of propane was investigated. The results from catalytic experiments are presented in Figure 6. The data from the conversion – temperature dependencies were used for fitting the kinetics parameters by using of one – dimensional pseudo-homogeneous model of plug-flow isothermal reactor [31,32].
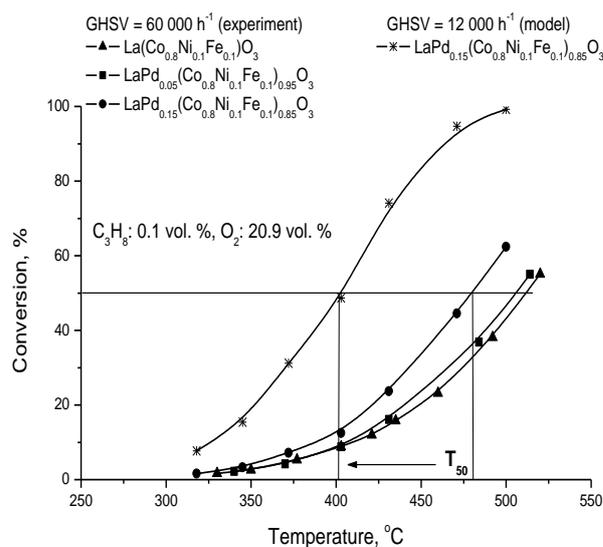
Figure 6. Dependencies of the conversion on the reaction temperature during complete oxidation of hydrocarbons on $La(Co_{0.8}Ni_{0.1}Fe_{0.1})O_3$ and $La(Co_{0.8}Ni_{0.1}Fe_{0.1})_{1-x}Pd_xO_3$, x=0.05 and 0.15.

For the calculations of the pre-exponential factors (k_o) and the apparent activation energies (E_{app}), data for conversions below 20-25 % were utilized. At such reaction conditions the calculated values for the average effectiveness factors (accounting for the irregular shaped catalyst particles) were within the limits 0.87–0.99 and therefore the effect of the internal diffusion effect had to be implemented in the reactor model by

applying of an iterative approach. The calculated reaction parameters are presented in Table 2.

The calculated values for the apparent activation energies are very close (within the limits of the experimental error), thus leading to the assumption for similarity of the reaction mechanism. Further, the model calculations show that at gas-hourly space velocity of 12 000 h^{-1} the expected T_{50} can be lowered with about 80 °C, which can be considered as a promising basis for development of catalyst for cleaning of waste gases containing saturated hydrocarbons (conversion of 99 % can be reached at 500 °C (GHSV = 12 000 h^{-1}).

Table 2. Reaction parameters for the complete oxidation of hydrocarbons on La(Co$_{0.8}$Ni$_{0.1}$Fe$_{0.1}$)O$_3$ and La(Co$_{0.8}$Ni$_{0.1}$Fe$_{0.1}$)$_{1-x}$Pd$_x$O$_3$, x = 0, 0.05 and 0.15.

Catalyst:	X = 0	X = 0.05	X =0.15
T_{50}, [°C]	511	505	479
k_o, [s^{-1}]	1.67×10^7	2.88×10^7	1.09×10^8
E_{app}, [kJ/mol]	87	89	94

As stated above, the XRD results indicate a formation of cobalt-based perovskite phases in which Pd ions are incorporated into the crystal structure. The quantitative analysis of the reaction rate parameters show that the incorporation of palladium in the basic composition with x=0.05 leads to an increase in the reaction rate constant with about 10 %, while the effect of x=0.15 is in the range of 70 %. When similar comparative analysis is applied to the Pd - containing samples only, the average increase of the reaction rate constants (Pd from x=0.05 to x=0.15) is 54 %, i.e. much less than the expected tentatively three times higher activity if the effect of the added palladium was proportional to its content. However, this result is in better accordance with the XPS – data for the concentration and forms of the palladium, exposed on the catalytic surface – the difference in the rate constants in this case is in the range of 30 % (higher being for x =0.15 sample). It should be pointed out that in our case XRD – results revealed that within the x=0.05 sample Pd is mostly incorporated into the perovskite structure, whereas for x=0.15 the palladium ions are distributed between the perovskite phase and a Pd-rich phase (PdO or La$_2$Pd$_2$O$_5$), at ratio between these two Pd species being of about 2:1. As reported by Eyssler at all [20], the highest catalytic activity for similar samples was measured for catalysts where palladium was predominantly dispersed as supported PdO particles thus stating that Pd incorporation in the perovskite-type lattice may not be favorable for methane oxidation. However, the main goal is the finding of stable palladium – based combustion catalyst and the incorporation of palladium within the perovskite-type lattice is a perspective approach to prevent sintering phenomena [20].

CONCLUSIONS

Using citrate precursors, monophase perovskite oxide La(Co$_{0.8}$Ni$_{0.1}$Fe$_{0.1}$)$_{0.95}$Pd$_{0.05}$O$_3$ can be prepared at 600 °C, in which the Pd ions are incorporated into the perovskite structure. For higher Pd content, traces of PdO and/or La$_2$Pd$_2$O$_5$ also appear .The amount and the forms of Pd in La(Co$_{0.8}$Ni$_{0.1}$Fe$_{0.1}$)$_{1-x}$Pd$_x$O$_3$ catalysts affect their thermal reduction properties. Pd has a significant effect on the reduction temperature of Co^{3+} to Co^{2+}, intermediate cobalt Brownmillerite - type phases that do not contain Pd being formed.

The observed increase in the reaction rate constant when palladium is incorporated into the perovskite structure is accordance with the concentration and forms of the palladium, exposed on the catalytic surface. Despite that the incorporation of palladium within the perovskite-type lattice leads to some lowering of the catalytic activity when compared to Pd/PdO – based samples, the applied approach for synthesis of materials with prevented sintering properties and self-regenerative function can be considered as perspective in searching of stable palladium – based combustion catalyst.

REFERENCES

1. R.J.H. Voorhove, J.P. Remeika, P.E. Freeland, B.T. Mathias, *Science*, **177**, 353 (1972).
2. T. Siyama, *Catal. Rev. – Sci. Eng.*, **34**, 281 (1992).
3. L. G. Tejuca, J. L. C. Fierro, Properties and Application of Perovskite-type Oxides, Marcel Dekker eds., New York, 1993.
4. W.B. Li, J. X. Wang, H. Gong, *Catal. Today*, **148**, 81 (2009).
5. M. S. Islam, M. Cherry, C. R. Catlow, *J. Solid State Chem.*, **124**, 230 (1996).
6. R. Leanza, I. Rossetti, L. Fabbrini, C. Oliva, L. Forni, *Appl. Catal. B*, **28**, 55 (2000).
7. S. Cimino, L. Lisi, S. De Rossi, M. Faticanti, P. Porta, *Appl. Catal. B*, **83**, 214 (2008).

8   B. Kucharczyk, W. Tylus, *Catal. Today*, **90**, 121 (2004).

9. M. A. Pena, J. L. G. Fierro, *Chem. Rev*., **101**, 1981 (2001).

10 Y. Nishihata, J. Mizuki, T. Akao, H. Tanaka, M. Uenishi, M. Kimura, T. Okamoto, N. Hamada, *Nature*, **418**, 164 (2002).

11 H. Tanaka, M. Taniguchi, M. Uenishi, N. Najita, I. Tan, Y. Nishihata, J. Mizuki, K. Narita, M. Kimura, K. Kaneko, *Angewandte Chemie*, **45**, 5998 (2006).

12. J. P. Dacquin, M. Cabie, C. R. Henry, C. Cancelot, C. Dujardun, C. R. Raout, P. G. Granger, *J. Catal.*, **270**, 299 (2010).

13. M. B. Katz, G. W. Graham, Y. Duan, H. Liu, C. Adamo, D. G. Schlom, X. Pan, *J. Amer. Chem. Soc.*, **133**, 18090 (2011).

14. E. Campagnoli, A. Tavares, L. Fabbrini, I. Rossetti, Yu.A.Dubitsky, A. Zaopo, L. Forni, *Appl. Catal. B,* **55**, 133 (2005).

15. M. M. Natile, E. Ugel, C. Maccoto, A. Glisenti, *Appl. Cat*al. *B*, **72,** 351 (2007).

16. A. E. Giannakas, A. K. Lavados, P. J. Pomonis, *Appl. Catal. B,* **49**, 147 (2004).

17. E. Tzimpilis, N. Moshoudis, M. Stoukides, P. Bekiaroglou, *Appl. Catal. B*, **84,** 607 (2008).

18. S. Stanchovska, E. Zhecheva, R. Stoyanova, A. Naydenov, unpublished results.

19. M. Uenishi, M. Taniguchi, H. Tanaka, M. Kimura, Y. Nishihata, J. Mizuki, T. Kobayashi, *Appl. Catal. B*, **57**, 267 (2005).

20. A. Eyssler, P. Mandaliev, A. Winkler, P. Hug, O. Safonova, R. Figi, A. Weidenkaff, D. Ferri, J. *Phys. Chem. C*, **114**, 4584 (2010).

21. A. Eyssler, A. Winkler, O. Safonova, M. Nachtegal, S. K. Matam, P. Hug, A. Eidenkaff, D. Ferri, *Chem. Mater.*, **24**, 1865 (2012).

22. O. H. Hansteen, H. Fjellvag, B. C.Hauback, *J. Mater. Chem.*, **8**, 2081 (1998).

23. C. L. Charello, J. –D. Grunwald, D. Ferri, F. Krumeich, C. Oliva, L. Forni, A. Baiker, *J. Catal*., **252,** 127 (2005).

24. S. Ivanova, A. Senyshyn, E. Zhecheva, K. Tenchev, R. Stoyanova, H. Fuess, *J. Solid State Chem.*, **183,** 940 (2010).

25. S. Ivanova, A. Senyshyn, E. Zhecheva, K. Tenchev, V. Nikolov, R. Stoyanova, H. Fuess, *J. Alloys Compd*., **480**, 279 (2009).

26. J. P. Dacquin, C. Dujardin, P. J. Granger, *J. Catal.*, **253**, 37 (2008).

27. S. Sartipi, A. A. Khodadadi, Y. Mortazavi, *Appl. Catal. B*, **83**, 214 (2008).

28. J.–M. Giraudon, A. Elhachimi, F. Wyrwalski, S. Siffert, A. Aboukais, J. F. Lamonier, G. Leclercq, *Appl. Catal. B,* **75**, 157 (2007).

29. H. Ziaei-Azad, A. Khodadadi, P. Esmaeilnejad-Ahranjani, Y. Mortazavi, *Appl. Catal. B*, **102**, 62 (2011).

30. W. J. Chen, M. Okumura, Y. Matsumura, M. Haruta, *Appl. Catal. A*, **213**, 225 (2001).

31. F. Duprat, *Chem. Eng. Sci.*, **57**, 901 (2002).

32. P. Harriot, Chemical Reactor Design, Marcel Dekker, Inc. (2003).

СИНТЕЗ И ОХАРАКТЕРИЗИРАНЕ НА СЪДЪРЖАЩИ ПАЛАДИЙ НИКЕЛ-ЖЕЛЯЗО-КОБАЛТОВИ ПЕРОВСКИТОВИ КАТАЛИЗАТОРИ ЗА ПЪЛНО ОКИСЛЕНИЕ НА ПРОПАН

С. Г. Станчовска[*], Р. К. Стоянова , Е. Н. Жечева, А. И. Найденов

Институт по обща и неорганична химия, Българска академия на науките, бул. Акад. Г. Бончев, бл. 11, София 1113, България

(Резюме)

Паладий-съдържащи перовскитови катализатори със състав $La(Co_{0.8}Ni_{0.1}Fe_{0.1})_{1-x}Pd_xO_3$, x=0.05 и 0.15, са синтезирани при 600 °C от лиофилизирани цитратни прекурсори. XRD, измервания на специфичната повърхност по метода на BET, TEM и XPS са използвани за структурното и морфологично охарактеризиране на образците, а редукционните им свойства са изучени чрез TPR с H_2 в комбинация с *ex-situ* XRD имервания на междинните продукти. Показано е образуването на смесени кобалтови перовскити, в които Pd йони са включени в кристалната структура. При катализатора с по-високо съдържание на Pd се наблюдават и следи от PdO и / или $La_2Pd_2O_5$. Перовскитите са изследвани като катализатори за пълно окисление на пропан като моделно съединение на наситените въглеводороди. Определени са реакционните параметри като температурата за достигане на конверсия от 50 %, предекспоненциалния фактор и наблюдаемата активираща енергия, като в използвания модел на реактор е отчетено влиянието на вътрешната дифузия. Установено е, че вграждането на паладия в перовскитовата кристална структура води до повишаване стойността на скоростната константа на реакцията, като нарастването корелира с концентрацията и формите на паладия в приповърхностния слой на катализаторите.

Effect of phase composition on the formation of active sites in titania-ceria catalysts for ethyl acetate total oxidation

G.S. Issa[1]*, M.D. Dimitrov[1], D.G. Kovacheva[2], J. Henych[3], V. Štengl[3], T.S. Tsoncheva[1]

[1]*Institute of Organic Chemistry with Centre of Phytochemistry, BAS, 1113 Sofia, Bulgaria*
[2]*Institute of General and Inorganic Chemistry, BAS, 1113 Sofia, Bulgaria*
[3]*Materials Chemistry Department, Institute of Inorganic Chemistry AS CR, Czech Republic*

The aim of current investigation is to elucidate the effect of phase composition of titanium-cerium mixed oxides on their textural, structural and surface properties. Nanosized mesoporous TiO_2-CeO_2 oxide materials were prepared by template-assisted hydrothermal synthesis using CTAB as a structure directing agent. The obtained samples were characterized by Nitrogen physisorption, X-ray diffraction, temperature-programmed reduction with hydrogen, UV-Vis, FTIR- and Raman spectroscopies. The catalytic activity of the obtained materials was tested in total oxidation of ethyl acetate as a representative member of hardly oxidized O-containing volatile organic compound (VOCs). All bi-component samples possess improved textural characteristics and redox properties due to the increased dispersion. All bi-component oxides demonstrate improved catalytic activity and selectivity in comparison with the mono-component materials in total oxidation of ethyl acetate. This could be a result of the improved textural characteristics and redox properties due to the increased particle dispersion.

Keywords: nanostructured metal oxides, ethyl acetate combustion.

INTRODUCTION

Recently, volatile organic compounds (VOCs) have gained a significant contribution to air pollution [1], which makes the control of their emissions strongly imperative. Nowadays, there are numerous different methods for VOCs elimination such as adsorption, thermal oxidation and catalytic oxidation [1, 2]. Among them, the catalytic total oxidation has been recognized as more economically efficient process for VOCs elimination even at low concentrations, reducing also the level of toxic by-products emissions in a high extent [1–4]. Transition metal oxides are one of the alternatives to noble metal-containing catalysts due to their thermal stability, low cost and high catalytic activity [2,4]. Nanostructured metal oxides have been found to be very active, both in total and selective oxidation of hydrocarbons and their catalytic properties are related to the type of metal oxide species involved in the oxidation process [5, 6]. Besides, the use of a multicomponent system could enhance the catalyst performance due to the synergism that may occur between the components. Anatase-type titanium dioxide has been extensively used in environmental applications due to its high activity, chemical stability, robustness against photocorrosion, low toxicity and availability at low cost, especially for the detoxification of water and air [7, 8]. The surface properties of TiO_2 are primarily dependent

upon various factors such as particle size, structural defects/distortion and the presence of other dopants [7]. It is well known that the properties of metal oxide can be modified by the incorporation of another metal oxide to form mixed oxides at surface level. It was established that the doping of titania with different metal oxides could improve the redox properties of the obtained nanocomposites due to the appearance of interaction and/or synergism between the components [8]. Such modifications generate novel material properties, including higher catalytic activity in various reactions. Among the doping metals, cerium species have attracted particular attention due to their excellent redox chemistry and oxygen storage capacity [8, 9]. The catalytic properties of cerium reflect two features, which are the redox couple Ce^{4+}-Ce^{3+} with the ability of cerium to shift between CeO_2 and Ce_2O_3 under oxidizing and reducing conditions, and the facile formation of labile oxygen vacancies with the relatively high mobility of bulk oxygen ions [9]. Recently, titania-ceria materials have been studied as good alternative for the oxidation catalysts and supports [8, 9]. Yang et al. [10] studied catalytic wet air oxidation (CWAO) of phenol over TiO_2–CeO_2 catalysts. They observed an increase in the efficiency of the mixed materials due to the promoting effect of ceria in the structural and redox properties of titania. They found that the catalytic activity was seriously influenced by Ti/Ce mol ratio. A lot of data in the literature aimed on the highlighting of the relationship between the

catalytic activity and the defective structure of these oxides.

The aim of current investigation is to study the catalytic behaviour of TiO_2-CeO_2 materials as catalysts in volatile organic compounds oxidation using ethyl acetate as a probe molecule. On the base of a complex study with different methods, such as Nitrogen physisorption, XRD, Raman-, FTIR-, UV-Vis spectroscopy and temperature-programmed reduction with hydrogen, the effect of Ti/Ce ratio on the structural, textural and catalytic properties of the obtained binary oxides are discussed.

EXPERIMENTAL
Materials

Titania (TiO_2) and ceria (CeO_2) materials were synthesized by template-assisted technique using hexadecyl-N,N,N-trimethyl ammoniumbromide (CTAB) as a template, hydrothermal treatment at 373 K and calcination at 773 K according to procedure described in [11]. Similar synthesis was applied for the bi-component oxides, denoted as TiCe where the Ti/Ce mol ratio was 1:1, 1:2 and 2:1.

Methods of characterization

Specific surface area (BET method) and total pore volume data were collected from nitrogen adsorption-desorption isotherms measured at 77 K using a Quantachrome NOVA 1200 apparatus. Powder X-ray diffraction patterns were collected on a Bruker D8 Advance diffractometer with Cu Kα radiation using a LynxEye detector. FTIR spectra in the region of skeletal vibrations were recorded on a Bruker Vector 22 spectrometer at a resolution of 1–2 cm^{-1}, accumulating 64–128 scans and KBr pellets technique. The UV–Vis spectra were recorded on a Jasco V-650 UV-Vis spectrophotometer equipped with a diffuse reflectance unit. Raman spectra were acquired with a DXR Raman microscope (Thermo Fischer Scientific, Inc., Waltham, MA) using a 780 nm laser. The TPR/TG analyses were performed on a Setaram TG92 instrument using a flow (100 cm3 min-1) of 50 vol. % H_2 in Ar and a heating rate of 5 K min-1.

Catalytic oxidation of ethyl acetate

The catalytic oxidation of ethyl acetate was performed in a flow type of microreactor, 0.030 g of the catalyst diluted with crash glass (weight ratio of 1:3), particle size of 0.3–0.6 mm and catalytic bed volume of about 0.5 cm with a mixture of ethyl acetate in air (1.21 mol %) and WHSV of 100 h-1. Before the catalytic activity experiments the samples were treated in argon at 373 K for 1 h. Gas chromatographic analyses were done on a HP 5890

apparatus using carbon-based calibration. The products distribution was calculated as selectivities to CO_2 (S_{CO2}), acetaldehyde (S_{AA}), ethanol (S_{Et}) and acetic acid (S_{AcAc}) calculated by the equation: $S_i = Y_i/X*100$, where S_i and Y_i were the selectivity and the yield of (i) product and X was the conversion value.

RESULTS AND DISCUSSION

In order to obtain information for the textural characteristics of the studied materials, nitrogen physisorption measurements are done (Table 1). According to IUPAC classification the acquired isotherms are of type IV, typical of materials with mesoporous structure (not shown) which could be expected when using CTAB as a structure-directing agent during synthesis and/or obtain a material comprised of nanosized particles. All obtained materials are characterized with high BET specific surface area and total pore volume. The addition of ceria to titania leads to an increase in the surface area and pore volume of the bi-component systems (Table 1). This effect is more pronounced for 8Ti2Ce sample. Note, that the BET surface area of all mixed oxide samples overcomes that one if the samples were mechanical mixtures of the individual oxides. This suggests interaction between the studied metal oxides.

Table 1. Nitrogen physisorption data and specific catalytic activity (T=600 K) of studied materials.

Sample	BET m^2/g	Total Pore Volume ml/g	Specific catalytic activity (SA)
CeO_2	46	0,26	1,76
TiO_2	85	0,28	0,29
2Ti8Ce	55	0,29	1,01
5Ti5Ce	99	0,45	0,61
8Ti2Ce	166	0,62	0,39
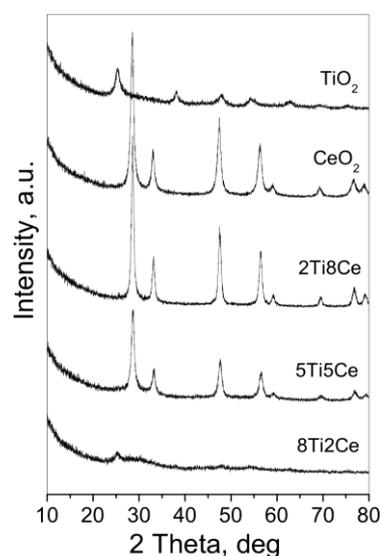
Figure 1. XRD patterns of TiO_2, CeO_2 and TiCe materials.

Fig. 1 shows the X-ray diffraction patterns of titania-ceria materials. For pure TiO_2, only reflections of anatase titania ($2\theta=25.6°$, $38.3°$, $47.8°$ and $62.5°$) were detected [12] (Fig. 1, Table 2). In bi-component material with high titanium content (8Ti2Ce), the reflections of anatase are still present and no reflections of ceria are observed. With further increase of Ce content the former reflections become weaker and the wider. This indicates a the decrease in the crystal size of TiO_2 with the increase of Ce content in the samples (Table 2). This can be due to large lattice distortion resulting from the cerium addition. For pure CeO_2, the strong reflections are attributed to cubic fluorite-like

structure ($2\theta = 28.5°$, $33.1°$, $47.5°$, $56.3°$ and $69.4°$) [13]. For the Ce-rich sample (2Ti8Ce), no titanium oxide phases are detected. In this sample, the registered diffraction reflections are characteristic of cerianite CeO_2 and they are slightly shifted to higher Bragg angles, which is due to a slight decrease of the ceria unit cell parameter (Table 2). Taking into account that the radius of Ti^{4+}-ion is 0.74 Å, CN=6 and that one for Ce^{4+}-ion is 0.97 Å, CN=6, the latter observation could be due to the incorporation of smaller Ti^{4+}-ions into the ceria lattice [14, 15]. However, the observed results are insufficient to assume formation of a solid solution with cerianite structure as was reported in [16].

Table 2. XRD data for TiO_2, CeO_2 and TiCe materials.

Sample	Space Group	Unit cell	Particles size, nm
TiO₂	Anatase, syn	3.7861	17.4
	Tetragonal – Body-centered I41/amd	9.493	
CeO₂	Cerium oxide	5.416	10.0
	Cubic - Face center - Fm-3m (225)		
2Ti 8Ce	Anatase, syn		
	Tetragonal – Body-centered I41/amd		
	Cerium oxide		
	Cubic - Face center - Fm-3m (225)	5.409	17.0
5Ti5Ce	Anatase, syn	3.782	< 5
	Tetragonal – Primitive P42/mnm (136)	9.514	
	Cerium oxide		
	Cubic - Face center - Fm-3m (225)		
		5.403	12.0
8Ti2Ce	Anatase, syn	-	-
	Tetragonal – Primitive P42/mnm (136)		
	Cerianite (Ce), syn		
	Cubic - Face center - Fm-3m (225)		
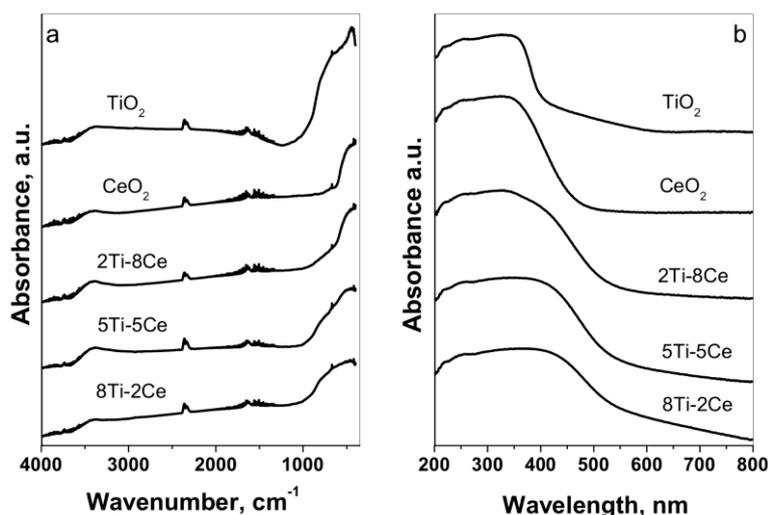
Figure 2. FTIR spectra (a) and UV-Vis spectra (b) of TiO_2, CeO_2 and TiCe materials.

In order to obtain more information about the state of various metal oxide species, FTIR measurements were also done (Fig. 2a). For the pure TiO_2 sample, the peaks at 460, 620 and the shoulder at 910 cm^{-1}, typical of anatase titania are registered (Fig. 2a) [14]. The broad and intensive band below 700 cm^{-1} observed for the pure CeO_2 sample is related to the Ce–O bond vibrations. The band around 1600 cm^{-1} is due to adsorbed water molecules [17]. The broad band in the interval 3100–3700 cm^{-1} is assigned to O-H stretching vibrations. The variations in the intensity of these peaks in the FTIR spectra of the bi-component samples with cerium content implies that a possible interaction of ceria with titania provides differences in the surface defects, which reflects on the amount of surface hydroxyl groups and adsorbed water.

The diffuse reflectance UV-Vis spectra were further recorded (Fig. 2b), since this technique is very sensitive to obtain more information for the environment of metal ions. The strong absorption feature in the UV-Vis spectrum of pure TiO_2 (Fig. 2b) at 350 nm is due to d-d electronic transition between Ti^{4+}-ion and O^{2-} ligand in anatase [18], which is consistent with the observation from XRD. The absorption in 300-500 nm range which is registered in the spectra of CeO_2 sample corresponds to $Ce^{4+} \leftarrow O^{2-}$ charge transfer (CT) [19]. The band at 250 nm could be due to the $O^{2-} \rightarrow Ce^{3+}$ CT transitions, which implies the occurrence of oxygen vacancy defects. In accordance with the XRD and nitrogen physisorption data, the observed changes in the 350–500 nm region for all bi-component materials confirm the assumption done above for the existence of strong interaction between the different metal ions and/or the increase in the metal oxides dispersion.
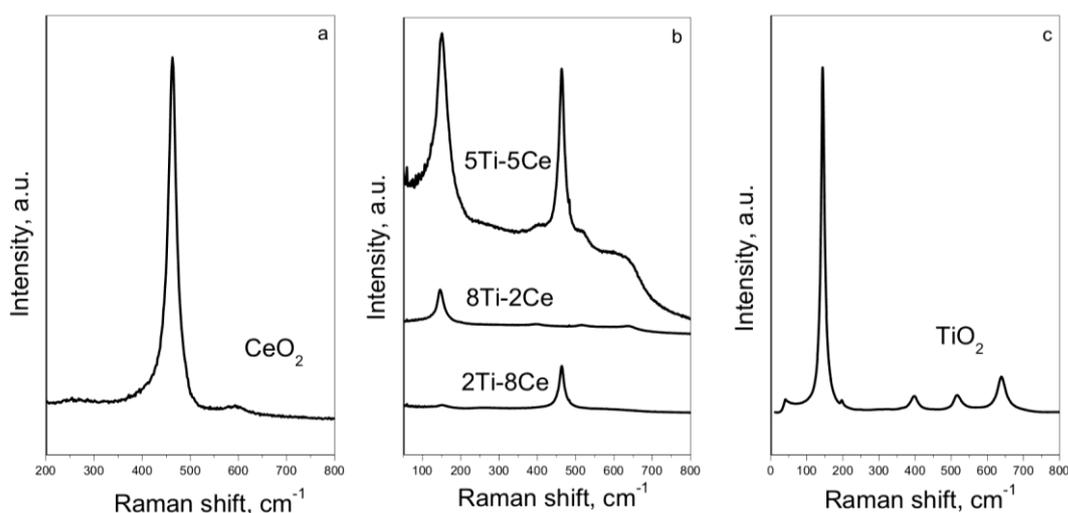
Figure 3. Raman spectra of CeO_2 (a), TiO_2 (b) and TiCe (c) materials.
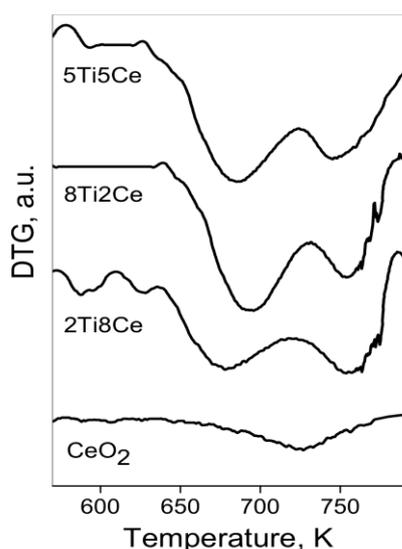
Figure 4. TPR–DTG profiles of TiO_2, CeO_2 and TiCe materials.

In order to obtain more information for the type of interaction between the metal oxide nanoparticles, Raman spectra were recorded (Fig. 3). The spectrum of pure TiO_2 sample (Fig. 3c) presents the main peaks at 149, 198, 398, 515 and 644 cm^{-1}, typical of anatase TiO_2 structure [20]. In case of the mixed samples, the observed decrease in the intensity of the main peak, typical of titanium oxide accompanied with its slight broadening could be due to particle size decrease, which is in accordance with the XRD data (Fig. 1, Table 2). The spectrum of CeO_2 consists of intense peak at 463 cm^{-1}, which is assigned to F2g mode of CeO_2 fluorite structure (Fig. 3a) [21]. The appearance of an additional intense and weak broad band at about 600 cm^{-1} is assigned to the formation of oxygen vacancies [15, 20]. For the bi-component materials, a slight shifting and broadening of the main Raman-active mode accompanied with a decrease

in its intensity is detected (Fig. 3b). This could be assigned to partial replacement of Ce ions with Ti ones, resulting in Ce-O bonds shortening and formation of smaller crystallites with defect structure. In the case of 8Ti2Ce sample, no peaks are observed for CeO_2. According to XRD and UV-Vis data, we assign these effect to the improved metal oxide dispersion and/or the formation of mixed oxide phases.

Fig. 4 presents the TPR-DTG profiles of the samples treated in hydrogen. In case of pure ceria (Fig. 4), the registered weight loss corresponds to about 14 % reduction of Ce^{4+} to Ce^{3+}. The reduction effect for the bi-components samples is larger in comparison with pure CeO_2 and starts at lower temperature. In accordance with the physicochemical measurements, the observed effects indicate increased mobility of lattice oxygen. This effect is especially well pronounced for the sample with the lowest Ce content.

In Figure 5 is presented the evolution of the catalytic behaviour of mono- and bi-component materials in oxidation of ethyl acetate with time on stream at selected temperature (600 K). Beside CO_2 which is the most important product of ethyl acetate oxidation, ethanol (EtOH), acetaldehyde (AA) and acetic acid (AcAc) are also registered as by-products. The catalytic properties of pure CeO_2 remain almost unchanged during the whole investigated interval (Fig. 5), however, it exhibits low selectivity to ethyl acetate total oxidation (27 %), while ethanol (47%) is detected as the main by-product. At the same time, well defined tendency of a decrease in the catalytic activity after two hours of time-on-stream was observed for the pure TiO_2 sample that could be due to the release of hardly desorbable carbon based by-products (Fig. 5). The TiO_2 sample demonstrated high selectivity

to CO_2 in the first two hours of the reaction (Fig. 5b), and then the selectivity steeply decreased at the expense of by-products formation, mainly AA (25 %), EtOH (22 %) and ethane (18 %) at 600 K. No changes in the catalytic activity with time on stream are registered for all bi-component materials (Fig. 5a). Note that all bicomponent materials represent better catalytic activity than the corresponding mono-component ones. Taking into account the physicochemical data we assign this result to the considerable improvement in the textural characteristics of the mixed oxide materials and/or to the presence of more active mixed oxide phase. In order to ignore the effect of different specific surface area of the samples (Table 1), the specific catalytic activity was calculated as conversion at selected temperature (600 K) per unit surface area (Table 1). The obtained results demonstrate well defined tendency for specific activity increase with ceria content for the bi-component samples and extremely high value is observed for the pure CeO_2. Thus the facilitated effect of doping of titania with cerium is not in simple relation with the increased specific surface area of metal oxides, as a result of the improved dispersion of the individual oxides. Moreover, TPR results clearly indicate presence of more readily reducible particles in bi-components materials (Fig. 4). In accordance with the XRD and Raman analyses, the improved reducibility of the mixed oxides could be due to the incorporation of Ti^{4+} ions into the ceria lattice. This weakens the Ce–O bond and promotes the mobility of bulk oxygen in CeO_2. As reported by Russo et al. [22], the lattice oxygen plays a crucial role in the VOCs oxidation catalysis *via* Mars-van Krevelen mechanism, which was also discussed for total oxidation of ethyl acetate [23].
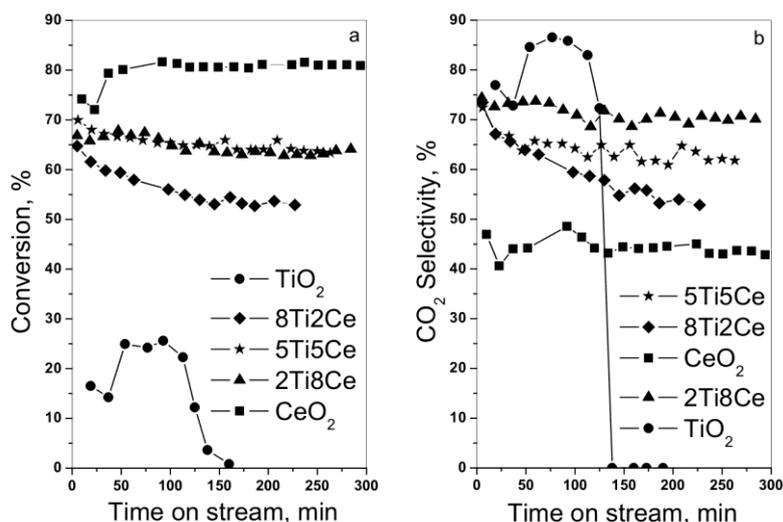
Figure 5. Ethyl acetate conversion (a) and selectivity to CO_2 (b) with time on stream at 600K of TiO_2, CeO_2 and TiCe materials.

In conclusion, as compared to the mono-component materials, bi-component ones were characterized with higher dispersion, better textural parameters and improved redox properties. This affects the catalytic activity and selectivity of the samples in ethyl acetate combustion, which could be successfully controlled by the Ti/Ce ratio. The formation of these finely dispersed mixed oxide crystallites promotes ethyl acetate oxidation *via* Mars van Krevelen mechanism, where the release of lattice oxygen is of primary importance. The increase in the Ti/Ce ratio for these materials promotes the segregation of finely dispersed and easily reducible mixed oxide nanoparticles which has a beneficial effect on the catalytic activity. Further investigation is in progress.

CONCLUSIONS

To obtain new insight into the structure–activity relationships for the titania-ceria mixed oxides, a series of mono-component and bi-component TiO_2–CeO_2 samples with different Ti/Ce molar ratios have been synthesized. Well defined effect of metal oxide dispersion improvement is registered for all bi-component systems. The strong interaction between CeO_2 and TiO_2 as well as the crystallization of particles in the nanoscale obviously improve the redox properties of the TiO_2–CeO_2 mixed oxides. All bi-component oxides demonstrate improvement in the catalytic activity and selectivity in comparison with the mono-component ones. In addition, the high specific surface area of CeO_2–TiO_2 mixed oxides also play an important role in enhancing their catalytic performance in the total oxidation of ethyl acetate.

REFERENCES

1. C.Y. Lu, M.Y. Wey, L.I. Chen, *Appl. Catal. A: Gen.,* **325**, 163 (2007).
2. J. Okal, M. Zawadzki, *Appl. Catal. B: Environ.,* **89**, 22 (2009).
3. D. Delimaris, T. Ioannides, *Appl. Catal. B: Environ.,***89**, 295 (2009).
4. P. Papaefthimiou, T. Ioannides, X.E. Verykios, *Appl. Therm. Eng.,* **18**, 1005 (1998).
5. F. Bertinchamps, C. Gregoire, E.M. Gaineaux, *Appl. Catal. B* **66**, 10 (2006).
6. Ch.-H. Wang, Sh.-Sh. Lin, Ch.-L. Chen, H.-Sh. Weng, *Chemosphere,* **64**, 503 (2006).
7. I.D. Gonzàlez, R.M. Navarro, W. Wen, N. Marinkovic, J.A. Rodriguèz, F. Rosa, J.L.G. Fierro, *Catal. Today,* **149**, 372 (2010).
8. G. Schmid, M. Baumle, M. Greekens, I. Heim, C. Osemann, T. Sawatowski, *Chem. Soc. Rev.,* **28**, 179 (1999).
9. Li, F.B., Li, X.Z., Hou, M.F., Cheah, K.W., Choy, W.C.H., *Appl. Catal. A*, **285**, 181 (2005).
10. S. Yang, W. Zhu, J. Wang, Z. Chen, *J. Hazard. Mater.,* **153**, 1248 (2008).
11. T. Tsoncheva, L. Ivanova, D. Paneva, I. Mitov, C. Minchev, M. Fröba, *Micropor. Mesopor. Mater.,* **120**, 389 (2009).
12. M. Altomare, M.V. Dozzi, G.L. Chiarello, A.D. Paola, L. Palmisano, E. Selli, *Catal. Today,* **252**, 184 (2015).
13. B. Zhao, B. Shi, X. Zhang, X. Cao, Y. Zhang, *Desalination,* **268**, 55 (2011).
14. H. Nur, *Mater. Sci. Eng. B – Sol* **133**, 49 (2006).
15. S. Yuesong , Z. Dahai, Y. Bo, N. Songbo, Z. Shemin, *J. Rare Earths*, **30**, No. 5, 431 (2012).
16. M.F. Luo, J.C.L.S. Chen, J.Q. Lu, Z.C. Feng, C. Li, *Chem. Mater.,* **13**, 197 (2001).
17. P. Innocenzi, *J. Non-Cryst. Solids* **316**, 309 (2003).
18. I. Nitoi, P. Oancea, M. Raileanu, M. Crisan, L. Constantin, I. Cristea, *J. Ind. Eng. Chem.,* **21**, 677 (2015).
19. L. Katta, P. Sudarsanam, G. Thrimurthulu, B.M. Reddy, *Appl. Catal. B: Environ.,* **101**, 101 (2010).
20. T. Kidchob, P. Falcaro, P. Schiavuta, S. Enzo, P. Innocenziw, *J. Am. Ceram. Soc.,* **91**, 2112 (2008).
21. G. Vlaic, R.D. Monte, P. Fornasiero, E. Fonda, J. Kaspar, M. Graziani, *J. Catal.* **182**, 378 (1999).
22. M. Piumetti, S. Bensaid, N. Russo, D. Fino, *Appl. Catal. B,* **180**, 271 (2016).
23. P.-O. Larsson, A. Andersson, *Appl. Catal. B* ,**24**, 175 (2000).

ВЛИЯНИЕ НА ФАЗОВИЯ СЪСТАВ ВЪРХУ ФОРМИРАНЕТО НА АКТИВНИ ЦЕНТРОВЕ В ТИТАН-ЦЕРИЕВИ КАТАЛИЗАТОРИ ЗА ПЪЛНО ОКИСЛЕНИЕ НА ЕТИЛАЦЕТАТ

Г.С. Исса[1]*, М. Д. Димитров[1], Д. Г. Ковачева[2], И. Хених[3], В. Щенгъл[3], Т. С. Цочева[1]

[1]Институт по органична химия с Център по фитохимия, БАН
[2]Институт по обща и неорганична химия, БАН
[3]Институт по неорганична химия, Чехия

(Резюме)

Цел на настоящото изследване е да се изясни влиянието на състава на получените титан-церий смесени оксиди върху техните текстурни, структурни и повърхностни свойства. За целта са получени титан-церий смесени оксиди чрез хидротермален синтез в присъствието на органичен темплейт. Образците са характеризирани с различни физикохимични техники – физична адсобция на азот, прахова ренгенова дифракция, дифузионно-отражателна ултравиолетова, инфрачервена и раман спектроскопии, както и температурно-програмирана редукция с водород. Каталитичната им активност е тествана в реакция на пълно окисление на етилацетат, като представител на трудноокисляемо О-съдържащо летливо органично съединение. Всички получени материали са добре кристални като бикомпонентните се характеризират с подобрени текстурни характеристики в сравнение с монокомпонентните оксиди, вследствие увеличаване дисперсността на изграждащите ги наночастици и техния значително по-голям поров обем. Показано е и наличие на взаимодействие между металните оксиди в смесените образци. Тези резултати благоприятстват каталитичното поведение на бикомпонентните образци в изследваната реакция и разкриват техния потенциал за елиминиране на токсични газови емисии.

BULGARIAN CHEMICAL COMMUNICATIONS

Instructions about Preparation of Manuscripts

General remarks: Manuscripts are submitted in English by e-mail or by mail (in duplicate). The text must be typed double-spaced, on A4 format paper using Times New Roman font size 12, normal character spacing. The manuscript should not exceed 15 pages (about 3500 words), including photographs, tables, drawings, formulae, etc. Authors are requested to use margins of 3 cm on all sides. For mail submission hard copies, made by a clearly legible duplication process, are requested. Manuscripts should be subdivided into labelled sections, e.g. **Introduction, Experimental, Results and Discussion**, *etc*.

The title page comprises headline, author's names and affiliations, abstract and key words.

Attention is drawn to the following:

a) **The title** of the manuscript should reflect concisely the purpose and findings of the work. Abbreviations, symbols, chemical formulas, references and footnotes should be avoided. If indispensable, abbreviations and formulas should be given in parentheses immediately after the respective full form.

b) **The author**'s first and middle name initials, and family name in full should be given, followed by the address (or addresses) of the contributing laboratory (laboratories). **The affiliation** of the author(s) should be listed in detail (no abbreviations!). The author to whom correspondence and/or inquiries should be sent should be indicated by asterisk (*).

The abstract should be self-explanatory and intelligible without any references to the text and containing not more than 250 words. It should be followed by key words (not more than six).

References should be numbered sequentially in the order, in which they are cited in the text. The numbers in the text should be enclosed in brackets [2], [5, 6], [9–12], etc., set on the text line. References, typed with double spacing, are to be listed in numerical order on a separate sheet. All references are to be given in Latin letters. The names of the authors are given without inversion. Titles of journals must be abbreviated according to Chemical Abstracts and given in italics, the volume is typed in bold, the initial page is given and the year in parentheses. Attention is drawn to the following conventions:

a) The names of all authors of a certain publications should be given. The use of "*et al*." in the list of references is not acceptable.

b) Only the initials of the first and middle names should be given.

In the manuscripts, the reference to author(s) of cited works should be made without giving initials, e.g. "Bush and Smith [7] pioneered...". If the reference carries the names of three or more authors it should be quoted as "Bush *et al*. [7]", if Bush is the first author, or as "Bush and co-workers [7]", if Bush is the senior author.

Footnotes should be reduced to a minimum. Each footnote should be typed double-spaced at the bottom of the page, on which its subject is first mentioned.

Tables are numbered with Arabic numerals on the left-hand top. Each table should be referred to in the text. Column headings should be as short as possible but they must define units unambiguously. The units are to be separated from the preceding symbols by a comma or brackets.

Note: The following format should be used when figures, equations, *etc*. are referred to the text (followed by the respective numbers): Fig., Eqns., Table, Scheme.

Schemes and figures. Each manuscript (hard copy) should contain or be accompanied by the respective illustrative material as well as by the respective figure captions in a separate file (sheet). As far as presentation of units is concerned, SI units are to be used. However, some non-SI units are also acceptable, such as °C, ml, l, etc.

The author(s) name(s), the title of the manuscript, the number of drawings, photographs, diagrams, etc., should be written in black pencil on the back of the illustrative material (hard copies) in accordance with the list enclosed. Avoid using more than 6 (12 for reviews, respectively) figures in the manuscript. Since most of the illustrative materials are to be presented as 8-cm wide pictures, attention should be paid that all axis titles, numerals, legend(s) and texts are legible.

The authors are asked to submit **the final text** (after the manuscript has been accepted for publication) in electronic form either by e-mail or mail on a 3.5'' diskette (CD) using a PC Word-processor. The main text, list of references, tables and figure captions should be saved in separate files (as *.rtf or *.doc) with clearly identifiable file names. It is essential that the name and version of

the word-processing program and the format of the text files is clearly indicated. It is recommended that the pictures are presented in *.tif, *.jpg, *.cdr or *.bmp format, the equations are written using "Equation Editor" and chemical reaction schemes are written using ISIS Draw or ChemDraw programme.

The authors are required to submit the final text with a list of three individuals and their e-mail addresses that can be considered by the Editors as potential reviewers. Please, note that the reviewers should be outside the authors' own institution or organization. The Editorial Board of the journal is not obliged to accept these proposals.

EXAMPLES FOR PRESENTATION OF REFERENCES

REFERENCES

1. D. S. Newsome, *Catal. Rev.–Sci. Eng*., **21**, 275 (1980).
2. C.-H. Lin, C.-Y. Hsu, *J. Chem. Soc. Chem. Commun*., 1479 (1992).
3. R. G. Parr, W. Yang, Density Functional Theory of Atoms and Molecules, Oxford Univ. Press, New York, 1989.
4. V. Ponec, G. C. Bond, Catalysis by Metals and Alloys (Stud. Surf. Sci. Catal., vol. 95), Elsevier, Amsterdam, 1995.
5. G. Kadinov, S. Todorova, A. Palazov, in: New Frontiers in Catalysis (Proc. 10th Int. Congr. Catal., Budapest, 1992), L. Guczi, F. Solymosi, P. Tetenyi (eds.), Akademiai Kiado, Budapest, 1993, Part C, p. 2817.
6. G. L. C. Maire, F. Garin, in: Catalysis. Science and Technology, J. R. Anderson, M. Boudart (eds), vol. 6, Springer-Verlag, Berlin, 1984, p. 161.
7. D. Pocknell, *GB Patent* 2 207 355 (1949).
8. G. Angelov, PhD Thesis, UCTM, Sofia, 2001.
9. JCPDS International Center for Diffraction Data, Power Diffraction File, Swarthmore, PA, 1991.
10. CA **127**, 184 762q (1998).
11. P. Hou, H. Wise, *J. Catal.*, in press.
12. M. Sinev, private communication.
13. http://www.chemweb.com/alchem/articles/1051611477211.html.

CONTENTS

СЪДЪРЖАНИЕ